An Integrated Aerodynamic-Ramp-Injector/ Plasma-Torch-Igniter for Supersonic Combustion Applications with Hydrocarbon Fuels

Lance S. Jacobsen

Dissertation submitted to the Faculty of the
Virginia Polytechnic Institute and State University
in partial fulfillment of the requirements for the degree of

Doctor of Philosophy
In
Aerospace Engineering

J. A. Schetz, Chair
W. F. O'Brien
B. Grossman
A. K. Jakubowski
U. Vandsburger

April 16, 2001
Blacksburg, Virginia

Keywords: Supersonic Combustion, Mixing, Plasma Torch, Scramjet, Hypersonic Propulsion, Fuel Injection

An Integrated Aerodynamic-Ramp-Injector/ Plasma-Torch-Igniter for Supersonic Combustion Applications with Hydrocarbon Fuels

Lance S. Jacobsen

(Abstract)

The first integrated, flush-wall, aero-ramp-fuel-injector/plasma-torch igniter and flame propagation system for supersonic combustion applications with hydrocarbon fuels was developed and tested. The main goal of this project was to develop a device which could be used to demonstrate that the correct placement of a plasma-torch-igniter/flame-holder in the wake of the fuel jets of an aero-ramp injector array could make sustained, efficient supersonic combustion with low losses and thermal loading possible in a high enthalpy environment. Three phases of research were performed to develop the device using the supersonic cold flow facilities at Virginia Tech. The experimental investigations included some of the following methods: shadowgraphs, surface oil flow, pressure-sensitive paint, high- or low-speed photography, aerothermodynamic sampling, and spectroscopy. During this research effort, a new mixing parameter was also developed to quantify the injector plume mass fraction concentration values using successive profiles of ambient or heated air as the injectant.

The first phase of the research effort was conducted at Mach 3.0 at a static pressure and temperature of 0.19 atm and 101 K. This phase involved component analyses to improve on the designs of the aero-ramp and plasma-torch as well as address integration and incorporation difficulties. The information learned from these experiments lead to the creation of the first prototype integrated aero-ramp/plasma torch design featuring a new simplified four-hole aero-ramp design.

The second phase of the project consisted of experiments at Mach 2.4 involving a cold-flow mixing evaluation of the new aero-ramp design and a resizing of the device for incorporation into a scramjet flow path test rig at the Air Force Research Laboratories (AFRL). Experiments were performed at a static pressure and temperature of 0.25 atm and 131 K, and at injector-jet to freestream momentum flux ratios ranging from 1.0 to 3.3. Results showed the aero-ramp to mix at a considerably faster rate than the injector used in the AFRL baseline combustor configuration due to high levels of vorticity created by the injector array. In addition, the plume of the aero-ramp lifted off the test section wall without trapping a secondary core inside the shear layer near the surface, unlike the earlier nine-hole aero-ramp arrays. The mitigation of the secondary fuel core leads to a lower level of combustion near the surface and a lower potential for thermal loading on the wall.

The last phase of the research involved testing the final device design in a cold-flow environment at Mach 2.4 with ethylene fuel injection and an operational plasma torch with methane, nitrogen, a 90-percent nitrogen 10-percent hydrogen (by volume) mixture, and air feedstock gases. Experiments were performed with injector jet to freestream momentum flux ratios ranging from 1.4 to 3.3, and 1.2 with the plasma torch at a nominal power level 2000 watts. Overall, the final integrated design showed a high mixing efficiency and a higher potential for repeatable main fuel ignition and flame propagation with the plasma torch placed at the middle of the three downstream torch stations tested ($x/d_{injector}$ = 8 downstream from the center of the injector area), with nitrogen as the torch feedstock. Furthermore, the integrated device created a sustained flame, demonstrating main fuel ignition in a cold and low pressure supersonic environment with a plasma-torch. Local intensity distributions of the major excited species generated from the interaction of the plasma-torch with the main fuel plume were also identified with a spectrometer. As a result of the research and development process, an injector block for scramjet combustor experiments consisting of four integrated aero-ramp-injector/plasma-torch-igniters was created for near future tests at the AFRL.

Acknowledgements

First and foremost, I would like to thank my advisor, Dr. Joseph Schetz, for his guidance and support through both my undergraduate and graduate years at Virginia Tech. Through the last four and a half years, working with him I have learned a lot about the art of research and heard quite a few memorable stories. I hope that I too have partaken in one or two memorable (hopefully positive) new stories for him to tell his future students.

I would also like to thank Dr. Walter O'Brien and my research partner Scott Gallimore for their efforts and support during the project. In addition, I would like to thank Ross Stilling for his high-quality and enthusiastic help with the various odd jobs that I gave him.

During my time at Virginia Tech, I also had an opportunity to work with Dr. Sadatake Tomioka from the NAL in Kakuda, Japan. I would like to thank him for his guidance, assistance, excellent work ethic, and friendship that developed in the year that we worked together.

My thanks also go out to Gary Stafford for his knowledge of electronics and operation of the supersonic wind tunnel lab and compressor. Without his knowledge of the wind tunnel facility, I doubt that anything would have run.

I would also like to thank the AOE Machine shop staff, in particular Bruce Stanger, for his involvement in the design and fabrication of the various injector and torch pieces throughout the years at Virginia Tech.

I would like to thank my Father, Dr. Robert Jacobsen, for introducing me to his love of science and engineering and inspiring me throughout the years to make it my own. Lastly, but definitely not the least, I would like to thank my wonderful Wife, Susanne, for her encouragement throughout my studies. Without her support and love through the difficult times of the Ph.D. process, (*e.g. prelims*), it would have been much harder to bear.

Table of Contents

List of Figures

List of Tables

Nomenclature

A = Cross-sectional area or downstream transverse injection angle in plasma torch study
β = Enthalpy deficit factor due to vorticity
α_s = C_2H_4-air stoichiometric mass fraction, 0.0680
α_{mix} = Mass fraction mixing analogy
$\alpha_{mix,max}$ = Maximum mixing analogy mass fraction
C_d = Discharge coefficient
d_{eff} = Effective diameter = $d_{eq} \sqrt{C_d}$
d_{eq} = Equivalent jet diameter =$\sqrt{4}\, d_j$ for a 4-hole array
d_j = Jet diameter
$h_{C_2,max}$ = Maximum excited C_2 line penetration height
h_{core} = Maximum total temperature core height
h_{mix} = Maximum concentration penetration height
h_s = Stoichiometric plume penetration height
λ = Jet to freestream mass flux ratio $(\rho u)_j / (\rho u)_\infty$
γ = Specific heat ratio
M = Mach number
l = Injector throat length
$\dot{m}_{j,a}$ = Actual injector mass flux $C_d \dot{m}_{j,i}$
$\dot{m}_{j,i}$ = Ideal injector mass flux
η_m = Mixing efficiency
p = Static pressure
p_t = Total Pressure
$\bar{q}$ = Jet to freestream momentum flux ratio
ρ = Density
R_b = Effective Radius
Re = Reynolds number
T = Static temperature
T_t = Total temperature
u = Flow speed
w_{core} = Plume core width
w_{edge} = Stoichiometric plume width
x = Streamwise coordinate
y = Spanwise coordinate
z = Vertical coordinate

Subscripts

C = Ambient injection temperature condition "Cold injection"
H = Heated injection temperature condition "Hot injection"
∞ = Freestream
j = Injector
T = Torch

Chapter 1 Introduction

In order for a launch vehicle to achieve orbit, it must first fly at hypersonic velocities. Currently, all launch vehicles are of an expendable nature, discarding staged boosters into the atmosphere as they rocket along their trajectories. Even the so-called *reusable* space shuttle expends rockets and its main fuel tank on its flight path. With this expendable nature comes increased cost.

In an effort to reduce launch costs nations around the world have made efforts to produce reusable launch vehicles, which in theory should dramatically reduce the cost per pound into orbit. In actuality, true reusability has proven harder to attain than was expected. In this push for reusability, the need for lighter systems has created the necessity to take advantage of the oxidizer in the Earth's atmosphere and has directed these efforts primarily towards full or partial air-breathing systems. Some air-breathing projects of the early race for reusability are the German two-stage to orbit, Sänger program and the American single stage to orbit, X-30 national aerospace plane, (NASP program). Both of these programs ended prematurely due to some unresolved technical issues, funding, and political reasons of their times. Even at the time of writing this document, other promising rocket-based single-stage-to-orbit programs like the X-33 and X-34 have been canceled, leaving no current program of this magnitude in operation.

For an air-breathing propulsion system to operate at hypersonic velocities, it is necessary for the flow in the combustor to be supersonic (Heiser and Pratt[1]). Supersonic flow alleviates the harsh thermodynamic effects associated with the deceleration of the flow to subsonic speeds, such as high static temperature, pressure, and inefficient expansion. Pressure losses in the compression system are also reduced with less deceleration of the flow in the engine.

Out of these early hypersonic air-breathing programs has come the understanding that it is first necessary to make smaller strides by developing technology demonstrators before it is possible to make a launch vehicle reusable. Application of a supersonic combustion ramjet engine, more commonly referred to as a scramjet, as the main power plant of a reusable launch vehicle or a tactical missile makes the concept viable. Single-stage-to-orbit concepts, such as the NASP program mentioned above, have developed preliminary scramjet propulsion systems. The current NASA X-43 Hyper-X program and Air Force missile programs are based on such concepts. Related work is ongoing in France (Scherrer et al.[2]), (Bouchez et al.[3]), Japan (Kanda et al.[4]), (Tomioka et al.[5]), (Mitani et al.[6]), Australia (Wendt et al.[7]), China (Situ et al.[8]), (Li et al.[9]), (Yu et al.[10]), Korea (Lee et al.[11]), (Moon et al.[12]), and Russia (Baev et al.[13]), (Zvegintsev[14]), (Roudakov et al.[15]). Another aspect of supersonic combustion is in the use of a rocket based combined cycle engine, RBCC (Thomas et al.[16]), (Georgiadis et al.[17]), (Trefney[18]), (Taguchi et al.[19]). In this ejector/ramjet/scramjet engine concept, the use of subsonic and supersonic fuel injection is employed to increase the total integrated average specific impulse over the flight trajectory into orbit. This gain in specific impulse would reduce the mass fraction of fuel required, allowing more room for payload in comparison to a rocket-only powered launch vehicle.

Up until the early 90's, the focus on scramjet research involved hydrogen-fueled concepts due to the high fuel specific impulse, cooling capability, short ignition time, and low ignition temperature of hydrogen. Due to hydrogen's low density, it must be stored in liquid or slush form in order to reduce the volume of the tank required for a potential launch vehicle. Furthermore, cryogenic systems required to store liquid hydrogen add additional weight, complexity, and volume. In an effort to reduce the required volume and complexity of a full hydrogen launch system, hydrocarbon fuel alternatives have been investigated for operation in flight Mach numbers less than or equal to 8 (Hunt and Eiswirth[20]). According to Hunt and Eiswirth, the hydrocarbon-fueled scramjet cruise limit is about Mach 8 due to preliminary estimates of the cooling capacity of endothermic hydrocarbon type fuels. Further investigation of hydrocarbon-fueled scramjets has been done for use as a Mach 4-8 missile by the Air Forces HyTech missile program (Siebenhaar et al.[21]) (Faulkner and Weber[22]) and as a possible first stage of a two stage to orbit concept in a future spin-off of the X-43 program (McClinton et al.[23]).

Supersonic combustion with hydrocarbon fuels is a challenge, mainly because of the longer ignition delay and auto-ignition temperatures compared to hydrogen, which has been studied more extensively. Under these circumstances, with hydrocarbon fuels both improved mixing and combustion enhancement are needed. To produce positive thrust, the mixing of fuel in the combustor of a scramjet, must take place in as short a distance as possible. With superior mixing enhancement, the length of the mixing chamber in a supersonic combustor can be minimized. If the combustion efficiency of the combustor is increased by enhancing the mixing characteristics of the injection system, then the total thrust produced by the scramjet will also increase. Thus, the maximization of mixing potential in such a flow must be achieved in order to open up new avenues to hypersonic air-breathing flight and make operation of such a system feasible. At the same time, total pressure losses that result from the injection process must be minimized in order to reduce the total drag produced by skin friction on the walls of the engine.

For lower Mach number hypersonic flight, the use of swept ramp injectors is prominent in both computational and experimental studies of scramjet combustors. A sketch of a swept ramp injector is shown in Figure 1.1. Fuel injection ramps have been proven to be an effective means for mixing fuel in a scramjet engine. The swept ramp provides near streamwise injection of the fuel, which supplies an additional component of thrust for the engine as well as axial vorticity generation and mixing, due to the sweep (Tishkoff et al.[24]). These ramps utilize vortex enhanced mixing, often referred to as "hypermixing", which involves the use of streamwise vortices to mix injected fuel into the combustor freestream flow (Hartfield Jr. et al.[25], Riggins and Vitt[26]). For true hypersonic applications, the protrusion of struts, ramps or other devices into the combustor flow should be avoided in order to minimize severe problems with thermal protection, drag, structural integrity, and total pressure losses (Tishkoff et al.[24]).

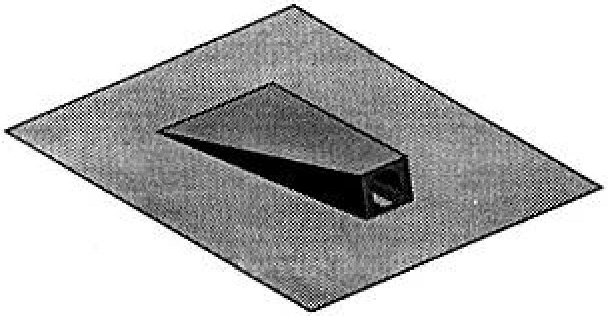

Figure 1.1 Physical Ramp Injector.

Further examination of specific injection devices is necessary in order to fully appreciate supersonic injection technology, especially the subject of transverse injection and its associated history. Various aspects of transverse wall injection have been studied including the effects of angled injection, yaw angle, injector hole geometry, vorticity, baroclinic torque, and injection schemes using different combinations and techniques. Fundamental studies of this type of injection process are given in Schetz[27] and Rogers[28]. The works up until 1990 were reviewed by Schetz et al.[29]. Low angled transverse injection studies in the range of 15- to 30-deg from the horizontal performed by Mays et al.[30] at Mach 3.0 analyzed the rate of mixing as affected by the ratio of exit jet pressure to effective back pressure. These studies found that the angle of injection primarily influences the initial disturbance but does not change the downstream mixing rate. This is important, because 90-deg injection implies larger total pressure losses in comparison to the lower angle transverse injection. Similar results were also presented by McClinton[31] for 30-, 45-, 60-, and 90-deg injection angles measured from the combustor wall. The results from McClinton's experiments indicated that there was less free-stream momentum loss required to turn and accelerate the injected gas downstream. Furthermore, increased penetration of the injectant into the freestream and lower total pressure losses were observed with the reduction in transverse injection angle. A comprehensive study of yaw angle was performed by Fuller et al.[32,33]. From the studies it was found that increasing the yaw angle of the injector increased the overall plume cross sectional area but decreased core penetration into the freestream. Some other noteworthy injection concepts are parallel slots (Lewis and Schetz[34]) and (Schetz et al.[35]), transverse slots (Spaid and Cassel[36]), and jet swirl (Jacobsen et al.[37]), (Kraus and Cutler[38]), (Cutler and Johnson[39]), (Schetz[40]), (Povinelli and Ehlers[41]), and (Schetz and Swanson[42]).

Studies of wedge-shape injectors with nozzles performed by Barber et al.[43] bring yet another interesting aspect of an injection system into view. They found that with the wedge-shaped injector there is an increased penetration depth over that of a round hole injector. This is accomplished by attaching the shock to the wedged injector jet. Furthermore, mixing was enhanced and lower total pressure losses were observed in comparison to the round hole injector. A further effort was undertaken by Tomioka et al.[44,45] with the study of diamond-shape injectors. The diamond-shape injector was similar to the wedge shaped injector in that both of them have a wedge-shape leading edge, but they differ in that the diamond-shape injector also had a wedged shaped trailing edge. Tomioka et al.[44] found that the diamond-shape injector reduced the losses generated from the back portion of the injector and performed considerably better than a single hole injector and helped improve mixing and jet penetration in the lower momentum flux ratios studied. Tomioka et al.[45] extended the analysis of the wedge injector to the study of downstream injection sweepback angle of 0-, 30-, and 60-deg normal to the test section floor and the effects of yaw angle of 0-, 15-, and 30-deg. In this study, it was found that the higher sweepback angle injector configuration reduced the size of the bow shock structure as seen by surface oil flow measurements, while increasing the penetration height, and also that the middle sweep-back angle produced the lowest maximum fuel mass fraction measured. They also found that increasing the 15-deg yaw angle configuration reduced the maximum mixing concentration while improving the overall penetration of the plume.

The general interference effects generated by multi-hole transverse injector arrays have been capitalized on in the design of the aerodynamic-ramp, “aero-ramp” injector first suggested by J.A. Schetz. Some of the first results of the aero-ramp’s performance have been reported by Cox et al.[46], Cox-Stouffer and Gruber[47,48,49], and R. Fuller et al.[50]. An overview of the combined works is presented in Schetz et al.[51]. This flush-wall design shown in Figure 1.2, which incorporates the positive aspects of low-angled injection and yaw angle, showed promising features, such as mixing characteristics near the same performance level of a physical ramp injector with lower pressure losses, while leaving a secondary core trapped in the shear layer near the wall. The aerodynamic ramp, as a transverse injector, also provided improved pressure recovery over the obtrusive physical ramp injector. This array incorporates the complex interaction between the nine holes, and the effects of baroclinic torque and shock-induced vorticity between its three rows of injectors to produce vortical flow and enhance mixing efficiency. The multiple yaw angles of the injector holes also induce vortical effects, which further enhance mixing. The studies performed by R. Fuller et al.[50] suggest that further testing was needed to better understand the phenomena associated with the nine-hole injector. Analysis of a single row of three holes was suggested. Studying the effects of transverse injection at higher jet to freestream momentum flux ratios was also suggested to better understand the trends of injector flow penetration into the freestream.

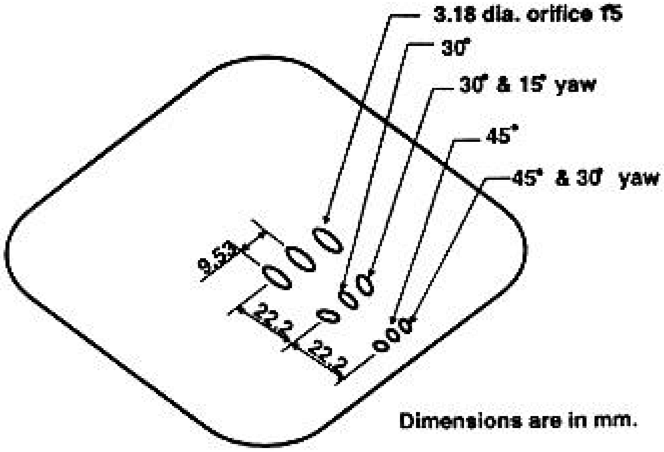

Figure 1.2 Aero-Ramp Injector.

In an effort to further the understanding of the aero-ramp injector, the effects of toe-in, or inward yaw of the injector jets to the centerline of the overall injector, on a single row injector array were examined by Jacobsen et al.[52]. In that study, it was found that increasing the toe-in angle of the exterior injector holes greatly increased the mixing efficiency and core penetration of the overall jet plume generated by the array.

An attempt to capitalize on the effects of an aero-ramp injector array in a scramjet combustor was first numerically studied by Eklund and Gruber[53] and then experimentally by Gruber et al.[54]. In the latter study, two hydrocarbon-fueled aero-ramps were compared to a single row of four 15-deg low downstream-angled holes. Each of these injector configurations was placed upstream of a cavity, which was used in conjunction with two sparkplugs as a flame-holder in the experiments. Results showed that the aero-ramp configuration did not work as well as the four single-hole injectors, due to the lateral placement of only two aero-ramp injectors in comparison to the four round-hole injectors, which allowed the fuel to spread more evenly laterally across the combustion chamber.

Let us now turn to ignition and combustion enhancement. Currently, all fuel injector designs for scramjet engine combustors have involved some kind of cavity, backward facing step, strut, or types of obtrusive, physical ramps for creating flame-holding regions in order to promote fuel mixing and stabilize combustion. These flame-holding mechanisms, while proven effective, each have their own problems and all reduce the total theoretical producible thrust in scramjet engines due to added viscous effects and increased pressure losses.

The use of cavities as flame-holders in supersonic engines has been documented extensively in Baurle and Gruber[55] and Ben-Yakar and Hanson[56]. One particular study of interest in relation to this body of work was performed by Mathur et al.[57]. In this study, which documents the performance of the four, round-hole, 15-deg low downstream-angled injectors with a cavity downstream mentioned above, Mathur et al.[57] estimated combustion efficiencies near 80% with ethylene fuel at a fuel-air equivalence ratio of 0.75. This configuration has become that particular research program's baseline gaseous hydrocarbon injector/flame-holder configuration, and it has been tested at flight Mach numbers between 4 and 5 corresponding to an initial combustor Mach number of 1.8, and fuel-air equivalence ratio range of 0.25-0.75. Tests have also been conducted with this baseline configuration in operation at a combustor Mach number of 2.2, corresponding to a flight Mach number range of 5 to 6, where true scramjet operation starts to prevail over subsonic ramjet-style combustion (Gruber et al.[58]). Furthermore, tests have also been conducted with a plasma torch in conjunction with the cavity as a comparison to the performance of sparkplugs.

In addition to cavities, numerous flame-holding experiments have been conducted with backwards facing steps (Wagner et al.[59]), (Sato et al.[60]), (Tomioka et al.[61]), swept ramps (Rogers et al.[62]), (Abdel-Salam et al.[63]), struts (Tomioka et al.[5]), (Thomas et al.[16]), (Siebenhaar et al.[21]).

One favorable type of ignition aide that has been used in supersonic combustion applications is the plasma torch. Over the years, several plasma torches have been developed involving continuous or pulsed operation (Weinberg, F.J.[64]), (Barbi[65]), (Stouffer et al.[66]), (Kim et al.[67]), (Kimura et al.[68]). Several experiments have been performed pertaining to the use of a plasma torch as a main fuel igniter in crossflows (Kimura et al.[68]), (Takita et al.[69,70,71]), (Masuya et al.[72]), (Wagner et al.[73]), (Northham et al.[74]), (Sato et al.[75]), (Warris and Weinberg[76]), (Shuzenji et al.[77]), (Fuji et al.[78]), (and Kanda et al.[79]).

All of this suggests the need for a truly integrated system to achieve good penetration, mixing ignition, and combustion.

This research project involves the development and creation of an integrated, flush-wall, fuel-injector-array, and plasma torch igniter/flame-holder system that does not include any of the aforementioned physically intrusive devices to sustain combustion. Instead, a flame holding region is to be created in the engine by manipulating the combustor flow field to create regions where flame propagation is possible by using the geometry of a flush walled injector itself. The main goal of this project is to demonstrate that the correct placement of a plasma torch igniter/flame-holder in the wake of the fuel jets of an aero-ramp injector array could make sustained, efficient supersonic combustion with lower losses and lower thermal loading possible. The development process consisted of three phases.

First, studies were undertaken to improve on the current designs of the aero-ramp and plasma torch as well as address integration and incorporation difficulties. These studies included first, a qualitative investigation into the incorporation of two plasma torches into the downstream end of a nine-hole aero-ramp injector array at Mach 3.0 with shadowgraphs and surface oil flow visualization. Then the influence of the downstream transverse injection angle of a plasma torch igniter operating alone was investigated for integration purposes. During this set of experiments, a 45-deg transversely mounted plasma torch was compared to a more conventional 90-deg configuration in a cold flow supersonic environment. The primary experimental methods used during this study consisted of shadowgraphs and temperature sampling at a downstream location to examine the shapes of the plumes and to assess the possibility of heat release from combustion in this Mach 3 flow with a static temperature of 100 K. The information learned from these experiments plus additional results from two other documented experiments in this phase lead to the creation of the first prototype integrated aero-ramp/ plasma torch design consisting of a new simplified four-hole aero-ramp design.

The second phase of the project consisted of a cold-flow mixing evaluation of the new design and a resizing of the device for incorporation into a scramjet flow path at the Air Force Research Laboratories. The evaluation of the first prototype design at Mach 2.4 consisted of shadowgraphs, surface oil flow visualization, and downstream aerothermodynamic sampling experiments. By comparing downstream total temperature profiles while injecting heated and ambient air through the array, a new mixing analogy parameter was created to assess the mixing potential of this device. Next, the aero-ramp injector was sized to fit in an existing combustor and compared to one of the injectors used in the combustor baseline configuration. This evaluation also took place at Mach 2.4, which was closer to the actual combustor Mach number of 2.2 than the earlier phase of the experiments. To document the performance of the injector, shadowgraph images were taken and Pressure Sensitive Paint was used at various momentum flux ratios to help qualitatively understand the nature of the flows. Furthermore, aerothermodynamic sampling was performed to quantify the pressure losses and mixing potential of the new aero-ramp injector via the new mixing analogy.

The last phase of the research to be reported here involved testing the final integrated design in a cold-flow environment at Mach 2.4 with hydrocarbon fuels and various torch feedstocks. Three downstream plasma torch locations in relation to the aero-ramp injector array were tried, and regions where flame ignition and propagation would be likely were identified for the various torch feedstocks tested. Shadowgraph images were taken and pressure-sensitive paint was used at various momentum flux ratios to help qualitatively understand the flowfields. Total temperature probing and spectroscopy were also performed at downstream locations with the torch in operation behind the ethylene fueled aero-ramp injector to help quantify differences in plasma torch effectiveness as a potential igniter. The phase three, cold-flow combustion tests lead to the design and creation of a fuel injector block for testing in the scramjet combustor at the AFRL in the near future.

The next chapter in this document describes the test articles of the three phases of research and the experiments performed on them. Further, it describes the test parameters used to evaluate the various aspects of performance being compared throughout the results sections of this document. A description of the experimental procedures used to study the various flowfields is given in the next chapter. Then, the following three chapters will present the results and individual conclusions for the experiments performed respectively in the three phases of research described above. After the results chapters, a discussion and conclusions chapter is presented, which overviews the entire project. Finally, a chapter is included which gives recommendations towards plans of study and investigation to further the concept of integrated fuel injection/ plasma ignition systems.

Chapter 2 Facility, Test Articles, and Test Matrices

2.1 Supersonic Blow-down Test Facility

Experiments were performed in the Virginia Tech 23 X 23 cm blowdown supersonic wind tunnel. The tunnel was designed and built at NASA Langley Research Center. The tunnel was acquired by Virginia Tech in 1958 and put into operation in 1963. During recent years, several modifications were introduced into the air pumping, tunnel control, and instrumentation equipment, which increased the capabilities of the facility. A schematic view of the tunnel is given in Figure 2.1.

The air pumping system consists of an Ingersoll-Rand Type 4-HHE-4 4-stage reciprocating air compressor driven by a 500 hp, 480V Marathon Electric Co. motor. The compressor can pump the storage system up to 51 atm. A drying and filtering system is provided which includes both drying by cooling and drying by absorption. Air storage system consists of two tanks with a total volume of 23 m^3. Tunnel control system includes quick opening butterfly valve and a hydraulically actuated pressure regulating 30.5 cm diameter valve. Typical run times of the blowdown facility lasted anywhere from 4 to 20 seconds depending on the experiment.

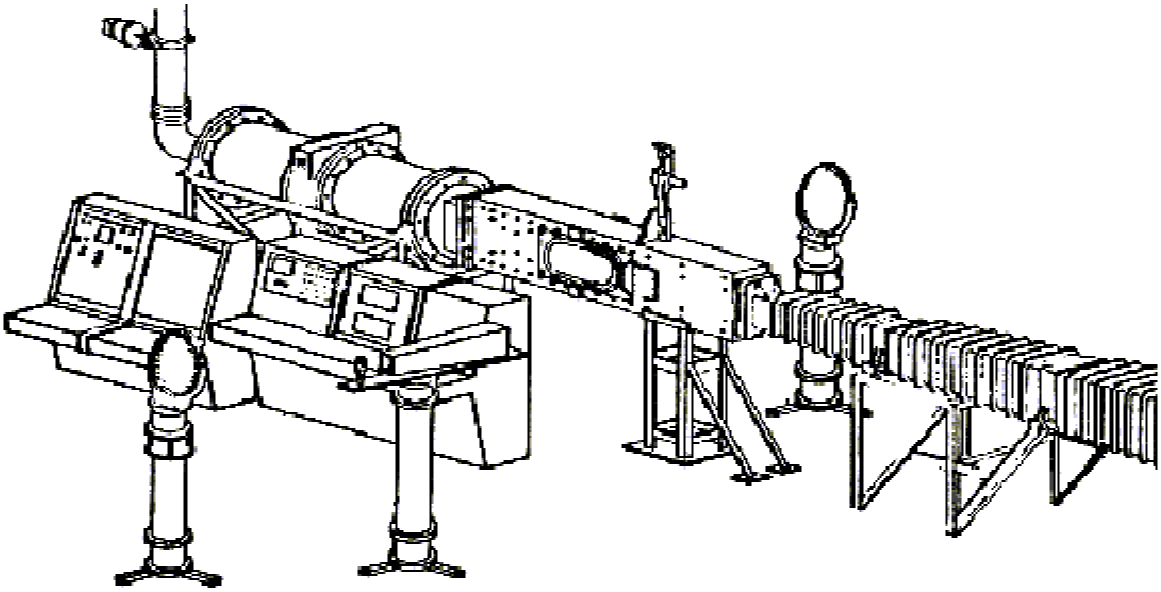

Figure 2.1 Virginia Tech Supersonic Blowdown Test Facility.

2.1.1 *Mach 3.0 Test Configuration*

During the experiments performed at a freestream Mach number of 3.0, the tunnel was configured with a 2-D, convergent-divergent, half-nozzle. Downstream of the nozzle, the test section dimensions were 23 cm wide by 11.5 cm high and 30 cm long in the streamwise direction. The injector plenum chamber was located in the bottom test section wall in the upstream end of the test section. A sketch of the Mach 3 half-nozzle block and injector plenum are shown in Figure 2.2.

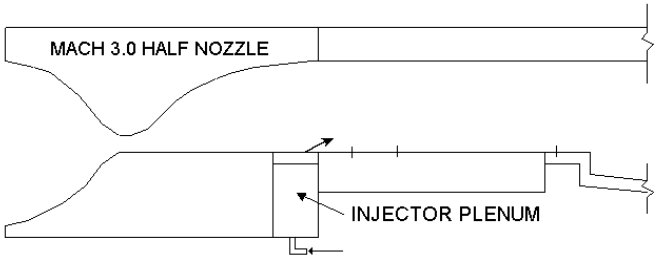

Figure 2.2 Mach 3.0 Half-Nozzle Test Section Showing Injector Plenum (Not to scale).

2.1.2 *Mach 2.4 Test Configuration*

During the experiments performed at a freestream Mach number of 2.4, the tunnel was configured with the normal 2-D, convergent-divergent nozzle. The test section dimensions were 23 cm wide by 23 cm high and 30 cm long in the streamwise direction. Figure 2.3 shows a sketch of the wind tunnel test section with the injector array and plasma torch.

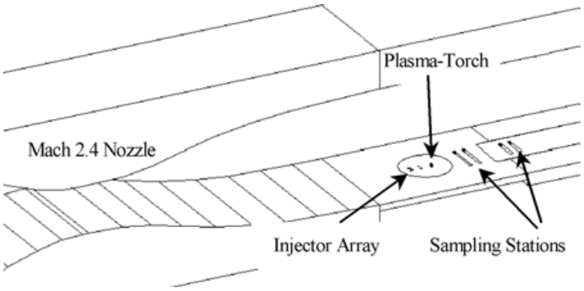

Figure 2.3 Mach 2.4 Nozzle and Test Section.

2.2 General Experimental Parameters

Experiments were performed in the Virginia Tech Supersonic Blowdown Facility at Mach 3.0 and 2.4. Table 2-1 presents the average freestream conditions during the five main experimental studies performed. During the experiments, the stagnation pressure was controlled to within ± 0.4 atm of the average value. The temperature in the stagnation chamber was dependent upon the outside ambient conditions of the day and varied annually from about 270 K to 300 K. During a typical blowdown of the wind tunnel, the quasi-steady-state total temperature would stay relatively constant with the Mach 3 test section, but would decrease on average about 1 K per second while using the Mach 2.4 section due to its higher mass flow levels and related expansion effects and heat transfer in the air storage tanks and lines.

Table 2-1 Average Experimental Freestream Conditions.

	9/8-Hole Aero-Ramp Study	***Transverse Angled Plasma Torch***	***1st Integrated Prototype***	***Aero-Ramp v Single-Hole***	***Integrated Cold Flow Combustion***	
M_∞	**3.0**	**3.0**	**2.4**	**2.4**	**2.4**	—
$P_{t,\infty}$	**6.12**	**6.87**	**3.78**	**3.69**	**3.74**	***atm***
$T_{t,\infty}$	**288**	**283**	**280**	**281**	**281**	***K***
P_∞	**0.17**	**0.19**	**0.26**	**0.25**	**0.26**	***atm***
T_∞	**103**	**101**	**130**	**131**	**131**	***K***
a_∞	**203**	**202**	**229**	**229**	**229**	***m/sec***
u_∞	**610**	**605**	**549**	**550**	**550**	***m/sec***
ρ_∞	**0.57**	**0.65**	**0.70**	**0.68**	**0.69**	***kg/m³***
γ_∞	**1.40**	**1.40**	**1.40**	**1.40**	**1.40**	—
$\dot{m}_\infty$	**9.1**	**10.3**	**20.1**	**19.6**	**19.8**	***kg/sec***
Re#/meter	**4.9E+07**	**5.6E+07**	**4.3E+07**	**4.2E+07**	**4.2E+07**	m^{-1}

The freestream flow coordinate system used in all of the injector configurations consisted of right-hand Cartesian coordinates with the origin placed at the center of the overall injector areas. The positive *x-axis* is in the downstream direction, the *y-axis* in the cross-stream direction, and the positive *z-axis* in the vertical direction.

2.3 Wind Tunnel Models and Test Conditions

In all the experiments performed, the flow through the various injectors in relation to the freestream was parameterized using the jet to freestream momentum flux ratio. The jet to freestream momentum flux ratio is defined:

$$\bar{q} = \frac{\left(\rho u^2\right)_j}{\left(\rho u^2\right)_\infty} = \frac{\left(\gamma p M^2\right)_j}{\left(\gamma p M^2\right)_\infty} \tag{2.1}$$

This quantity was used because many injector properties tend to vary with it, and it is hard measure the effective backpressure, p_{eb}, of an array of jets, which is needed to use the expansion ratio p_j/p_{eb}.

2.3.1 9/8-Hole Aero-Ramp with Swirl

Figure 2.4 Shows a picture of the nine-hole aerodynamic ramp injector with two simulated plasma torch holes placed in the downstream end of the array. This particular aero-ramp incorporates the toe-in and transverse angles of the original aero-ramp shown in Fuller et al.[50] the injector spacing from Cox-Stouffer et al.[46,47],with the substitution of the outer two downstream holes by the simulated plasma- torches. The design permits the study of incorporating the effects of swirl produced by a real plasma torch due to it internal flow swirler, which is used for arc rotation. The aero-ramp test model consisted of nine holes each with a diameter of 3.175-mm and an equivalent diameter for the whole array of 9.525-mm. The simulated plasma torch orifices each were at a 2 to 1 scale with flow swirlers inserted inside to positively reinforce the direction of the main plume vortex. The two simulated plasma torch holes were placed perpendicular to the mainstream flow. A more detailed pictorial of the aero-ramp and simulated plasma torch hole geometry with its two counter-rotating flow swirlers is given in Figure 2.5 and Figure 2.6. The two counter-rotating arrows in the top-view sketch denote the direction of swirl induced by the internal flow swirlers in the simulated plasma torch orifices. The flow swirlers have a guide vane angle of 45-deg. This gives them a swirl number of 1.0, where the swirl number is defined as the ratio of tangential to freestream velocity of the internal simulated plasma torch flow. Viscous effects will reduce the swirl number below one on its way outside of the torch geometry.

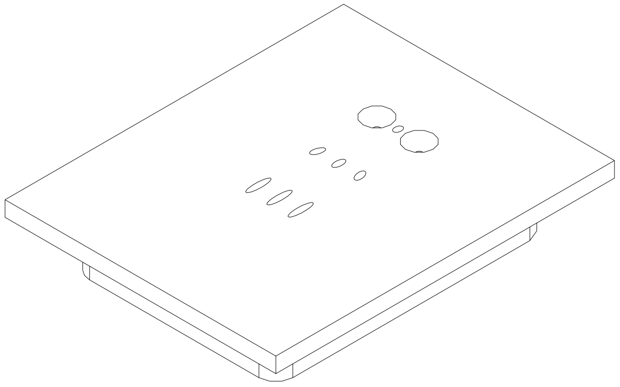

Figure 2.4 Nine-Hole Aero-Ramp Injector Array with Two Simulated Plasma torches.

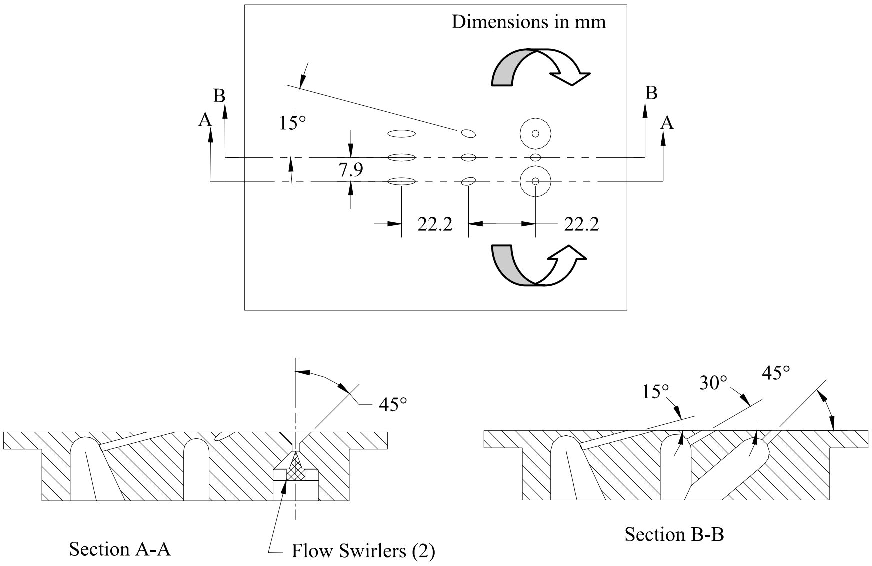

Figure 2.5 Nine-Hole Aero-Ramp Injector Array Design Details.

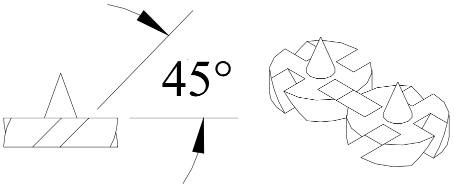

Figure 2.6 Simulated Plasma Torch Internal Jet Flow Swirlers.

This series of tests was performed at a freestream Mach number of 3.0, while injecting air in order to simulate hydrocarbon fuels without the safety hazard associated with combustion. Eight- and nine-hole aero-ramp configurations were tested to assess the incorporation of two simulated plasma torch orifices. Tests were performed on the nine- and eight-hole configurations with jet to freestream momentum flux ratios of 1.9 (9-hole) to 2.0 (8-hole). The momentum flux ratio for the nine-hole array was lower because of higher pressure losses in the injector plenum due to a higher mass flow rate. Since air from the plenum chamber of the supersonic wind tunnel was also used as the source of injectant through the injector block, the momentum flux ratios were limited to a maximum value of 2.0.

Table 2-2 9/8-Hole Aero-Ramp Injector Jet Exit Parameters.

	9-Hole $\bar{q}=1.9$	***8-Hole*** $\bar{q}=2.0$	
M_j	**1.0**	**1.0**	—
$P_{t,j}$	**5.40**	**5.68**	***atm***
$T_{t,j}$	**290**	**290**	***K***
P_j	**2.85**	**3.00**	***atm***
T_j	**242**	**242**	***K***
a_j	**312**	**312**	***m/sec***
u_j	**312**	**312**	***m/sec***
ρ_j	**4.16**	**4.38**	kg/m^3
γ_j	**1.40**	**1.40**	—
$\dot{m}_j$	**92.5**	**86.5**	***gm/sec***
P_j/P_∞	**17.1**	**18.0**	—
T_j/T_∞	**2.35**	**2.35**	—
u_j/u_∞	**0.51**	**0.51**	—
ρ_j/ρ_∞	**7.28**	**7.66**	—
λ	**3.72**	**3.92**	—

2.3.2 Plasma Torch

The plasma torch used in the experiments is shown in Figure 2.7 and Figure 2.8. The DC constant-current operation device has an operation power range of about 500-4500 Watts for 5-60 Amp of current. This plasma torch is the third generation design developed at Virginia Tech, incorporating some of the features from the previous VT designs by Barbi[65], Wagner et al.[73] and Stouffer et al.[66] along with other aspects from a plasma torch developed by Phoenix Solutions, Incorporated. The studies that lead to this final configuration are documented by Gallimore[80]. The feedstock runs into the torch body through an inlet tube, shown as item (K) in Figure 2.7, and then flows through the flow swirler (F) on its way to the throat of the anode, where the cathode (C) is positioned inside. When in operation, electrons travel from the tip area of the cathode (C), through the feedstock gas inside the anode throat (A) and attaches to the outside edge of the anode throat. This process transfers energy into the feedstock gas, exciting a percentage of it, effectively creating plasma. The plasma torch was designed for operation primarily with methane and nitrogen feedstocks. However, some experiments involving ethylene and air feedstocks have been performed with the torch, although with the current tested choices of electrode material used, electrode wear was a significant issue. During the integrated cold flow combustion experiments, a mixture of 10-percent hydrogen 90-percent nitrogen by volume was also tested for use as a torch feedstock. The torch ran well with this mixture. A list of the electrode materials used for the different feedstocks is shown in Table 2-3.

Table 2-3 Plasma Torch Electrode Material Selection.

Feedstock	***Anode Material***	***Cathode Material***
Methane	**Molybdenum or Copper**	**2% Thoriated Tungsten**
Ethylene	**Molybdenum or Copper**	**2% Thoriated Tungsten**
Nitrogen	**Copper**	**2% Thoriated Tungsten**
90%Nitrogen + 10%Hydrogen	**Copper**	**2% Thoriated Tungsten**
Air	**Copper**	**Hafnium**

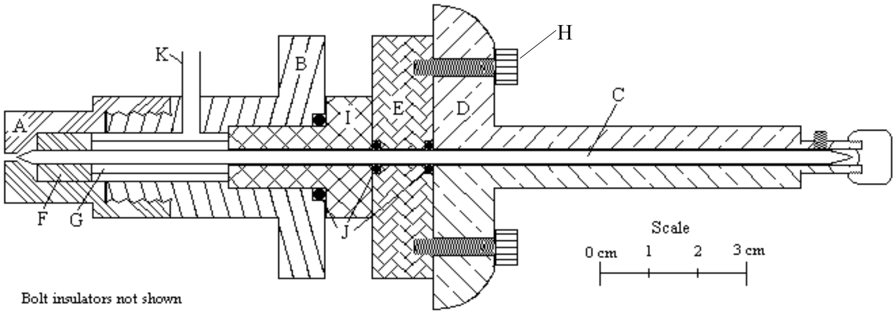

Figure 2.7 Sketch of the Plasma torch. A-Anode, B-Torch Body, C-Cathode, D-Depth Micrometer, E-Cathode Assembly, F-Flow Swirler, G-Cathode Insulator, H-Bolts, I-Electrode Isolator and Insulation, J-O-Rings, K-Feedstock Inlet Tube.

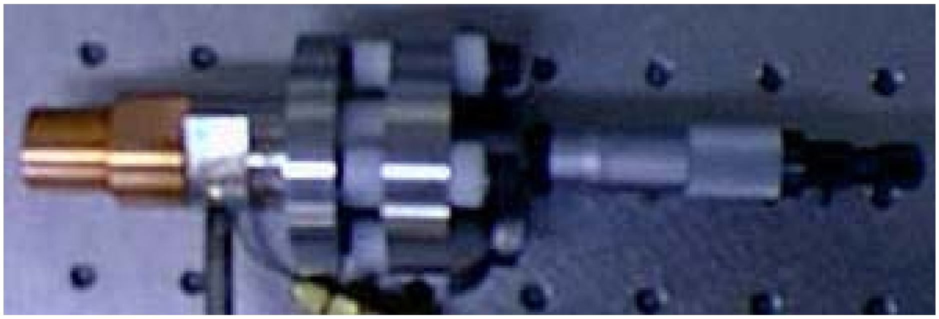

Figure 2.8 Photo of the Plasma Torch.

Experiments were performed with the plasma torch igniter shown above with two different anode configurations, shown in Figure 2.9. The geometries of the two anode configurations differ in their transverse angle to the freestream, 90-deg (normal to the test section floor) in Figure 2.9(a) and 45-deg in Figure 2.9(b). Both models had throat length to diameter ratios, t/d_j, of 2.2. These anodes were constructed to fit flush into specially made floor plates for the supersonic tunnel. The idea of the 45-deg transverse angled plasma torch geometry was created from the notion of placing a torch into the aero-ramp injector array. The low-downstream angle of the torch anode, in comparison to the 90-deg anode, allows closer incorporation of the torch into an aero-ramp injector design while lowering the pressure losses produced from jet-freestream interactions. Furthermore, the 45-deg anode allows the incorporation of yaw, or toe-in in a two-torch configuration, of the torch into the injector plume. The effects of toe-in of a two-torch configuration along with the plasma torch flow-swirlers inside the array would enhance mixing and penetration of the main plume.

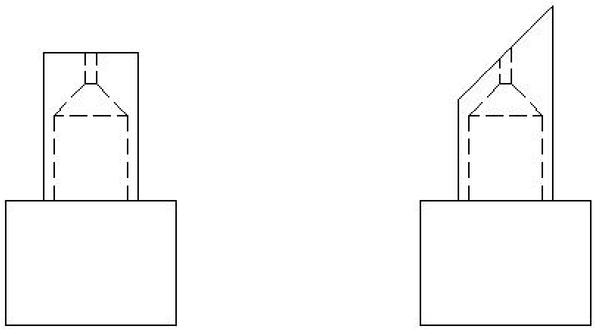

a) A = 90-deg **b) A = 45-deg**

Figure 2.9 Plasma Torch Angled Anodes Geometry.

This group of tests was performed at a freestream Mach number of 3.0. The plasma torch was operated with methane as its feedstock at power levels ranging from 900- to 3500-Watts. Tests were conducted with the torch in operation at nominal jet to freestream momentum flux ratios of 1.03 and 2.06, corresponding to torch plenum total pressures of 3.4 and 6.8 atm for a nominal freestream total pressure of 6.8 atm. Table 2-4 presents the plasma torch feedstock injection parameters for methane gas. The parameters were calculated at the throat of the torch, where the cathode constricted the anode throat down from 1.59-mm to 0.63-mm. This constriction of area corresponds to an arc gap setting between the cathode and throat of the anode of 0.178-mm.

While the torch was in operation, the ideal feedstock mass flow rate ranged from 0.18 to 0.37 grams per second for the desired pressure settings (calculated with the torch not in operation). In order to get the torch to run at a given pressure, the torch plenum pressure levels were set to about 86-percent of the desired value before the arc was started. After the arc was established, thermal choking in the anode throat raised the pressure up to the desired level. A little fine-tuning was needed about every third run to account for the increase in area due to wear of the electrodes.

Table 2-4 Plasma Torch Jet Throat Exit Parameters.

	$\bar{q}=1.0$	$\bar{q}=2.1$	
M_j	1.0	1.0	—
$P_{t,j}$	3.40	6.80	*atm*
$T_{t,j}$	292	292	*K*
P_j	1.86	3.71	*atm*
T_j	254	254	*K*
a_j	414	414	*m/sec*
u_j	414	414	*m/sec*
ρ_j	1.43	2.86	kg/m^3
γ_j	1.30	1.30	—
$\dot{m}_j$	0.18	0.37	*gm/sec*
P_j/P_∞	9.9	19.9	—
T_j/T_∞	2.52	2.52	—
u_j/u_∞	0.68	0.68	—
ρ_j/ρ_∞	2.19	4.37	—
λ	1.50	2.99	—

A sketch of the 45-deg plasma torch flush with the test section floor and the downstream sampling station location is presented in Figure 2.10. The sampling location for the 45-deg torch was 94.9-mm downstream from the center of the torch hole at the start of test section diffuser section. Although the station was in the diffuser section, the freestream Mach number at the sampling station was still at Mach 3, and the deceleration of the flow started further downstream inside the diffuser. Due to machining errors, the downstream location of the sampling station for the 90-deg test section was 93.5-mm.

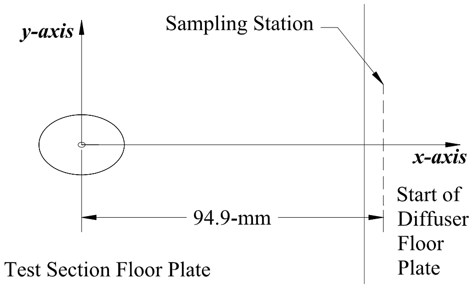

Figure 2.10 Test Section Dimensions for Plasma Torch with 45-deg Anode.

2.3.3 First Prototype Integrated Injector/Plasma-Torch Design and New Aero-Ramp Concept

Figure 2.11 presents a sketch of the first prototype aerodynamic ramp/ plasma torch igniter for use with hydrocarbon fuels and supersonic combustion. The prototype contains a 4-hole aerodynamic ramp concept injector and three plasma anode holes downstream of the injector. Some of the main issues associated with the evolving design and purpose of the aero-ramp injector are the mitigation of a secondary core of fuel in the shear layer near the surface found in early studies, ways to generate vorticity and enhance mixing with the arrangement of the holes, and the possible accommodation of a spark, pilot, or plasma igniter downstream of the injector array. The current four-hole aero-ramp design is a simplification the old nine-hole version. By the removal of the center row of holes in the nine-hole array and the inclusion of high toe-in angles in the existing holes, the current design encourages axial vortex formation, which helps to lift the entire plume off of the wall, leaving little to no secondary fuel core near the surface. This mitigation of the secondary core in the shear layer will help reduce the thermal loading to the surface of the combustor. Further simplification of the aero-ramp design involves the removal of one of the cross-stream rows of holes from the original nine-hole design as well. The angular placement and arrangement of the four-hole aero-ramp was designed to create a lean channel in between the two downstream rows of jets. This jet arrangement was also created to produce a sheltered region downstream, where flame ignition and propagation would be enhanced.

The aero-ramp injectors shown Figure 2.11 and Figure 2.12 used in the cold flow mixing experiments, consisted of two rows of two holes, spaced 4.0 equivalent jet diameters apart in the streamwise direction and with a cross stream spacing of 2.0 equivalent jet diameters between the holes. The first and second pair of injector holes had transverse injection and toe-in angles of 20- and 40-degrees and 15- and 30-degrees, respectively. These details are shown in Figure 2.13. The aero-ramp injector shown in Figure 2.12 and Figure 2.13 was constructed after the initial investigation of the first integrated prototype design, and was sized for comparison to single-hole injector discussed in the next section, which was used in a scramjet test combustor at AFRL. This model had an equivalent jet diameter of 4.76-mm and the distance between the exits of the injector holes was 19.05-mm in the cross-stream direction and 38.1-mm in the downstream direction. The aero-ramp was constructed from Naval Bronze, to give it a low thermal conductivity without the machining penalties of steel. This was done to reduce the amount of heating of the injector during the experiments performed with heated air injection.

The four sonic exit holes of the first, smaller aero-ramp injector were each 1.59-mm in diameter giving the array an equivalent single circular jet diameter of 3.18-mm. The exits of the injector holes had a 6.35-mm cross spacing from each other and a 12.7-mm downstream spacing. The ratio of the injector equivalent diameter to the torch exit diameter is 2.0 and the ratio of the injector equivalent diameter to the physical throat of the plasma torch, where the cathode is closest to the anode, is about 5.1. Since the torch exit hole is located downstream of the fuel injector array, the difference in size of the torch relative to the array will surely change it effectiveness as a main flow fuel igniter. Thus, the smaller the injector array size is relative to the torch, the larger the plasma jet will be relative to the injector plume. The plasma torch holes, each with an exit diameter of 1.59-mm, have been placed on a circular copper plate such that a rotation of 120-deg of the plate will orient a torch hole at a different downstream location relative to the injector array. In the current configuration, the torches have been placed at a 60-deg transverse angle relative to the test section floor in the downstream direction. While one torch is in use, the other two off-centered torch holes are closed off from behind. This allows us to vary the downstream torch position relative to the center of area of the injector array from 6.0 to 10.0 equivalent diameters, d_{eq}. A sketch of the plasma torch station locations is shown in Figure 2.14. Further views of each component are shown in Figure 2.15. The aero-ramp was constructed from Naval Bronze, for the reasons given above.

The injector array/ plasma torch can be easily incorporated into a multiple prototype scheme for integration into a scramjet combustor flow path by placing torches downstream of the arrays where it is desirable. With its versatile shape and dimensions, the injector could be scaled to fit any combustor geometry and used alone or in a multiple injector configuration where necessary.

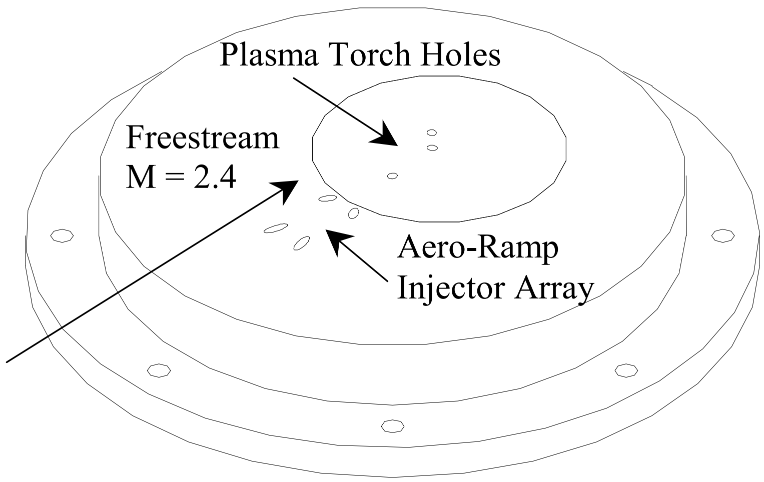

Figure 2.11 Integrated Aero-Ramp Injector Array/ Plasma Torch Prototype.

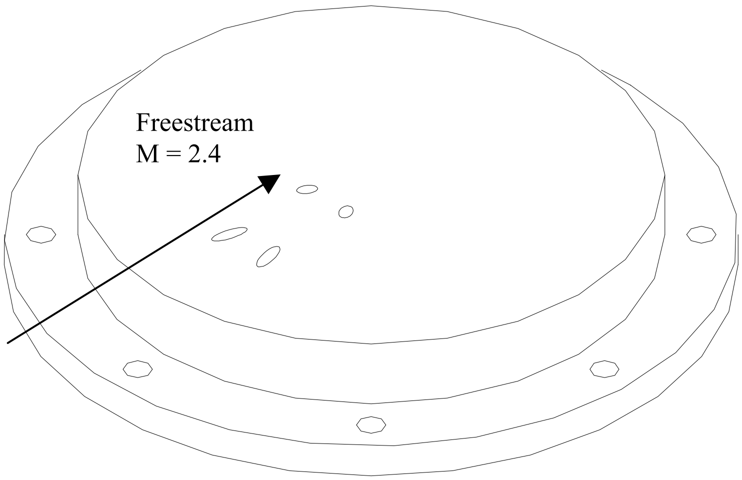

Figure 2.12 Aerodynamic ramp injector array.

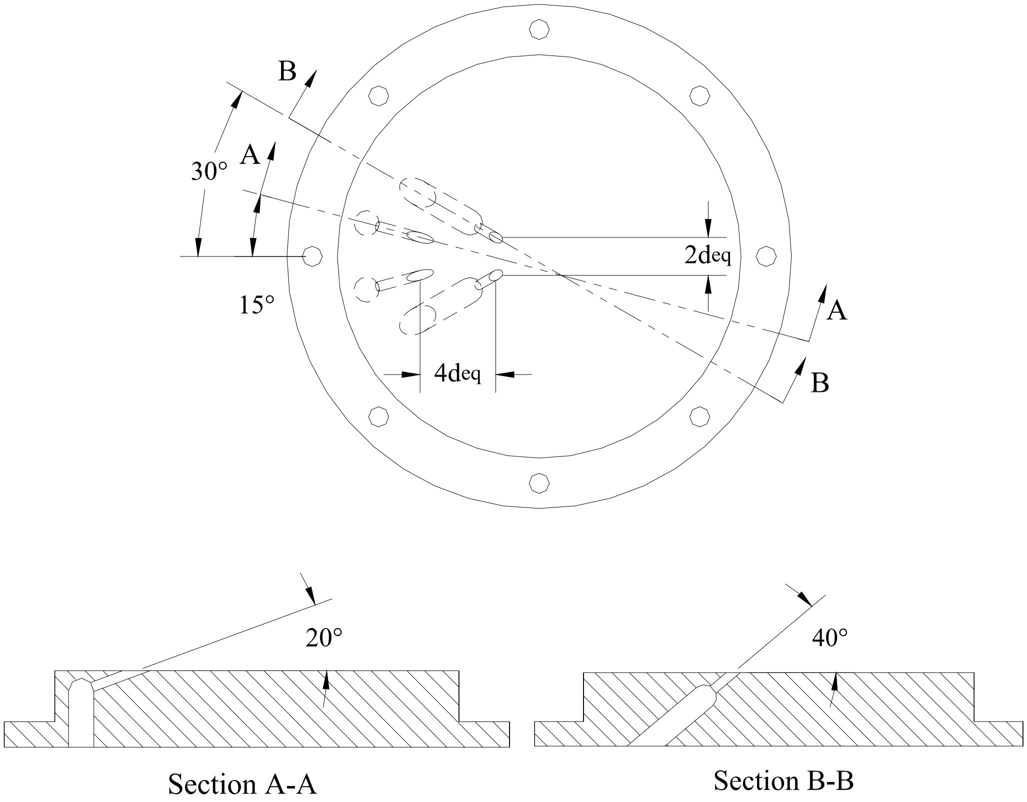

Figure 2.13 Aero-Ramp Non-Dimensional Hole Geometry.

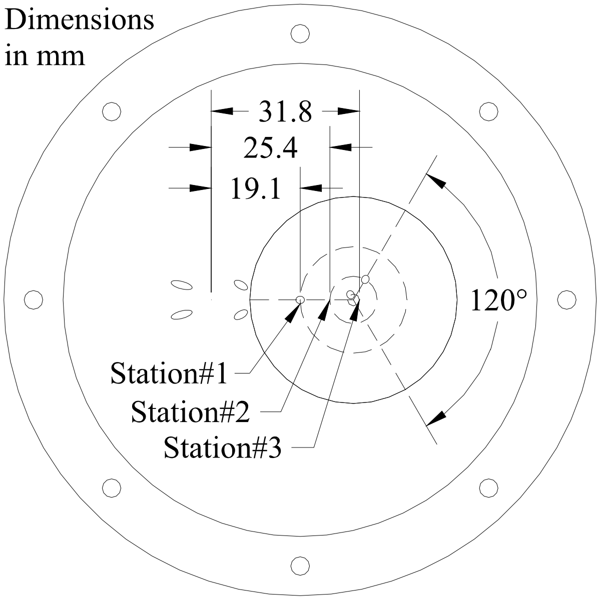

Figure 2.14 Plasma Torch Station Locations.

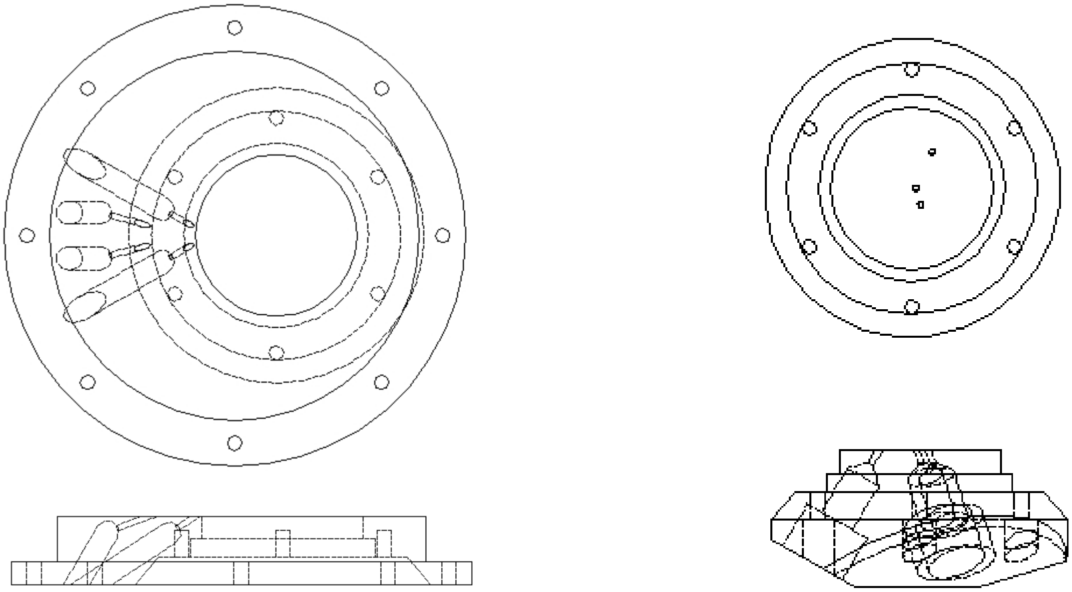

a) Aero-Ramp Injector. **b) Plasma Torch Anode**

Figure 2.15 Integrated Aero-Ramp Injector Array/ Plasma Torch Prototype.

2.3.4 Transverse Angled Single-Hole Injector

A single low-downstream-angled injector hole with a diameter of 5.61-mm was constructed for comparison to the aerodynamic ramp injector array. This sonic, single-hole injector was transversely angled 15-deg downstream from the test section floor as seen in Figure 2.17. The single-hole injector had a throat length of 6.0-d_j (measured from the center of the hole). This injector was chosen for comparison because it is the baseline injector in an injector/cavity configuration being tested in a scramjet test combustor at the Air Force Research Labs.

Low-downstream angled injectors offer a low-pressure loss alternative to injectors normal to the flow direction, without reduction in mixing performance or plume penetration. Furthermore, the 15-deg downstream angle of the injector relative to the main flow imparts an additional component of thrust to the overall engine, which is quite useful at higher hypersonic flight Mach numbers. However, in the flight Mach number range of hydrocarbon type scramjets ($M \leq 8$), this component is negligible. Nevertheless, the simplicity of a single-hole injector and the low-downstream angle makes it a good benchmark injector to test against the performance of the aero-ramp.

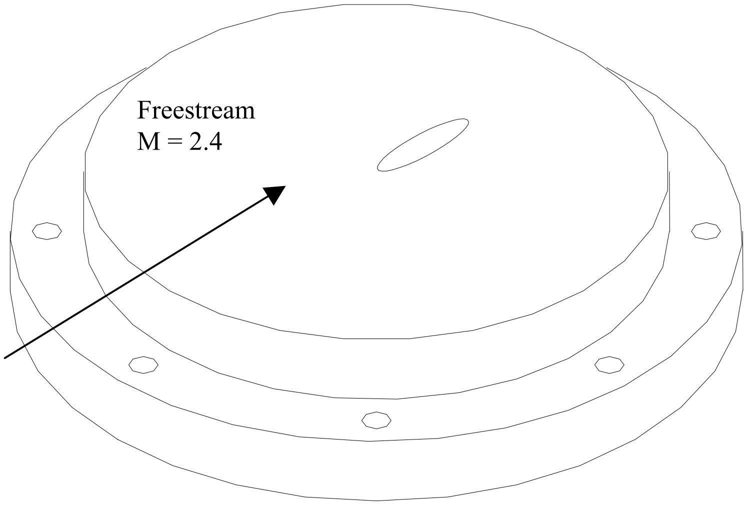

Figure 2.16 Low-Transverse-Angled Circular Injector Hole.

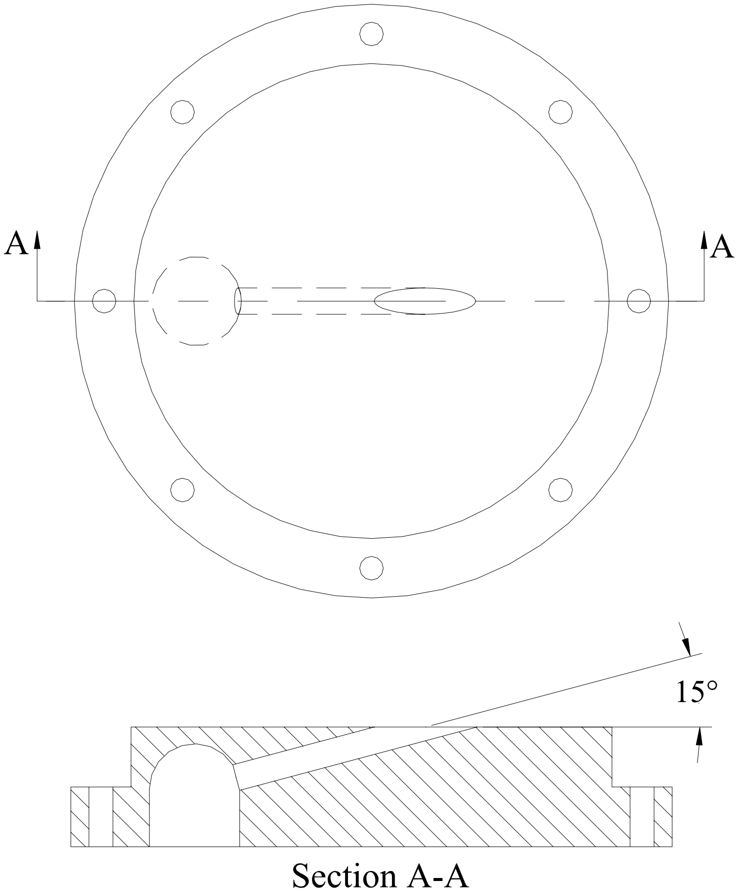

Figure 2.17 Single-Hole Injector.

2.3.5 1st Prototype Integrated Injector/Plasma Torch Concept

During these experiments, air was injected out of the injector array and helium was injected out of the torch. Helium was used because it simulates an ionized gas with a low molecular weight, which is what would come out of the torch if the torch fuel, such as methane, were being ionized by an electric arc. Tests were performed with nominal jet to freestream momentum flux ratios of 3.0 and 2.68 for the aero-ramp and plasma torch respectively. Table 2-5 presents the injector and plasma torch average test conditions associated with the experiments. During the experiments, either heated (hot) or ambient (cold) air was run through the aero-ramp injector array. The air in the injector plenum chamber was pre-heated using two 2000-watt cartridge heaters inside a heating chamber. The hot air from the heating chamber unit was then run to the injector through insulated lines. The inside walls of the injector plenum chambers were insulated to minimize the non-uniformity of temperature through each injector hole due to heat transfer. To further reduce non-uniformity due to heat transfer, the air from the heater was ran through the lines for a period of time to heat them so that when the tunnel was run, the heat transfer to the line from the air was minimized. The average rise in total temperature over the ambient conditions was about 50 K. Heating the air reduced the mass flow rate about 7.5-percent for the given momentum flux ratio. Once again, the jet exit parameters of the plasma torch were calculated at the throat of the torch, where the cathode constricted the anode throat down from 1.59-mm to 0.63-mm, corresponding to a torch arc gap setting of 0.178-mm. A sketch of the downstream sampling probe station location is shown in Figure 2.18. The location of the front of the probes was 33.0-mm downstream from the center of area of the aero-ramp injector array.

Table 2-5 1st Prototype Jet Exit Parameters.

	Cold $\bar{q}=3.0$	*Hot* $\bar{q}=3.0$	*Torch* $\bar{q}=2.7$	
M_j	**1.0**	**1.0**	**1.0**	—
$P_{t,j}$	**8.37**	**8.37**	**6.80**	***atm***
$T_{t,j}$	**289**	**338**	**290**	***K***
P_j	**4.42**	**4.42**	**3.31**	***atm***
T_j	**241**	**282**	**217**	***K***
a_j	**311**	**336**	**868**	***m/sec***
u_j	**311**	**336**	**868**	***m/sec***
ρ_j	**6.48**	**5.54**	**0.74**	kg/m^3
γ_j	**1.40**	**1.40**	**1.67**	—
$\dot{m}_j$	**16.0**	**14.8**	**0.20**	***gm/sec***
P_j/P_∞	**17.1**	**17.1**	**12.8**	—
T_j/T_∞	**1.85**	**2.16**	**1.67**	—
u_j/u_∞	**0.57**	**0.61**	**1.58**	—
ρ_j/ρ_∞	**9.23**	**7.90**	**1.06**	—
λ	**5.23**	**4.84**	**1.67**	—

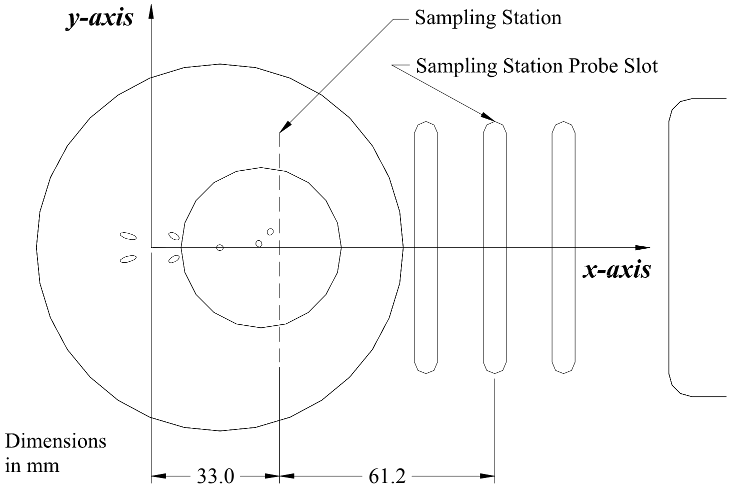

Figure 2.18 Sampling Station Location for Measurement Probes.

2.3.6 4-Hole Aero-Ramp Sizing, Evaluation, and Performance

All wind tunnel tests were performed at a freestream Mach number of 2.4. Experiments were performed while injecting ambient or heated air in order to simulate hydrocarbon fuels without the safety hazard. Tests were performed with jet to freestream momentum flux ratios of 1.1 to 3.3. Air from a supply tank was used as the injectant through the injector block and the momentum flux ratios were limited to a maximum value of 3.5. A throttling valve in the line allowed reduction to a nominal value of 1.1. Table 2-6 shows the matrix of test conditions examined in the experiments. Since the aero-ramp was designed to inject a set amount of gas at a higher jet to freestream momentum flux ratio than the single-hole injector, for better comparison the experiments were segmented by set mass flow values. Thus, for a given mass flow, the two injectors have an equivalent effective radius, and so it was used to normalize axial distance. During the experiments, either heated (hot) or ambient (cold) air was run through the aero-ramp injector array. The average jet exit conditions for the two injector models used in this study with ambient and heated air are shown in Table 2-7 and Table 2-8, respectively. The average rise in total temperature over the ambient conditions was about 84 K for the aero-ramp portion of the experiments and about 55 K for the single-hole. The discrepancy in average temperature rise was due to an initial measurement error, which made the plenum temperature of the single-hole injector cases look about 30 K hotter than they were due to an incorrect setting of the type of thermocouple. Correction of this error was made after the fact. Heating the air on average reduced the mass flow rate 10.7-percent for the aero-ramp configuration and 6.2-percent for single-hole for the given momentum flux ratios and amount of heating. Figure 2.19 shows the position of the aero-ramps three sampling stations where measurements were made. The stations were 16.5-, 54.6-, and 127.6-mm downstream from the center of area of the aero-ramp injector array. The insert slot shown just downstream of the aero-ramp array was used in the integrated experiments with plasma torch inserts. During the experiments with the aero-ramp alone, the slot was sealed with a blank aluminum insert. A sketch of the single-hole injectors sampling station locations is shown in Figure 2.20. The two sampling stations were located 57.6- and 131.2-mm downstream of the center of the single-hole injector. No data was taken at sampling station #1 with the single-hole configuration.

Table 2-6 Nominal Injector Test Conditions.

	$\dot{m}_{j,i} =$ **18 gm/s**	$\dot{m}_{j,i} =$ **26 gm/s**	$\dot{m}_{j,i} =$ **36 gm/s**
Aero-Ramp	$\overline{q} = 1.5$	$\overline{q} = 2.2$	$\overline{q} = 3.0$
15-deg Hole	$\overline{q} = 1.1$	**N/A**	$\overline{q} = 2.2$

Table 2-7 Ambient Average Test Parameters.

	4-Hole Cold $\bar{q}=1.5$	*4-Hole Cold* $\bar{q}=2.2$	*4-Hole Cold* $\bar{q}=3.0$	*1-Hole Cold* $\bar{q}=1.1$	*1-Hole Cold* $\bar{q}=2.2$	
M_j	1.0	1.0	1.0	1.0	1.0	—
$P_{t,j}$	4.19	6.03	8.37	3.01	6.03	*atm*
$T_{t,j}$	289	292	291	295	297	*K*
P_j	2.21	3.18	4.42	1.59	3.18	*atm*
T_j	241	243	242	246	247	*K*
a_j	311	313	312	314	315	*m/sec*
u_j	311	313	312	314	315	*m/sec*
ρ_j	3.24	4.62	6.44	2.29	4.54	*kg/m*^{3}
γ_j	1.40	1.40	1.40	1.40	1.40	—
$\dot{m}_j$	18.0	25.7	35.8	17.8	35.4	*gm/sec*
P_j/P_∞	8.8	12.6	17.5	6.3	12.6	—
T_j/T_∞	1.84	1.86	1.86	1.88	1.90	—
u_j/u_∞	0.57	0.57	0.57	0.57	0.57	—
ρ_j/ρ_∞	4.75	6.77	9.44	3.35	6.66	—
λ	2.69	3.85	5.36	1.92	3.82	—

Table 2-8 Heated Average Test Parameters.

	4-Hole Hot $\bar{q}=1.5$	*4-Hole Hot* $\bar{q}=2.2$	*4-Hole Hot* $\bar{q}=3.0$	*1-Hole Hot* $\bar{q}=1.1$	*1-Hole Hot* $\bar{q}=2.2$	
M_j	1.0	1.0	1.0	1.0	1.0	—
$P_{t,j}$	4.19	6.03	8.37	3.01	6.03	*atm*
$T_{t,j}$	360	366	368	337	335	*K*
P_j	2.21	3.18	4.42	1.59	3.18	*atm*
T_j	300	305	307	281	279	*K*
a_j	347	350	351	336	335	*m/sec*
u_j	347	350	351	336	335	*m/sec*
ρ_j	2.60	3.69	5.09	2.00	4.03	*kg/m*^{3}
γ_j	1.40	1.40	1.40	1.40	1.40	—
$\dot{m}_j$	16.1	23.0	31.8	16.6	33.4	*gm/sec*
P_j/P_∞	8.8	12.6	17.5	6.3	12.6	—
T_j/T_∞	2.30	2.33	2.35	2.15	2.14	—
u_j/u_∞	0.63	0.64	0.64	0.61	0.61	—
ρ_j/ρ_∞	3.82	5.41	7.46	2.93	5.90	—
λ	2.41	3.44	4.77	1.79	3.60	—

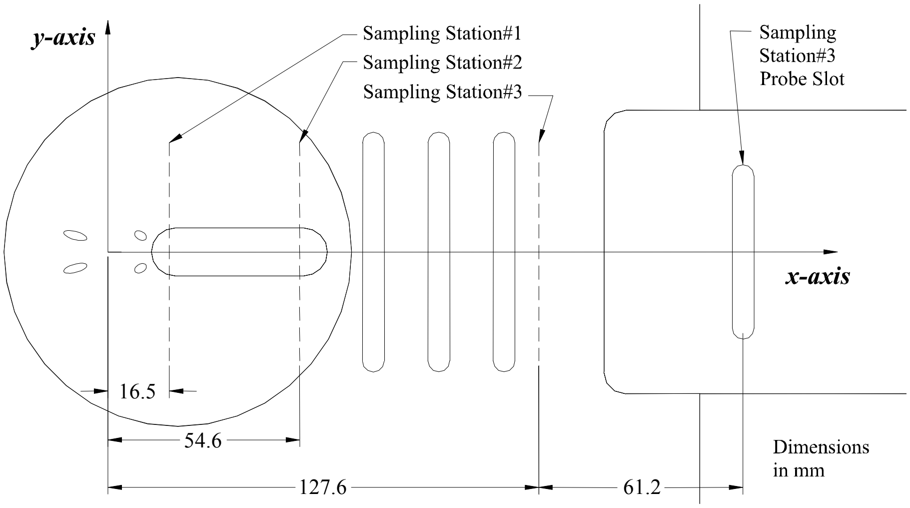

Figure 2.19 Sampling Stations for Measurement Probes.

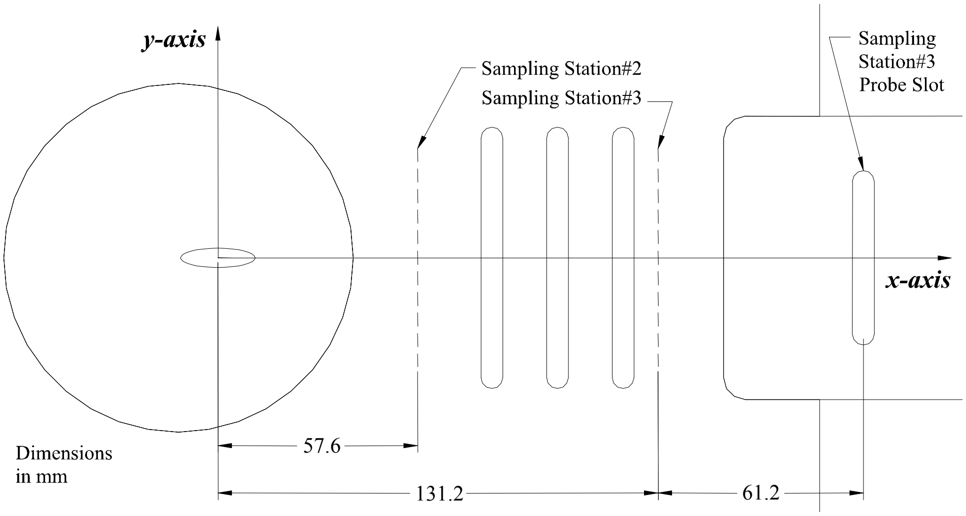

Figure 2.20 Sampling Stations for Measurement Probes.

2.3.7 Cold Flow Combustion Experiments: Integrated Design

Figure 2.21 shows pictures of the aero-ramp injector model with an integrated plasma torch (the back hole) used in this study. The aero-ramp used was the second injector constructed, which had a larger equivalent diameter (4.76-mm) than the first integrated injector configuration (3.18-mm). For this study, the DC plasma torch was operated from about 1500 to 3000 watts with various feedstocks. In addition, different electrode materials were used depending on the torch feedstock. The integration of the aero-ramp injector and plasma torch igniter consisted of an aero-ramp, which was sized for planned combustion experiments (See Section 5.2), and a plasma torch downstream of the centerline of the injector array. In order to vary the position of the torch relative to the array in this configuration, several slot inserts were created. The downstream torch location relative to the center of area of the injector array could be varied to 6, 8, or 10 d_{eq}, dubbed Station#1, #2, and #3, respectively. A picture of the plasma torch stations relative to the aero-ramp injector array is shown as Figure 2.22. The slot was purposefully made larger than the area required to place the torch at the three stations in case it became necessary to test the torch closer or further away from the injector array. Ultimately, the experimental results did not warrant any further investigation of torch position in the testable near-field range. A sketch of the two plasma torch inserts constructed for the integrated tests is shown in Figure 2.23.

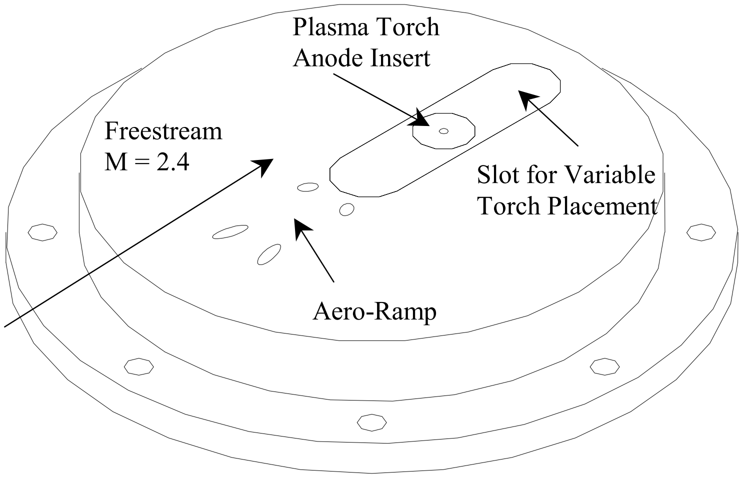

Figure 2.21 The Integrated Injector-Array/ Plasma torch igniter/Flame-holder models.

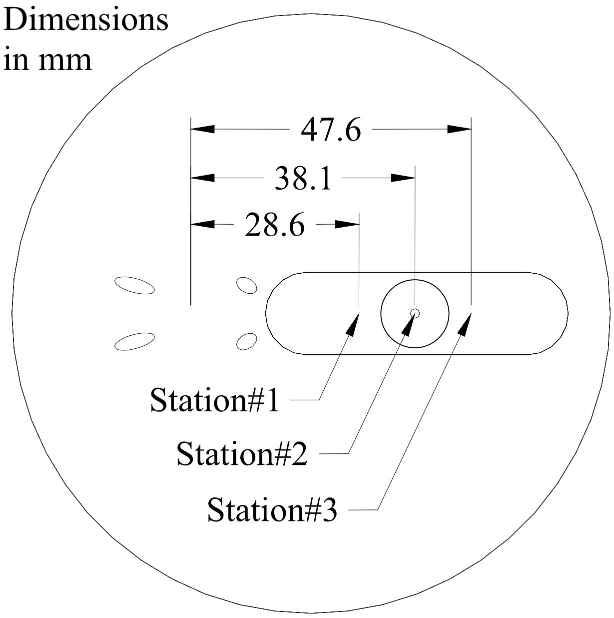

Figure 2.22 Plasma torch Station Locations.

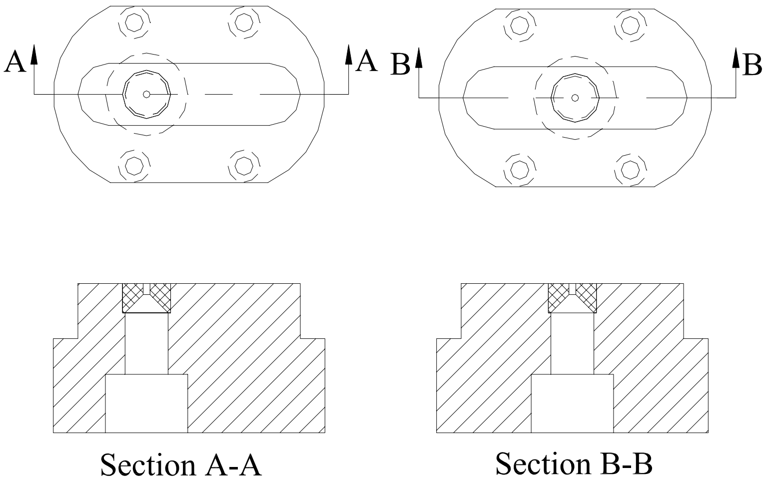

Section A-A

Section B-B

Figure 2.23 Slots with Plasma Torch Anode Inserts.

All wind tunnel tests for cold flow combustion experiments of the integrated design were performed at a freestream Mach number of 2.4. Experiments were performed first while injecting ambient air in order to simulate hydrocarbon fuels without the safety hazard associated with combustion or ethylene fuel for the combustion phase of the experiments. Tests were run with jet to freestream momentum flux ratios of 1.5 to 3.0. Air from a supply tank was used as the injectant through the injector block and the momentum flux ratios were limited to a maximum value of 3.5. A throttling valve in the line allowed reduction of the injector plenum pressure. Similar constraints confined the flow of ethylene to roughly the same range of momentum flux ratios (1.0 to 3.5). The plasma torch was operated at a nominal jet to freestream momentum flux ratio of 1.2 for all feedstocks used (methane (1.17), nitrogen (1.22, nitrogen/hydrogen (1.24), and air (1.22)) corresponding to the torch plenum pressure of 3.40 atm. Table 2-9 presents the average test parameters for the integrated configuration for the cold flow combustion experiments.

Figure 2.24 shows the location of the sampling station used to measure the plume temperature, 127.6-mm downstream from the center of area of the aero-ramp injector array. The corresponding downstream distances from the center of the plasma torch holes to the sampling plane were 99.0-, 89.5-, and 80.0-mm for torch stations#1-3 respectively.

Table 2-9 Average Test Parameters for Integrated Design Combustion Tests.

	4-Hole $\bar{q}=1.5$	***4-Hole*** $\bar{q}=3.0$	***Torch*** CH_4 $\bar{q}=1.2$	***Torch*** N_2 $\bar{q}=1.2$	***Torch*** N_2+H_2 $\bar{q}=1.2$	***Torch Air*** $\bar{q}=1.2$	
M_j	**1.0**	**1.0**	**1.0**	**1.0**	**1.0**	**1.0**	—
$P_{t,j}$	**4.50**	**9.01**	**3.40**	**3.40**	**3.40**	**3.40**	***atm***
$T_{t,j}$	**287**	**288**	**292**	**292**	**292**	**292**	***K***
P_j	**2.51**	**5.02**	**1.86**	**1.80**	**1.78**	**1.80**	***atm***
T_j	**257**	**258**	**254**	**244**	**241**	**244**	***K***
a_j	**307**	**307**	**414**	**318**	**336**	**313**	***m/sec***
u_j	**307**	**307**	**414**	**318**	**336**	**313**	***m/sec***
ρ_j	**3.34**	**6.66**	**1.43**	**2.52**	**2.29**	**2.60**	***kg/m^3***
γ_j	**1.24**	**1.24**	**1.30**	**1.40**	**1.43**	**1.40**	—
$\dot{m}_j$	**18.3**	**36.5**	**0.18**	**0.36**	**0.35**	**0.37**	***gm/sec***
P_j/P_∞	**9.8**	**19.7**	**7.3**	**7.0**	**7.0**	**7.0**	—
T_j/T_∞	**1.97**	**1.97**	**1.95**	**1.87**	**1.84**	**1.87**	—
u_j/u_∞	**0.56**	**0.56**	**0.75**	**0.58**	**0.61**	**0.57**	—
ρ_j/ρ_∞	**4.84**	**9.64**	**2.07**	**3.65**	**3.31**	**3.77**	—
λ	**2.70**	**5.39**	**1.56**	**2.11**	**2.02**	**2.15**	—

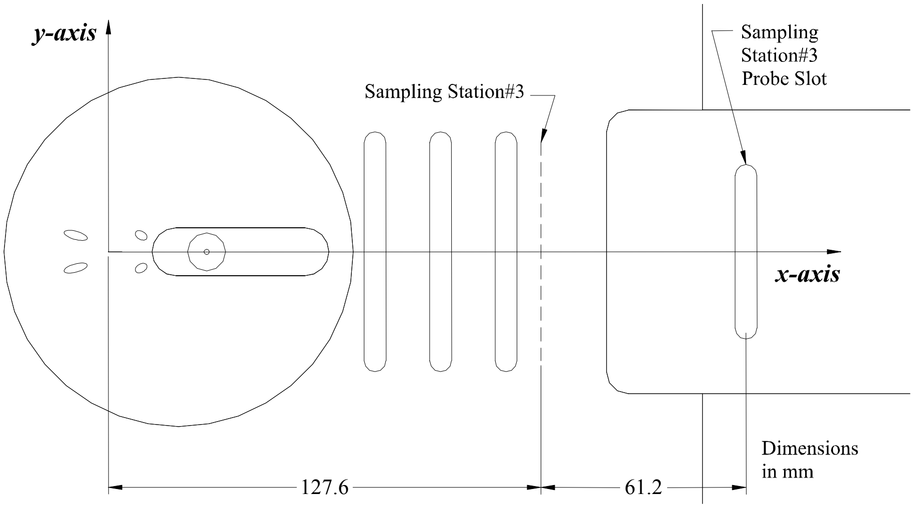

Figure 2.24 Sampling Probe Measurement Station.

2.4 Injectant Mass Flow Calculations

Calculation of the mass flow rates through the various injectors in this study was performed to account for the viscous losses in the injection processes and allow scaling of the injector dimensions for comparison with each other. The actual mass flow rates through the injectors and their corresponding discharge coefficients were measured with an orifice flow meter. Calculation of the injectors discharge coefficients and actual mass flow rates requires the following steps; first, the ideal mass flow rate through the orifice flow meter is calculated. For differential pressure producing flow meters, such as an orifice type, this can be done using the following equation, assuming incompressible flow (Miller[81]):

$$\dot{m}_{i,Orifice} = \frac{\pi}{4}\sqrt{2}\frac{d^2}{\sqrt{1-(d/D)^4}}\sqrt{\Delta P \rho} \tag{2.2}$$

where, the differential pressure across the orifice, ΔP, is in N/m^2, and the density value, ρ, is in kg/m^3 and *d* and *D* are the diameters of the orifice hole and pipe, respectively. Then the actual mass flow rate is calculated using the orifice discharge coefficient, which is a function of the orifice flow meter geometry and the pipe Reynolds number. For pipe flow with a Reynolds number above 4000, the following equation for the orifice discharge coefficient may be used:

$$C_{d,Orifice} \equiv \frac{\dot{m}_{a,Orifice}}{\dot{m}_{i,Orifice}} = C_\infty + \frac{b}{\mathrm{Re}_D^n} \tag{2.3}$$

where, for an orifice flow meter with corner taps, this equation becomes:

$$C_{d,Orifice} = 0.5959 + 0.0312\beta^{2.1} - 0.184\beta^{8} + \frac{91.71\beta^{2.5}}{\mathrm{Re}_D^{0.75}} \quad \textbf{(2.4)}$$

where, $\beta = d/D$. Once the actual mass flow rate through the meter is known, then as long as there are no leaks in the piping from the meter to the injector plenum, it is equal to the actual mass flow rate through the injector. Now all that is left is to calculate the injector discharge coefficient by calculating the ideal flow rate through the injector by the following equation:

$$\dot{m}_{i,Injector} = P\sqrt{\frac{\gamma}{RT}}A = \frac{\dot{m}_{a,Orifice}}{C_d} \quad \textbf{(2.5)}$$

where, P and T are the static pressure and temperature at the throat of a sonic injector, and A is the injector throat area.

Distance normalization was accomplished in the experiments using either the effective diameter or the effective radius. The effective diameter is defined as:

$$d_{eff} = d_{eq}\sqrt{C_d} \quad \textbf{(2.6)}$$

where C_d is the discharge coefficient and d_{eq} is the injector equivalent jet diameter. This parameter was used in the early parametric experimental work and for individual injector assessment in this body of work due to its geometric nature, which allows for an easy physical interpretation of the injector diameter accounting for viscous blockage affects.

The effective radius was originally defined in Barber et al.[43] as the radius of the equivalent circular area of freestream flow with a mass flux equal of that of the injectors except for a factor of π in the denominator. In effect, it is not a “radius” but an effective proportionate mass-flux length-scale. The effective radius is defined:

$$R_b = \sqrt{\frac{\dot{m}_{j,a}}{\rho_\infty u_\infty}} \quad \textbf{(2.7)}$$

where $\dot{m}_{j,a}$ is the actual injector mass flux, equal to the ideal mass flux times the injector discharge coefficient, $\dot{m}_{j,i}C_d$. For an injector design comparison based on a set mass flow range of operation for a set of given freestream conditions, such as designing a replacement fuel injector for a scramjet combustor, the effective radius is an appropriate tool for sizing an injector. This allows the relative size of the injector to be determined, knowing its desired operational range of jet to freestream momentum flux ratio in comparison to another, baseline injector.

Table 2-10 through Table 2-12 presents the discharge coefficients, effective diameters, and radius for the injector models and respective set of experiments which involve distance normalization. Viscous effects during the plasma torch experiments were not accounted for and not used during distance normalization. Instead, the anode throat diameter was used (1.59-mm). This was done for several reasons. First, the transverse anode study only involves a comparison of two geometries with the same anode throat diameter. Furthermore, due to electrode erosion and thermal choking, the true effective radius and diameters would vary with the lifetime of the electrodes. The rest of the experiments involving plasma torches focused more directly on the dimensions of the injector arrays used and their corresponding plumes. Thus for these experiments, the injectors effective diameters or radii were used. Table 2-13 through Table 2-15 present the normalized sampling station location information for the various experiments performed. The information is shown in terms of both effective diameter and radius, though only one or the other term might be used in the corresponding results sections.

Table 2-10 Normalization Parameters: 1st Prototype Aero-Ramp Injector (Air).

	4-Hole $\bar{q}=1.5$	***4-Hole*** $\bar{q}=3.0$	
C_d	**0.746**	**0.765**	—
d_{eff}	**2.74**	**2.78**	***mm***
R_b	**3.81**	**5.45**	***mm***

Table 2-11 Normalization Parameters: Aero-Ramp Sizing Experiments (Air).

	4-Hole $\bar{q}=1.5$	***4-Hole*** $\bar{q}=2.2$	***4-Hole*** $\bar{q}=3.0$	***1-Hole*** $\bar{q}=1.1$	***1-Hole*** $\bar{q}=2.2$	
C_d	**0.873**	**0.877**	**0.880**	**0.869**	**0.883**	—
d_{eff}	**4.45**	**4.46**	**4.47**	**5.23**	**5.27**	***mm***
R_b	**6.47**	**7.76**	**9.17**	**6.42**	**9.14**	***mm***

Table 2-12 Normalization Parameters: Cold Flow Combustion Experiments (Ethylene).

	4-Hole $\bar{q}=1.5$	***4-Hole*** $\bar{q}=3.0$	
C_d	**0.839**	**0.845**	—
d_{eff}	**4.36**	**4.38**	***mm***
R_b	**6.35**	**9.01**	***mm***

Table 2-13 Normalized Station Locations: 1st Prototype Aero-Ramp Injector (Air).

Sampling Station	*4-Hole* $\bar{q}=3.0$
(x/d_{eff})	**11.9**
(x/R_b)	**6.1**

Table 2-14 Normalized Station Locations: Aero-Ramp Sizing Experiments (Air).

Sampling Station	*4-Hole* $\bar{q}=1.5$	*4-Hole* $\bar{q}=2.2$	*4-Hole* $\bar{q}=3.0$	*1-Hole* $\bar{q}=1.1$	*1-Hole* $\bar{q}=2.2$
#1 (x/d_{eff})	—	—	**3.7**	—	—
#1 (x/R_b)	—	—	**1.8**	—	—
#2 (x/d_{eff})	**12.3**	**12.2**	**12.2**	**11.0**	**10.9**
#2 (x/R_b)	**8.4**	**7.0**	**6.0**	**9.0**	**6.3**
#3 (x/d_{eff})	—	—	**28.6**	—	**24.9**
#3 (x/R_b)	—	—	**13.9**	—	**14.4**

Table 2-15 Normalized Station Locations: Cold Flow Combustion Experiments (Ethylene).

Sampling Station	*4-Hole* $\bar{q}=1.5$	*4-Hole* $\bar{q}=3.0$
(x/d_{eff})	**29.2**	**29.1**
(x/R_b)	**20.1**	**14.2**

Chapter 3 Experimental Methods

3.1 Shadowgraphs

Visualization of the jet-freestream shockwave interactions, injector-jet plume, and boundary layer were made possible with shadowgraph photography. Also known as a direct-shadow schlieren method, the shadowgraph is an optical method for observing the changes in refractive index that accompany the changes in density, which are present in the flow past an injector at sufficiently high Mach number (Holder and North[82]). In a typical flowfield in a supersonic wind tunnel with non-uniform density gradients or inhomogeneous gases, if one shines a uniform, parallel beam of light perpendicularly through the test section, the density differences will give rise to local changes of the index of refraction. These changes will deflect the light rays from the beam in the direction of increasing density, leaving dark and light regions near the location of shockwaves and turbulent structures. The shadow effect shows a two-dimensional picture of the flow disturbances in which the variation of distance to the disturbance source would change the width of the deflected light as seen at the viewing plane. Therefore, the change in illumination is roughly proportional to the rate of change of the density gradient. For the experiments encompassed in this body of work, shadowgraphs were taken with one of two methods. During the investigation of the shock structures near the injector jets, the shadowgraphs involved the use of a Nanopulser spark light source and Polaroid instamatic film. Due to additional light from the plasma torch in operation, the experiments that dealt with the plasma torch used an alternate method involving the use of a laser as a light source and a CCD camera. The two methods used are described in the subsequent subsections.

3.1.1 Spark Light Source

Spark shadowgraphs were taken using a Nanopulser spark with an exposure time of $2\text{x}10^{-8}$ sec. At Mach 3.0 and 2.4, with a 20-nanosecond pulse of light, it is possible to see the turbulent eddy structures in the flow significantly larger than 0.012-mm and 0.011-mm respectively. Figure 3.1 shows the setup used in these experiments. Light from the Nanopulser spark was expanded using a converging-diverging lens and shone upon a 30.5-cm diameter parabolic mirror with a focal length of 2.03-meters. This created a beam of near parallel light, which was directed perpendicularly through the wind tunnel test section. The light was then exposed to Polaroid Type-57 instamatic short exposure time film.

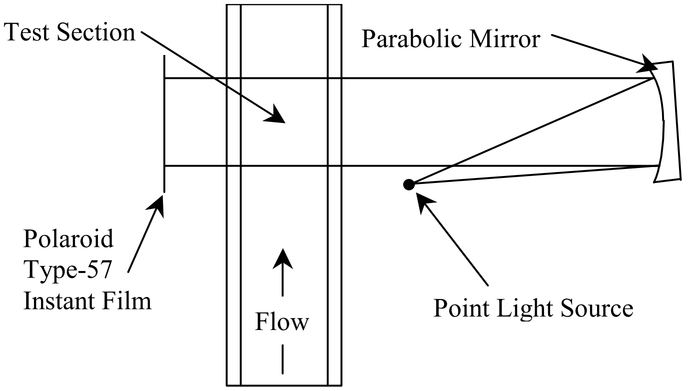

Figure 3.1 Spark Shadowgraph Setup.

3.1.2 High-Speed Camera

Shadowgraphs were taken using a Hadland Photonics 4-CCD Imacon 468 high-speed digital BW camera and a Spectra Physics 2.5-watt continuous-beam argon-ion laser with a Model 265 Exciter as the light source. The laser beam was expanded into a cone of light using a microscope objective lens reflected off a flat mirror, and then reflected off a parabolic mirror, which created a near parallel beam of light which perpendicularly crossed the wind tunnel test section as seen in Figure 3.2. After crossing the test section, the beam was reflected with another parabolic mirror and then off another mirror on its way down to another focal point in a standard Z-formation. During the transverse angled anode study with the plasma torch, the laser was operated with a internal prism type mirror which enabled tuning of the laser to a wavelength of 514.5-nm, with a peak power of about 0.7 watts. At the second focal point in the optical setup described above, the refocused 514.5-nm beam was then shone through a narrow band pass filter, which blocked out any additional light produced from the plasma jet of the torch, and then focused with a converging-diverging lens directly onto the High-Speed Cameras 4-CCD array. This setup worked, but it had its problems. Due to hard to reach dust particles and scratches on the microscope objective lens, the quality of the images was reduced and the addition of the band-pass filter created interference patterns on the images and an integration time of $10\text{x}10^{-8}$-sec (100-ns) was obtained. In addition, as it turns out and will be described in Section 6.1.6, there happens to be a C_2^* line at 516.5 nm that is very close to the filters wavelength, and is very intense in hydrocarbon plasma plumes.

The next time it became necessary to use this setup was during the integrated combustion experiments. At that time, a new microscope objective lens was used to enhance the clarity of the images. In addition to maximize power output from the laser, a broadband mirror was used to take advantage of all six wavelengths that the laser is capable of producing, bringing the total intensity of the laser light up to 2.5 watts. Furthermore, the converging-diverging lens was replaced with a Nikkor 75 – 240-mm f4.5 – 5.6D AF camera lens, which made it easier to focus on the focal plane past the disturbances in the test section. This configuration made it possible to take pictures with exposure times of $2x10^{-8}$ sec. With 20-nanosecond exposure times, the intensity of the incident light from the torch was not high enough to be noticed by the CCD's, and it was not necessary to use the band-pass filter.

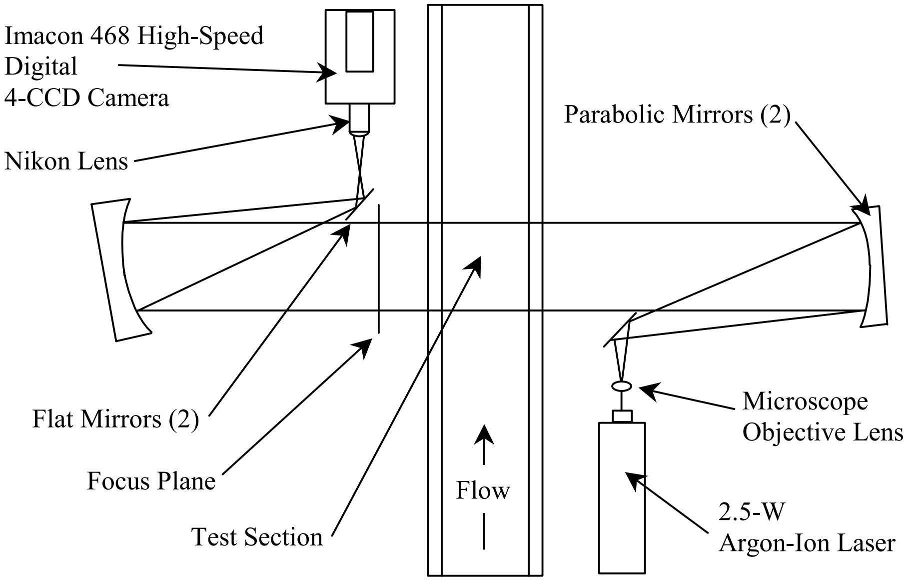

Figure 3.2 Laser Shadowgraph Setup.

3.2 Flame-Plume Imagery

Pictures of the flame plumes produced in the combustion phase of the experiments were taken with either a 35-mm camera or the Hadland Photonics 4-CCD Imacon 468 high-speed digital BW camera. Pictures were taken of the torch plume in the visible spectrum or with various band-pass filters, which enabled imaging of the reacting species of the combustion plumes. The position and focus of the cameras were held relatively constant and perpendicular to the test section in front of the torch plume. Pictures were taken of known objects at the plane of the torch exit to reference the dimensions seen in the images.

3.3 Surface Oil Flow

Visualization of the surface flow patterns near the injectors was accomplished via the use of 500-cSt silicone oil mixed with two colors of fluorescent dye. A thin layer of fluorescent green oil was placed all around the injector, and a thin strip of fluorescent red oil was placed in front of the injector holes. This was done to help show the direction of the surface flow as it passed the injector holes. The tunnel was run for about 8-seconds to let the paint move downstream of, and around, the injector configurations with the flow. After each run, the patterns were illuminated with a 100-watt ultraviolet lamp and pictures were taken with a 35-mm camera. The surface oil flow patterns were also recorded on videotape during tunnel operation. The unstarting of the tunnel at the end of each run can sometimes have a distorting effect by pushing the paint on the surface in all directions. Although the unstart causes some distortion in the images, the surface flow pictures still accurately represent the patterns created from the air injection as determined by video and direct observations during the runs.

3.4 Pressure-Sensitive Paint

Measurements of the static pressure fields around the injector were made using Pressure-Sensitive Paint (PSP). The PSP employed is based on the widely-used fluoroacrylic copolymer (FIB) binder and incorporates the fluorinated platinum porphyrin species, meso-Tetra-(pentafluorophenyl) porphine, Pt(TfPP). The PSP was illuminated in the near UV range with a Light-Emitting Diode (LED)-based array. The wavelength of the resulting luminescence of the paint occurred in the 500- to 600-nm range and was imaged on a CCD camera. Due to oxygen quenching effects, the resulting intensity profile is inversely proportional to the static pressure field around the injector.

Figure 3.3 shows a sketch of the static pressure ports around the two injector models examined in this study. 1.59-mm copper tubes were glued to the back of the pressure port holes on the injector models with epoxy and 30-cm lengths of Tygon flexible tubing attached to the pressure ports to six ±1.0 atm differential pressure transducers with built in amplifiers. The signals were then fed directly into the data acquisition system. Calculation of the local static pressure field was done using an in-situ method involving sample calibration information of intensity as a function of temperature, pressure, and information from one of the pressure taps, typically tap #5, on the surface near the injector. With the unsteady temperature variations associated with the blow down facility, the maximum error in calculated static pressure was estimated to be 10-percent based on comparison between the other static ports and the deduced pressure field. A detailed description of the PSP theory and reduction process is given in Crites[83]. A detailed description of the process used in these tests is given here in Appendix A.

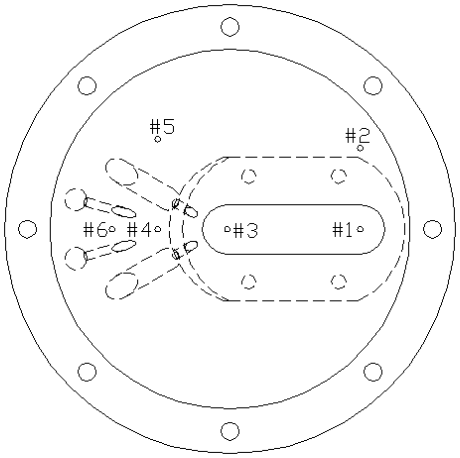

a) Aero-Ramp

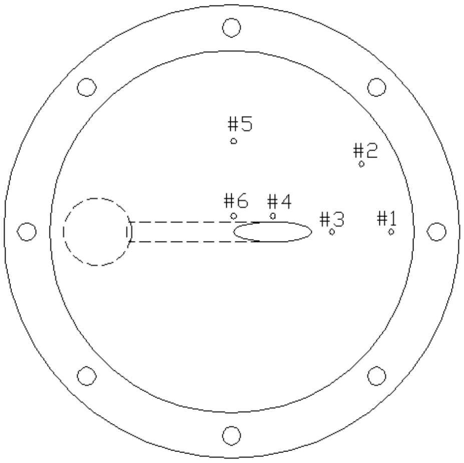

b) Single-Hole

Figure 3.3 Static Pressure Port Locations.

3.5 Aerothermodynamic Sampling

Aerothermodynamic sampling was accomplished with two wedge-shaped rakes with either pressure or temperature probes attached to them. A Pitot, total temperature, and cone-static probe were attached to one of the rakes and three total temperature probes were attached to the other. Using the total temperature rake to perform profiles reduced the number of runs per profile by a factor of three. This proved useful during the deduced mixing analogy profiles, which were based on total temperature measurements. The probes on the two rakes were spaced 6.4-mm apart.

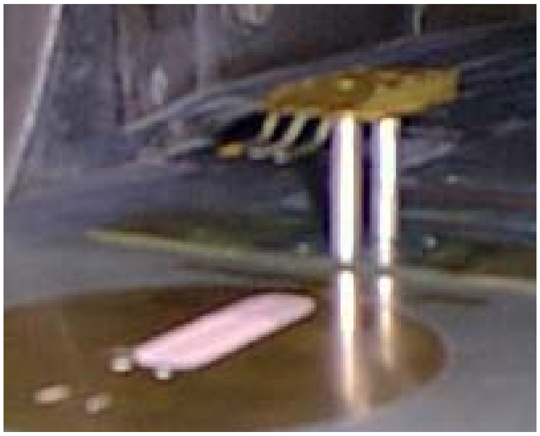

Figure 3.4 Pressure Rake in the Mach 2.4 Test Section Behind the Aero-Ramp Injector.

3.5.1 Pitot Pressure Probe

The Pitot probe had a 1.59-mm outer diameter and 1.04-mm inner diameter, which gave a capture area of 0.85-mm^2. A sketch of the Pitot probe is shown in Figure 3.5. The Pitot probe was attached to a Statham 0-3.40 atm pressure transducer by a 15-cm length of flexible Tygon tubing and pressure fittings. The output voltage was amplified by a Measurements Group 2310 Signal Conditioning Amplifier and inputted into the data acquisition system.

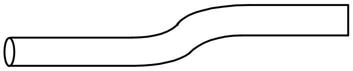

Figure 3.5 Pitot Pressure Probe.

3.5.2 Cone-Static Probe

The cone-static probe consisted of 1.59-mm-outer-diameter pipe with a 10-degree cone half-angle. There were four small ports (diam. = 0.38-mm) arranged symmetrically around the cone to help reduce the effects of misalignment of the probe to the flow. A sketch of the Cone-static probe is shown in Figure 3.6. The cone-static was attached to a Statham 0-20.4 atm pressure transducer by a 15-cm length of flexible Tygon tubing and pressure fittings. The output voltage was amplified by an Ectron Model 516-5SG Excitation Supply and Amplifier and inputted into the data acquisition system.

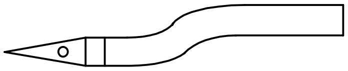

Figure 3.6 Cone-Static Probe.

3.5.3 *Total Temperature Probe*

Temperature profiles were measured with a sampling rake consisting of three 1.59-mm-outer-diameter tubes spaced 6.4-mm apart with thermocouples inside. Each tube had an inner diameter of 1.04-mm giving each probe a 0.85-mm^2 capture area. The total temperature probes each had four small holes (diam. = 0.23-mm) drilled around their tubes. This was done to improve the recovery factors of the probes. Each total temperature probes capture to recovery area ratio was 5 to 1 resulting in a recovery factor of 0.98. Exposed junction type-E thermocouples with 0.25-mm diameter beads were placed inside the three total temperature probes. The millivolt signals from the thermocouples were read directly into the data acquisition system. A sketch of one of the total temperature probes is shown in Figure 3.7.

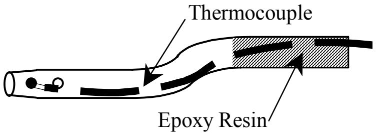

Figure 3.7 Total Temperature Probe.

3.5.4 *Aerothermodynamic Sampling Traverse*

The traverse used in the aerothermodynamic sampling experiments used a 4-Phase stepper motor made by Rapid Syn (Model 34D-9209A) and an American Precision Industries (Model DMA-64) stepper motor controller. The step angle was 1.8-deg. The tunnel control program was generally set to move 240 steps at speed of 600 steps a second up over ~8 seconds stopping at 27 Locations (~25-mm) along the way, and then 600 steps per second down to the original position. The travere motor was powered by a 24-volt DC power supply. The position of the traverse is measured by an LVDT (Linear Variable Differential Transformer). The LVDT is calibrated with dial calipers and a voltmeter. The dial calipers allow an accuracy of 0.0025-mm, which is sufficient for the experiments performed.

3.5.5 Calibration

All the pressure transducers used in the experiments were calibrated using a dead weight test unit. The pressure transducers were connected to the unit and calibrated over a range of 0 to 6.8 atm relative to the atmospheric pressure. Upon calibration, ten or more data points were taken for each transducer and a check for hysteresis was made. A linear regression technique was used to create a linear relationship between the input pressure and the output voltage. After the transducers were calibrated, they were connected to the data acquisition system, and the calibration curve fits were checked with the dead weight test unit.

Thermocouple calibration was accomplished by use of an onboard cold junction compensator in the National instruments AMUX-64T multiplexer board used in conjunction with a built-in LabVIEW thermocouple calibration routine to adjust the signals from the thermocouples to temperature. This method calculated the Type-E thermocouple temperature with an uncertainty of ±1.8 K.

3.5.6 Flow Property Data Reduction

The aerothermodynamic measurements with heated air injection made with the three probes were reduced in a standard fashion. The reduction was performed using an iterative scheme involving the perfect gas relations, the Rayleigh-Pitot formula, and the Taylor-McColl cone flow solutions. See Appendix A for a detailed description of the process.

3.5.7 Mixing Analogy

Aerothermodynamic sampling tests with total temperature probes were performed with ambient and heated air as the injectant. This was done to obtain temperature profiles analogous to the mass fraction of a simulated hydrocarbon gas with a molecular weight similar to air, such as ethylene. To obtain the mixing analogy, profiles were generated with both heated and ambient air in the injector plenum chamber. A detailed analysis of the Mixing Analogy and its development are given in Appendix A.

3.6 Spectroscopy

Spectroscopic data was taken with an Ocean Optics S2000 3-CCD fiber-optic Spectrometer. Each individual channel in the spectrometer had its own grating and CCD array with a spectral resolution of 0.08 nm. The overall spectral range observed in increments by the three spectrometers was 196- to 730-nm. A sketch of the spectrometer and its viewing assembly are shown in Figure 3.8. At the Spectrometer housing, each CCD spectrometer has its own fiber optic cable. Then, the three cables are joined into one main cable with a trifurcating cable splitter. To localize the viewing area, a collimating lens was attached to the end of the fiber optic cable. This reduced the width of the viewing area to about a 2.0-mm diameter. Further reduction of the width of the viewing area to a 0.5-mm diameter was made with a scope that fit over the collimating lens.

In order to point the collimating lens of the fiber optic spectrometer toward different sections of the plume in the test section, a two-axis traversing system was used. This system consisted of two Velmex, Inc. UniSlide Assembles linear traverses mounted to each other, operated by 200-steps per revolution Warner Electric stepping motors. This enabled movement in the downstream and vertical directions. The two traverses were operated by a Velmex, Inc. stepping motor controller, which was in turn operated by the PC, which controlled the spectrometer using LabVIEW software. The whole traverse assembly was mounted to a 1.2x1.2-m Melles Griot optical breadboard at the side of the wind tunnel test section.

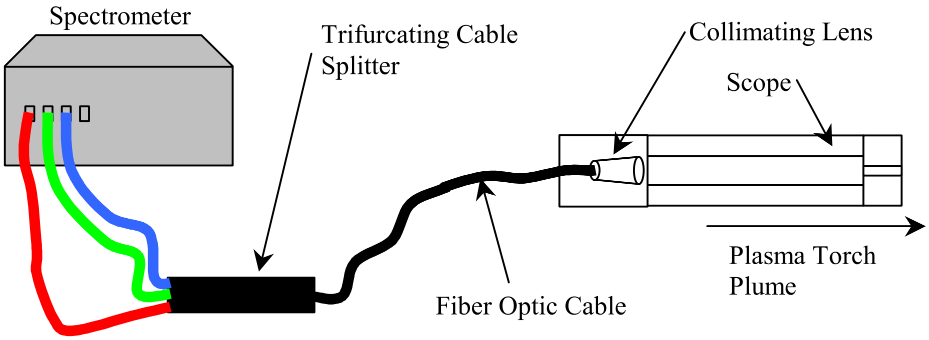

Figure 3.8 Fiber Optic Spectrometer.

3.7 Data Acquisition System

General data acquisition was performed with a Pentium-120 personal computer running with a Windows-95 operating system and a 16-bit, 16-channel single ended A/D converter made by National Instruments, Model AT- MIO-16XE-50. To reduce signal noise, the A/D converter was used in an 8-channel differential input mode. The converter was configured with a National Instruments, Model AMUX-64T multiplexer board to increase the total number of usable differential channels to 32. The multiplexer was also equipped with an onboard cold junction compensator for temperature measurement. To minimize signal noise, the multiplexer was placed in a metal box, which was grounded to a copper water pipe in the room. The data acquisition system used LabVIEW software to process and record the input signals. During an experiment, the input signals were sampled at a rate of 100 Hz.

During the cold flow combustion experiments, information about the flame plume from the spectrometer was recorded on a Pentium2-450 personal computer running Windows NT 4.0 and LabVIEW data acquisition software. An Ocean Optics ADC1000 high-speed ISA-bus A/D card was used to create a spectrometer interface to the PC. The 12-bit, 8-channel, single-ended A/D card can acquire spectral data from multiple channels simultaneously. The ADC1000 features 1.0 MHz sampling frequency and is designed for use with the S2000 Miniature Fiber Optic Spectrometer used in the experiments. This computer was also equipped with a National Instruments, Model AT-MIO-16XE-50 A/D converter, which was used to trigger the spectrometer system to acquire data and move its traverse.

Chapter 4 Initial Aero-Ramp Development and Integration Studies

The purpose of this Chapter is to explain the early work done on this project involving the refinement of the aero-ramp injector and the integration of a plasma torch into the flowfield of the injector. The refinement of the original nine-hole aerodynamic-ramp injector developed by J.A. Schetz began from the conclusions of the experiments based on the comparison of the performance of the aero-ramp to a physical ramp injector, published by R. Fuller[84]. From this body of work, the realization was concluded that an optimization of the nine-hole array was a cumbersome endeavor with a multitude of parameters, and the suggestion was made that a single row of three holes should be studied to reduce the total number of variable parameters. The following two sections deal with the refinement of the aero-ramp conceptual design based on the experimental investigation of toe-in on a single row of three injector holes, the first attempt at the integration of plasma torch into the three-hole array, and the first attempt to incorporate these ideas into a nine-hole aero-ramp injector array. A section on the initial development of the plasma torch in operation in a supersonic crossflow is presented next.

Finally, from the results and ideas developed in these studies and other research investigations involving aero-ramp injectors and plasma torches, an initial prototype integrating four-hole aero-ramp injector-array with a plasma-torch injector/igniter was developed. Results for this new prototype device are presented in Chapter 5 and Chapter 6.

4.1 3-Hole Row Injector Studies: Effects of Toe-in and Swirl

In an effort to further the understanding of the aero-ramp injector, the effects of toe-in (i.e. inward yaw of the injector jets to the centerline of the overall injector) on a single-row, three-hole injector array were investigated first. Other interesting parameters of study were recognized, such as the lateral injector spacing, the transverse injection angles of the array, and non-circular injector orifices. Nevertheless, toe-in was chosen as the first parameter to vary because it was thought to be one of the main factors for augmenting the axial vorticity of the main plume based on a row-to-row basis. The entire body of work pertaining to this preliminary study is presented as Appendix B. Only the main results are presented here. Three different configurations were tested involving three, 30-deg transversely angled, round injection holes in a row exposed to a Mach 3.0 cross stream. The two exterior holes of the injector row were set at toe-in angles of 0-, 15-, and 30-deg. The 30-deg injector model is shown in Figure 4.1(a). It was found that increasing the toe-in angle of the exterior injector holes greatly increased the mixing efficiency and core penetration of the overall jet plume generated by the array. However, with the increase in mixing due to high toe-in angles came increased total pressure losses. Interestingly enough, the observed oblique shock angle also increased with jet to freestream momentum ratio and toe-in angle of the exterior holes of the injector, but the integrated total pressure losses associated with the injector shock structure were found to be minimized with the 15-deg toe-in array injector, not 0-deg.

The second cold flow mixing study performed on a three-hole injector array involved studying the affects of induced injector jet swirl on downstream mixing performance. The configuration consisted of a row of three holes configured to model the geometry of two plasma torches with a single hole in between them, as shown in Figure 4.1(b). Each of the simulated plasma torch orifices was equipped with a flow-swirler similar to the one used in a real plasma torch. The study involved changing the direction of swirl of the two simulated plasma torch jets in an attempt to reinforce the natural jet vortices produced by the injector array in a Mach 3.0 flow. The details of this early study are presented as Appendix C. Only the main results are noted here. Results from the experiments showed improved mixing with an increase of jet to freestream momentum ratio and swirl of the injector array. Swirl also reduced the total pressure losses.

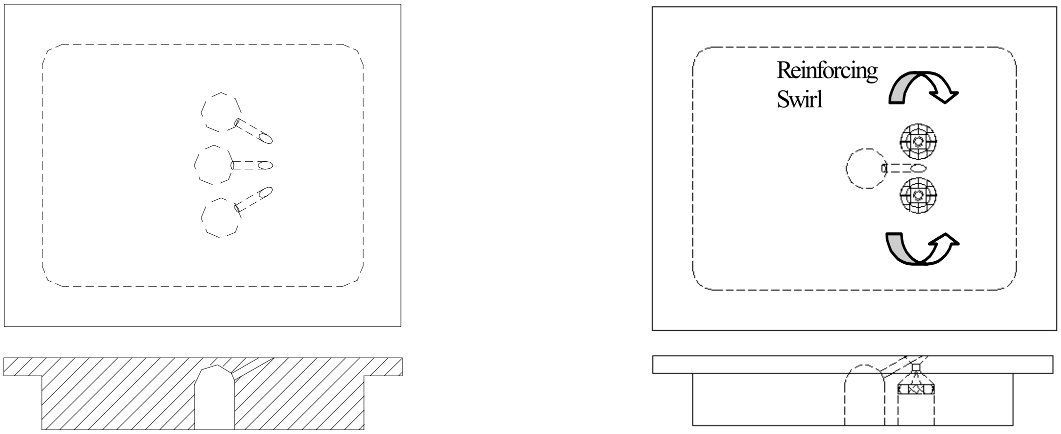

a) Toe-in Angle Study (30-deg model) **b) Swirl Study**

Figure 4.1 Transverse Injector Models Used in First Studies.

4.2 9-Hole Aero-Ramp with Swirl

The incorporation of the results found in the jet swirl study with the three-hole array into a nine-hole aero-ramp injector was performed in a Mach 3.0 crossflow at Virginia Tech. This was done to simulate the integration of two plasma torches into the downstream end of the injector array. The aero-ramp test model consisted of nine holes each with a diameter of 3.18-mm and an equivalent diameter for the whole array of 9.53-mm. The simulated plasma torch orifices each were at a 2 to 1 scale with flow swirlers inserted inside to positively reinforce the direction of the main plume vortex. The two plasma torch holes were placed perpendicular to the mainstream flow. See section 2.3.1 for details.

A preliminary qualitative assessment of the flowfield around the injector was performed by taking shadowgraph pictures and running surface oil flow visualization experiments. After an assessment of the pictures, the hole in between the two simulated plasma torches was plugged (creating an eight-hole array) and an additional shadowgraphs and surface oil flow measurements were made. The experiments were performed to gain an initial understanding of the issues involved with the incorporation of a plasma torch into a multi-port fuel injector system.

Figure 4.2 presents the shadowgraph pictures of the nine- and eight-hole aero-ramp injector configurations with two simulated plasma torch orifices located in the downstream end of the array. These pictures were taken in a Mach 3.0 crossflow moving from left to right and the injection up from the bottom. The injector holes are located just to the right of the main shock waves. The second weaker shock wave shows a small disturbance where the injector plate mates with the test section floor. The turbulent boundary layer on the wall can be clearly seen. These shadowgraphs give an integrated 2-D image across a 3-D flow. One can observe penetration trends of the injected air into the air freestream as well as the oblique shock waves. The shadowgraph images show many interesting features such as the structure of the bow shocks, the plume, kinks in the bow shocks, and penetration trends. As the distance increases downstream from the injector holes, the angles of the shocks can be seen to approach that of a Mach wave, which is approximately 19.5 deg. in a Mach 3 flow. The thick boundary layer interferes with the interpretation of the shock wave structure of the region inside it and obscures the front part of the jet plume. The reduction in momentum flux ratio in the nine-hole array (1.9) as compared to the eight hole version (2.0) was due to the higher mass flow rate and corresponding higher pressure losses in the pipe plumbing from the tunnel plenum chamber to the injector.

The feature of most relevance to the incorporation of two simulated plasma torch orifices into the array is the jet bow shock formed from their interaction with the freestream and the rest of the injector array. This shockwave, as can be seen in the Figure 4.2(a) is very unsteady and has many kinks along its length. In an effort to create a leaner “fuel” region near the plasma torch orifices and a passage between them for the main injector plume to travel, the hole in between the two torches was filled with dental plaster and sanded smooth. Figure 4.2(b) shows the results of this modification to an eight-hole configuration. In this picture, the unsteadiness of the bow shock in question does somewhat seem to be reduced, but is still unsteady. However, not seen in these pictures, there is now a channel for the rest of the injector plume to travel in between the two torch holes. This will become apparent in the surface oil flow visualization pictures.

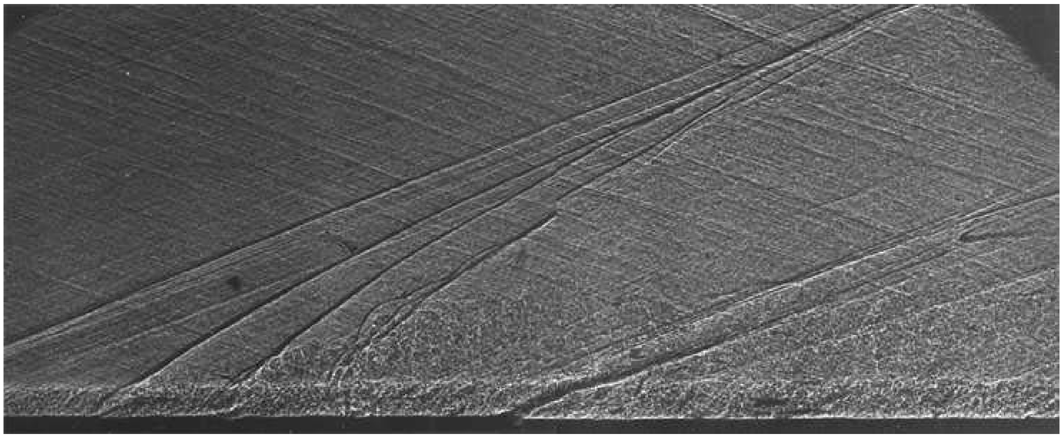

a) 9-Hole Aero-Ramp, $\bar{q}$ = 1.9

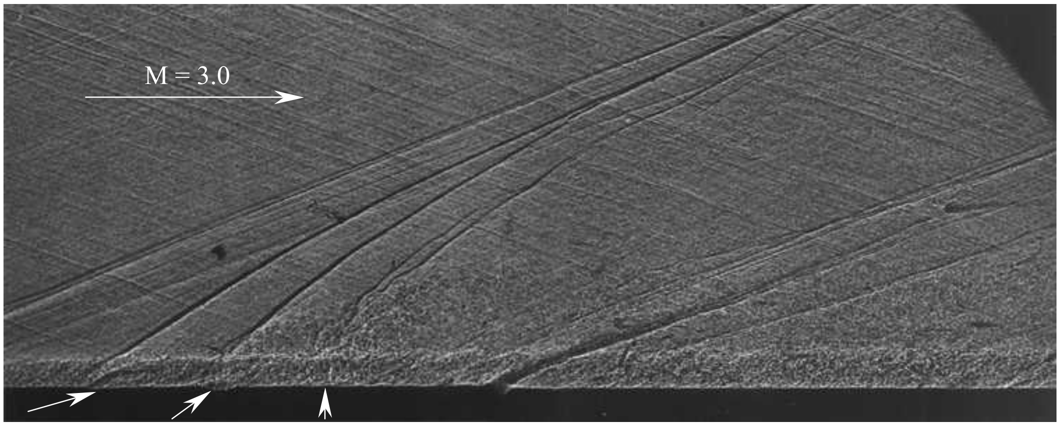

b) 8-Hole Aero-Ramp, $\bar{q}$ = 2.0

Figure 4.2 9/8-Hole Aero-Ramp Shadowgraphs.

Figure 4.3 presents the results of the surface oil flow visualization experiments in a Mach 3.0 flow. In these pictures, the freestream flow is from left to right, and the exit of the injectors can be seen as a three by three array of black, round or elliptical holes. The boundary where the downstream end of the injector block mates with test section floor can be seen at the right end of the pictures. A close inspection of the images can tell much about the various features involved with the flow patterns created by the injectors. Some of these important features are the trajectory of the jet plumes along the wall, the width of the individual jets and overall plumes, the size of the separation zones in front of the injector hole, the separation regions behind the exterior hole trailing edges, and the rate at which the overall plume width recovers from the effects of swirl in the exterior injector holes. The plume width is apparent in these pictures, because the plume impacts the wall at these modest momentum flux ratios.

Notice the large separation/recirculation zones between the rows of injectors, which are evident from the build-up of paint on the surface. In the eight-hole injector configuration, the hole between the simulated plasma torches in the back row is plugged up to reduce the size of the recirculation zone between the second and third row of holes and effectively produce a channel for the rest of the plume to travel in between the two plasma torch holes. Plugging the middle hole did not reduce the size of the separation zone between the two upstream rows of holes.

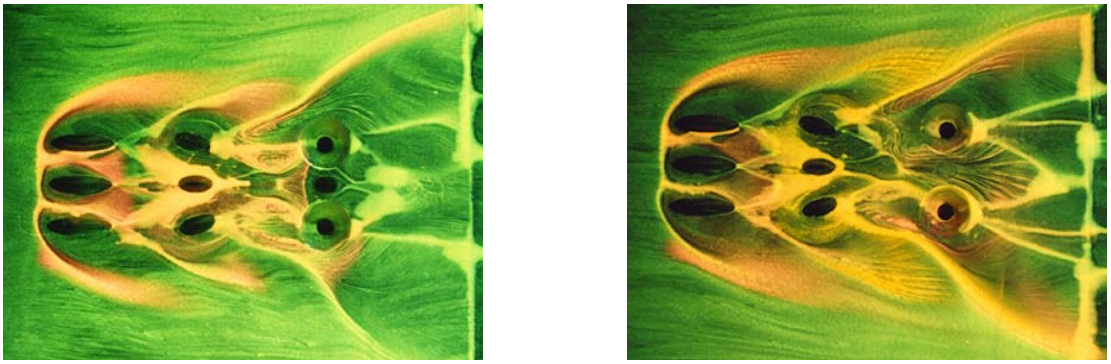

a) 9-Hole Array, $\bar{q}$ = 1.9 **b) 8-Hole Array, $\bar{q}$ = 2.0**

Figure 4.3 9/8-Hole Aero-Ramp Surface Oil Flow Visualization.

Conclusions from these experiments are as follows:

1) The addition of the two perpendicular plasma torch holes into the injector array created a large unsteady area in between the second and third row of jets. The recirculating flow in this region could lead to unwanted hot spots and higher cooling requirements around the injector array area. The removal of the hole in between the two torch holes greatly reduced the size of the separation zone and created a passage for the rest of the injector plume to travel.

2) In a real combustion type environment with hydrocarbon fuel being injected through the array, this configuration would potentially ignite the main fuel plume from its outside bottom edges possibly providing an anchor for the flame to help propagate downstream.
3) Although the nine and eight hole aero-ramp configurations with the two plasma torches have some benefits, the complexity of a working system with two closely spaced plasma torches plus the additional operating costs of running two plasma torches per aero-ramp injector makes this concept less desirable. Thus, a simpler system with one plasma torch would be more desirable and reduction of the number of holes in the aero-ramp array should be considered.

4.3 Plasma Torch Transverse Angled Injection Study

The downstream transverse orientation of a plasma torch, flush with the test section floor, was studied in a Mach 3.0 flow. This set of experiments was performed for two reasons: 1) to understand how to operate the plasma torch efficiently in a supersonic crossflow, and 2) to compare two anode configurations, which may aid with the development of the integrated design concept. Two different anode geometries were tested; a 90-deg conventional configuration (normal to test section floor) and a 45-deg downstream-angled anode configuration. The main anode geometries studied had a throat length to diameter ratio, t/d_j, of 2.2 and some additional data was taken with an anode with a t/d_j equal to 0.9. See section 2.3.2 for details. A brief qualitative analysis of the 45-deg configurations shockwave structure was made with shadowgraph images, and then total temperature sampling was done at a downstream location to look at the torch plumes and assess the possibility of combustion in this cold flow (101 K) low static pressure (0.19 atm) environment. Experiments were also performed in a Mach 2.4 flow with 90 and 60-deg downstream angled anode configurations. A detailed description of the findings from this study is presented in Gallimore [80], a brief description of the results, as relevant to the Mach 3.0 experiments is presented here in terms of total temperature measurements only.

4.3.1 Shadowgraphs

Figure 4.4 is a representation of some of the shadowgraph pictures for the two different anode configurations. The shadowgraph pictures were taken with two different methods. In order to take pictures with the torch in operation (power on), an argon ion laser (514.5-nm) was used in conjunction with a CCD Camera and a 514.5-nm band pass filter, which filtered out the light generated by the torch (Figure 4.4(a) and (b)). This setup allowed taking shadowgraphs with a 100-ns exposure time. Since this method did not produce the same clarity level pictures as spark-shadowgraphs, additional pictures were taken with the torch injecting methane fuel into the freestream, but with no power. This permitted the use of the Nanopulser spark-shadowgraph system. The spark-shadowgraphs pictures shown in Figure 4.4(c) and (d) have a 20-ns exposure time.

In all of the shadowgraph pictures, the flow is from left to right. The boundary layer at the torch location is about 3/8 in. thick, and the bow shock wave produced from the torch can be seen emanating from it, going up to the right. In these pictures, methane is being injected through the array at jet to freestream momentum flux ratios of about 2.0. The pictures in Figure 4.4(a) and (b) illustrate the effect of power from the torch on the plume and shock wave structure. As can be seen, the oblique bow shock wave produced from the torch grows in strength (greater oblique angle) with an increase in power. Furthermore, the shock wave moves further upstream from the exit of the torch with the increase of power. This means that the upstream injector jet separation zone is increasing in size with an increase of torch power. This increase of power is adding more thermal energy to the injector jet, which enhances the chance of combustion in the near-jet region. This thermal energy is what is increasing the size of the forward separation zone, creating a higher level of blockage from the injector process. This means that the total pressure losses created from the injector may increase with the power level at which the torch is operated and it also means that the static pressure in front of the torch would be higher. The pictures in Figure 4.4(c) and (d) show what the injector jet looks like without the additional energy input from the arc of the torch and the jets location in the images. They also show the relation in size of the thickness of the boundary layer to the diameter of the plasma torch jet, δ/d_{Torch}, which was about 5.7.

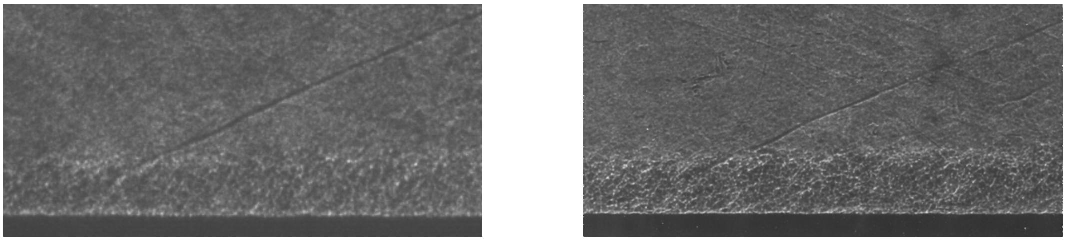

a) A = 45°, $\bar{q}$ = 2.1, P=2500 W (Methane)

c) A = 45°, $\bar{q}$ = 1.9, P = 0 W (Methane)

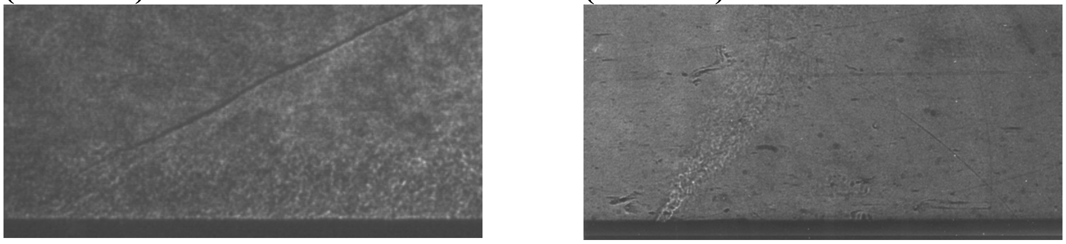

b) A = 45°, $\bar{q}$ = 2.1, P = 4000 W (Methane)

d) A = 45°, $\bar{q} = \infty$, P = 0 W (Methane - No Main Flow)

Figure 4.4 Shadowgraphs of the 45-Deg Angled Anode Plasma Torch. Images Taken with Laser-Shadowgraph (a & b), and Spark-Shadowgraph (c & d) Setups.

4.3.2 Total Temperature Surveys

Total temperature measurements were made with a thermocouple-type total temperature probe at a station about 60 jet-diameters, d_j, downstream of the two different plasma torch configurations. Total temperature profiles for the two anode configurations were created at a mean power level of 1540 watts with a variation of the individual run mean power level of ±42 watts (Figure 4.5). In addition, centerline measurements were made at various power levels (Figure 4.6) for plasma torch jet to freestream momentum flux ratios of 1.03 and 2.06.

These temperature measurements show that the profiles produced from the 45-deg anode configuration are generally hotter than the 90-deg configuration. In addition, they show that the plumes produced from the 45-deg anode configuration have a better maximum temperature core penetration into the freestream.

A look at electrode erosion and its influence on the plasma torch performance is shown in Figure 4.7. The first of the four consecutive temperature profiles in this figure was taken at a lower current setting, then the current setting was raised and held constant over the next three runs. As the electrodes erode, the voltage level required to sustain an arc increases. Furthermore, since the current was held relatively constant, the output level of energy put into the feedstock has not changed, but the overall power requirements have increased.

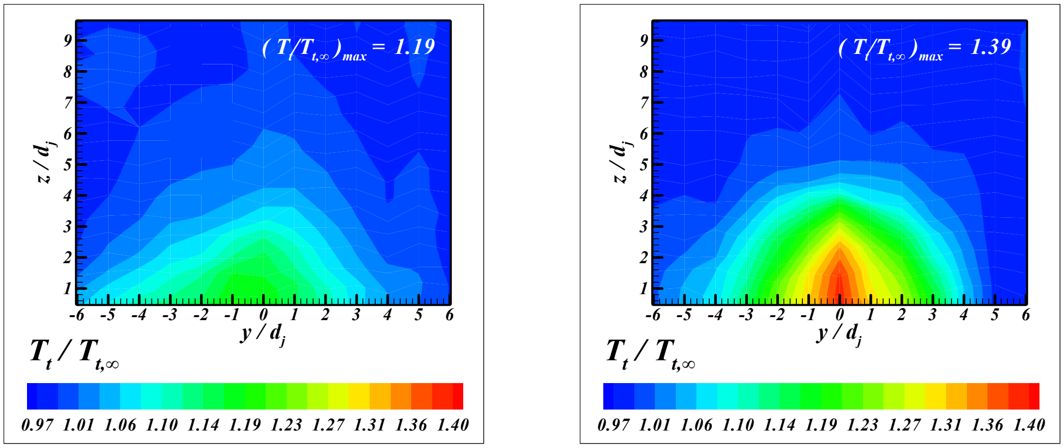

a) A = 90-deg, $\overline{q}$ = 1.0, P = 1540 W x/d_j = 58.8

b) A = 45-deg, $\overline{q}$ = 1.0, P = 1540 W x/d_j = 59.7

Figure 4.5 Total Temperature Profiles of 45- and 90-Deg Transverse Angled Plasma Torch Injection with a Methane Feedstock at 1540 Watts.

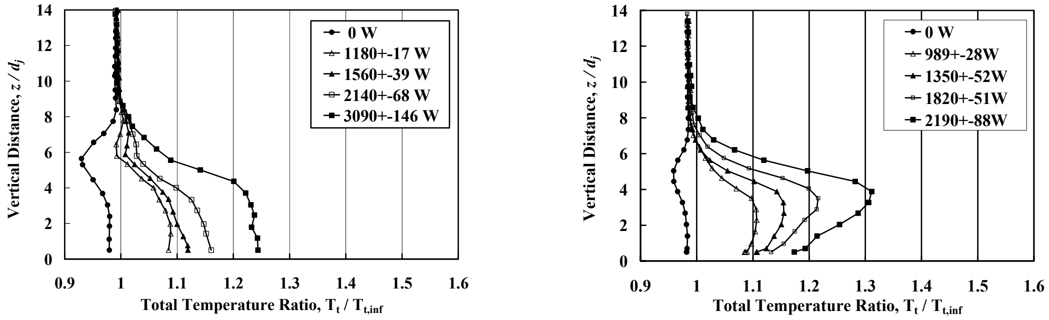

a) A = 90-deg, $\overline{q}$ = 2.1, x/d_j = 58.8

b) A = 45-deg, $\overline{q}$ = 2.1, x/d_j = 59.7

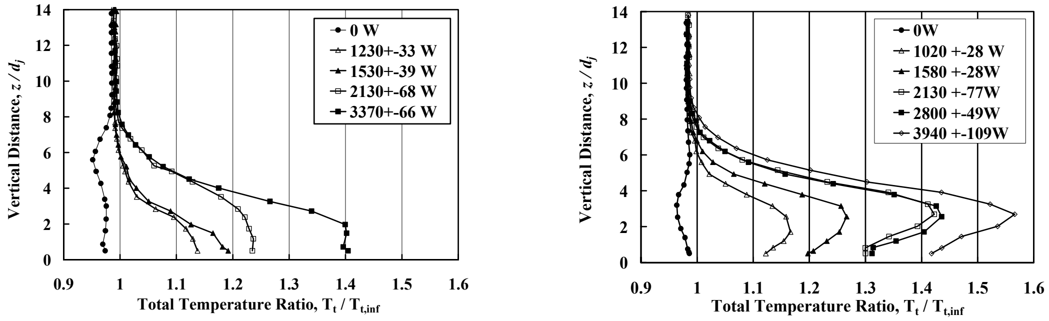

c) A = 90-deg, $\overline{q}$ = 1.0, x/d_j = 58.8

d) A = 45-deg, $\overline{q}$ = 1.0, x/d_j = 59.7

Figure 4.6 Centerline Total Temperature Profiles of 45- and 90-Deg Transverse Angled Plasma Torch Injection with Methane Feedstock at various Power Levels.

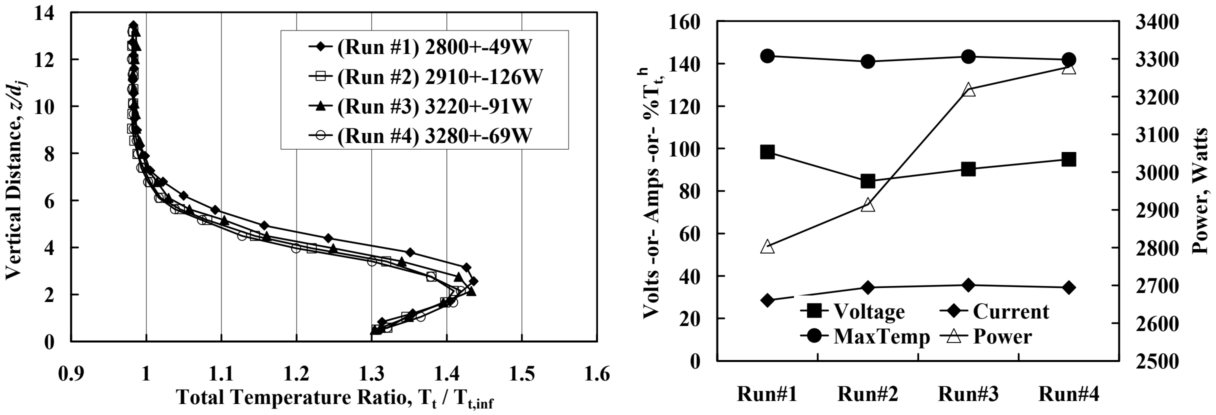

Figure 4.7 Effects of Electrode Erosion on Performance over Four Consecutive Runs with A = 45-Deg, x/d_j = 59.7.

Figure 4.8 presents the plume core maximum temperature results for the 45- and 90-deg anode configurations as a function of plasma torch power. Results are shown for the temperature profiles in Figure 4.7 along with additional data taken with a 45-deg anode with extensive wear to the throat area due to the arc. Note that the anodes used in the 90-deg tests were considered to be in good condition. Further information is presented for a 45-deg anode with a short anode throat to diameter ratio, t/d_j, equal to 0.9.

The results show that the 45-deg anode core temperature was higher than the 90-deg configuration and that the core temperatures of the fresh electrode varied in general, linearly with power level. In addition, the graph also shows that as the 45-deg anode wears, the core temperature rise can be significantly lowered. Interestingly, the 45-deg anode with the throat t/d_j of 0.9 had a significantly higher core temperature for the power levels tested, though the anode only ran three times before the arc wore through the throat into the converging section of the anode and the torch stopped working. The electrode wear reduction on performance for the 90-deg anode was considerably lower than the 45-deg case, and the anodes were found to perform at near the same level over the lifetime of the electrodes. This effect was due to the 90-deg corners of that torch in comparison to the varying 45- to 135-deg corners in the 45-deg anode. The arc had a tendency to wear away at the 135-deg corner, reducing the length anode throat and arc significantly. This made the arc effectively transfer less of its energy into the jet plume and reduced the temperature of the plume.

Figure 4.9 shows the core penetration heights of the good condition 45- and 90-deg anode configurations. These trends show that the main heat addition to the feedstock plumes was higher in the 45-deg anode configuration with the throat t/d_j equal to 2.2. This temperature rise is due to energy transfer from the mostly from the charged particles (ions) to the gas in an arc discharge between the cathode and the anode, and heat release from the plasma interaction effects with the fuel plume, which seems likely since the plume is significantly hotter than the 90-deg configuration. However, the 90-deg jet will tend to have a higher rate of mixing, and thus the temperature plumes core could be lower due to this as well. The 45-deg anode with the throat t/d_j equal 0.9 shows the exact opposite trend in core penetration height than the longer 45-deg configuration. This difference in performance is most probably due to the difference in arc length, but since the short anode also produces a hotter plume, the arc may be attaching in a different area near the throat. Since the only analysis performed in this study was downstream temperature sampling, it is impossible to speculate on the possibility of additional heat release in this configuration due to combustion without further detailed analysis.

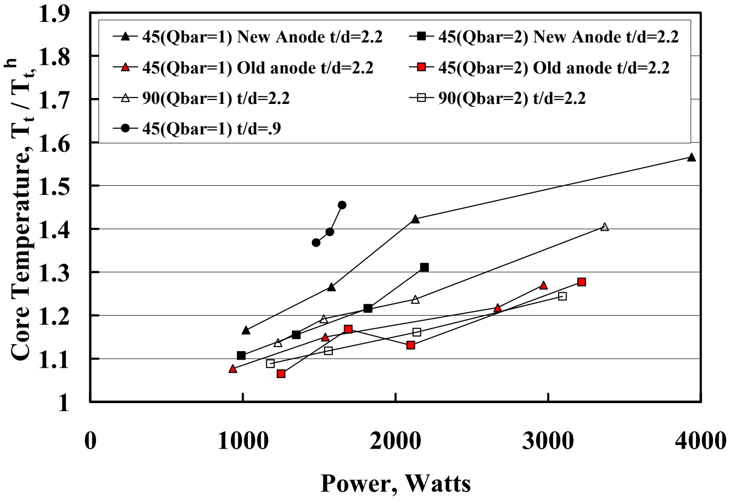

Figure 4.8 Core Temperature of 45- and 90-Deg Transverse Angled Plasma Torch Injectors with Methane Feedstock at various Power Levels.

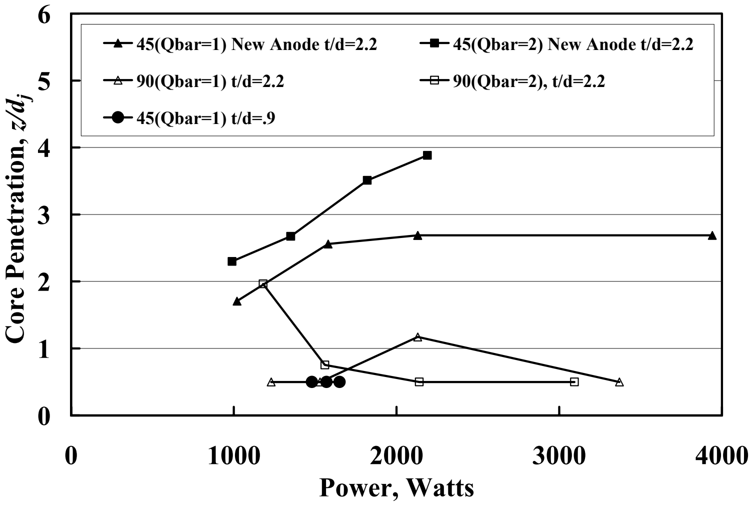

Figure 4.9 Core Penetration of 45- and 90-Deg Transverse Angled Plasma Torch Injectors with Methane Feedstock at various Power Levels.

4.3.3 Plasma Torch in Operation at Mach 2.4

Total temperature surveys were performed on the plasma torch in operation with methane gas in a Mach 2.4 flow. The temperature-sampling plane was 49.8 x/d_j downstream from the center of the torch. The following temperature sampling results, presented in Figure 4.10 show the effectiveness of the 90- and 60-deg downstream angled anode configurations. Interestingly enough, the results seem to indicate the opposite trend, as far as maximum temperature and penetration are concerned, as the Mach 3.0 experiments with the 90- and 45-deg anodes. Data was taken, here with new and used 90-deg electrodes and with a new 60-deg electrode at a Momentum flux ratio of 1.2. Now, the 90-deg anode seems to have a hotter and higher (penetration) maximum core temperature than the 60-deg config. In order to try to come to grasp with this difference in trends, one must first take in to account all sources of error associated with the experimental measurement of temperature, variation of flow conditions, and the effective condition of the electrodes. These measurements are also effected by the methane flame plume itself, as illustrated in Figure 4.11. Though the picture of the total temperature probe in the flame plume was taken at 4500 watts, the flame plume did nearly reach the temperature sampling plane at 2500 watts. The 90-deg old configuration temperature data in Figure 4.10 not only is a victim of electrode erosion, but also turns out to be also effected by degradation to the thermocouple inside the probe shown in Figure 4.11. Once this was realized, the thermocouple probe was replaced with the three-temperature-probe rake with new thermocouples as mentioned in section

3.5.3 *Total Temperature Probe.* Neglecting the effects of electrode erosion for the minute, and assuming that the temperature profiles are repeatable, an accurately represent the temperature plumes from the two anode configurations, it then seems that there is no advantage of the 60-deg anode over the 90-deg anode. Since the 45-deg configuration was not tested in the Mach 2.4 flow, we are left only to speculate over the potential advantage (if any) over the 90-deg configuration. To more accurately determine if there is any potential to having a 45-deg anode configuration over the 90-deg configuration, further experiments are recommended. In addition, to more clearly estimate the repeatability of the performance of the electrodes, a condition tested should be repeated at least three to five times with new pairs of electrodes, and then with various amounts of degradation to the electrodes (repeated back to back runs).

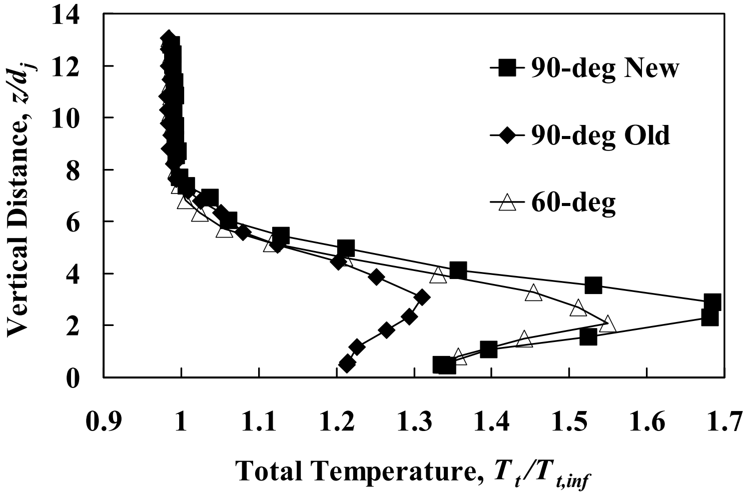

Figure 4.10 Total Temperature Profiles for 90- and 60-Deg Downstream Angled Anode Configurations

Figure 4.11 Plasma Torch in Operation at Mach 2.4 with Methane Feedstock at 4500 Watts.

4.3.4 Conclusions

Overall, the 45-degree anode with the main t/d_j equal to 2.2 performed better than the 90-deg configuration in the Mach 3.0 flow. However, the 45-deg anode also had a higher electrode wear rate over the 90-deg case. The important advantages that the 45-deg anode had over the 90-deg case were a hotter thermal core with a higher penetration height. This should lead to less thermal loading on the wall in an actual scramjet combustor environment. The increase in wear decreased the torch performance below that of the 90-deg anode case, whose erosion tended to have less of an effect on the performance of the torch. Ultimately, the choice of plasma torch anode will depend on the applications expected operational time constraints and the necessity for long-term repeatable performance. Perhaps with cooling and better electrode material selection, the 45-deg anode may be the best long-term solution for operation in a supersonic cross flow. It is also important to note that the results differed in comparison to the Mach 2.4 experiments. In these experiments, the 90-deg transverse angled plasma torch out performed a 60-deg configuration. This in some sense contradicts the findings in the Mach 3.0 flow, however, the 45-deg anode configuration was not tested in the Mach 2.4 flow. In the following two chapters, regarding the integration of the torch into the array, it is important to note the sequence of events and how they relate to the first and final prototypes. Firstly, after the experiments with the plasma torch in a Mach 3.0 flow, the first prototype injector array/plasma torch was designed. It was thought too complicated to incorporate a 45-deg angled plasma torch into the integrated design because of the need for space by the injector pluming and room under the wind tunnel, not to mention the rather large size of the existing plasma torch in use at the time. Thus, a compromise was mad to go with a 60-deg angled plasma torch in the integrated configuration. At that time, test were transitioning into the Mach 2.4 test section and it was agreed to test the 60-deg angled torch against the more conventional 90-deg, since the 45-deg seemed out of the question. It is estimated that a plasma torch can be made about the size of a sparkplug, and thus, in conclusion to these remarks, the 45-degree configuration may yet still show some merit as an igniter in a supersonic cross flow. Though one must realize, as shall be shown in the next chapter, that placing a torch downstream of the counter rotating vortex-plume of an injector array is very different that placing it in a cross flow.

4.4 Design Development and Aero-Ramp Evolution

From the knowledge gained from experiments described in this chapter and other literature on the subject of aero-ramps parametrics and plasma torches, the design of the aero-ramp was evolving. The 9/8-hole aero-ramp studies provided a basis for improvement and simplification of the aero-ramp design by reduction of the number of holes. Figure 4.12 shows the first conceptual change in the conventional nine-hole aero-ramp configuration to a six-hole one by removal of the middle row of holes, with this philosophy in mind. Furthermore, the internal geometry of the holes was created to resemble the internal geometry of transversely angled plasma torches.

At this time in the story, there was a shift in injector plate design from rectangular, for the Mach 3.0 test section, to circular, for the Mach 2.4 test section. This change in Mach number was done in an effort to more accurately simulate the flow conditions of the Mach 2.2 test section of the scramjet combustor test section at the Air Force Research Labs (AFRL). At the time of that switch the non-functionality and issues related to constructing a device with two plasma torches inserted inside it, lead a reduction to one torch at the centerline (see Figure 4.13). At that time, two alternate configurations involving a 90-deg plasma torch and a 90-deg plasma torch/cavity were also looked at as possible candidates for the next generation integrated design. These two configurations are shown in Figure 4.14. Finally, after much thought, the first integrated four-hole aero-ramp injector plasma torch model was constructed for testing. This model is shown in Figure 4.15(a) and has three 60-deg downstream-angled (30-deg from vertical) plasma torch holes placed in a circular block. Rotation of this block allows variation in the placement of the torch on the centerline relative to the injector array. The model shown in Figure 4.15(b) is the final prototype design built, consisting of a larger scaled four-hole aero-ramp array with a downstream slot for variation of plasma torch position. This model was scaled for future combustion experiments in the hot-flow facilities at the AFRL. Details have been provided in section 6.2.

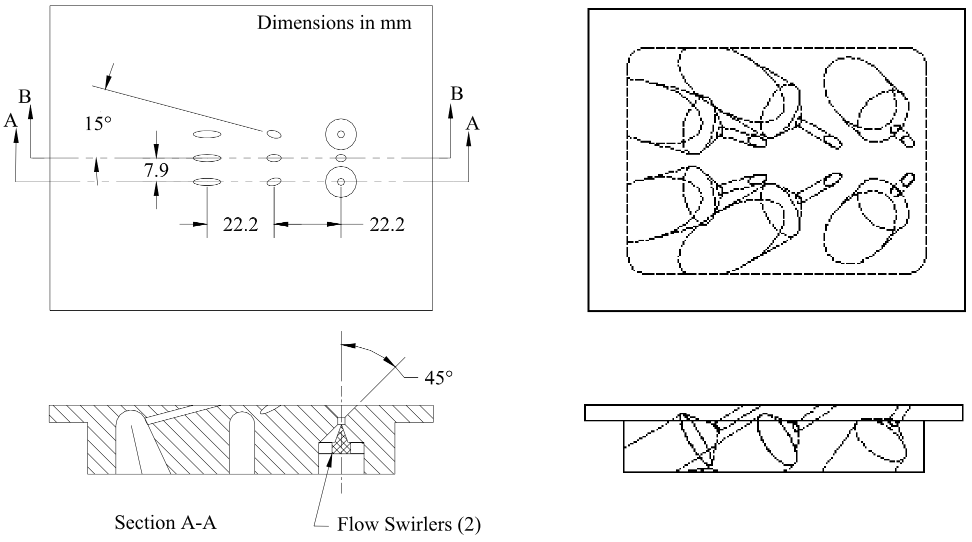

a) 9/8-Hole Aero-Ramp **b) 6-Hole Aero-Ramp**

Figure 4.12 Early Concepts of Simplification for the Aero-Ramp.

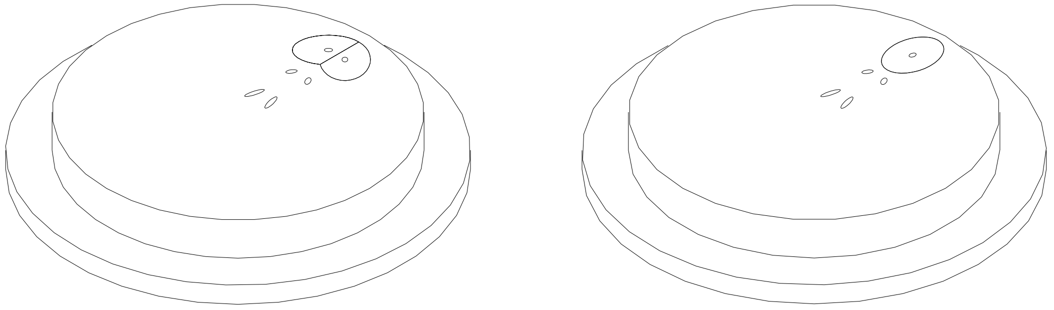

a) Two Torch Configuration **b) One Torch Configuration**

Figure 4.13 Reduction of Number of Plasma Torches Downstream of Aero-Ramp.

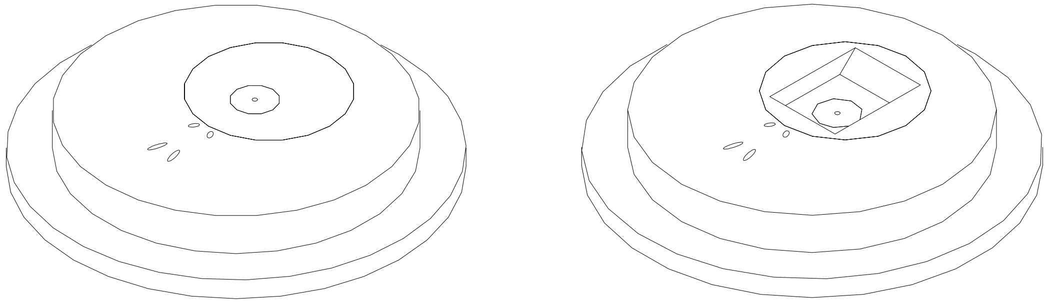

c) 90-deg Plasma Torch Configuration **d) Plasma Torch/Cavity Configuration**

Figure 4.14 Possible Candidates for the 2nd Generation Integrated Design.

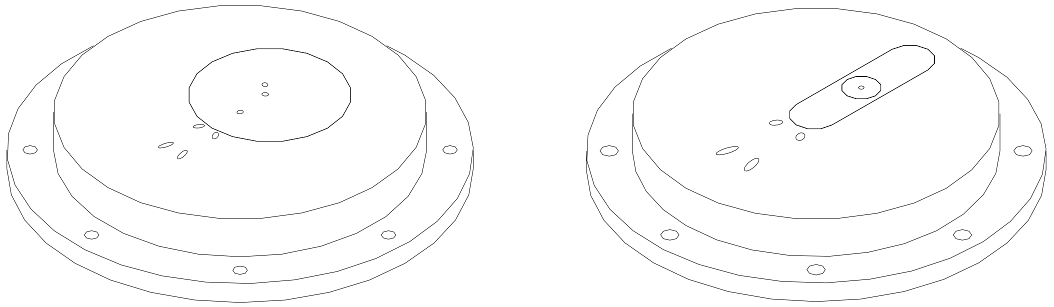

a) 1st Prototype Design **b) Final Design.**

Figure 4.15 Test Articles Constructed for Experiments.

Chapter 5 Advanced Integrated Concept: Cold-Flow Mixing Studies

The next step of the program was to evaluate the integrated four-hole aero-ramp injector and plasma torch igniter concept created from the research and ideas presented or discussed in Chapter 4. This process started with the evaluation of the first prototype design consisting of an aero-ramp with an equivalent-jet-diameter of 3.18-mm and a 60-deg downstream-angled plasma torch placed at one of three downstream stations relative to its location. See Figure 2.14. After the initial evaluation of this design, a larger version was created, scaled for future combustion experiments in a scramjet test facility at the Air Force Research Laboratory, AFRL, in Dayton Ohio. This design consisted of an aero-ramp with an equivalent-jet-diameter of 4.76-mm, this time with a plasma torch perpendicular to the freestream again at one of three downstream locations with the same non-dimensional scaling as the previous design. See Figure 2.22. Upon construction of this design, a full evaluation of the mixing performance of the aero-ramp injector alone was performed. For comparison, a single 15-deg downstream-angled injector, used in the AFRL's baseline combustor configuration in their scramjet facility, was also tested. After documentation of the aero-ramps performance, a series of cold flow supersonic combustion tests were performed with this full-scale integrated device involving ethylene fuel at Virginia Tech. The details of these cold-flow reactive mixture experiments are presented in Chapter 6.

5.1 First Prototype Integrated Injector/Plasma Torch Concept

The first prototype design shown in Figure 2.11 was studied in a cold flow at Mach 2.4 while injecting air through the aero-ramp and helium through a downstream placed plasma torch to simulate plasma torch operation without actually operating the torch (no power). A preliminary assessment of the injector performance characteristics involving shadowgraphs and surface oil flow visualization techniques was performed, and cross-stream aerothermodynamic measurements were taken at a downstream location to obtain information on the plume pressure field and mixing characteristics. Helium concentration measurements of the "plasma torch" plume were also made at this same station with an aspirating helium concentration probe (see Cox et al.[46] and R. Fuller[84] for details) to give insight into the torch plumes trajectory as it mixes into the main plume of the aero-ramp injector.

5.1.1 Shadowgraphs

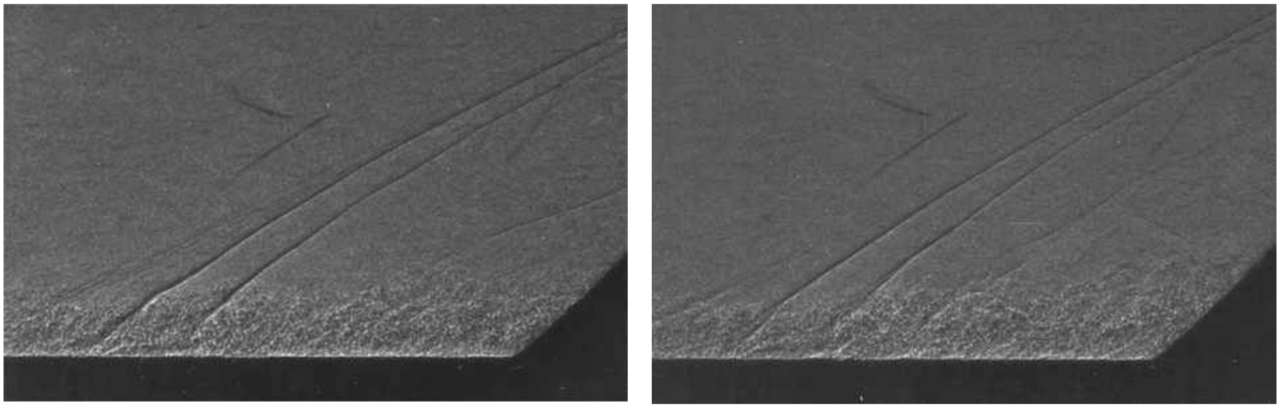

a) $\overline{q}_j = 2.4$, $\overline{q}_T = 0.0$ (No Torch)

b) $\overline{q}_j = 2.7$, $\overline{q}_T = 2.4$

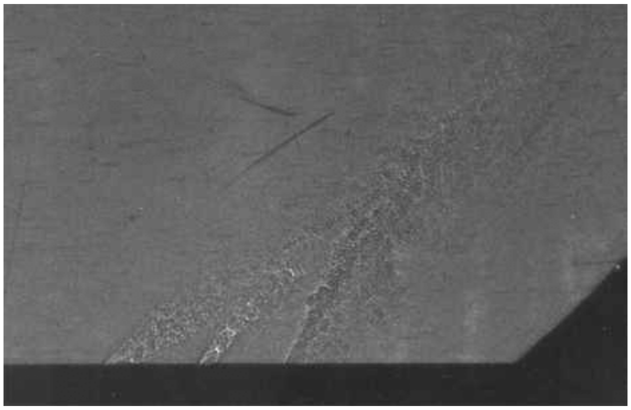

c) No Crossflow

Figure 5.1 Shadowgraphs of Small Aero-Ramp Array.

Figure 5.1 shows some shadowgraph pictures taken of the prototype injector where the main flow is moving from left to right. In Figure 5.1(b), the simulated torch is at station#1, 6 d_{eq} downstream from the center of area of the injector array with helium injection. The boundary layer at the simulated torch location is about 9-mm thick, and the bow shock wave produced from the simulated torch can be seen emanating from it, going up to the right. With these pictures, it is possible to examine the injector bow shock structure in detail. It is interesting to note that the shockwave produced by the simulated plasma torch is very weak and unsteady compared to the ones produced by the injector. This is because the mass flow through the simulated torch is only about one percent of the mass flow through the injector array, due to the constriction of the cathode inside the torch orifice. The simulated torch is also behind the injector array. Furthermore, orthogonal shockwaves can be seen emanating from the kinks in the simulated torch bow shockwave. This unsteadiness is associated with high turbulence levels near the simulated plasma torch orifice, due to the plume of the main injector.

5.1.2 Surface Oil Flow Visualization

Figure 5.2 shows the results of some of the surface oil flow visualization experiments. In these pictures, the flow is left to right. The pictures were taken with injector jet to freestream momentum flux ratios, $\overline{q}_i$, of 3.0, and torch jet to freestream momentum flux ratios, $\overline{q}_T$, of 0.0 (No Torch) and 2.7 at simulated torch station#2, 8 d_{eq} from the injector center of area. These pictures give an indication of what the surface flow around the injector and the mid-space simulated torch injector looks like. The large circle seen on the left side of the pictures is where the plasma torch anode insert joins with the main injector block. Also, the lines seen drawn on the surface of the anode insert, underneath the surface oil mark the location of the aerothermodynamic measurements discussed in the next two sections. The buildup of paint shown in front of, in between, and downstream of the aero-ramp shows regions of separation created by injection-crossflow interactions. An inspection of the downstream separation zone of the aero-ramp in Figure 5.2(b) shows that it has merged with the front separation zone of the plasma torch. This merged separation zone is significant, in that it provides a sheltered area for the simulated plasma torch plume to penetrate into the main plume of the injector. This sheltered area also means there is an increase in fuel residence time at lower speeds near the simulated plasma torch plume, which may help to overcome the high ignition delay times associated with hydrocarbon combustion. Another feature shown in Figure 5.2(a) are the lines along the surface created by small chunks of paint as they moved downstream while the tunnel was in operation. These lines approximate the average particle paths of the flow along the surface near the injector array. Note that as the lines approach the injector from the upstream direction, they move away from the centerline of the injector. Then, as they move past the aero-ramp they move back towards the centerline moving essentially underneath the injector jet plume. This indicates that the plume is being lifted up off the wall. This trend is still apparent in Figure 5.2(b), but it is harder to follow after the main injector plume meets with simulated plasma torch injector plume, which seems to trap all of the tracer paint in its wake.

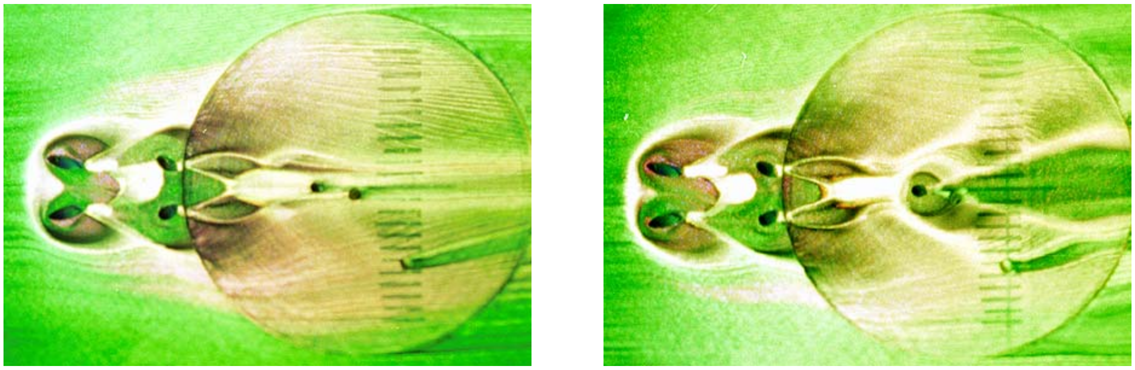
a) $\bar{q}_j = 3.0$, $\bar{q}_T = 0.0$ (No Torch) **b) $\bar{q}_j = 3.0$, $\bar{q}_T = 2.7$**

Figure 5.2 Surface Oil Flow Visualization.

5.1.3 Total Pressure Profiles

Total pressure loss profiles of the prototype injector/igniter are shown in Figure 5.3. These pictures show the results from the aerothermodynamic measurement experiments using Pitot and cone static probes at a station 11.9 d_{eff} downstream from the center of area of the injector array and 6.9 torch diameters downstream from the center of the station#2 simulated plasma torch anode orifice. These iso-line profiles, which are generated by 33 vertical traverses of the probes spaced 1.6-mm apart, illustrate the total pressure losses produced by the injection process. The profiles were generated with nominal injector and simulated torch momentum flux ratios of 3.0 and 2.7. The variation of the average value of the momentum flux ratio between runs was kept within ±5-percent of the nominal value. Profiles were completed with the injector alone and with the simulated torch hole at station#2, 8.0 d_{eq} from the injector center of area. A visual representation of the station location can be seen by the location of the lines drawn on the surface of the injector in the surface oil flow visualization pictures in Figure 5.2. These profiles allow a quantitative assessment of the total pressure losses incurred by the injector. Due to the low concentration of helium at the sampling station, as seen by the results of the helium concentration measurements in the next section, the pressure measurements involving both air and helium injection were calculated assuming that the flowfield consisted only of air.

Figure 5.3 shows the total pressure iso-line profiles for the aero-ramp injector alone, (a), and with the simulated plasma torch plume, (b). These profiles are shown looking from the downstream perspective relative to the injector array and simulated plasma torch. In the middle of the pictures, the total pressure field generated by the interaction of the freestream and the injector jets can be seen. This indicates that the two columns of injector jets have merged into one central jet with the maximum area of pressure loss in the center of the plume. On the right and left edges of the profiles, the total pressure loss profile is approaching that of the boundary layer alone to the sides of the plume. In addition, the injector plume is effectively reducing the height of the boundary layer on the edges of the plume. This is indicative of a large pair of counter-rotating vortices from a single jet plume. These profiles show us the effective changes in the total pressure loss field with the addition of the simulated plasma torch plume compared to that of the aero-ramp injector alone. This is evident by the higher pressure losses shown in the center of the jet plume area (from $P_t/P_{t,\infty} = 0.17$ to 0.14) and the additional ring structure around the plume from the additional simulated plasma torch bow shockwave.

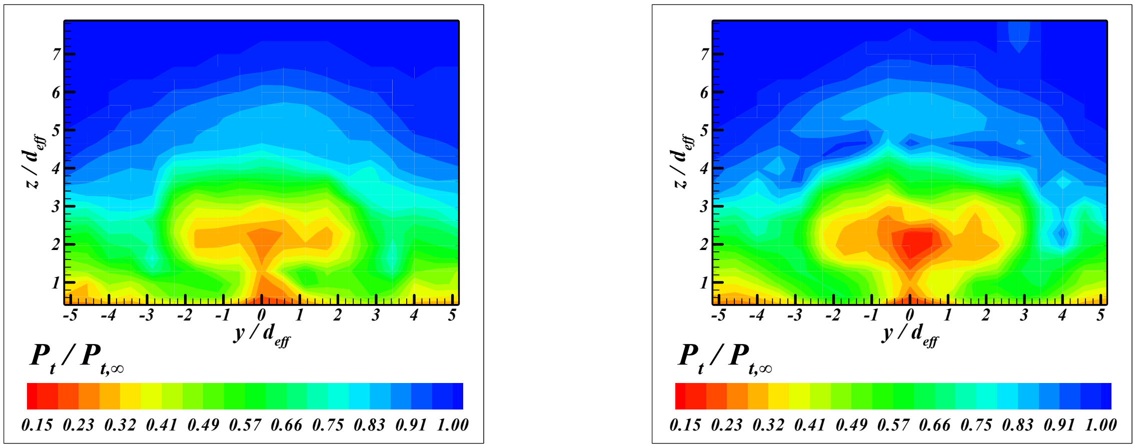

a) $\bar{q}_j = 3.0$, $\bar{q}_T = 0.0$ (No Torch) **b) $\bar{q}_j = 3.0$, $\bar{q}_T = 2.7$**

Figure 5.3 Total Pressure Contours $x/d_{eff} = 11.9$.

5.1.4 Mixing Analogy and Helium Mass Fraction Concentration Measurements

The mixing analogy measurements shown in Figure 5.4 were made with a thermocouple-type total temperature probe. These figures show iso-line profiles of the total temperature field expressed analogously as the mass fraction of the jet plumes 11.9 d_{eff} downstream of the leading edge of the injector array. Profiles have been completed with the injector alone and with the middle simulated torch station (#2) at, 8.0 d_{eq} from the injector center of area. During these experiments, heated or ambient air was injected through the injector array to obtain the analog to the mass fraction concentration profile. The mixing analogy is defined here as:

$$\alpha_{mix} = \frac{\left.\frac{T_t}{T_{t,\infty}}\right|_H - \left.\frac{T_t}{T_{t,\infty}}\right|_C}{\left(\left.\frac{T_t}{T_{t,\infty}}\right|_H - \left.\frac{T_t}{T_{t,\infty}}\right|_C\right) - \left(\left.\frac{T_t}{T_{t,\infty}}\right|_H \left.\frac{T_{t,j}}{T_{t,\infty}}\right|_C - \left.\frac{T_t}{T_{t,\infty}}\right|_C \left.\frac{T_{t,j}}{T_{t,\infty}}\right|_H\right)} \qquad \textbf{(5.1)}$$

where, the H and C subscripts stand for the heated and ambient temperature profiles, T_t is total temperature and the additional subscripts, p, ∞, and j represent the temperatures measured by the probe, freestream and injector. For a detailed description of the mixing analogy, see Appendix A. Figure 5.4(a) presents the results for the aero-ramp injector plume. The results of helium concentration sampling of the simulated plasma torch plume in addition to the mixing analogy measurements are shown in Figure 5.4(b). These iso-line profiles show that the maximum mass fraction analog, $\alpha_{mix,max}$, is lowered with the addition of the simulated plasma torch to the injector array. To perform this, unheated helium was injected through the simulated plasma torch orifice during the generation of both the heated and unheated injector profiles. These profiles prove that a significant vortex structure has been created by the injector array, which is evident from the generation of two main cores of the aero-ramp injector plume. Furthermore, the injected fuel and simulated plasma torch jet have been lifted away from the test section floor by the vortex motion. In addition, the simulated plasma jet plume has been lifted, and spread directly between the two primary injector cores. The helium concentration levels shown in Figure 5.4(b) at first might seem somewhat lower than expected, but it is important to remember that the simulated plasma torch 1.59-mm diameter orifice is constricted by the cathode inside the plasma torch to an effective diameter of only about 0.63-mm. This means that the helium plume has been laterally spread about 20 effective torch diameters by the aero-ramp injector plume. According to Eklund et al.[53], the flammability limits range for ethylene in this type of flow, but in a high enthalpy environment, is about $0.5 \leq \Phi \leq 6.5$. This corresponds to a fuel concentration range of $0.03 \leq \alpha_{mix} \leq 0.44$. This puts relatively, the whole plume is inside the flammability limits, and hence this is an ideal place to initiate combustion with a plasma torch.

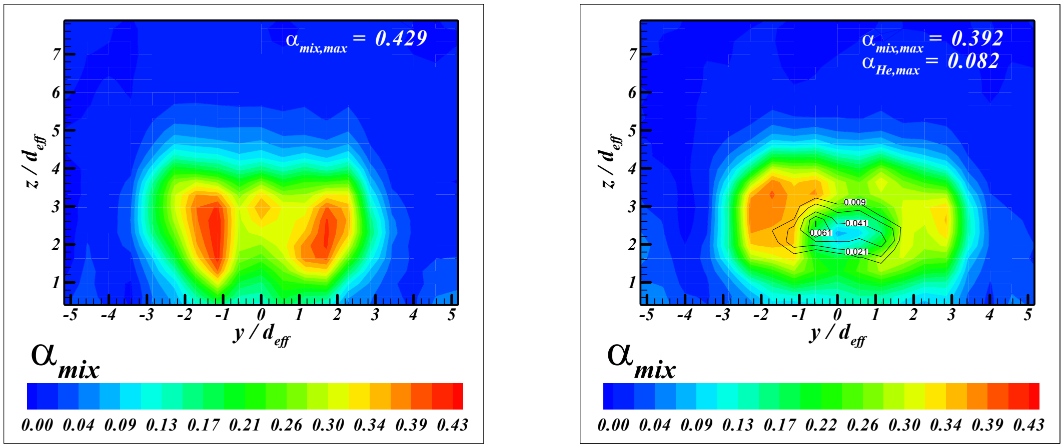

a) $\overline{q}_j = 3.0$, $\overline{q}_T = 0.0$ **(No Torch)**

b) $\overline{q}_j = 3.0$, $\overline{q}_T = 2.7$

Figure 5.4 New Mixing Analogy Profiles.

5.1.5 Design Development and Conclusions

The results show that the prototype has promising features, which may lead to enhanced combustion in a high-enthalpy, supersonic flow with lower pressure losses than existing cavity-flame-holding configurations.

The main conclusions drawn from the experiments are as follows:

1) The shockwave produced by the simulated plasma torch is very weak and unsteady compared to the ones produced by the injector. This unsteadiness is associated with high turbulence levels in the vicinity of the simulated plasma torch orifice, due to the plume of the main injector. This implies that the simulated plasma torch plume is being rapidly broken apart, hence it is mixing into the main injector plume. This should produce a environment conducive to ignition and downstream flame propagation.

2) The rear separation zone of the aero-ramp has merged with the front separation zone of the simulated plasma torch. This creates a sheltered region, which should aid with ignition and downstream flame propagation. Furthermore, the lifting ability of the main injector plume should help to lift the flame away from the wall, reducing heat transfer and spread the flame between the plumes.

3) The total pressure profiles show that the two columns of injector jets have merged into one central jet with the maximum area of pressure loss in the center of the plume. Further, the plume is lifted off the wall, as evident by the mushroom shape of the plume. This correlates nicely with the oil flow dye chunk particle paths, which move from the

sides of the plume towards its center essentially, showing that the plume has been lifted off the wall.

4) A significant vortex structure has been created by the injector array, which is evident from the generation of two main cores of the aero-ramp injector plume. Furthermore, the injected fuel and simulated plasma torch jet have been lifted away from the test section floor by the vortex motion.
5) The new four-hole aero-ramp plume looks more like the plume generated by a physical ramp than the original nine-hole aero-ramp plumes studied by Cox et al.[46], Cox and Gruber[47], and R. Fuller et al.[50]. This implies that the hole spacing and orientation of the new design are generating a strong pair of streamwise vortices by directing the flow around the injector similar to the physical ramp, and it is not only relying on multiple jet interactions to create its vorticity.

5.2 Aero-Ramp Sizing, Evaluation, and Performance

A new four-hole aero-ramp injector was developed which showed promising features. Up until this point, the mixing performance of that device had yet to be compared with any other injector. Therefore, to document the injector performance characteristics, further experiments were performed on the new, four-hole, aero-ramp injector to obtain a more complete understanding of its flowfield, and the results were compared to a reference injector to see if the design stood up to the competition. Several candidate reference injectors were considered for the comparison, of these the most favorable choices were the swept ramp, a single hole normal to the flow, or a single-hole injector, downstream-angled at either 15-deg or the equivalent composite angle of the injector array. Since the aero-ramp injector was being designed for experiments in comparison to the baseline injector configuration at AFRL, which consisted of four, 15-deg downstream angled holes, a single 15-deg downstream-angled hole was chosen. To make the comparison more direct in terms of the AFRL combustor configuration, the two injectors were compared on an equivalent mass flow basis. Thus, the aero-ramp was scaled up to an equivalent diameter of 4.76-mm for comparison to a full-scale 5.61-mm single 15-deg downstream-angled hole to operate in a range thought favorable to aero-ramp type injectors. This placed the operating momentum flux ratio range of the aero-ramp at $1.1 \leq \bar{q} \leq 3.5$ for an equivalent injector mass flow comparison to the single-hole injector at $0.8 \leq \bar{q} \leq 2.5$, which was the AFRL test range. Shadowgraph and surface flow visualization pictures were taken at various momentum flux ratios to help qualitatively understand the nature of the flows. Total temperature measurements were performed at three downstream locations with heated air injection to help quantify the mixing capability of the injector array and compare it to the single-hole injector. Further, pressure sensitive paint and aerothermodynamic probing studies were performed to assess the pressure losses incurred by the two injectors.

5.2.1 Shadowgraphs

Shadowgraph pictures of the aerodynamic ramp and single-hole injectors in a Mach 2.4 flow are shown in Figure 5.5. In all of the shadowgraph pictures, excluding the ambient environment cases, the main flow is from left to right. The boundary layer near the injector is about 9-mm thick, and the bow shock waves produced from the two rows of injector holes in the injector array can be seen emanating from them, going up to the right. In these pictures, air is injected through the aero ramp injector at jet to freestream momentum flux ratios, $\overline{q}$, of 1.4, and 3.3 and through the single-hole injectors at 1.0 and 2.3. The lower and higher momentum flux ratios correspond, nominally, to the same mass flow levels through the two injectors. Due to the installation of new fused silica test section windows and the increase in size of the aero-ramp from the earlier model, the shadowgraph pictures turned out much clearer than the ones presented in Figure 5.1 for the earlier experiments.

In the ambient environment pictures, the aero-ramp jets are underexpanded (Figure 5.5(a)) 5.2-X, and a clear image of the expanding jets shock structures can be seen, including the barrel shocks, Mach discs, and shock trails. The ambient injection picture of the 3.5-X under-expanded, single-hole jet (Figure 5.5(b)) has a roughly 9-percent lower mass flow level than that of the aero-ramp picture. In this picture, less of the shock structures can be seen since the gas is less over expanded than for the aero-ramp, although a shockwave is evident emanating off the trailing edge of the injector hole. In these two ambient environment images, the relative injection angles of the injector plumes are also visible. From inspection, the aero-ramp plume direction has about twice the relative transverse angle of that of the single hole plume.

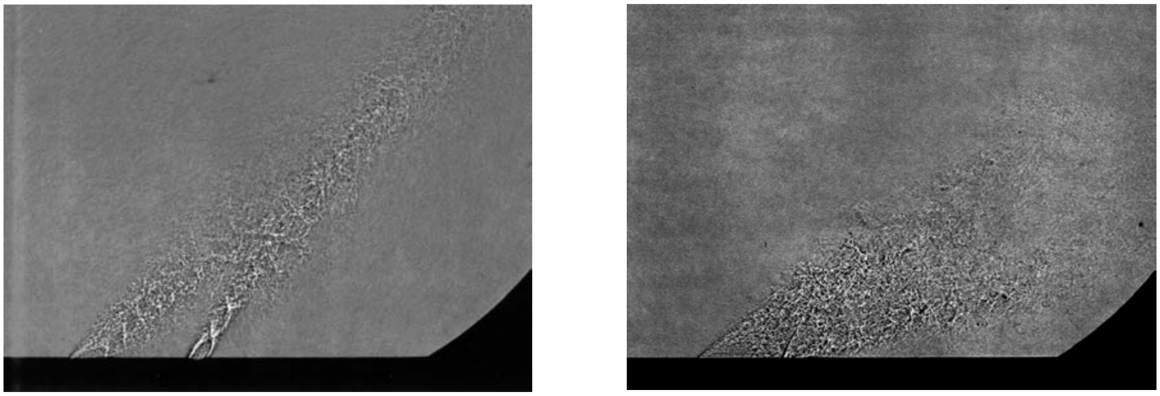

a) Aero-Ramp, Ambient jet. 5.2-X underexpanded. $\bar{q} = \infty$.

b) Single Hole, Ambient jet. 3.5-X underexpanded. $\bar{q} = \infty$.

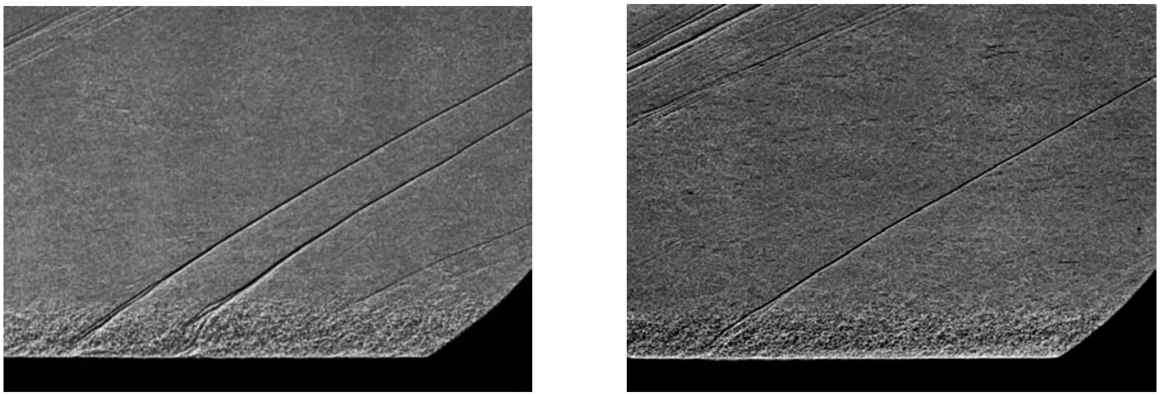

c) Aero-Ramp, $\bar{q} = 1.4$, $\dot{m}_{j,i} = 18$ gm/s

d) Single Hole, $\bar{q} = 1.0$, $\dot{m}_{j,i} = 18$ gm/s

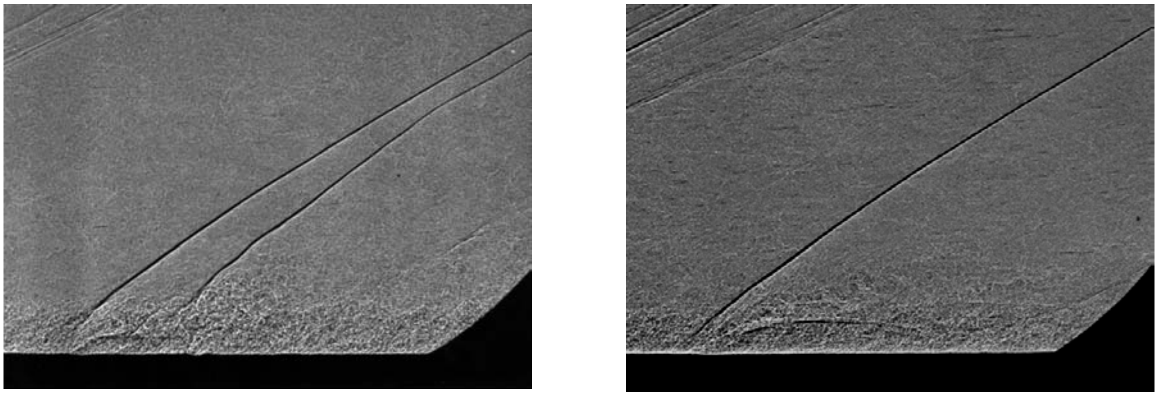

e) Aero-Ramp, $\bar{q} = 3.3$, $\dot{m}_{j,i} = 36$ gm/s

f) Single Hole, $\bar{q} = 2.3$, $\dot{m}_{j,i} = 36$ gm/s

Figure 5.5 4-Hole Aero-Ramp and Single-Hole Injector Shadowgraph Images.

The jet plumes of the injectors in the Mach 2.4 crossflow (Figure 5.5(c - f)) are masked by the turbulent structures in the boundary layer and are only partially visible. Still, it is possible to see how the plumes are turned downstream by the crossflow. This effect is especially visible in Figure 5.5(e) and (f). Due to the relatively small change in density associated with air injection into an air freestream and the thick boundary layer on the test section floor, the injector jet plumes are only slightly visible. Nevertheless, it is still possible to see the injected air in the vicinity of the aero-ramp array and single-hole injector, but any estimate of the penetration height of the injected air would be purely speculative. The two bow shock wave structures, which are readily seen emanating from above the injector jet plumes in the supersonic region of the boundary layer are at oblique angles and approach the angle of a Mach wave as they move away from the initial jet disturbances. As can be seen, the oblique bow shock waves produced from the injectors grow in strength (oblique angle) with an increase in $\overline{q}$. This means that the total pressure losses created from the injector may increase with the momentum flux ratio and mass flux at which the injector is operated due to increased blockage effects. Separation zones can also be seen just in front of the two injector bow shocks. The upstream separation zones increase with $\overline{q}$ and, hence, injector mass flow, while the downstream separation zones are distorted too much by the boundary layer and the unsteadiness of the injector to draw any conclusions about size or growth.

In the aero-ramp injector shadowgraphs, kinks in the bow shock can be seen emanating from the downstream row of injector jets. These kinks show the inherent unsteadiness created by the interactions of the jet plumes. Upstream of the injector, at the top left of the pictures are other extraneous weak waves, which were created at the junction of the test section plate and the converging diverging nozzle. In the aero-ramp images, a third, weaker shock wave created by the injection process can also be seen behind the two initial injector bow shocks. This shock wave is even unsteadier than the second bow shock and is the first shock in a trail of recompression shocks, created by the injector. The shock trail is especially evident in the surface flow visualization pictures and pressure sensitive paint images shown in the next two sections.

5.2.2 Surface Oil Flow Images

Figure 5.6 shows the results of the surface oil flow visualization experiments. The pictures were taken with injector jet to freestream momentum flux ratios, $\overline{q}$, of 1.5 and 3.2 for the aero-ramp and 1.1 and 2.3 for the single-hole injector. These pictures give an indication of the surface flow around the two injectors. In all of the top-view surface flow pictures, the freestream flow was from left to right. The exits of the injectors can be seen as elliptical black holes near the left edge. Just downstream of the aero-ramp injector, the presence of an oblong insert in the wall can be seen in the pictures (see Figure 2.23). This insert was sealed with epoxy and sanded smooth to mitigate its effect on the surface flow visualization experiments.

A close inspection of the individual images can tell much about the various features involved in the flow patterns created by the injectors. Some of the important features are the trajectory of the jet plumes along the wall, the width of the individual jets and overall plumes, the size of the separation zones in front of the injector holes, and the separation regions behind the hole trailing edges. The plume width is not apparent in these pictures, because it is affected by the interaction of the toe-in angle of the injector and the freestream flow, which acts to lift the plume off the test section floor.

The overlapping of the plumes due to the high toe-in angles of the aero-ramp injector indicates increased mixing between the individual injector jets. It was found in Jacobsen et al.[23] (shown as Appendix B) that, as the jet momentum is angled in toward the center of the injector array, the penetration height of the injectant is increased. Furthermore, as the jets are expanding inward, they reduce the width of the overall shock and confine the blockage to a narrower cross-stream space with a higher overall plume penetration.

The separation zones in front of the aero-ramp injector holes can be seen especially in the higher momentum flux ratio picture (Figure 5.6(c)). In the cases with lower momentum flux ratios, the buildup of oil in this zone is seen to leak through between the first row of holes in the injector. As the momentum flux ratio increases, the surface flow through this region is reduced and finally stopped in the $\overline{q} = 3.2$ case. This separation zone is also seen in the higher $\overline{q}$ shadowgraph pictures and in the surface flow video footage, which clearly shows the unsteady nature of this flow. The separation zone helps let the jet plume initially penetrate further by reducing the influence of the freestream momentum upon that of the jets. However, such separations may create unwanted “hot spots” on the wall of a real combustor. The third separation zone can be seen directly behind the rear injector holes by the build up of oil in this region. This zone increases in size with momentum flux ratio. Examination of the video footage shows the paint spinning and jumping around in the middle and downstream separation regions during tunnel operation, clearly indicating that the injector creates strong vortices, which terminate on the wall. This downstream separation zone, as also shown in Figure 5.2 with the smaller aero-ramp array in the earlier preliminary experiments should provide a sheltered region good for ignition and flame propagation purposes. The size of the separation zones in front of and behind the single-hole injector are a lot smaller and no conclusive trend can be drawn about their growth in size with momentum flux ratio and mass flow from the two pictures presented, but it is evident is that they are significantly smaller than the ones created by the aero-ramp array.

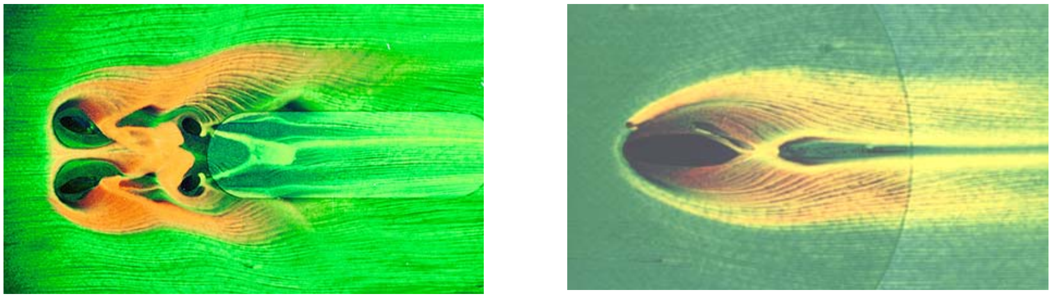

a) Aero-Ramp, $\bar{q} = 1.5$, $\dot{m}_{j,i} = 18$ gm/s **b) Single-Hole, $\bar{q} = 1.1$, $\dot{m}_{j,i} = 18$ gm/s**

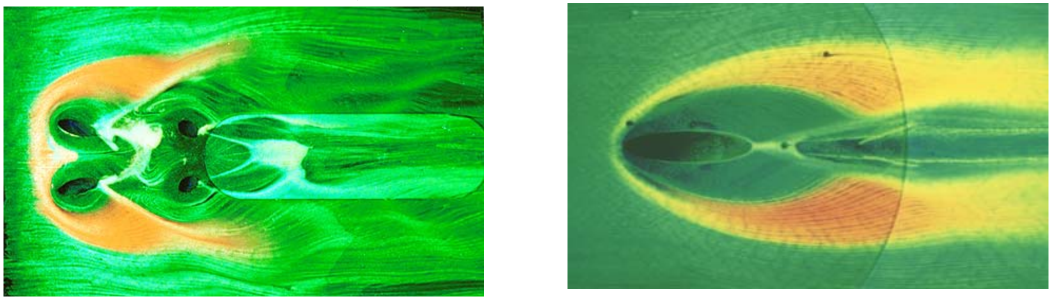

c) Aero-ramp, $\bar{q} = 3.2$, $\dot{m}_{j,i} = 36$ gm/s **d) Single-Hole, $\bar{q} = 2.3$, $\dot{m}_{j,i} = 36$ gm/s**

Figure 5.6 Surface Oil Flow Visualization pictures.

5.2.3 Pressure-Sensitive Paint Results

Experiments using pressure-sensitive paint (PSP) were conducted on the two injectors for ideal mass flow values of 18 ($\bar{q}_{\text{4-Hole}} = 1.5$, $\bar{q}_{\text{1-Hole}} = 1.1$) and 36 ($\bar{q}_{\text{4-Hole}} = 3.0$, $\bar{q}_{\text{1-Hole}} = 2.2$) grams/sec. The results from this experiment, presented in Figure 5.7, provide information about the static pressure field on the surface around the injector. In these images, the flow is moving from left to right, the pressure field is normalized by the freestream static pressure, P_∞, and each image has the same scale to help with comparison. While painting the injectors, the pressure tap holes and injector holes were plugged with small wires and tape respectively. There was some seepage of the paint onto the surface in the injector holes as can be seen in Figure 5.7(b) and (d). The thickness of the paint is only a few micrometers, so no effects on the performance of the injector holes were expected. The dark circle around the injector area is where the surface of the tunnel mates with the injector blocks, and there is no paint. Due to a difference in temperature between the injector block and the test section wall, the pressure information outside of the circular injector block has a higher amount of error associated with it. This is due to the fact that the pressure field was calculated using information from a pressure tap on the injector block, which was used to estimate the injector block temperature field.

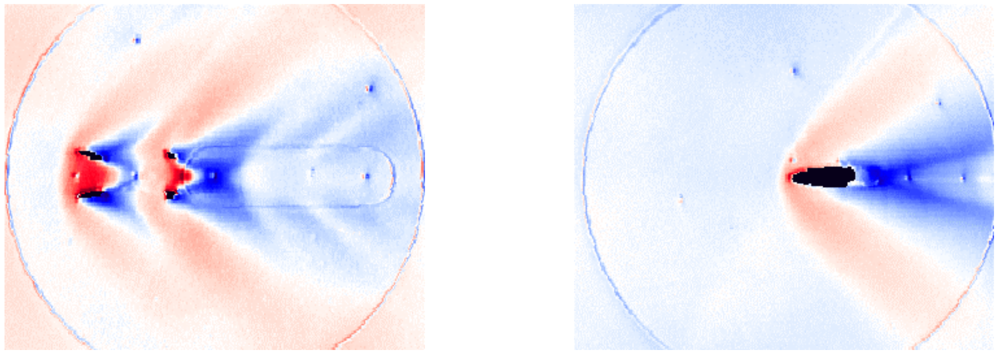

a) Aero-Ramp, $\bar{q} = 2.8$, $\dot{m}_{j,i} = 36$ gm/s **b) Single-Hole, $\bar{q} = 2.2$, $\dot{m}_{j,i} = 18$ gm/s**

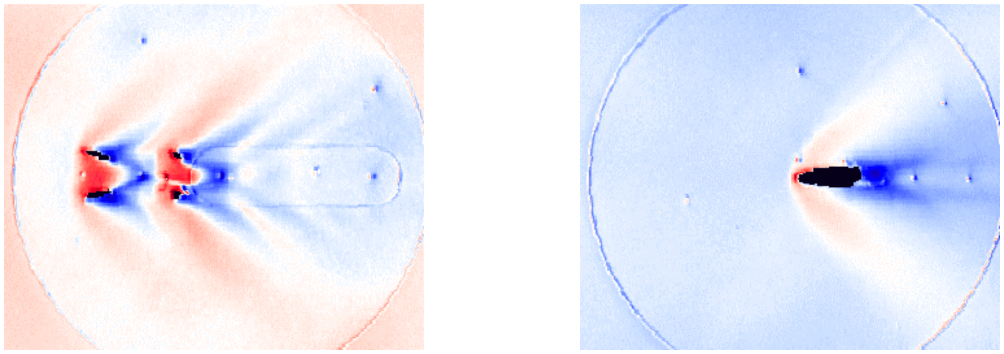

c) Aero-ramp, $\bar{q} = 1.5$, $\dot{m}_{j,i} = 36$ gm/s **d) Single-Hole, $\bar{q} = 1.1$, $\dot{m}_{j,i} = 18$ gm/s**

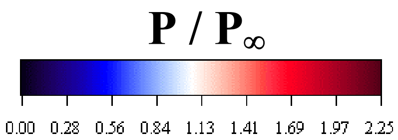

Figure 5.7 Pressure Sensitive Paint Images.

In these pictures, the bow shocks in front of the injector holes are shown by the left boundary between the blue and red regions, which notes the position of the pressure increase from the low freestream static pressure value to the high value behind the shock wave. The bow shock wave oblique angle and thus strength, increases with injector $\bar{q}$ and mass flow. The dark blue, low-pressure regions behind the injector holes are the regions where the injector jets are expanding to reach the local surrounding backpressure. An interesting feature of the aero-ramp pressure profiles shown in Figure 5.7(a) and (c) is the shock trail shown downstream of the injector. This shock trail is due to the under-expanded nature of the jet flow field. It also suggests that there might be a lower pressure design condition where the injector might operate more efficiently. This feature is not evident on the single-hole images.

5.2.4 Total Pressure Profiles

Total pressure loss profiles for the aerodynamic ramp injector are shown in Figure 5.8. These plots show the results from the aerothermodynamic measurement experiments, using Pitot and cone-static probes. The measurements were made at sampling station #2, which normalized by the effective radius, corresponds to non-dimensional distances of 6.0- and 6.3-R_b from the centers of the aero-ramp and single-hole overall areas, respectively. The profiles were made at an ideal mass flux of 36 gm/sec ($\overline{q}_{\text{4-Hole}} = 3.0$, $\overline{q}_{\text{1-Hole}} = 2.2$) with both injectors. These isobar profiles illustrate the total pressure field produced by the injection process near the plumes of the injectors and allow a quantitative assessment of the losses incurred by the injectors. The local total pressure profiles are normalized by the freestream total pressure, and both profiles are set to the same non-dimensional scale for ease of comparison.

In these total pressure loss profiles, it can be seen that the aero-ramp produced higher pressure losses in a larger area as compared to the single-hole injector. The minimum pressure cores of the aero-ramp are lower and penetrate less into the freestream. The two outer minimum total pressure cores are also spread further apart, which is directly due to the cross-stream injector spacing of the array. This implies that reducing the cross-stream spacing of the jets in the aero-ramp injector array will reduce the pressure losses by decreasing the total amount of freestream blockage. The total pressure losses are quantified in a later section using two different parameters involving numeric integration of the pressure field over the sampled area.

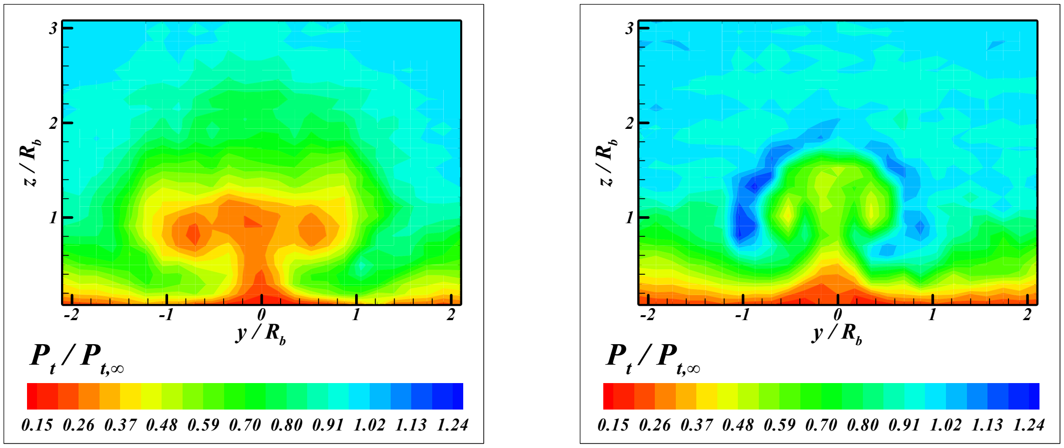

a) Aero-Ramp Injector, S-Station#2
$\dot{m}_{j,i}$ = 36 gm/s, $\bar{q}$ = 3.0, x/R_b = 6.0

b) Single-Hole Injector, S-Station#2
$\dot{m}_{j,i}$ = 36 gm/s, $\bar{q}$ = 2.2, x/R_b = 6.3

Figure 5.8 Total Pressure Profiles.

5.2.5 Mach Number and Velocity Contours

Figure 5.9 and Figure 5.10 present the Mach number and velocity contours of the aero-ramp and single-hole injectors at an ideal mass flux of 36 gm/sec ($\bar{q}_{\text{4-Hole}}$ = 3.0, $\bar{q}_{\text{1-Hole}}$ = 2.2). The measurements were made at sampling station #2, which normalized by the effective radius, corresponds to non-dimensional distances of 6.0- and 6.3-R_b from the centers of the aero-ramp and single-hole overall areas respectively. The Mach number profiles of the aero-ramp and single-hole injector plumes are very different. For example, in the cores of the jets, the Mach number of the aero-ramp is below the freestream Mach number of 2.4 at a value of 1.7, while the plume core of the single-hole injector has increased above the freestream value to about 2.7. This same trend is apparent in the velocity contours as well. The lower velocity at the core of the aero-ramp plume shows a loss of axial momentum due to the relatively higher angle of injection compared to the single-hole injector and also perhaps as a result of the multiple jet interactions of the array. While this loss of momentum will reduce the thrust component of the injector needed in high Mach number flight, in the flight range where hydrocarbon scramjet combustors are effective, up to Mach 8, this thrust component does not effect the overall performance of the engine (Billig[85]). Furthermore, the lower velocity plume of the aero-ramp should aid with the combustion of hydrocarbon type fuels by giving the fuel-air mixture of the plume a higher residence time in the combustor, needed to overcome their long ignition delay and combustion times.

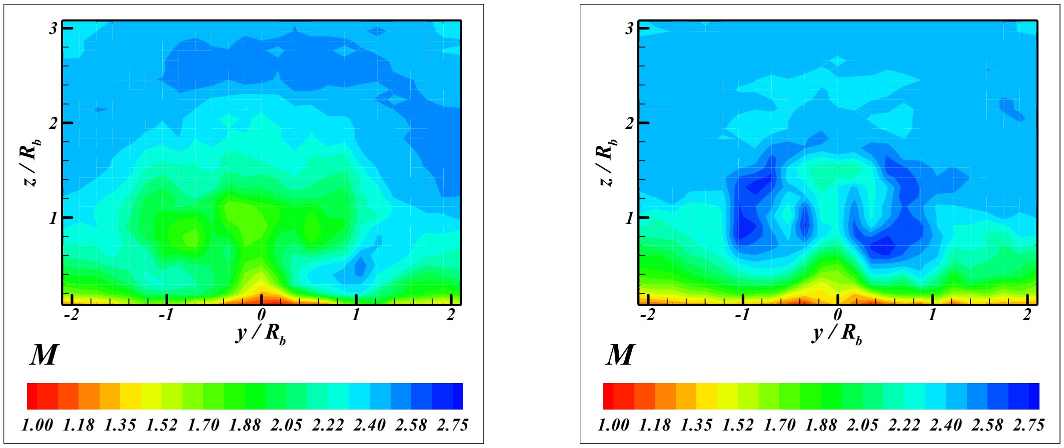

a) Aero-Ramp Injector, S-Station#2
$\dot{m}_{j,i}$ **= 36 gm/s,** $\bar{q}$ **= 3.0,** x/R_b **= 6.0**

b) Single-Hole Injector, S-Station#2
$\dot{m}_{j,i}$ **= 36 gm/s,** $\bar{q}$ **= 2.2,** x/R_b **= 6.3**

Figure 5.9 Mach Number Contours.

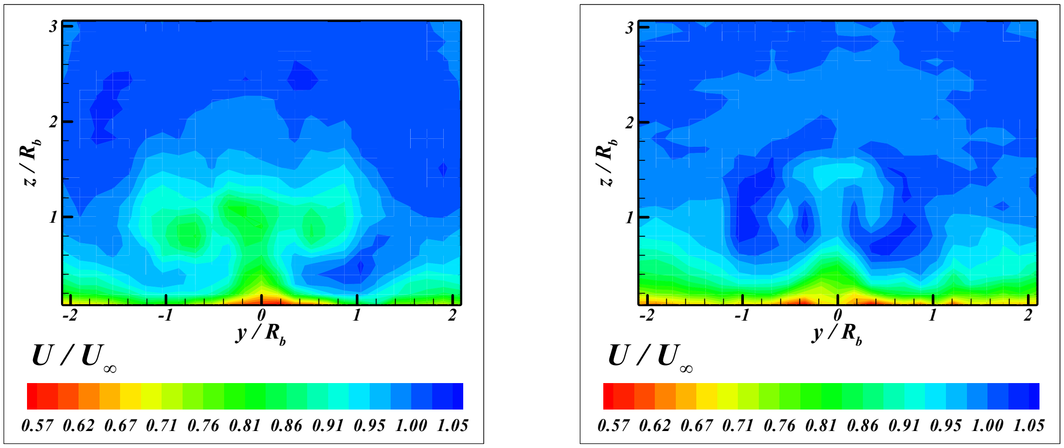

a) Aero-Ramp Injector, S-Station#2
$\dot{m}_{j,i}$ **= 36 gm/s,** $\bar{q}$ **= 3.0,** x/R_b **= 6.0**

b) Single-Hole Injector, S-Station#2
$\dot{m}_{j,i}$ **= 36 gm/s,** $\bar{q}$ **= 2.2,** x/R_b **= 6.3**

Figure 5.10 Velocity Contours.

5.2.6 Static Properties

Figure 5.11 through Figure 5.13 present the static pressure, density, and temperature profiles of the aero-ramp and single-hole injectors at an ideal mass flux of 36 gm/sec ($\bar{q}_{\text{4-Hole}}$ = 3.0, $\bar{q}_{\text{1-Hole}}$ = 2.2) at sampling station #2. The static pressure profiles for the two injectors appear symmetric minus a few defective areas, due to slight angularity or probe strut interference. Overall, both profiles share similar features. Both have two low-pressure cores with relatively high-pressure areas on both sides and a small patch directly above. In addition, both injectors have a rainbow like band stretching out on the top half of the pictures. Where the profiles differ the most is in magnitudes in these areas. First, the pressure in the cores of the aero-ramp profile are 22-percent higher than those of the single-hole injector. Second, the high-pressure regions at the sides of the aero-ramp have pressures about 6-percent lower than the single-hole injector. Furthermore, at the center of the low-pressure band above the aero-ramp injector is a region, which have pressures 25-percent lower than the other injector. Not much of the freestream can be seen in these images, and all of the area shown is definitely affected by the jet-freestream interactions either by the two injector bow shockwaves or the plume itself. Due to spatial constraints involving the traverse and probe placement, any additional information above the sampled area could not be measured and added to the profile.

The density profiles look very similar to the static pressure profiles. There is a stronger decrease in density near the plume cores in the aero-ramp injector profile. Overall, the density field of the aero-ramp plume is lower than the single-hole injector at most spatial locations.

The static temperature profiles are very similar to the Mach number and total pressure profiles. This is due to the strong influence of Mach number on the total temperature field, which is relatively constant in comparison. The static temperature of the aero-ramp plume is significantly higher than that of the single-hole injector. The high temperature coupled with lower flow velocities and higher pressure in the core regions of the plume should promote ignition and flame spreading through an increase in flammability limits. Furthermore, the relatively high temperature region at the center of the aero-ramp core should also be a good place to put some type of ignition aid like a plasma torch igniter. Due to the low static pressure in this area, this region should effectively lift the plume of the plasma torch up off the floor and into the two cores of the injector plume.

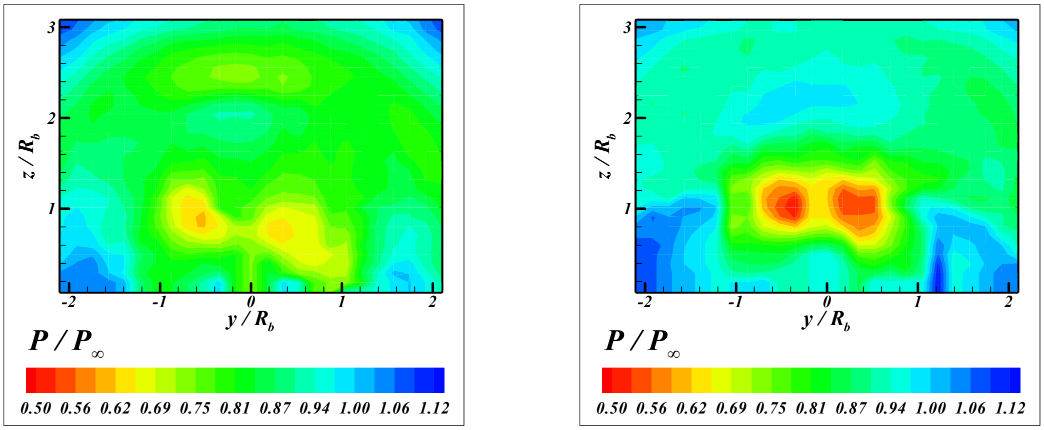

a) Aero-Ramp Injector, S-Station#2
$\dot{m}_{j,i}$ = 36 gm/s, $\bar{q}$ = 3.0, x/R_b = 6.0

b) Single Hole Injector, S-Station#2
$\dot{m}_{j,i}$ = 36 gm/s, $\bar{q}$ = 2.2, x/R_b = 6.3

Figure 5.11 Static Pressure Profiles.

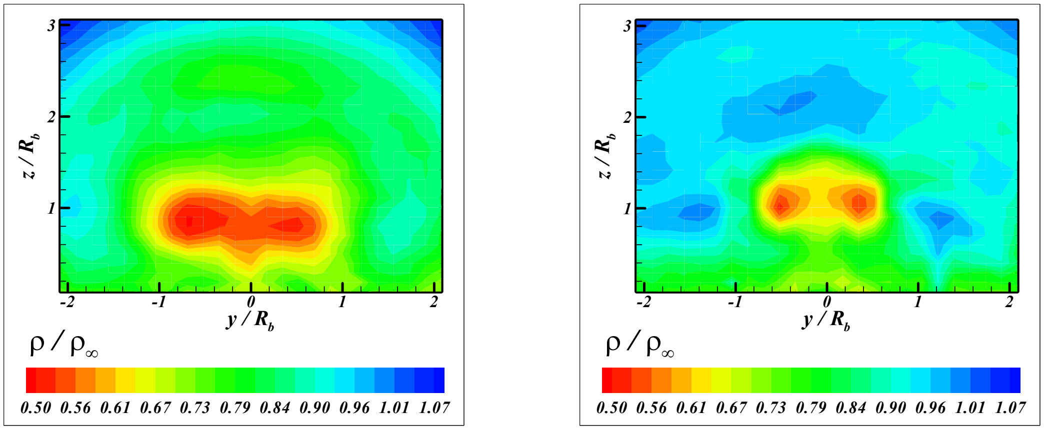

a) Aero-Ramp Injector, S-Station#2
$\dot{m}_{j,i}$ = 36 gm/s, $\bar{q}$ = 3.0, x/R_b = 6.0

b) Single Hole Injector, S-Station#2
$\dot{m}_{j,i}$ = 36 gm/s, $\bar{q}$ = 2.2, x/R_b = 6.3

Figure 5.12 Static Density Profiles.

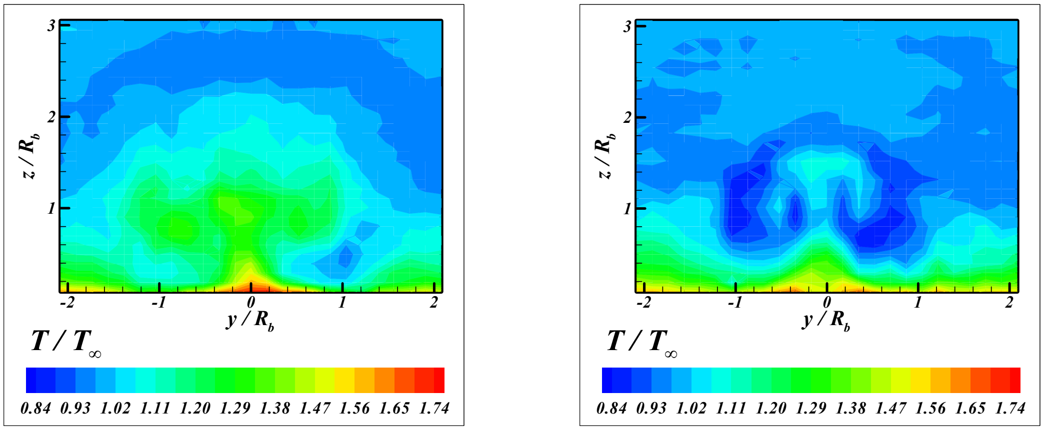

a) Aero-Ramp Injector, S-Station#2
$\dot{m}_{j,i}$ = 36 gm/s, $\bar{q}$ = 3.0, x/R_b = 6.0

b) Single Hole Injector, S-Station#2
$\dot{m}_{j,i}$ = 36 gm/s, $\bar{q}$ = 2.2, x/R_b = 6.3

Figure 5.13 Static Temperature Profiles.

5.2.7 Species Composition Mixing Analogy Results

The mixing analogy profiles created using Equation 5.1 for the aero-ramp and single-hole injectors are presented in Figure 5.14 and Figure 5.15, respectively. The scale of the iso-line mixing analogy profiles shown in both of these figures are set the same from zero to the highest concentration level observed by the aero-ramp injector at the closest measurement station to the injector. The downstream distances of the cross-stream profiles are measured from the centers of the overall injector area and are normalized by the effective radius. The aero-ramp mixing analogy profiles in Figure 5.14 show that a significant counter rotating axial vortex structure has been created by the injector array, which is evident by the shape of the two primary injector cores. Furthermore, the injected air has been lifted away from the test section floor by the vortex motion, leaving no secondary core trapped on the surface by the shear layer. This is a significant improvement over the earlier nine-hole aero-ramp injector plumes, which have been shown to trap a secondary core along the surface in the shear layer (R. Fuller et al.[50]). Figure 5.15 presents the mixing analogy profiles for the single-hole injector. For comparison to the aero-ramp, only a limited number of profiles were obtained with the single-hole injector. A comparison of the aero-ramp and single-hole injector mixing analogy profiles show the aero-ramp to have a lower maximum mass fraction with a larger overall plume area and faster decay rate. These items will be quantified below.

An interesting feature of the single-hole injector mixing analogy plumes is the horseshoe shaped structure especially apparent in Figure 5.15(a). This shape is often associated with a vortex structure generated by the interaction of a jet with a cross-flow and is the main mechanism for mixing enhancement of the single-hole jet. The aero-ramp on the other hand, generates vorticity not only by freestream-jet interactions, but also from the interference effects of the multiple jet interactions, and the toe-in of the jets, not to mention the additional vorticity generated by the multiple curved jet bow shocks. With the aero-ramp generating vorticity in so many different ways, one might ask oneself: which vorticity generating mechanisms are more important for mixing enhancement? Only by inspection of the trends associated with Figure 5.14 and Figure 5.15 will any answers become apparent.

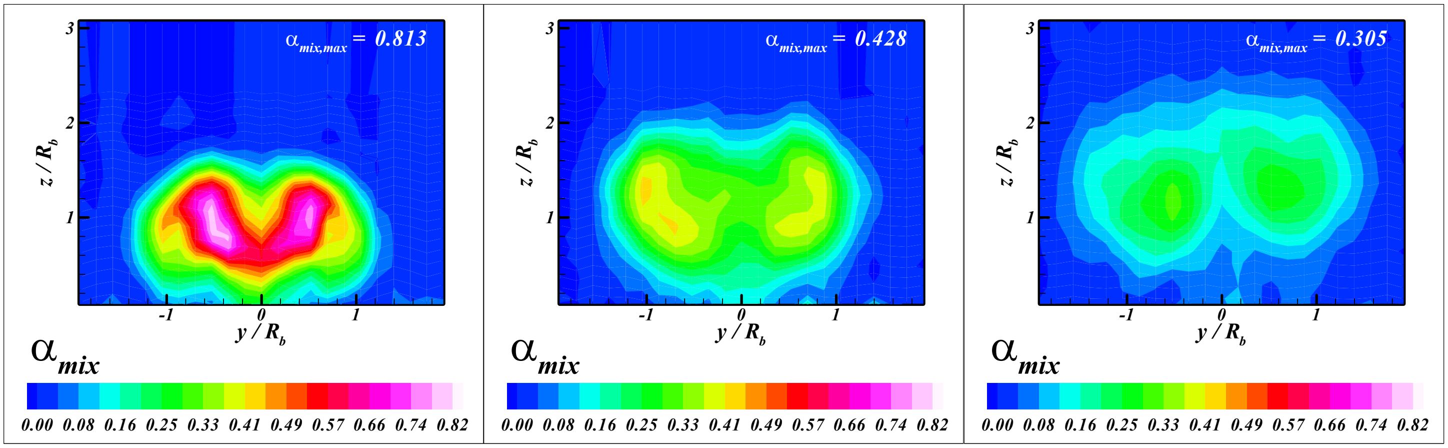

a) Sampling-Station#1
$\dot{m}_{j,i}$ = 36 gm/s, $\bar{q}$ = 3.0, x/R_b = 1.8

b) Sampling-Station#2
$\dot{m}_{j,i}$ = 36 gm/s, $\bar{q}$ = 3.0, x/R_b = 6.0

c) Sampling-Station#3
$\dot{m}_{j,i}$ = 36 gm/s, $\bar{q}$ = 3.0, x/R_b = 13.9

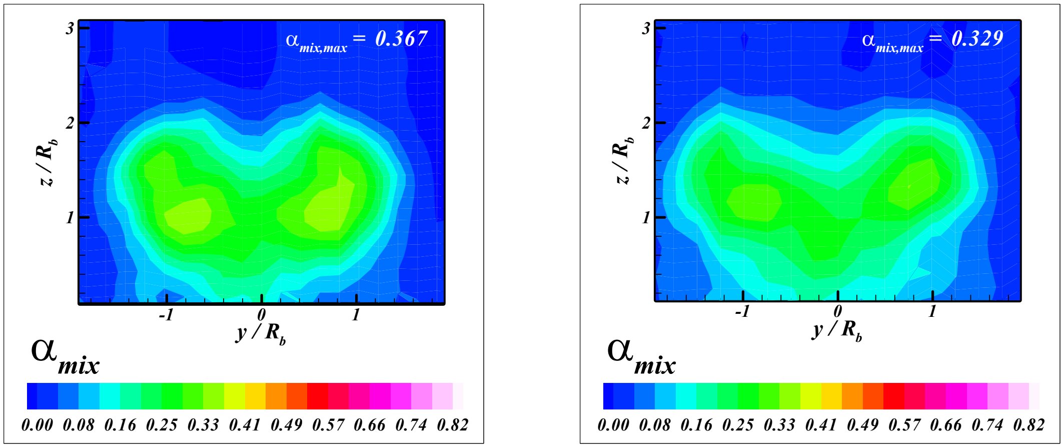

d) Sampling-Station#2
$\dot{m}_{j,i}$ = 26 gm/s, $\bar{q}$ = 2.2, x/R_b = 7.0

e) Sampling-Station#2
$\dot{m}_{j,i}$ = 18 gm/s, $\bar{q}$ = 1.5, x/R_b = 8.4

Figure 5.14 Aero-Ramp Species Composition Mixing Analogy Profiles.

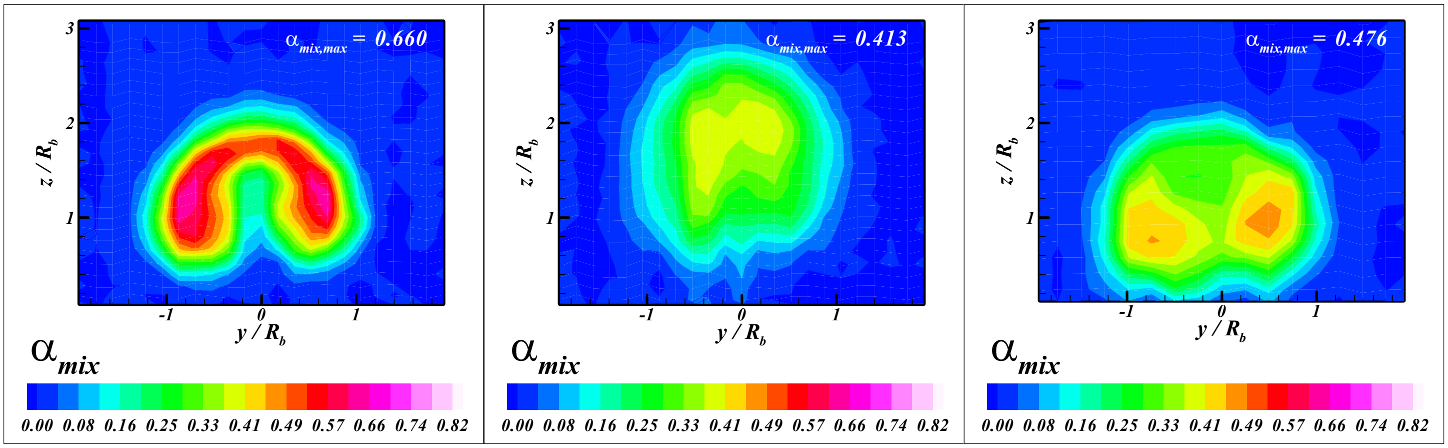

a) Sampling-Station#2
$\dot{m}_{j,i}$ = 36 gm/s, $\bar{q}$ = 2.2, x/R_b = 6.3

b) Sampling-Station#3
$\dot{m}_{j,i}$ = 36 gm/s, $\bar{q}$ = 2.2, x/R_b = 14.4

c) Sampling-Station#2
$\dot{m}_{j,i}$ = 18gm/s, $\bar{q}$ = 1.1, x/R_b = 9.0

Figure 5.15 Single Hole Species Composition Mixing Analogy Profiles.

Consider first the maximum concentration decay. The maximum concentration decay of the aero ramp using the mixing analogy, $\alpha_{mix,max}$, is shown in Figure 5.16 and the vertical heights of the local core maximums, h_{mix}/R_b, are shown in Figure 5.17. These graphs suggest that the both injectors are better mixers at lower momentum flux ratios, but also that the penetration heights of the plume cores are reduced. The aero-ramp provides better mixing at all conditions. Another interesting trend shown in Figure 5.17 is the higher initial penetration height of the aero-ramp injector, however, further downstream the single-hole core penetrates higher. This could be due to the higher composite downstream angle of the aero-ramp array (>30-deg) compared to that of the single-hole injector (15-deg).

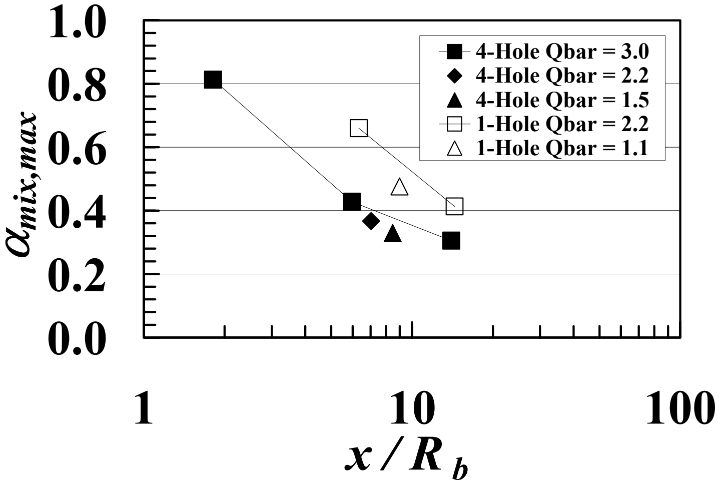

Figure 5.16 Maximum Analogous Concentration Decay.

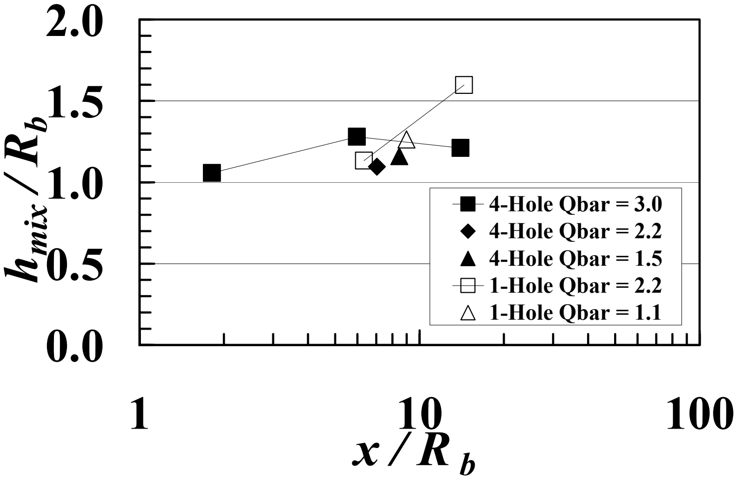

Figure 5.17 Maximum Analogous Concentration Core Penetration Height.

Second, the plume penetration, h_s, is defined here as the vertical distance from the wall to the upper edge of the mixing region where the mass fraction mixing analogy is equal to the stoichiometric value of ethylene, 0.0680. The maximum penetration heights of the mixing analogy plumes, h_s/R_b, were measured, and the results are presented in Figure 5.18. The results show that the single-hole injector plume penetrates further at the higher mass flow and momentum flux ratio.

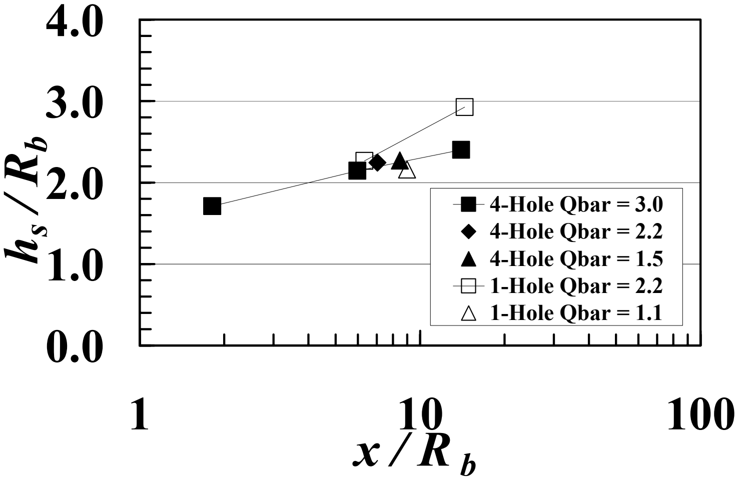

Figure 5.18 Plume Top Penetration Height.

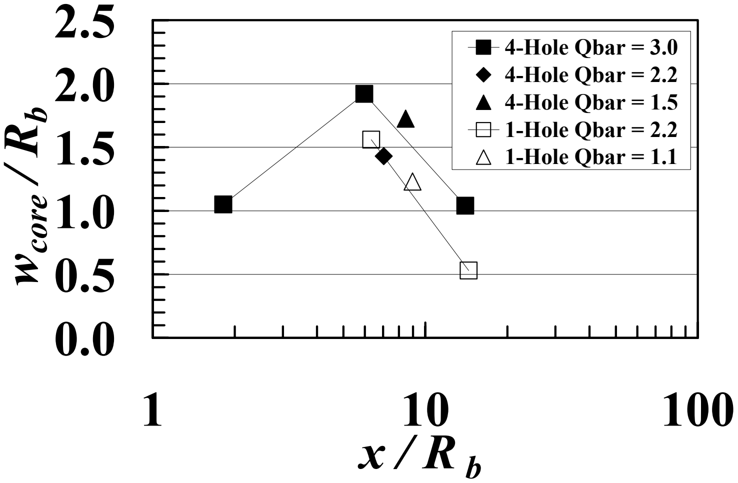

Figure 5.19 Width Between the Plume Cores.

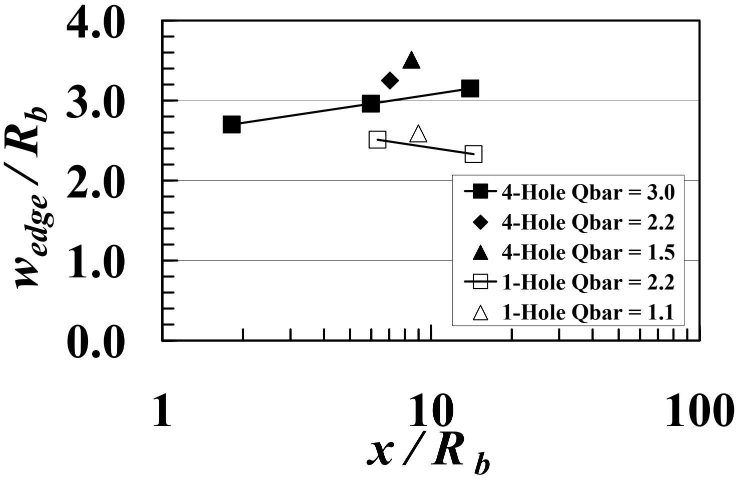

Figure 5.20 Overall Plume Width.

Third, Figure 5.19 and Figure 5.20 present the results from the plume width studies using widths defined by the distance between the plume cores, w_{core}, and the stoichiometric side edges, w_{edge}, respectively. In the plume core width study, it is interesting to note that the cores start at an initial close relative position, move outward, and then return towards the centerline of the plumes. Also, as shown in Figure 5.20, the width of the aero-ramp overall plume increases as a function of downstream distance while that from the single-holes decreases. This means that the aero-ramp produces a significant amount of lateral mixing.

Fourth, the overall plume area is defined here as the total area of the plume which has an α_{mix} greater than or equal to the stoichiometric value of ethylene, 0.0680. Results from this study are presented in Table 5-1 for the data taken with a mass flow level of 36 grams/sec corresponding to a $\overline{q}$ of 3.0 and 2.2 for the aero-ramp and single-hole injectors, respectively, at station #2. The over-stoichiometric plume areas are normalized by A_u, the area of an isentropically expanded jet with a static pressure equal to that of the freestream. The results show that the over-stoichiometric plume area from the aero-ramp injector array is larger than that from the single-hole injector

Finally, consider the mixing efficiency, as defined by Mao et al.[86], "that fraction of the least available reactant which would react if the fuel-air mixture were brought to a chemical equilibrium without additional local or global mixing"[50]. This means that the local fuel and air are considered mixed in the rich and lean fuel areas, respectively. Here:

$$\eta_m \equiv \frac{\dot{m}_{f,mix}}{\dot{m}_{f,tot}} = \frac{\int \alpha_r \rho u dA}{\int \alpha_{mix} \rho u dA} \tag{5.2}$$

where,

$$\alpha_r \equiv \begin{cases} \alpha_{mix} & ,\alpha_{mix} \le \alpha_s \\ \left(\dfrac{1-\alpha_{mix}}{1-\alpha_s} \right) \alpha_s & ,\alpha_{mix} > \alpha_s \end{cases} \tag{5.3}$$

Table 5-1 presents the results for the sampling station ~6 R_b from the center of areas of the two injectors, which show that the mixing efficiency value of the aero-ramp injector model is higher than that for the single-hole injector model.

5.2.8 Total Pressure Loss Parameter

The total pressure losses have been quantified using the global total pressure loss parameter defined by R. Fuller et al.[50]. This method simplifies the analysis by allowing an assessment of the overall losses within the sampling area. This total pressure loss parameter is defined as:

$$\Pi = \frac{\int \rho u \left(p_{t,\infty} - p_t \right) dA}{\rho_\infty u_\infty p_{t,\infty} A_s + \rho_j u_j p_{t,j} A_j} \tag{5.4}$$

where

$$A_s = \frac{\lambda}{\alpha_s} A_j \tag{5.5}$$

Thus, a fuel injector incurring no losses would have $\Pi = 0$. Table 5-1 presents the results of the total pressure loss parameter for the sampling station ~6 R_b from the center of areas of the two injectors. These results show the single-hole injector to have only slightly lower total losses compared to the aero-ramp injector. At first glance, this may seem counter-intuitive, due to the significantly lower “raw” total pressure losses shown in the total pressure profiles shown in Figure 5.8. However, since the total pressure loss parameter is a mass averaged quantity, the parameter is not assessed on pressure alone, but density and velocity as well. It turns out that the plume of the single-hole injector has a higher velocity field near the jet plume. This high velocity field significantly offsets the reduction in the total pressure loss parameter due to the lower total pressure losses, since this would imply a higher mass flow in the sampling area.

Table 5-1 Injector Plume Parameters for $x/R_b \approx 6$.

Parameter	*Aero-Ramp*	*Single-Hole*
A/A_u	**6.4±0. 1**	**4.5±0. 1**
η_m	**0.302±0.01**	**0.230±0.01**
Π	**0.234±0.05**	**0.212±0.05**

5.2.9 Enthalpy Deficit Factor

The enthalpy deficit factor was originally defined by Tomioka et al.[44] by assuming a total enthalpy equation of the form:

$$h_t = \left(h_{t,j}\alpha + h_{t,\infty}(1-\alpha)\right)(1-\beta) \quad \mathbf{(5.6)}$$

where, α is the fuel mass fraction, β, is the enthalpy deficit due to vorticity effects in the flowfield. Assuming constant specific heats, air injection into an air freestream and that α is equal to α_{mix}, the mass fraction distribution of the hot and cold air injection profiles are equal. Then, one can write the following equation for β:

$$\beta = \frac{\alpha\left(\frac{T_{t,j}}{T_{t,\infty}} - 1\right) - \left(\frac{T_t}{T_{t,\infty}} - 1\right)}{\alpha\left(\frac{T_{t,j}}{T_{t,\infty}} - 1\right) + 1} \quad \mathbf{(5.7)}$$

Figure 5.21 presents the results of using (5.7 for the total temperature and mixing analogy data at station #2 corresponding to a nominal distance of $x/R_b \approx 6$ downstream from the center of the injector areas, with an ideal mass flow level of 36 grams/sec ($\bar{q}_{\text{4-Hole}} = 3.0$, $\bar{q}_{\text{1-Hole}} = 2.2$). From these graphs, the locations of maximum total temperature alteration due to vorticity can be seen as the high and low β regions at and around the cores of the jets. It is interesting to note that the β cores in the aero-ramp injector profile shown in Figure 5.21(a) are a lot higher than those for the single-hole injector, while the low β regions around the injector cores are lower in the single-hole injector profile. This means that the aero-ramp is producing a higher level of vorticity, as seen from the higher enthalpy deficit factor due to vorticity in the cores of the jet plumes.

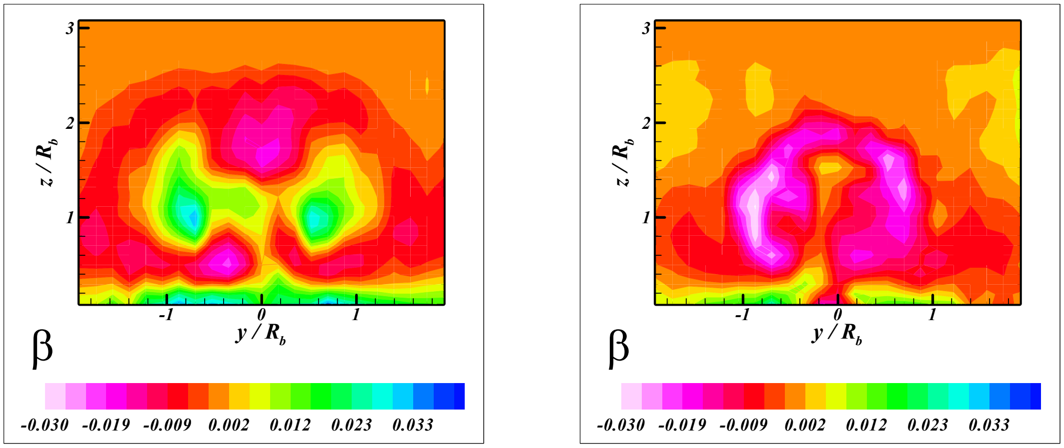

a) Aero-ramp Injector, S-Station#2
$\dot{m}_{j,i} = 36$ gm/s, $\bar{q} = 3.0$, $x/R_b = 6.0$

b) Single-hole Injector, S-Station#2
$\dot{m}_{j,i} = 36$ gm/s, $\bar{q} = 2.2$, $x/R_b = 6.3$

Figure 5.21 Enthalpy Deficit Factor Due to Vorticity.

5.2.10 Conclusions

Experiments were performed at Virginia Tech to investigate the flowfield near a new aerodynamic ramp injector array. The new aero-ramp injector featured four holes, compared to the original nine, and was tested and compared to a single, low-angled circular injector hole. Both were exposed to a Mach 2.4 cross-stream. Shadowgraph and surface flow visualization pictures were taken at various momentum flux ratios to help qualitatively understand the nature of the flows. Total temperature measurements were also performed at three downstream locations with heated air injection to help quantify the mixing capability incurred by the injector array and compare it to the single-hole injector. Further, pressure sensitive paint and aerothermodynamic probing were performed to assess the pressure losses incurred by the two injectors.

The main conclusions drawn from the experiments are as follows:

1) The aero-ramp injector mixed better than the single-hole injector did. The decay rate was faster and level of the maximum mixing analogy concentration was lower for the aero-ramp than the single-hole injector.
2) The plume of the aero-ramp had a larger plume area than the single-hole injector due to lateral spreading. This was due to the greater cross-stream distance between the

individual injector holes. This large cross-stream distance caused an overall reduction of the obtainable penetration height of the aero-ramp type injector plume.

3) The aero-ramp plumes created a higher level of vorticity as seen by the higher value of the enthalpy deficit factor in the cores of the jet plumes.
4) The aero-ramp injector showed somewhat higher local total pressure losses than the single-hole injector. This was due to the higher composite angle injection of the aero-ramp array and the multiple shock structures from the two rows of jets. Although the local total pressure losses appeared more substantial, the mass averaged total pressure loss parameter shows the aero-ramp to have only slightly higher overall losses.
5) The aero-ramp produced larger separation zones in front, in between, and behind the injector jets. This would allow more opportunity for flame holding in a high enthalpy flow, but might also create hot spots on the surface near the injector.
6) Further development of the design of the aero-ramp may include an array with lower downstream transverse injection angles, with a closer cross-stream spacing of the jets to reduce blockage. The size of the separation zones can also be reduced with a decrease of toe-in angle of the injector jets. This, however, may reduce mixing performance of the overall injection process. Without disregard for the size of the separation zones, one may opt to increase the toe-in angle, which may offer increased mixing and penetration of the aero-ramp injector jet plume.
7) A sheltered channel is created by the aero-ramp injector, which could be capitalized on with some type of ignition aid such as a spark, pilot or plasma torch igniter. The relatively large area of mixed fuel and air between the aero-ramp plume cores, coupled with the low velocity region behind the rear separation zone of the aero-ramp could provide a suitable region for flame initiation and rapid spreading into the jet plume.

Chapter 6 Final Integrated Concept Injector/Igniter: Reactive Flow

6.1 Cold-Flow Reactive Mixture Experiments

These tests were conducted in the low static pressure and temperature conditions ($M = 2.4$, $P = 0.26$ atm, $T = 131$ K) in the Virginia Tech supersonic wind tunnel (see Section 2.1). Thus, one cannot expect efficient combustion. The tests were intended to document the behavior of the integrated device in a supersonic cross-flow with real feedstocks through the plasma torch and injector array.

6.1.1 Shadowgraphs

Shadowgraph pictures of the aerodynamic ramp injector and plasma torch in a Mach 2.4 flow are shown in Figure 6.1. In all of the shadowgraph pictures, the flow is from left to right, and the wall is on the bottom. The curved surface at the lower right is the window frame. The turbulent boundary layer just ahead of the injector is about 1.9 d_{eq} thick, and the bow shock waves produced from the two rows of injector jets in the array and the plasma torch jet can be seen emanating from them up to the right and then turning downstream, approaching the angle of a Mach wave (24.6-deg for M=2.4). In these pictures, ethylene is being injected through the aero-ramp injector at nominal jet to freestream momentum flux ratios, $\overline{q}$, of 1.5 and 3.0, and nitrogen is being injected through the plasma torch at a nominal $\overline{q}$ of 1.2 with a power level of 2000-watts.

Figure 6.1(a) and (b) are shadowgraph pictures of the aero-ramp and plasma torch by themselves. In Figure 6.1(a), some details of the jet shock structure of the aero-ramp can be observed. In particular, the jet plume barrel shocks can be seen, along with the separation zone in front of the first pair of injectors. Evidence of a shock trail is also seen by a third highly oblique and somewhat unsteady shock downstream of the first two injector-jet bow shockwaves. It has been shown that the shock trail extends downstream with up to three more oblique shockwaves in this highly under-expanded flowfield (See Section 5.1.2). Due to the thickness of the boundary layer in relation to the plasma torch jet in Figure 6.1(b), it is hard to pick out any details pertaining to the plasma jet shock structure in this picture. It is important to note that no illumination from the torch in operation at 2000-watts can be seen in the image. This was due to the high intensity output of the laser light source in comparison to the light produced by the torch in the direction of the optical setup in the 20-nanosecond integration time of the high-speed camera 4-*CCD* arrays.

The combined aero-ramp and plasma torch flowfields with torch placement at torch-stations #1, #2 and #3 are presented in Figure 6.1(c) through (h). General trends that can be noticed include an increase in bow shock wave height and unsteadiness in the downstream bow shock of the aero-ramp injector with increased jet to freestream momentum flux ratio. Compare Figure 6.1(c) and (d), for example. Some condensation of ethylene in the area of the jet plumes may also be present, due to the sudden expansion of the highly under-expanded gas. This is indicated by the blurry regions above the injector holes. This feature also increases with an increase of momentum flux ratio. Another interesting feature of the integrated aero-ramp/ plasma-torch flowfield shown for the lower injector momentum flux ratio conditions is the merging of the downstream recompression shock with the bow shock from the plasma torch jet. This feature is shown in Figure 6.1(c), (e), and (g), and it is interesting to note that in the furthest downstream torch position (#3) the recompression shock is finally separated from the bow shock of the plasma torch. This is not apparent in the high injector momentum flux ratio cases, because the re-compression shock is further downstream. In all of the integrated configuration test cases, the plasma torch bow shock is very unsteady showing numerous kinks and orthogonal shockwaves emanating from them. This unsteadiness is indicative of increased turbulent mixing in this region. Weak orthogonal shockwaves can also be seen emanating from the downstream bow shock of the aero-ramp in the higher momentum flux ratio cases.

Figure 6.2 shows a set of sequential images taken with the 4-CCD Imacon 468 High Speed Camera. The four images are spaced 6.06 microseconds apart, which allows the freestream to move 1-cm downstream during the sequence. This sequence was selected because in it, a nice eddy structure of ethylene can be seen moving downstream just behind the shock wave. In addition, there is a local kink in the second injector row bow shock wave, which runs partially down its length as the clump moves further downstream from the injector array. This is a good example of the way turbulent eddys in the jet/freestream mixing layer create unsteady motion in the bow shock structure by effectively creating additional intermittent blockage.

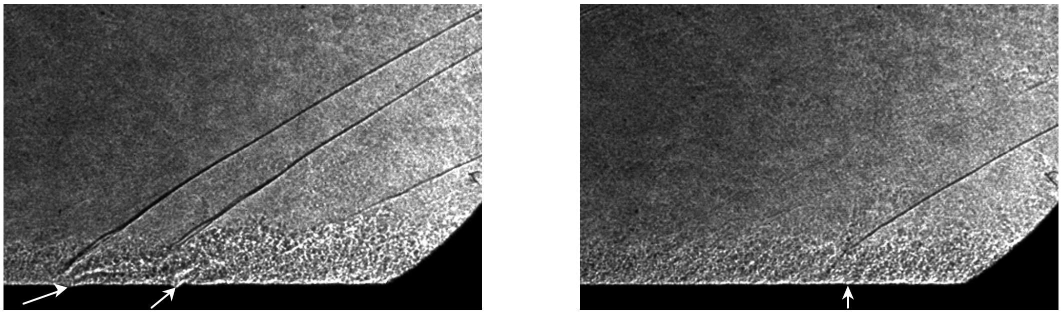

a) Aero-Ramp Injector Only
$\bar{q}_j = 1.5$, $\bar{q}_T = 0$, $P = 0$ W.

b) Plasma Torch Only
$\bar{q}_j = 0$, $\bar{q}_T = 1.2$, $P = 1990$ W.

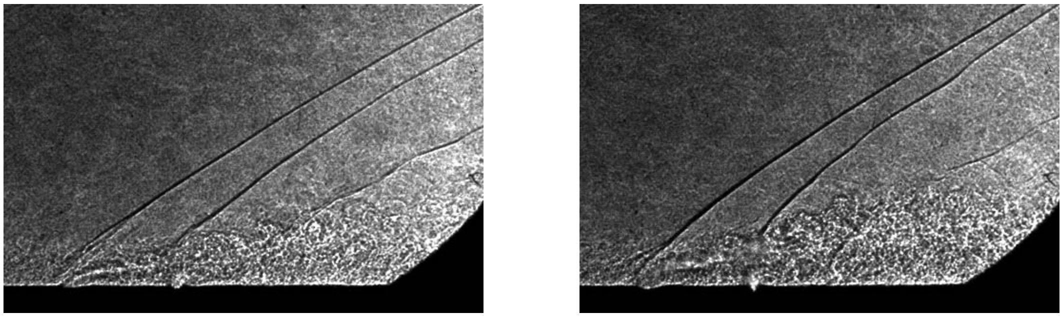

c) Torch-Station #1
$\bar{q}_j = 1.6$, $\bar{q}_T = 1.3$, $P = 1970$ W.

d) Torch-Station #1
$\bar{q}_j = 2.8$, $\bar{q}_T = 1.1$, $P = 2000$ W.

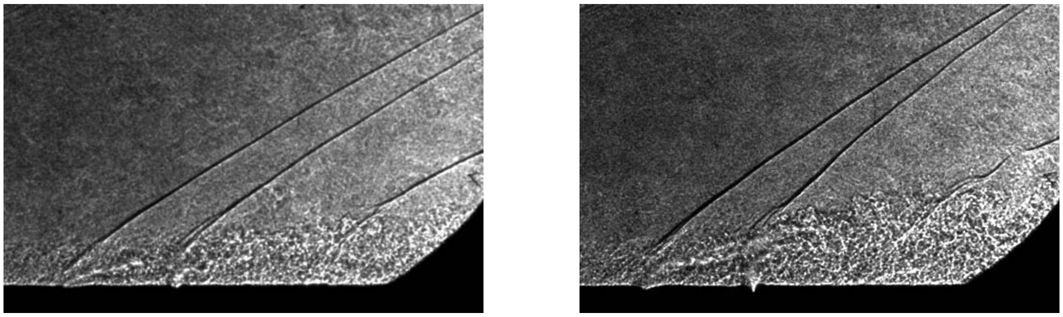

e) Torch-Station #2
$\bar{q}_j = 1.4$, $\bar{q}_T = 1.2$, $P = 1970$ W.

f) Torch-Station #2
$\bar{q}_j = 3.1$, $\bar{q}_T = 1.2$, $P = 1960$ W.

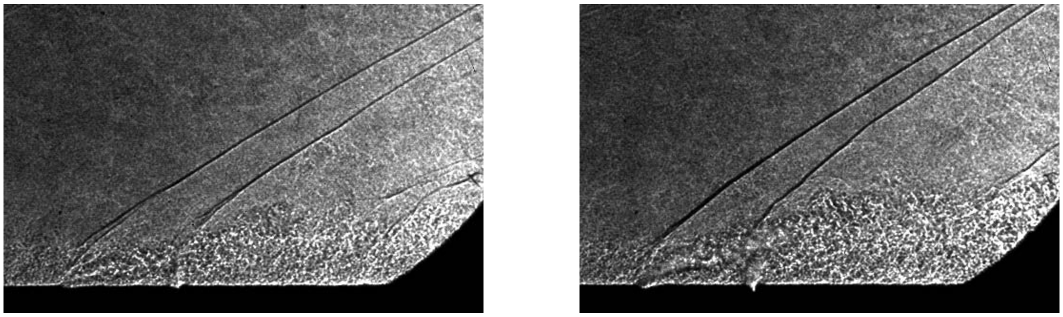

g) Torch-Station #3
$\bar{q}_j = 1.6$, $\bar{q}_T = 1.3$, $P = 2000$ W.

h) Torch-Station #3
$\bar{q}_j = 2.9$, $\bar{q}_T = 1.2$, $P = 1960$ W.

Figure 6.1 Integrated Configuration Shadowgraphs with Plasma Torch in Operation.

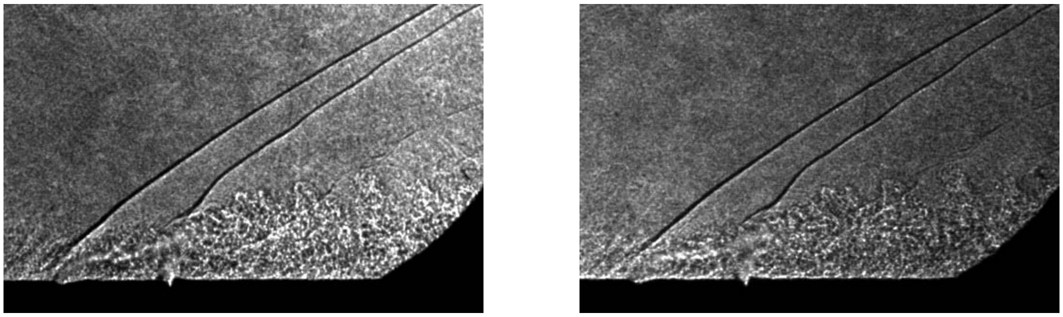

a) $t = 0\ \mu s$ **b) $t = 6.1\ \mu s$**

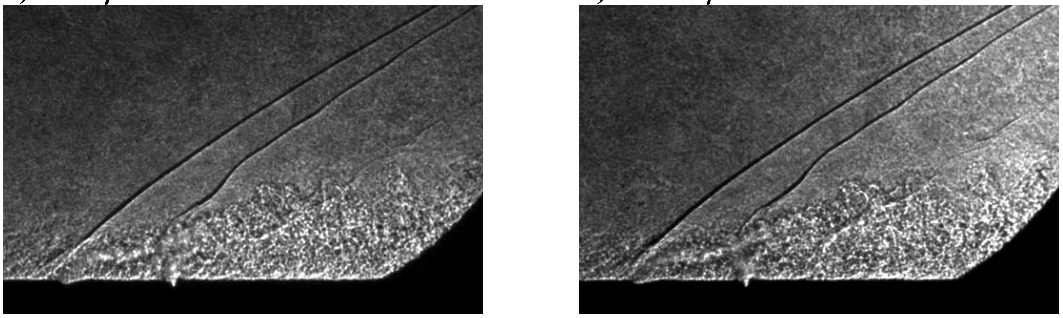

c) $t = 12.1\ \mu s$ **d) $t = 18.2\ \mu s$**

Figure 6.2 Sequential Shadowgraph Images. Torch-Station #1.
$\overline{q}_j = 2.7$, $\overline{q}_T = 1.1$, $P = 1990$ Watts.

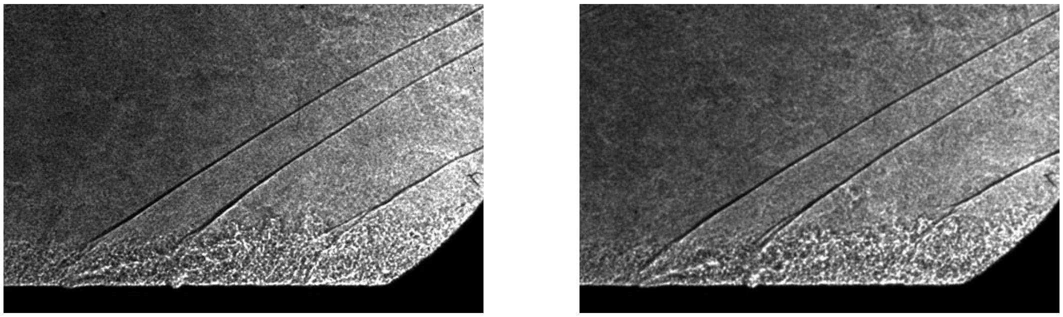

a) Torch-Station #2
$\overline{q}_j = 1.5$, $\overline{q}_T = 1.2$, $P = 0$ W.

b) Torch-Station #2
$\overline{q}_j = 1.4$, $\overline{q}_T = 1.2$, $P = 1970$ W.

Figure 6.3 Effect of Plasma Plume on Injector Plume and Shock Structure.

Figure 6.3 shows two more shadowgraph images taken nominally at the same injector and torch momentum flux ratios. The difference between the two pictures is that one is taken with the torch not in operation but with flow through it (a) and one is taken with the torch in operation at 1970 watts. There is a small difference in the position of the shock wave of the plasma torch injector. However, this difference could be accounted for by image-to-image unsteadiness in the shockwave due to turbulence. Since no images were produced with the torch in operation at a higher power level, it is unclear how much the shock wave structure would change with additional energy input.

6.1.2 High-Speed Flame Plume Images

High-speed images of the flame plumes generated by the integrated injector array/ plasma torch were created with the Hadland Photonics Imacon 468 4-CCD digital camera. The high-speed images were taken 1.39-milliseconds apart, with an integration time per frame of 10-microseconds with a camera gain setting of three. The images were spaced at one quarter of the time it takes to go through one cycle of the rectified DC power supplies 180 *Hz* AC frequency (5.56 milliseconds). Figure 6.4 presents the four images produced with a nitrogen torch-feedstock at a nominal power level of 2000 watts and ethylene fuel at a momentum flux ratio of 1.5. The images are shown at three times their normal scale for closer inspection. In these images, the flow is from left to right and the flame plume generated from the plasma torch is seen emanating from the bottom left side of the images. Electrode chunks are also emitted from the plasma torch, as seen in Figure 6.4(c), by the bright balls on the left hand side of the plasma torch plume, near the orifice. The resulting flame plume is created from the interaction of the plasma torch plume with the ethylene fuel plume.

As is evident from the images, the flame plume size is very dependent upon the cycle of the power supply. One must note that the image in Figure 6.4(a) is very dim for the camera integration time. This does not mean that the flame plume is necessarily as small as in the image, but rather that at that time in the power cycle the plume is emitting a lower level of intensity. This cyclic behavior may turn out to be very important, and further work should be done to attempt to vary the cyclic frequency. This in turn may lead to the excitation of possible resonant frequencies associated with the turbulence of the multiple-jet mixing processes. Upon analyzing the distance traveled by an eddy, as seen in the general area above the torch in the sequential shadowgraph images in Figure 6.2, an estimate of the frequency of the pulsation in the eddies in these images can be made. Assuming that the length scale of the turbulent eddies is on the order of the diameter of the aero-ramp individual jets (2.38-mm) and tracking of an eddy above the general torch area yields a velocity of 393 m/s (estimated 2.38-mm traveled in 6.06×10^{-6} seconds as measured from pictures – the 2.38-mm travel distance of the eddy and the injector jet diameter is a coincidence), an estimate of the turbulent eddies frequency is on the order of 165 KHz. This frequency, or a multiple of, may yield a good starting place for the investigation of the interaction dynamics of the plasma-torch/ injector-jet plume interactions of the integrated configuration with a variable high frequency torch power supply or other means of excitation/pulsation.

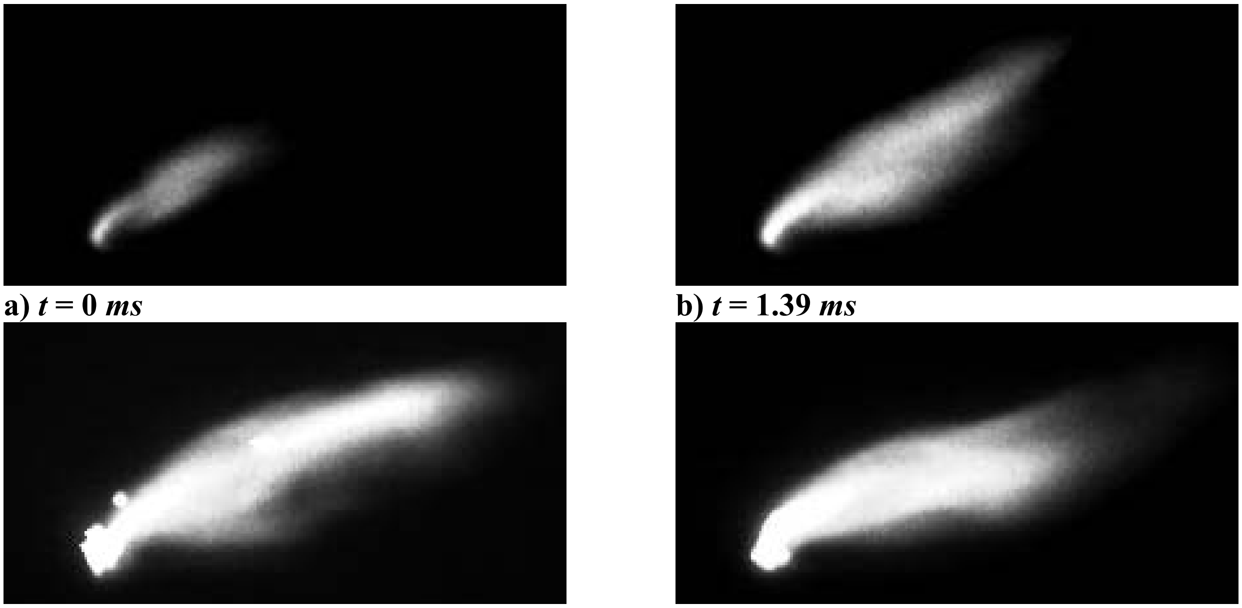

a) ***t* = 0 *ms***

b) ***t* = 1.39 *ms***

c) ***t* = 2.78 *ms***

d) ***t* = 4.17 *ms***

Figure 6.4 High-Speed Flame Plume Images with Nitrogen Torch-Feedstock and Ethylene Fuel, P = 2040 Watts, $\bar{q}_j = 1.5$, $\bar{q}_T = 1.2$, Scale 3:1.

A comparison of the scale of the plasma torch flame plume to the injector-jet plume is shown in Figure 6.5. In this image, the flame plume shown in the figure above has been superimposed over a shadowgraph. The flame plume image is actually an overlay of all four images, which was done to help get an averaged flame plume shape. Both the flame plume and shadowgraph images are nominally at a power level of 2000 watts, with nominal injector and plasma torch momentum flux ratios of 1.5 and 1.2. Both cases involve ethylene fuel and a nitrogen torch-feedstock. As can be seen, the flame plume reaches about midway into the injector fuel plume. This location corresponds well with the initial helium torch plume data (unpowered) presented with the fuel plume of the small aero-ramp array shown in Section 5.1.4. In this mixing analogy profile, though for a higher momentum flux ratio, the plasma torch plume penetrated to the center of the injector-jet plume in between its two primary cores. This shows that the flame plume is being lifted into a low relative velocity area, with a lower overall equivalence ratio than at the cores, which could lead to the possibility of entrainment of the flame into the upper portion of the jet/freestream mixing layer at the top of the fuel plume core. If the flame reaches there in a high enthalpy flow, the flame would then have the chance to propagate through the mixing layer and spread around the entire fuel plume with help from the plume's vortex motion.

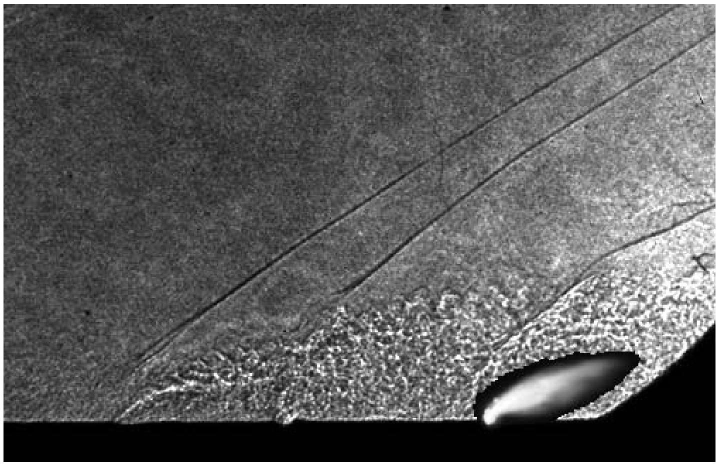

Figure 6.5 Superimposed Flame plume Images embedded in a Shadowgraph Image with Nitrogen Torch-Feedstock and Ethylene Fuel (Shadowgraph: P = 1970 Watts, $\bar{q}_j$ = 1.4, $\bar{q}_T$ = 1.2, Flame Plume Image: P = 2040 Watts, $\bar{q}_j$ = 1.5, $\bar{q}_T$ = 1.2) Scale 1:1.

6.1.3 Pressure-Sensitive Paint Results

PSP experiments were performed while injecting air through the aero-ramp injector and an unpowered plasma torch igniter, but with injection through the torch nozzle. It is not practical to conduct PSP studies with the torch in operation, since that leads to severe heating and temperature variations on the wall. Surface pressure was measured around the aero-ramp injector with the plasma torch at torch-stations #1, #2, and #3 at nominal injector momentum flux ratios of 1.5 and 3.0 and a nominal torch momentum flux ratio of 1.2. Results from these experiments are presented in Figure 6.6. In the images, the flow is moving from left to right, the pressure field is normalized by the freestream static pressure, p_∞, and each image has the same scale to help with comparison. Again, the dark circular ring around the injectors is where the surface of the tunnel mates with the injector blocks, and there is no paint.

In these pictures, the bow shocks in front of the injector holes are shown by the left boundary between the blue and red regions, which notes the position of the pressure increase from the low freestream static pressure value to the high value behind the shock wave. Figure 6.6(a) and (d), (b) and (e), and (c) and (f) show the injector with the torch downstream at torch-stations #1, #2, and #3, respectively. One area of interest in the combined configurations is the low-pressure region behind the downstream row of injector holes. This region was shown to be a separation region in Section 5.1.2 using a surface oil flow visualization technique. As the plasma torch is moved towards the injector, from torch-station #3 to #2, there is relatively no effect on this region. But, as the torch is moved closer to torch-station #1, the static pressure in this region is increased due to the high pressure in front of the torch. The trailing recompression shock system mentioned in the earlier shadowgraph section is also seen in these images. Another interesting feature is the weaker pressure rise near the torch in the high momentum flux cases. This is indicative of a lower velocity region around the plasma torch area.

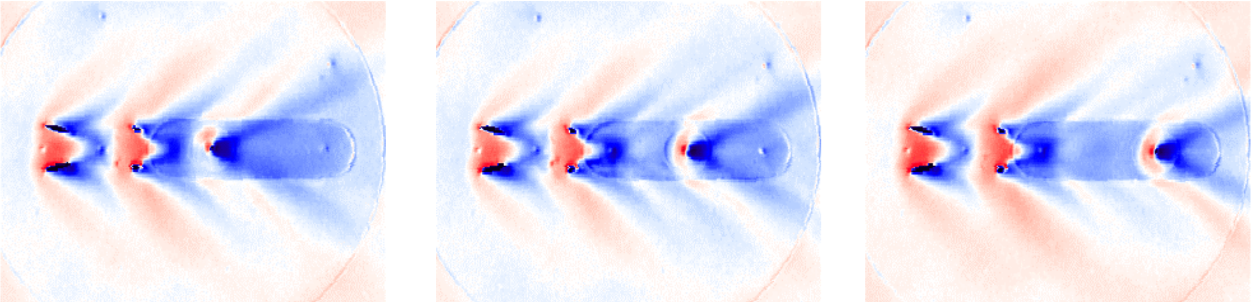

a) Torch-Station #1

$\bar{q}_j = 1.6$, $\bar{q}_T = 1.3$

b) Torch-Station #2

$\bar{q}_j = 1.5$, $\bar{q}_T = 1.2$

c) Torch-Station #3

$\bar{q}_j = 1.6$, $\bar{q}_T = 1.3$

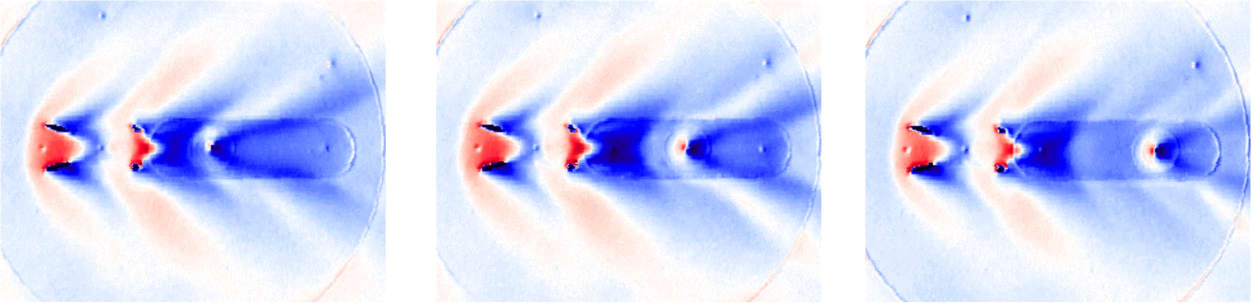

d) Torch-Station #1

$\bar{q}_j = 3.0$, $\bar{q}_T = 1.2$

e) Torch-Station #2

$\bar{q}_j = 3.2$, $\bar{q}_T = 1.3$

f) Torch-Station #3

$\bar{q}_j = 2.7$, $\bar{q}_T = 1.1$

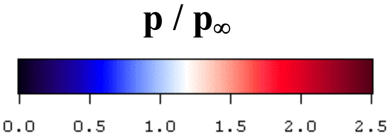

Figure 6.6 Pressure Sensitive Paint Experiments.

6.1.4 Plume Photography

Figure 6.7 through Figure 6.9 show the longer exposure time (low-speed) flame plume photographs taken of the integrated configuration for nominal injector momentum flux ratios of 1.5 and 3.0 for the aero-ramp with ethylene as injectant and 1.2 for the plasma torch with either methane or nitrogen as the feedstock. These pictures were all taken with a 35-mm camera with a shutter speed of 1/250 seconds. Further, these pictures are unfiltered, and the scale is 1:1. The flow is from left to right, and the plasma torch is situated behind the aero-ramp fuel injector array at torch-stations #1, #2, or #3, excluding the plasma torch alone plume pictures in Figure 6.9. The smaller plume images to the left in some of the pictures are reflections off the fused silica glass window on the other side of the test section.

In all the flame plume photographs, the flames are eventually quenched before further propagation into the main flow can be achieved. This is primarily due to the very low static freestream temperature (131 K) and pressure (0.26 atm) of the wind tunnel facility. With this in mind, one can extrapolate the following notion: whichever ethylene-fuel/ plasma-torch-feedstock combination produces the largest flame plume in this cold, harsh environment will probably lead to the highest level of main flow/fuel ignition, combustion, and flame propagation in a higher enthalpy environment where supersonic combustion applications are used.

A comparison between the results with methane, nitrogen and a mixture of nitrogen and hydrogen (90/10 percent by volume) torch feedstocks is given in Figure 6.7 with a nominal torch power of 2000 watts at a nominal aero-ramp momentum flux ratio of 1.5. A bright white flame can be seen with a light blue color on the outer edge of the downstream portion of the flame, which is common with the combustion of ethylene and air. The bright white portion of the flame is a highly excited region. In the methane torch feedstock pictures (Figure 6.7(a), (b), and (c)), the flame plume penetrates the furthest with the torch at torch-station #1, but it appears to have the longest plume at torch-station #3. The light to the left of the flame plume in Figure 6.7(b) is a reflection off the spectrometer. The nitrogen feedstock flame plumes (Figure 6.7(d), (e), and (f)) are larger than the methane plumes and the torch-station #2 picture shown in Figure 6.7(e) has the largest plume with the highest penetration level. The mixture of nitrogen and hydrogen was examined only with the torch at at torch-station #2. Since the flame plume looked similar to that with nitrogen alone and the addition of hydrogen reduced the length of the flame, no other torch-stations were tried with the feedstock mixture due to a lack of time. One question that this raises is: how does the addition of fuel into the mixture affect the reaction zone in the highly excited flame plume. On inspection of the photographs and by the notion that the lack of fuel in the plasma will create a leaner interface between the plasma plume and the jet/freestream main plume, it seems that the plasma propagates further in a leaner environment. However, one must still also acknowledge the role of feedstock choice in the plasma propagation. For example, nitrogen and argon are neither oxidizers nor fuels, but there are strong differences in their effect on ignition delay and reaction times. In addition, in a reactive environment with nitrogen and oxygen, nitrogen helps to increase the breakup of diatomic oxygen into monatomic oxygen through the thermal mechanism. This break up of the oxygen molecules helps to speed up the overall reaction and may lead to chain branching in a high temperature environment. This effect does not occur with an inert gas, such as argon, although there is nitrogen in the atmosphere, just less will be in the interface between the plasma and the fuel/freestream jet.

Photographs of the aero-ramp injector at a nominal ethylene fuel $\overline{q}$ of 1.5 and 3.0 with nitrogen as the torch feedstock at a nominal power level of 1500 watts are shown in Figure 6.8. In the photos taken with the lower injector momentum flux ratio, Figure 6.8(a) through (c), the plumes with the torch at torch-station #2 and #3 are the largest and nearly the same size. The main difference between the two plumes is the shape. The plume at torch-station #2 lifts up higher and the plume with the torch at torch-station #3 is longer in the downstream direction. In the higher injector momentum flux ratio pictures shown in Figure 6.8(d) through (f), the plume penetration height is increased and the flame plume generated with the torch at torch-station #3 appears the largest. In addition, the flame plume shapes with the torch at torch-station #2 and #3 are very similar and show a high level of penetration through the middle of the two injector fuel-jet counter-rotating plume cores. A noteworthy feature about the plume with the torch at torch-station #1, in Figure 6.8(a) and (d), is that the excited plume reaches upstream of the plasma torch location. This feature occurs because the plasma torch front separation zone has merged with the rear separation zone of the fuel injector array, creating a low velocity subsonic region near the torch allowing the flame plume to propagate upstream.

Figure 6.9 shows photographs of the methane, nitrogen and nitrogen-hydrogen mixture feedstocks plasma torch plumes operating alone at 1500 or 2000 watts. These pictures are presented to give the reader an idea of the size of the plasma torch plumes at a 1/250 second exposure time for comparison to the other pictures shown in the previous two figures. The methane torch plume is substantially larger than the other two plumes due to additional energy release from the feedstock (fuel)/freestream reactions in comparison to the nitrogen and the mixture, which had a 10-percent by volume (molar) portion of hydrogen.

Figure 6.10 shows photographs taken of the plasma torch in operation at 3000 watts behind the aero-ramp injector ($\bar{q}$ =1.5) at torch-station #2 with methane (a), nitrogen (b), and air (c) as the torch feedstocks. The pictures were taken through a 388-nm band-pass filter with an exposure time of 1/30 sec., which for combustion plumes lets in light from the $CH^*/CN^*/N_2^*$ lines. Thus, the pictures are a good marker for the plasma zone of the torch combustion plume. From the three pictures, it is evident that the flame plume produced with air is larger than the one produced by nitrogen, which is in turn larger than the one with the methane feedstock. The photograph shown in Figure 6.10(c) with air as the torch feedstock is from a preliminary set of data and was added to show the great potential of air as a feedstock.

a) Station #1, Methane Feedstock.
$\bar{q}_j$ = 1.6, $\bar{q}_T$ = 1.2. *P* = 2070 W.

b) Station #2, Methane Feedstock.
$\bar{q}_j$ = 1.4, $\bar{q}_T$ = 1.1. *P* = 1990 W.

c) Station #3, Methane Feedstock.
$\bar{q}_j$ = 1.5, $\bar{q}_T$ = 1.3. *P* = 2070 W.

d) Station #1, Nitrogen Feedstock.
$\bar{q}_j$ = 1.5, $\bar{q}_T$ = 1.2. *P* = 1970 W.

e) Station #2, Nitrogen Feedstock.
$\bar{q}_j$ = 1.5, $\bar{q}_T$ = 1.2. *P* = 2020 W.

f) Station #3, Nitrogen Feedstock.
$\bar{q}_j$ = 1.5, $\bar{q}_T$ = 1.2. *P* = 2050 W.

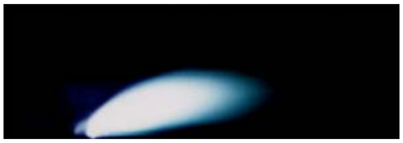

g) Station #2, $N_2 + H_2$ Feedstock.
$\bar{q}_j$ = 1.5, $\bar{q}_T$ = 1.2. *P* = 2090 W.

Figure 6.7 Flame Plume Photographs of Integrated Configuration with Ethylene Fueled Injector and CH_4, N_2, or $N_2 + H_2$ Torch Feedstocks. Scale 1:1.

a) Station #1, Nitrogen Feedstock.
$\bar{q}_j = 1.5$, $\bar{q}_T = 1.2$, $P = 1440$ W.

b) Station #2, Nitrogen Feedstock.
$\bar{q}_j = 1.6$, $\bar{q}_T = 1.3$, $P = 1570$ W.

c) Station #3, Nitrogen Feedstock.
$\bar{q}_j = 1.5$, $\bar{q}_T = 1.2$, $P = 1570$ W.

d) Station #1, Nitrogen Feedstock.
$\bar{q}_j = 3.2$, $\bar{q}_T = 1.3$, $P = 1480$ W.

e) Station #2, Nitrogen Feedstock.
$\bar{q}_j = 2.9$, $\bar{q}_T = 1.2$, $P = 1520$ W.

f) Station #3, Nitrogen Feedstock.
$\bar{q}_j = 2.9$, $\bar{q}_T = 1.2$, $P = 1560$ W.

Figure 6.8 Flame Plume Photographs of Integrated Configuration with Ethylene Fueled Injector and a N_2 Torch Feedstock. Scale 1:1.

a) Methane Feedstock
$\bar{q}_j = 0$, $\bar{q}_T = 1.2$. $P = 2076$ W.

b) Nitrogen Feedstock
$\bar{q}_j = 0$, $\bar{q}_T = 1.1$. $P = 2010$ W.

c) $N_2 + H_2$ Feedstock
$\bar{q}_j = 0$, $\bar{q}_T = 1.2$. $P = 1930$ W.

d) Nitrogen Feedstock
$\bar{q}_j = 0$, $\bar{q}_T = 1.3$. $P = 1520$ W.

Figure 6.9 Flame Plume Photographs of the Plasma Torch in Operation (Alone) with CH_4, N_2, or $N_2 + H_2$ Torch Feedstocks. Scale 1:1.

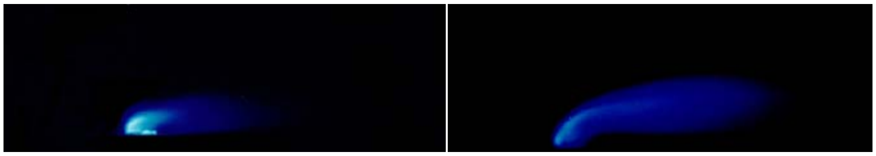

a) Station #2, Methane Feedstock $\bar{q}_j = 1.5$, $\bar{q}_T = 1.2$.

b) Station #2, Nitrogen Feedstock $\bar{q}_j = 1.5$, $\bar{q}_T = 1.2$.

c) Station #2, Air Feedstock; $\bar{q}_j = 1.5$, $\bar{q}_T = 1.2$.

Figure 6.10 High Power Flame Plume Photographs, Scale 1:1, Power nominally 3000 W.

6.1.5 Temperature Survey Results

Figure 6.11 and Figure 6.12 present the results from the total temperature surveys made downstream of the integrated injector array and plasma torch. The data presented in these figures is for the torch at torch-stations #1, #2, and #3 with methane, nitrogen, and a mixture of nitrogen and hydrogen (90/10 percent by volume) as the torch feedstocks with a $\bar{q}$ of 1.2±0.1 and an injector $\bar{q}$ of 1.5±0.1 or 3.0±0.15 with ethylene injection. All of the total temperature profiles were made with the torch in operation at 1500 or 2000 ±75 watts. These cross-stream, iso-therm profiles consist of measurements taken just over $x/d_{eff} = 29$ downstream from the center of the overall area of the aero-ramp injector holes. The three torch stations, #1, #2, and #3 are each about 6.5, 8.7, and 10.9 x/d_{eff} downstream from the center of the overall injector area. This also corresponds to downstream distances from the center of the plasma torch hole to the temperature sampling plane of 62.4, 56.4, and 50.4 x/d_{torch}.

The local total temperature measurements were normalized by the freestream conditions, and all the profiles were set to the same scale for better interpretation. Figure 6.13 presents the total temperature profiles for the plasma torch in operation with methane, nitrogen, and nitrogen/hydrogen feedstocks located at torch-station #2 without fuel from the injector array. The scale of the three total temperature profiles with the plasma torch in operation by itself were set to the same scale, but different from that of Figure 6.11 and Figure 6.12, because the torch cores alone were much hotter since they did not have a large counter rotating vortex pair to disperse the torch jet.

Some of the general trends associated with the temperature profiles of the plasma torch using a nitrogen feedstock and ethylene fuel from the injector shown in Figure 6.11 involve the widening of the temperature plume as the torch is moved further upstream. This effect is due to an increase in distance between the torch and the total temperature probe, which allows the torch plume to mix further with that of the injector and the mainstream. This trend is not fully observed in the profiles with methane as the torch feedstock (Figure 6.11(a) through (c)). In the methane feedstock cases, the plume is still the largest with the torch at the near station (Figure 6.11(a)), it continues to shrink as the torch is moved from torch-station #1 to #2 (Figure 6.11(b)), but then grows slightly again from torch-station #2 to #3 (Figure 6.11(c)). This trend agrees with methane flame plume pictures in Figure 6.7.

In the profiles with the torch at torch-station #3 for both methane and nitrogen feedstocks (Figure 6.11(c) and (f)), there is a secondary temperature core near the surface of the test section floor. This implies that the plasma torch station is far enough downstream that its plume does not get entirely caught up in the fuel injector plume.

Another feature observed in the profiles with the torch at station #3 behind the fuel injector array, in Figure 6.11(c) and (f), is how the main temperature plume cores are off-center to the right side in the positive y-direction. This behavior is also apparent in the methane plasma torch profile, with the torch in operation alone, shown in Figure 6.13(a), but not apparent in the nitrogen or nitrogen/hydrogen feedstock torch plumes in Figure 6.13(b and c). This could be due to the width between sampling stations, or it could also be due to some relationship between the swirling of the torch plume and its effects on the mixing layer where combustion would take place between the torch and the injector plumes. Note that the plasma torch has a flow-swirler inside the plasma torch, which has a swirl number of 1.0, where the swirl number is defined as the ratio of tangential to streamwise velocity of the jet. This would correspond to a counter clockwise rotation on the profiles, which in itself is interesting because the temperature plume is off center in the other direction (right). This may mean that there could be a relationship between the counter rotation effects of the torch and injector plumes and the asymmetric mixing of the temperature field. If one looks at the temperature profiles for the torch at the closer station in relation to the injector fuel plume (Figure 6.11(a) and (d)), it is apparent that the temperature plume core is now off-center towards the left. Further, the temperature profiles with the torch at station #2 shown in Figure 6.11(b) and (e) look symmetric. Therefore, as the torch is moved further away from the fuel injector array, the total temperature plume core is shifted from left to right. It is unclear what this might imply towards ignition and combustion of the main plume in a high-enthalpy environment. However, symmetric burning of both sides of the fuel plume would definitely be desirable. This effect is also seen in the high momentum flux ratio (3.0) profiles in Figure 6.12, but now it seems that the plumes are all over to the right-hand side of the fuel plume, however, the same left to right trend of the first through third torch stations is preserved. This is probably due to additional vortex strength from the higher momentum flux ratio levels. Another interesting feature of the plumes in Figure 6.12 is that the plume with the torch at torch-station #2 is hotter than the one at #3. This may indicate a higher level of heat release due to the reactions in the plasma/plume interface, since having the plume at a location further upstream should tend to mix the temperature to a lower level by the time it gets to the temperature probe sampling station location.

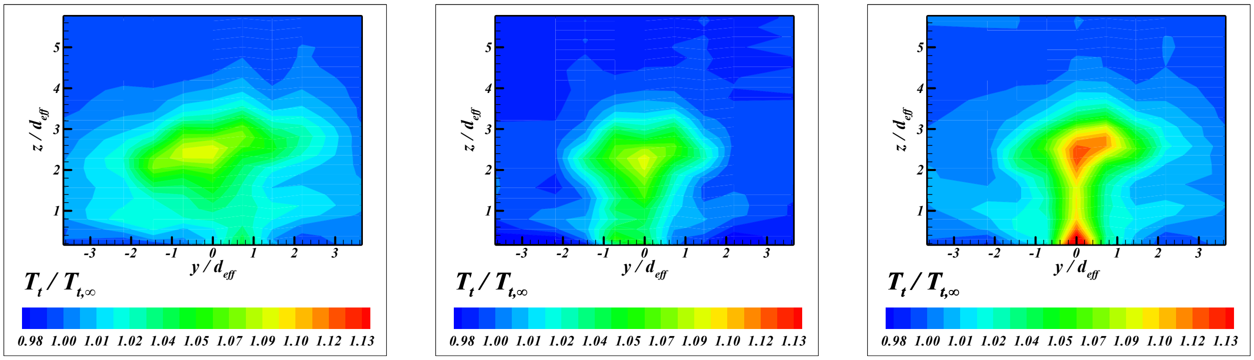

a) Torch-Station #1 Methane Feedstock $\bar{q}_j = 1.5$, $\bar{q}_T = 1.2$.

b) Torch-Station #2 Methane Feedstock $\bar{q}_j = 1.5$, $\bar{q}_T = 1.2$.

c) Torch-Station #3 Methane Feedstock $\bar{q}_j = 1.5$, $\bar{q}_T = 1.2$.

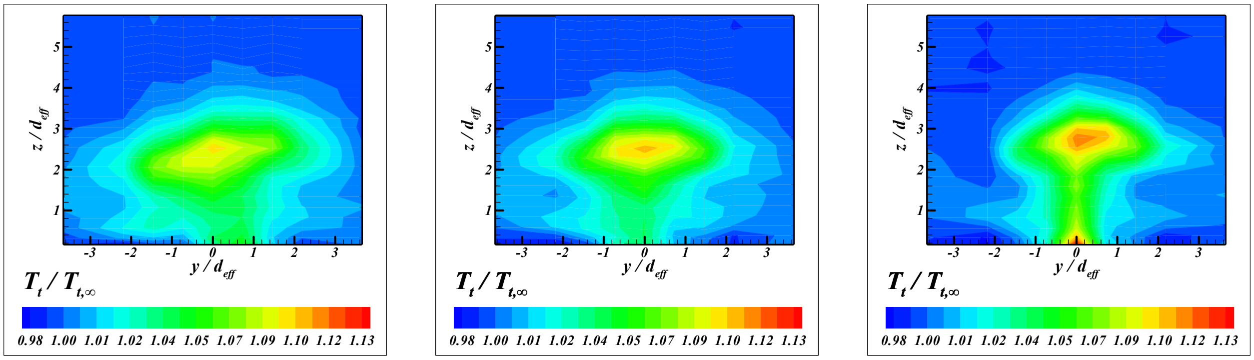

d) Torch-Station #1 Nitrogen Feedstock $\bar{q}_j = 1.5$, $\bar{q}_T = 1.2$.

e) Torch-Station #2 Nitrogen Feedstock $\bar{q}_j = 1.5$, $\bar{q}_T = 1.2$

f) Torch-Station #3 Nitrogen Feedstock $\bar{q}_j = 1.5$, $\bar{q}_T = 1.2$.

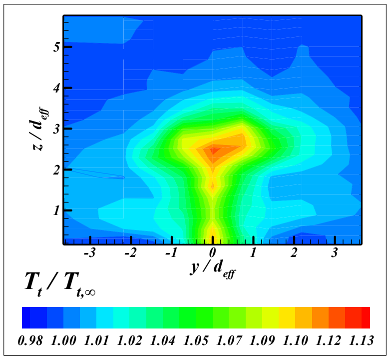

g) Torch-Station #2 $N_2 + H_2$ Feedstock $\bar{q}_j = 1.5$, $\bar{q}_T = 1.2$.

Figure 6.11 Downstream Total Temperature Plumes, Power Nominally 2000 Watts.

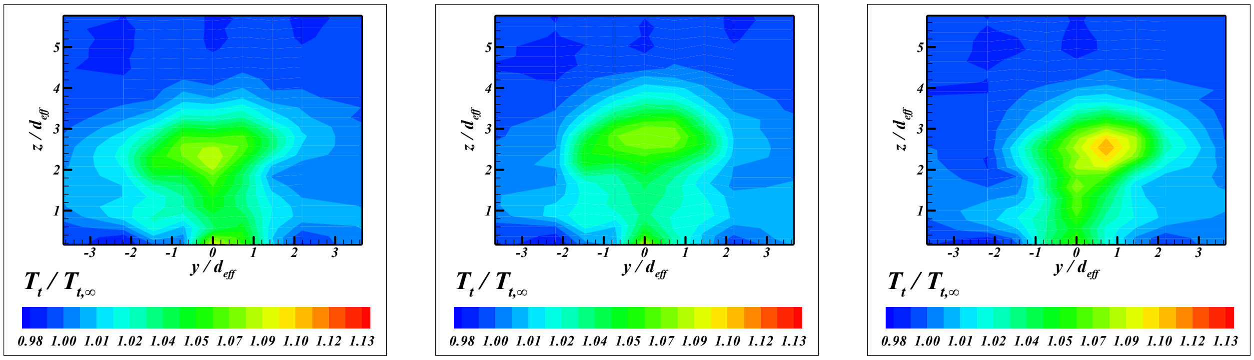

a) Torch-Station #1
Methane Feedstock
$\bar{q}_j = 1.5$, $\bar{q}_T = 1.2$.

b) Torch-Station #2
Methane Feedstock
$\bar{q}_j = 1.5$, $\bar{q}_T = 1.2$.

c) Torch-Station #3
Methane Feedstock
$\bar{q}_j = 1.5$, $\bar{q}_T = 1.2$.

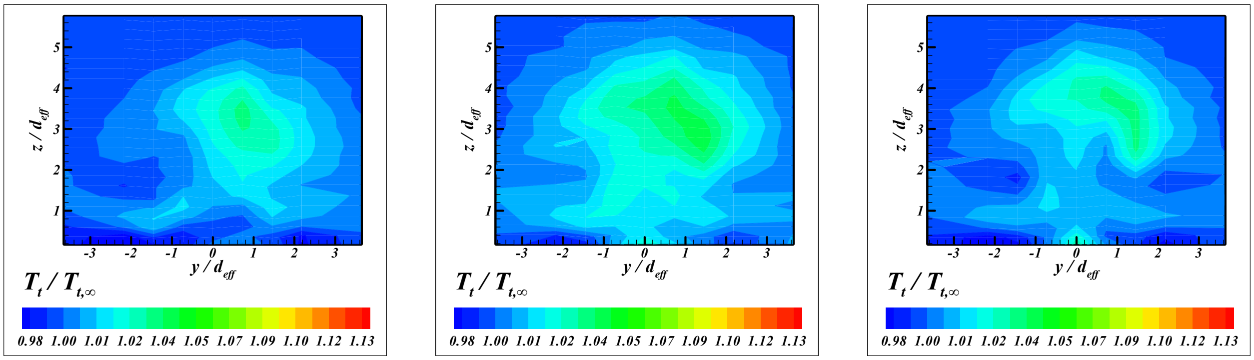

d) Torch-Station #1
Nitrogen Feedstock
$\bar{q}_j = 1.5$, $\bar{q}_T = 1.2$.

e) Torch-Station #2
Nitrogen Feedstock
$\bar{q}_j = 1.5$, $\bar{q}_T = 1.2$.

f) Torch-Station #3
Nitrogen Feedstock
$\bar{q}_j = 1.5$, $\bar{q}_T = 1.2$.

Figure 6.12 Downstream Total Temperature Plumes, Power Nominally 1500 Watts.

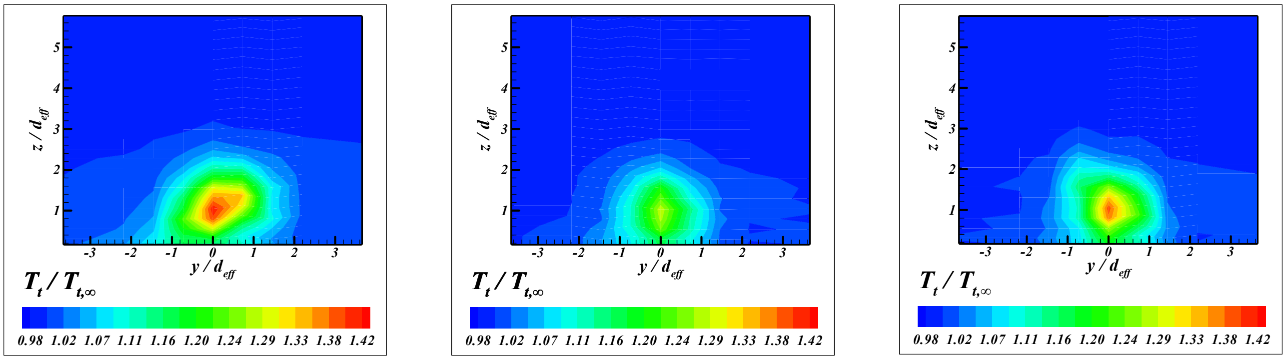

a) Torch-Station #2
Methane Feedstock
$\bar{q}_{\text{injector}} = 0.0$, $\bar{q}_{\text{torch}} = 1.2$.

b) Torch-Station #2
Nitrogen Feedstock
$\bar{q}_{\text{injector}} = 0.0$, $\bar{q}_{\text{torch}} = 1.2$.

c) Torch-Station #2
N_2 + H_2 Feedstock
$\bar{q}_{\text{injector}} = 0.0$, $\bar{q}_{\text{torch}} = 1.2$.

Figure 6.13 Downstream Total Temperature Plumes with the Plasma Torch Alone, Power Nominally 2000 Watts.

Figure 6.14 and Figure 6.15 are graphs of the plume core temperature and penetration height, respectively, which were created from the total temperature surveys. In these plots, data is presented for the aero-ramp operating at a $\overline{q}$ of 1.5 with the torch at a $\overline{q}$ of 1.2, and the torch in operation alone. In both cases, the torch is operating at 2000 watts with methane, nitrogen, and nitrogen/hydrogen mixture feedstocks. There is also data presented for the injector operating at a $\overline{q}$ of 1.5 and 3.0 with the plasma torch operating with a nitrogen feedstock at 1500 watts at a $\overline{q}$ of 1.2. These results show that the plumes generated with the nitrogen torch feedstock and ethylene fuel were in general, hotter and penetrated further than those produced with the methane feedstock.

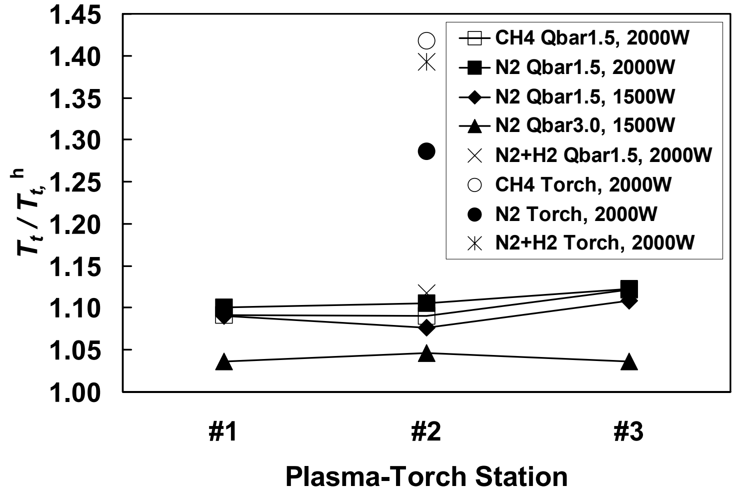

Figure 6.14 Core Temperature.

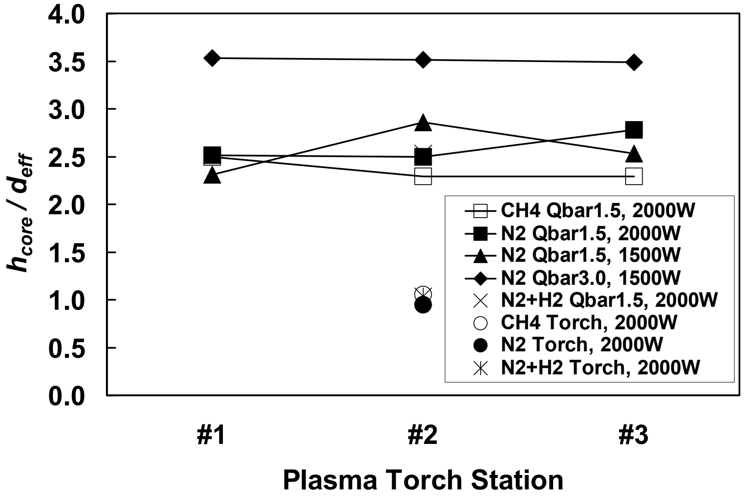

Figure 6.15 Core Penetration Height

6.1.6 Spectroscopy

Spectroscopic measurements were performed while injecting ethylene through the aero-ramp injector and methane, nitrogen, nitrogen/hydrogen mixture, or air feedstocks through the plasma torch igniter. Data was measured for the aero-ramp injector at nominal momentum flux ratios of 1.5 and 3.0 with the plasma torch at torch-stations #1, #2, and #3, and a nominal torch momentum flux ratio of 1.2.

General spectrograms of the feedstock/injector combinations and the plasma torch in operation alone are presented in Figure 6.16. The intensity scales in these graphs are equal for ease to aid in interpretation of the magnitudes between various feedstocks. Results are shown in Figure 6.16(a) and (c) for the nitrogen and methane plasma torch feedstocks at their corresponding "brightest" torch station. The results with the Nitrogen/Hydrogen mixture and air feedstocks were taken where available.

The results in Figure 6.16 were created with a three-channel spectrograph. In order to help show the various peaks associated with the spectrograms, close-ups of the results from the three channels with the nitrogen/ethylene feedstock/fuel case shown in Figure 6.16(a) are given as Figure 6.17, Figure 6.18, and Figure 6.19.

Figure 6.17 shows the spectral line data for the 200- to 400-nm range. Definite peaks were identified here for monotonic carbon, C^* (247.9 nm), and the $CN^*(0,0)$ Band (388.3 nm). The CN^* band is part of a strong violet system, $B^2\Sigma - \Sigma^2X$, which appears in arc sources containing, of course, nitrogen and carbon compounds, and has heads at 359.0- (1,0), 388.3- (0,0), 421.6- (0,1), and 460.6-nm (0,2) degraded to the violet (Pearse and Gaydon[87]). Other more questionable peaks in this figure are shown at 333.4 and 356.5-nm. These peaks are more questionable, since there are a lot of peaks (CN^*, NH^*, N_2^*, CN^*) at and around 333-334-nm range and the peak shown as N_2^* at 357.6-nm is actually on the graph as 356.7-nm. This 1-nm discrepancy in wavelength could be due to many factors, ranging from miscalibration of the spectrometer, to Doppler shifting of the line due to the high particle velocity. Furthermore, this area has multiple possibilities for peaks and definite superposition of the local $CN^*(1,0)$ band onto the rest of the area. In addition, the N_2 band in regular flames usually has a secondary peak (2,1) at 353.7, which has been shown to have a intensity of about 80-percent of the (1,0) peak (Pearse and Gaydon[87]). Thus, there must be some significant contribution to the apparent (1,0) peak from some other excited species.

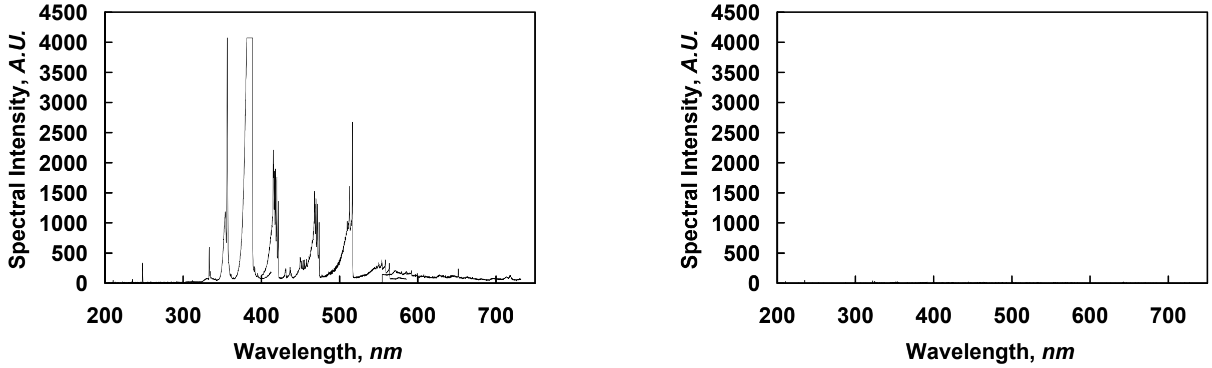

a) N_2 S#2, 2040 W, $\bar{q}_j = 1.5$, $\bar{q}_T = 1.2$

b) N_2 (Torch only), 2030 W, $\bar{q}_j = 0$, $\bar{q}_T = 1.2$

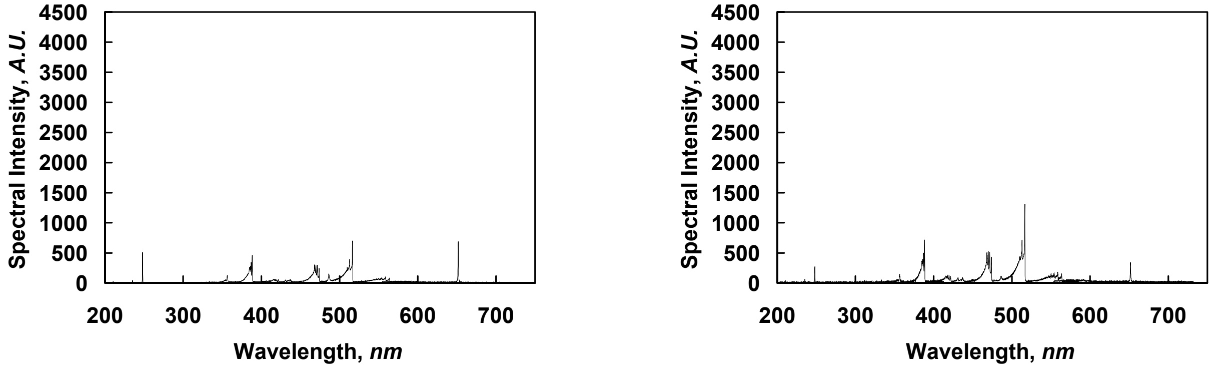

c) CH_4 S#1, 2080 W $\bar{q}_j = 1.6$, $\bar{q}_T = 1.2$

d) CH_4 (Torch only), 1960 W, $\bar{q}_j = 0$, $\bar{q}_T = 1.2$

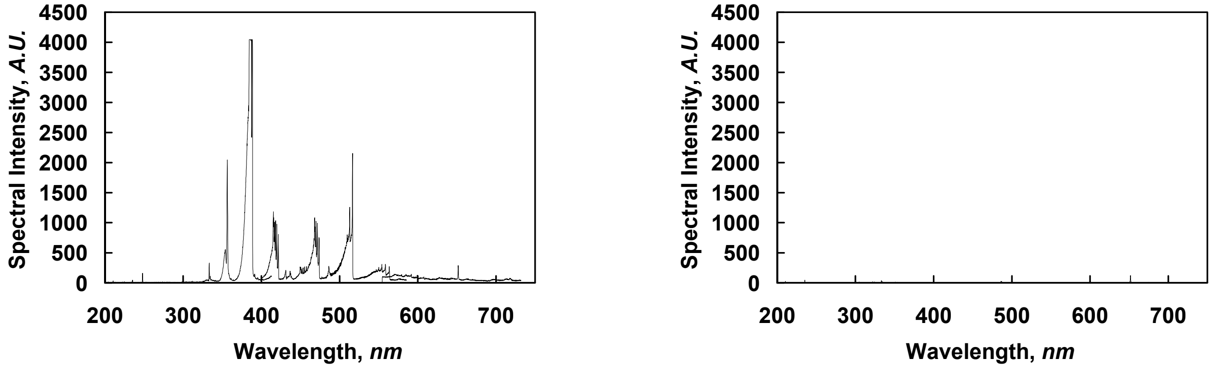

e) $N_2 + H_2$, S#2, 2050 W, $\bar{q}_j = 1.5$, $\bar{q}_T = 1.1$

f) $N_2 + H_2$, (Torch only), 1910W, $\bar{q}_j = 0$, $\bar{q}_T = 1.2$

Figure 6.16 Spectrograms of Integrated Configuration with Various Plasma Torch Feedstocks and Ethylene Fuel

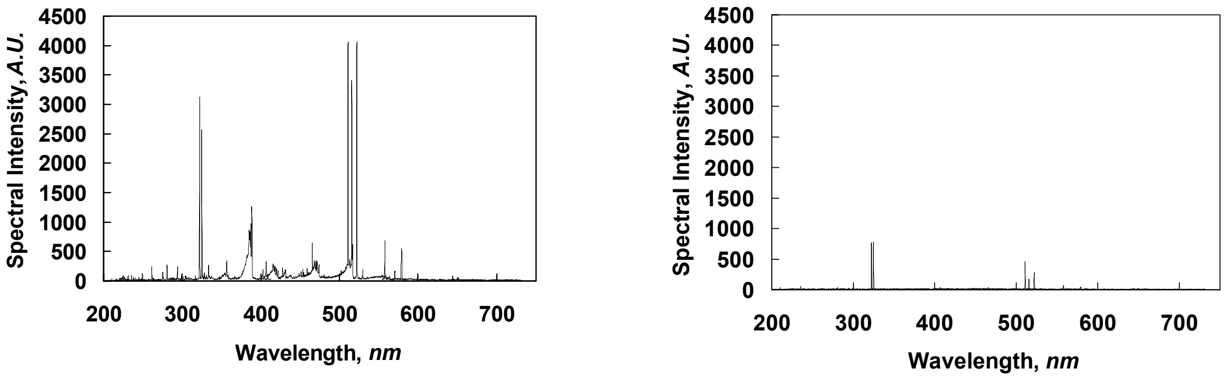

g) Air, S#1, 1800W, $\bar{q}_j = 1.6$, $\bar{q}_T = 1.1$

h) Air (Torch only), 1430W, $\bar{q}_j = 0$, $\bar{q}_T = 0.9$

Figure 6.16 Cont'd. Spectrograms of Integrated Configuration with Various Plasma Torch Feedstocks and Ethylene Fuel.

Figure 6.18 shows the spectral data for the 400 – 575-nm range with the nitrogen feedstock and methane fuel at 2000 watts. The peaks shown in this spectrogram are more readily identifiable than those in the 200-400 nm range. First, the CN^* 421.6- (0,1) and 460.6-nm (0,2) bands, degraded to the violet, are shown. The most prevalent system shown in this spectral range is the C_2^* Swan bands ($A^3\Pi_g$ – $X'^3\Pi_g$), with its most prevalent bands ranging as follows: 438.2- (2,0), 473.7- (1,0), 516.6- (0,0), 563.5- (0,1), and 619.1-nm (0,2). Typically, these bands degrade to the violet, and are very common in sources containing carbon, such as Bunsen flames and in discharges through hydrocarbons and other organics (Pearse and Gaydon[87]). They also appear in a carbon arc and in active nitrogen reacting with organic vapors. The 430.0-nm CH^* band is also apparent at 431.5-nm (0,1). This band degrades to the red and is readily excited during the combustion of hydrocarbons in electrical discharges (Pearse and Gaydon[87]). Another small additional peak is evident at the tail end of the CN^* (0,2) band and is located around 449.7-nm. This could be part of the 390.0-nm CH^* system, whose main peak (0,0) is at 388.9-nm, since there is a peak from this system at 449.5-nm. Since the 388.9-nm peak would be washed out from the CN^* (0,0) band, it is hard to say with utmost certainty that this is CH^*.

Figure 6.19 shows the spectral data for the 575-750-nm range with the nitrogen feedstock and ethylene fuel at 2000 watts. The most important line in this figure is the monatomic H_α^* line at 656.3-nm. This peak actually shows up in the graph at 651.7-nm due to mis-calibration of the particular channel. Fortunately, there are no other peaks around it, so it is easily identifiable. The H_β^* line is shown in Figure 6.20. This figure shows spectral data in the 400 to 575-nm range with the methane as the torch feedstock and ethylene fuel. The H_β^* line is at 486.1-nm and is more apparent in the methane spectral data, since methane plasma involves the direct dissociation and excitation of hydrogen instead of by indirect means of the ethylene stream, as with the nitrogen plasma.

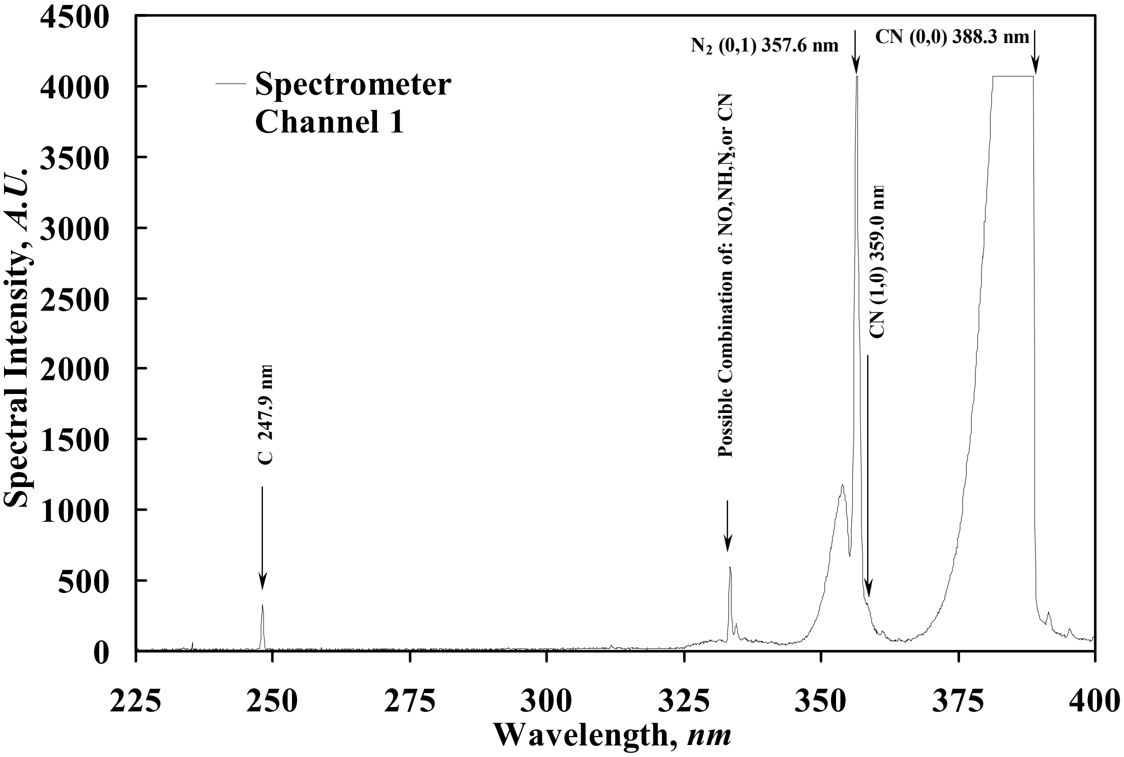

Figure 6.17 Close up of Nitrogen/Ethylene Spectrogram, Spectrometer Channel 1.

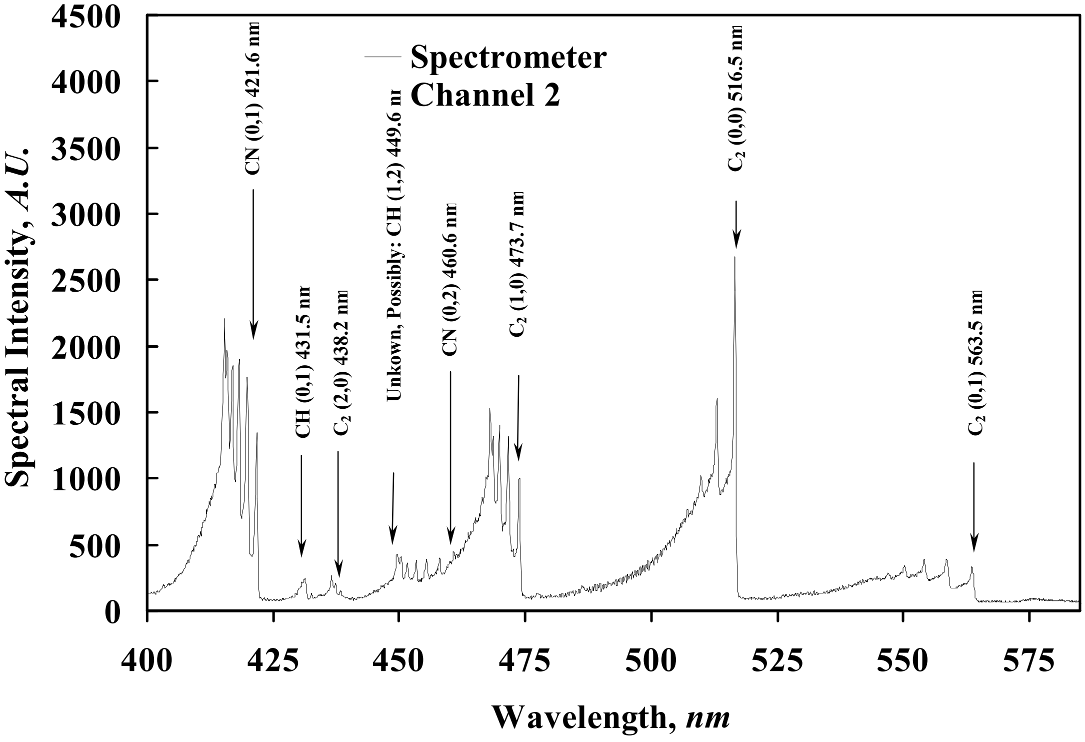

Figure 6.18 Close up of Nitrogen/Ethylene Spectrogram, Spectrometer Channel 2.

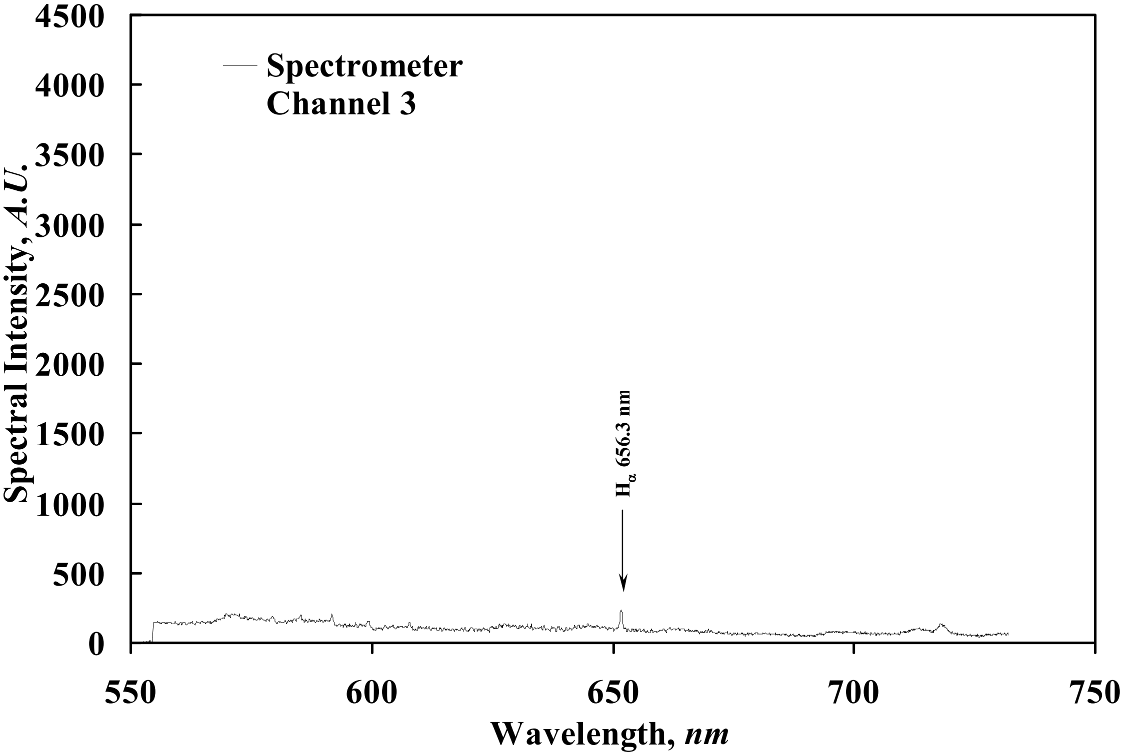

Figure 6.19 Close up of Nitrogen/Ethylene Spectrogram, Spectrometer Channel 3.

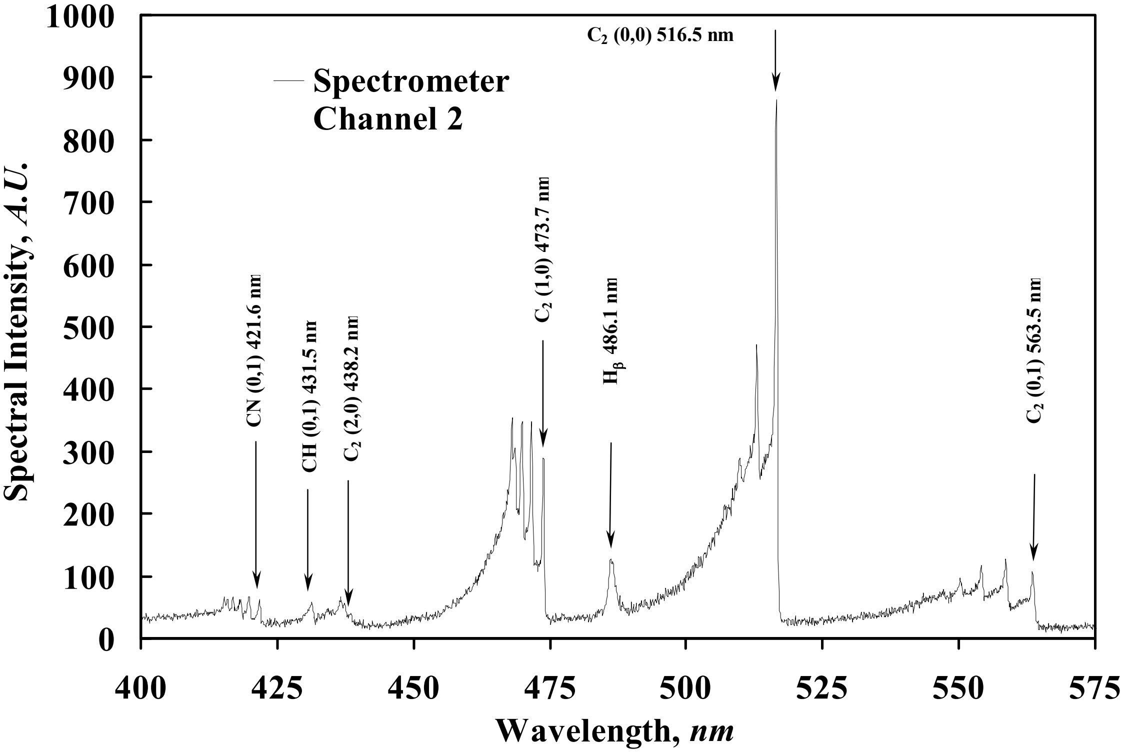

Figure 6.20 Close up of Methane/Ethylene Spectrogram, Spectrometer Channel 2.

The main intensity trends of the spectral line data obtained while using methane and nitrogen feedstocks as a function of torch station relative to the injector array are presented in Figure 6.21 and Figure 6.22. These data points represent the maximum intensity locations of a vertical sweep with the spectrometer placed 1.0-cm downstream from the exit of the torch. During these experiments, the spectrometer had a 0.125-second integration time at each station with a local viewing area with a diameter of 0.5-mm. Due to the location of the fused silica windows relative to the plasma torch, it was necessary to place the spectrometer at a 3-degree angle off the perpendicular to make measurements at torch-station #3. The results show that the torch stations with the brightest spectral line intensities were stations #2 and #1 for nitrogen and methane, respectively. In addition, they show that the spectral line intensities all share the same general trends of variation in intensity as a function of torch location relative to the fuel injector array for the two main feedstocks tested.

More results for the data obtained while using methane and nitrogen feedstocks are presented in Figure 6.23 and Figure 6.24. These figures show the excited C_2^* (0,0) line at 516.5-nm. From the data in the graph in Figure 6.23 with the methane torch feedstock, it is seen that the intensity of the excited C_2^* line with ethylene fuel from the injector and the plasma torch is lower than its intensity from the torch alone. In addition, as the torch is moved further downstream from the fuel injector array, the excited C_2^*concentration falls off and the penetration of the flame into the main fuel plume is diminished. This could mean that the excited C_2^* near the surface is actually from the methane plasma rather than from the ethylene fuel, however further experiments would be necessary to prove this. The experiments with the nitrogen feedstock showed results that are more favorable compared to the methane feedstock in terms of excited C_2^* levels. Because the levels produced by the nitrogen feedstock are higher and since all the C_2^* radicals must come from the interaction of the torch plasma with fuel plume as the only source of carbon is from ethylene, this indicated a higher level of excited species flame propagation in the fuel plume. This could also be interpreted as indicating a higher amount of heat release, which would be required to increase the amount of excited species in the plume. This is illustrated by the increase in C_2^* line intensity and penetration height of the excited species in Figure 6.25 and Figure 6.26.

In addition, there is also evidence of a small concentration of excited hydroxyl radicals in the flame plume as identified by the peaks in Figure 6.27. This figure was generated with the fiber optic spectrometer with its viewing area focused with a collimating lens to a diameter of about 2.0-mm. The spectrometer was focused on a region 1-cm downstream of the plasma torch and 4.5-mm off above the surface with a 1-second integration time. This location corresponds to a normalized vertical distance of 1.03 d_{eff}. The data shown in this picture were for an injector momentum flux ratio of 1.5, with a nitrogen feedstock through the torch at 2000 watts. In the graph, excited hydroxyl peaks are shown at 281.1-and 306.4-nm. The 306.4-nm peak is also masked by several other peaks near its wavelength involving excited nitrogen species, making it hard to see.

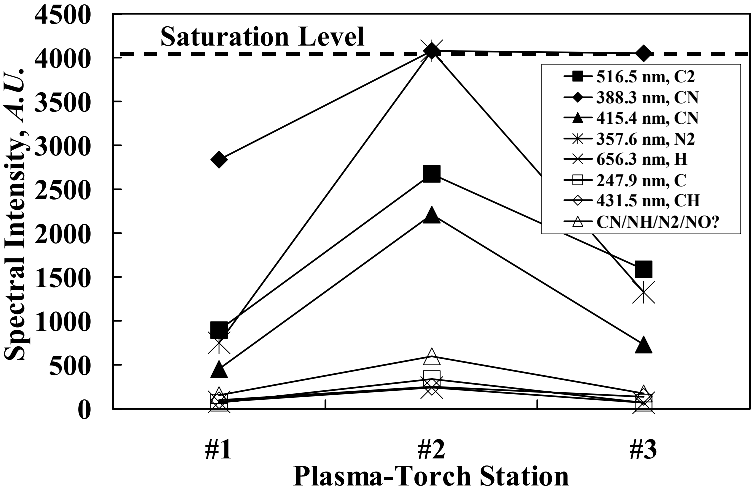

Figure 6.21 Spectral Line Intensity Trends as a function of Plasma Torch Station for Nitrogen Feedstock/Ethylene Fuel at 2000 Watts, $\bar{q}_j = 1.5$, $\bar{q}_T = 1.2$.

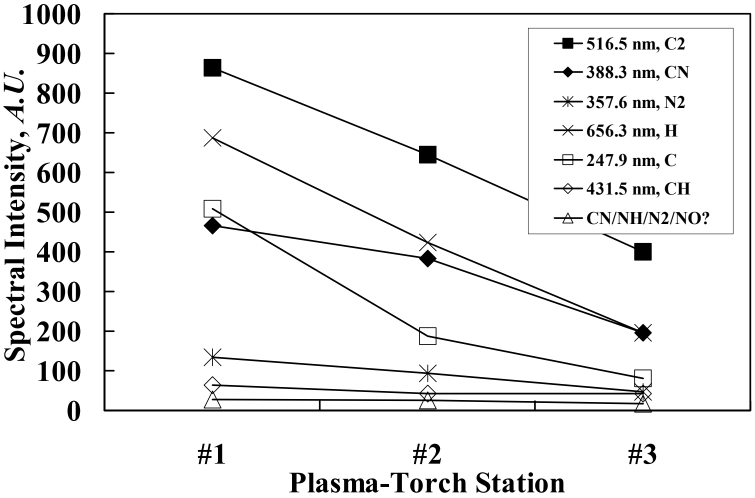

Figure 6.22 Spectral Line Intensity Trends as a function of Plasma Torch Station for Methane Feedstock/Ethylene Fuel at 2000 Watts, $\bar{q}_j = 1.5$, $\bar{q}_T = 1.2$.

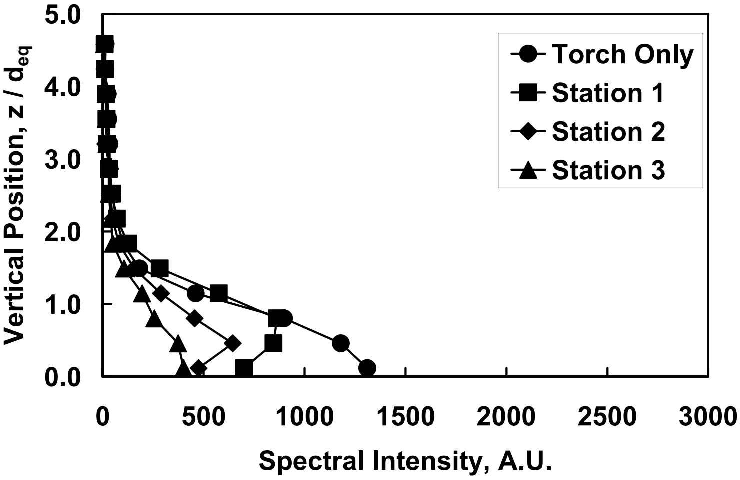

Figure 6.23 C_2^* Line Spectra with a Methane Feedstock and Ethylene Fuel, 2000 Watts, $\overline{q}_j$ = 1.5, $\overline{q}_T$ = 1.2.

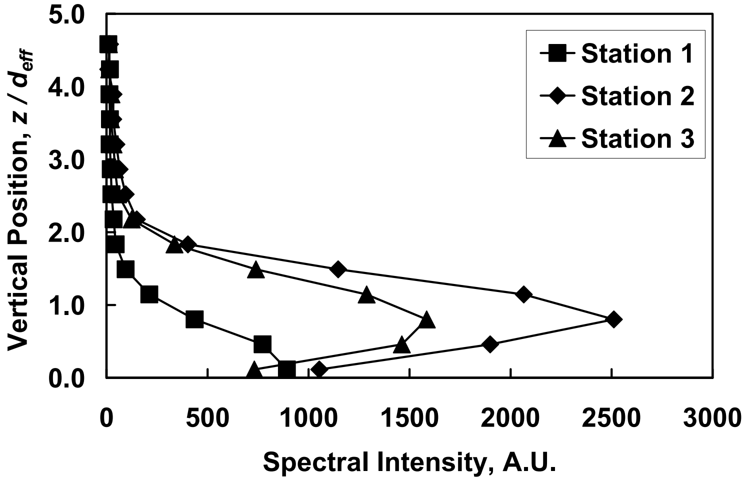

Figure 6.24 C_2^* line Spectra with a Nitrogen Feedstock and Ethylene fuel, 2000 Watts, $\overline{q}_j$ = 1.5, $\overline{q}_T$ = 1.2.

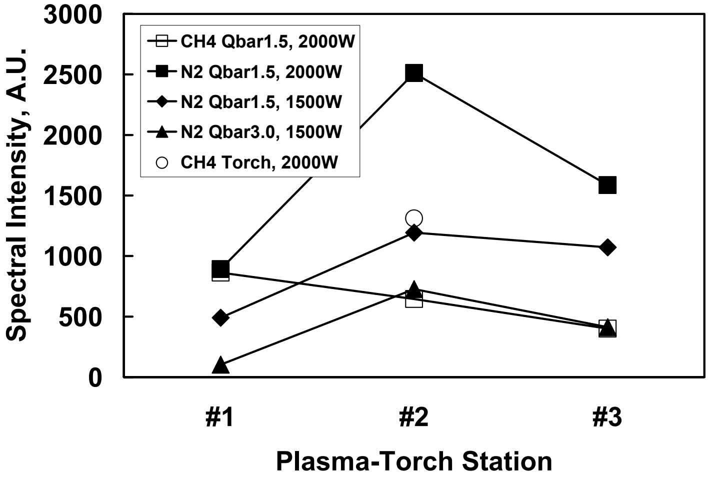

Figure 6.25 Maximum C_2^* Line Intensity Trends. Methane or Nitrogen Feedstocks with Ethylene.

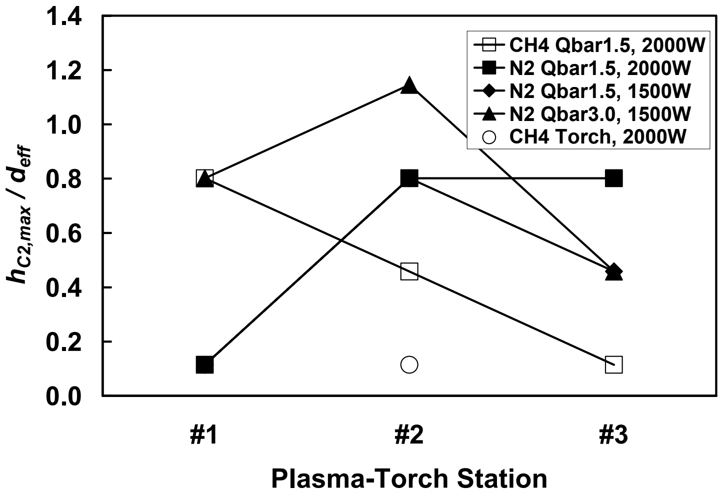

Figure 6.26 Maximum C_2^* Line core penetration height.

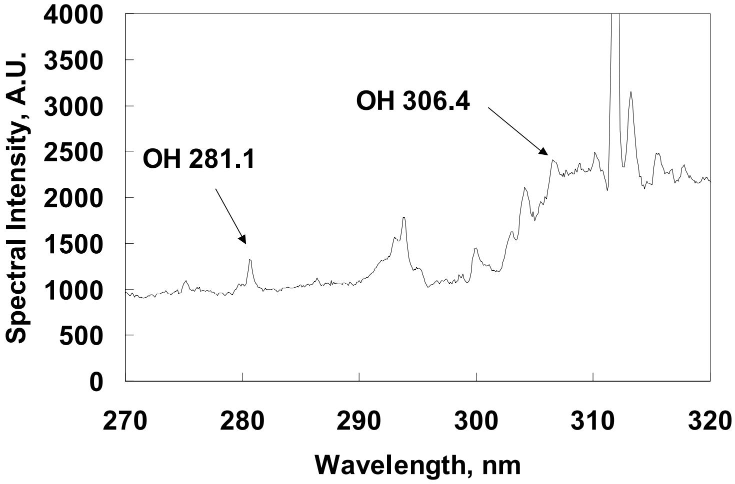

Figure 6.27 Excited Hydroxyl Peaks.

6.1.7 Conclusions

Experiments were performed at Virginia Tech to evaluate a new integrated fuel injection and ignition/flame-holding system consisting of an aerodynamic ramp injector array with ethylene as the injectant and a plasma torch with various feedstocks. The plasma torch was placed at three downstream locations relative to the injector array and was exposed to an unheated Mach 2.4 cross-stream.

Conclusions from the experiments are as follows:

1) There is a lot of unsteadiness in the injector flowfield, as seen in the shadowgraph images. Pulsations from the plasma torch at the right frequency may possibly help to excite the unsteadiness and increase mixing. An estimate of the frequency of the large-scale turbulence structures of the injector plume was made by examination of the sequential high-speed shadowgraph images, and is estimated to be 165 KHz. This estimate takes into account only two-dimensional motion as seen in the shadowgraphs, and does not account for any of the counter rotating vortex motion of the plume.
2) When the plasma torch is operated with a methane feedstock, more exited C_2^* radicals are produced, which penetrate further into the main ethylene fuel jet plume with the torch at the closest station (#1) to the injector in the cases studied. In addition, the configuration

also had the highest intensity level of all the excited species measured with the spectrometer (C^*, H^*, CN^*, N_2^*, and CH^*).

3) Nitrogen, when compared to methane as a plasma torch feedstock used as an igniter gas for an ethylene fuel jet plume, produces more excited C_2^* radicals, indicating more plasma-fuel interactions. These excited species penetrated further into the main fuel plume and created a larger temperature rise associated with a higher level of heat release in the main fuel plume. Nitrogen also produced higher intensities of CH^*, N_2*, CN* and C_2^* than methane, although, methane did produce higher levels of C^* and H^*.
4) When the fuel injector is operated at a momentum flux ratio of 1.5 with nitrogen as the torch feedstock, the torch at the torch-station #2 location produced the highest level of excited C_2^* as measured with the spectrometer at the measurement station 1 cm downstream of the torch orifice. Furthermore, the flame plume pictures show that in this case the excited species penetrated furthest into the main fuel plume. In addition, the configuration also had the highest intensity level of all the excited species measured with the spectrometer (C^*, H^*, CN^*, N_2^*, and CH^*).
5) When the fuel injector is operated at the higher momentum flux ratio studied (3.0) with nitrogen as the torch feedstock, torch station #2 produced the highest amount of excited C_2^* as measured with the spectrometer. It is interesting to note that in the excited flame pictures, the flame plumes produced by placing the torch at stations #2 and #3 look very similar, with the plume at station #3 being slightly larger. However, the flames did flicker a little, and the differences in flame size may be due to this unsteadiness.
6) A small amount of excited hydroxyl (OH^*) was measured with the spectrometer in the flame plumes using nitrogen as the torch feedstock. OH^* is an important chain branching intermediate reaction in the overall reaction of hydrogen-based fuels with air, such as ethylene. This is important, because it means that as the temperature is raised, as in a high temperature environment such as a scramjet combustor, there is a good chance for the flammability limits to be reached in a larger region near the plasma torch fuel-jet interface and increased flame propagation to occur.

6.2 Hot Flow Tests: Design of Model for AFRL Combustor

The last step in this project involved the design and fabrication of a multi-fuel-injector test article for future combustion experiments at the Air Force Research Labs, AFRL. The model designed was conceived as a replacement injector configuration for the AFRL baseline injector configuration that consists of a row of four laterally spaced 15-deg downstream angled holes with a downstream cavity for flame-holding purposes. A drawing of the AFRL configuration is shown in Figure 6.28. In this figure, the tunnel flow would be from left to right. The four 15-deg single holes are shown to the left of the model and two locations for sparkplugs are shown as the circles in the cavity on the right hand side of the model.

The injector model and plasma torches designed for comparison to the baseline model is shown in Figure 6.29. This model consists of four aero-ramp injectors with variable downstream locations for plasma torches behind each one. Due to geometrical constraints, the lateral spacing between the aero-ramp injectors, 35.6-mm, was slightly smaller than the AFRL baseline injector spacing of 38.1-mm. The design allows for as many as four plasma torches operating at the same time, either close to the array in the best location found for the torches in operation with a nitrogen feedstock, or further downstream in a location equivalent to the positions of the spark plugs in the baseline configuration. Variable position inserts were also created at the two middle injectors front torch location. This was done to allow two of the torches to be at the best location found with the methane feedstock.

An aero-ramp injector block with four main injectors was also created for use with the AFRL baseline cavity combustor configuration. This injector block, which is shown in Figure 6.30, was constructed for comparison of the aero-ramps primary ignition mechanism: a cavity or a plasma torch. This also allows a closer comparison to the integrated plasma torch ignition system configuration without the mismatched type of injectors in the AFRL baseline.

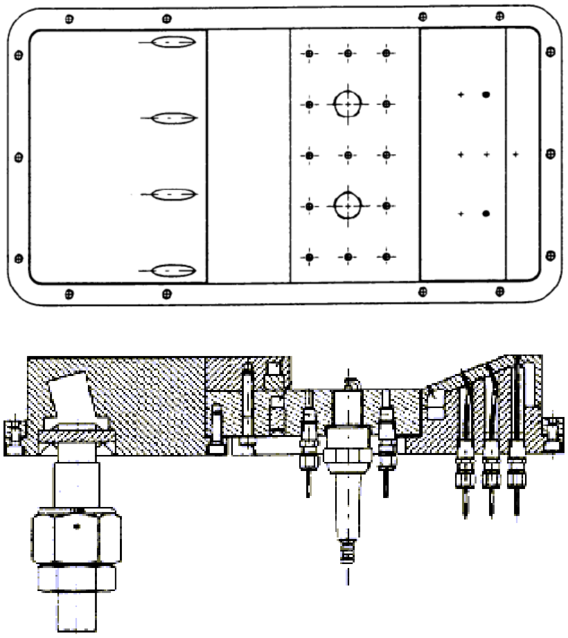

Figure 6.28 AFRL Baseline Injector Model.

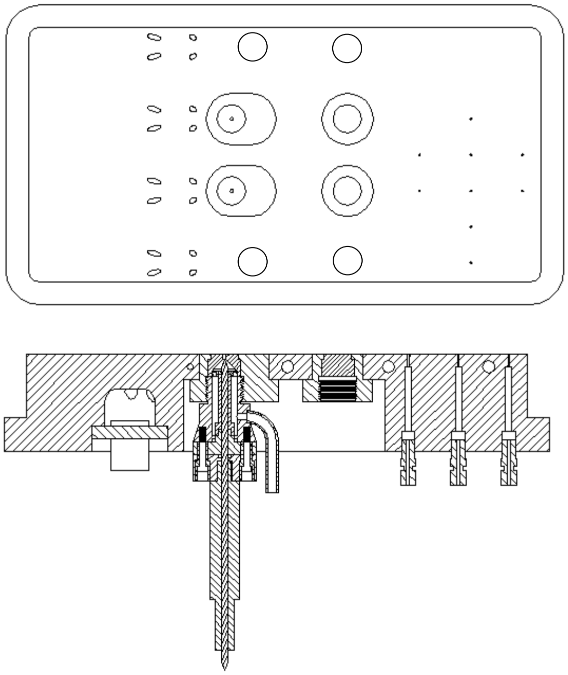

Figure 6.29 Integrated Injector/Igniter Prototype Combustor Model.

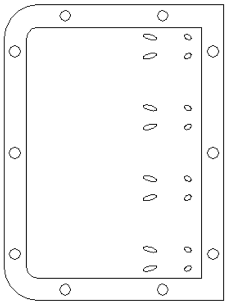

Figure 6.30 Aero-Ramp Injector Block for Cavity Configuration.

Chapter 7 Conclusions and Recommendations

The first integrated, flush-wall, aero-ramp-injector/plasma-torch-igniter and flame propagation system for supersonic combustion applications with hydrocarbon fuels was developed and tested. This device is intended to create a flame holding region by manipulating the combustor flow field such that flame propagation is possible by using the geometry of a flush walled injector itself. The main goal of this project was to develop a device that could demonstrate that the correct placement of a plasma torch igniter/flame-holder in the wake of the fuel jets of an aero-ramp injector array could make sustained, efficient supersonic combustion with low losses and thermal loading possible in a high enthalpy flow. Three phases of research were performed.

The first phase of the research effort was a component analysis to improve on the designs of the aero-ramp and plasma torch as well as address integration and incorporation difficulties. The first of these studies involved a qualitative investigation with shadowgraphs and surface oil flow visualization into the incorporation of two simulated plasma torches into the downstream end of a nine-hole aero-ramp injector array in a Mach 3.0 flow. Experiments were performed at a nominal jet to freestream momentum flux ratio of 2 at a freestream static pressure and temperature of 0.17 atm and 103 K. This design showed some promising features, and the removal of the middle injector hole between the two simulated plasma torches reduced the large recirculating area between the second and third rows of injector holes. This reduction of the separation zone could be seen especially well in the surface oil flow visualization experiments. By removal of the hole between the two simulated plasma torches, the buildup of paint between the second and third row (simulated plasma torch holes) of main plume then had a channel to flow through between the two torches. The nine- and eight-hole configurations had some benefits, such as the high unsteadiness shown by the shadowgraph images, which should be good for mixing. Unfortunately, the complexity of a system working with two closely spaced plasma torches plus the additional operating costs of running two plasma torches per aero-ramp injector in a multiple injector combustor makes this concept less attractive. It was concluded that a simpler system with one plasma torch would be more desirable and that further reduction of the number of holes in the aero-ramp array should be considered.

The downstream transverse injection angle of a plasma torch igniter operating alone, with methane as the torch feedstock, was also investigated for integration purposes during the first phase of the project. During this set of experiments, a 45-deg transversely mounted plasma torch was compared to a 90-deg configuration in a cold flow supersonic environment. The primary experimental methods used during this study consisted of shadowgraphs and total temperature sampling at a downstream location to examine the shapes of the plumes and to assess the possibility of heat release in the 0.19 atm, 101 K, Mach 3.0 flow. Experiments with the plasma torch in operation in a Mach 2.4 flow were also conducted with 90- and 60-deg transversely mounted plasma torches at 0.26 atm and 131 K. The 60-deg configuration was tested, because it was felt at the time that it was too complicated to incorporate the existing 45-deg plasma torch into an integrated configuration in the Virginia Tech supersonic wind tunnel.

Results from the experiments at Mach 3.0 showed that the plasma torch temperature plume from the 45-deg anode configuration was significantly hotter and the temperature plume core penetrated further into the freestream than the plume produced by the 90-deg case. This was seen in the downstream total temperature profiles of the plumes with heat addition from the torch in operation at about 1500-watts with the methane feedstock. Ultimately, it was discovered that in terms of plume core temperature maximums, a relatively new 45-deg arrangement worked better than the 90-deg arrangement, but as the electrodes eroded, the performance dropped below the 90-deg configuration. This was also seen by the total temperature centerline profiles. Therefore, what one had was a design problem that may require the need for active cooling or better material selection.

Results from the Mach 2.4 experiments found with the comparison of a 90-deg configuration to the 60-deg case, that the 90-deg case produced hotter temperature cores that the 60-deg one. Originally, the 60-deg configuration was a compromise, to try to hopefully keep some of the advantages of the 45-deg configuration. Contrary to the Mach 3.0 experiments, the 90-deg case performed better than the 60-deg configuration. However, since there are many factors involved in the differences in the two studies, for example, higher static pressure and temperature, and the possibility of electrode erosion distorting the performance of the plasma torch, more experiments should be performed. Since the 45-deg configuration was not tested in the Mach 2.4 flow, we are left only to speculate over the potential advantage (if any) over the 90-deg configuration. To more accurately determine if there is any potential to having a 45-deg configuration over the 90-

deg configuration, further experiments are recommended. In addition, to more clearly estimate the repeatability of the performance of the electrodes, a condition tested should be repeated at least three to five times with new pairs of electrodes and then with various amounts of degradation to the electrodes (repeated back to back runs).

The information learned from these experiments plus additional results from two other documented experiments (Appendices B and C) in this phase lead to the creation of the first prototype integrated aero-ramp/plasma-torch design featuring a new simplified four-hole aero-ramp. This design incorporated many of the features and conclusions obtained from the experimental investigations performed in this body of work. Two of these features were high toe-in angles and transverse-angled plasma torch injection. Further, the position of the torch was moved to the centerline in an effort to capitalize on the potential of a single-torch injector configuration.

The second phase of the project consisted of a cold flow mixing evaluation of the new design at Mach 2.4 and a resizing of the device for incorporation into a scramjet flow path test rig at the Air Force research laboratories (AFRL), which has a combustor entrance Mach number of 2.2. The evaluation of the first prototype design in the Virginia Tech supersonic wind tunnel at Mach 2.4 at a freestream static pressure and temperature of 0.25 atm and 131 K, consisted of shadowgraphs, surface oil flow visualization, and downstream aerothermodynamic sampling experiments. By comparing downstream total temperature profiles while injecting heated and ambient air through the injector, a new mixing analogy parameter was created to assess the mixing potential of this new device. The new approach proved to be quite useful and it was used to estimate the mass fraction distribution from the aero-ramp injector.

The injector produced a large pair of counter rotating vortices and two plume cores as seen in the mixing analogy profiles described above. The vortex structures shown in the mixing analogy profiles, along with the surface oil flow visualization pictures and results from the PSP experiments suggest that this four-hole aero-ramp created a strong pair of jet vortices by directing the flow around the array, similar to the way a physical ramp injector does. This redirection of the flow around the aero-ramp could be seen in the surface oil flow visualization pictures by the direction of travel of the oil around the injector and its movement towards the centerline downstream of the injector orifices. The effects of this redirection could be seen by the shape of the mixing analogy plume cores, which resembled the plume of a physical ramp injector more than the original nine-hole aero-ramp as seen in R. Fuller[84]. The high toe-in angles effectively turned in the injectant towards the center of the array to make the aero-ramp look more like a physical ramp. Further, there was no secondary plume core trapped in the boundary layer, which in itself is an improvement over the original nine-hole design.

Next, the aero-ramp injector was sized to fit in an existing AFRL combustor for comparison to one of the injectors used in the combustor baseline configuration. This design was also evaluated at Mach 2.4. To document the performance of the injector, shadowgraph images at various momentum flux ratios were taken, and pressure-sensitive paint (PSP) was used to help quantitatively understand the nature of the flows. Further, aerothermodynamic sampling was performed to quantify the pressure losses and mixing potential of the new aero-ramp injector via the new mixing analogy.

The new mixing analogy was used extensively to document the mixing performance of the new larger-scale four-hole aero-ramp in comparison to a single, low-downstream angled hole as used at the AFRL. Results showed the aero-ramp to mix at a considerably faster rate than the single-hole injector due to high levels of vorticity created by the injector array. This was seen in the mixing analogy concentration profiles. Though the injector mixing performance was very good, the plume produced slightly higher pressure losses and did not penetrate as high as the single-hole beyond the immediate downstream region near the array. This is somewhat to be expected, since high levels of vorticity, which are good for mixing, are bad for entropy production. Further, the overall composite downstream angle of the aero-ramp injector was over twice the angle of the single-hole injector. This difference alone will cause higher losses to occur in a supersonic flow, since injection at a higher angle relative to the freestream will create higher shock angles, and larger total pressure losses.

The array was designed with a high cross-stream spacing arrangement created with the intention of providing a leaner, larger area of shelter behind the injector plume with a relatively low velocity for the aid of ignition and combustion with a plasma torch. The combination of high cross-stream spacing and toe-in created a large separation zone on the injector centerline behind the last row of jet, as seen by surface oil flow in the small array (first prototype) and the low pressure locations in the PSP measurements in the above mentioned region. Since this region is downstream of the array, it is a low pressure expansion region, however as the torch jet was moved closer to the array, the high pressure region in front of the torch separation zone merged with the back injector separation zone. This effectively raised the overall pressure in that zone. Though the pressure rise was not too large, the additional pressure rise that the plasma torch hole would create if it were operational might help to raise the pressure in this zone even more, which would tend to create a base for the flame to originate and hopefully propagate downstream in a hot-flow environment.

It is important to realize that the four-hole aerodynamic ramp injector was designed by the study of parametric tends associated with the toe-in angle and swirl (See Appendices B and C), along with various other nine-hole aero-ramp studies, mainly involving CFD (Cox et al.[46], Cox-Stouffer and Gruber[47,48,49], R. Fuller et al.[50], and Schetz et al.[51]). The existing injector model is not formally optimized, however many of the features were selected to enhance its performance based on results from the similar studies listed above. In an effort to further improve the performance of the array, several main parameters should be investigated. Reducing the transverse injection angles of the injector array may help to reduce the total pressure losses incurred by the injection process and may also help to improve the overall penetration of the injector jet. One may want to create and test an aero-ramp injector with the same overall injection angle as the single-hole 15-deg downstream angled injector or one where all four holes have 15-deg transverse angles. If one wanted to increase the penetration performance of the device, reducing the cross-stream spacing of the injector holes or increasing the toe-in angles of the array might be tried. The high toe-in angles of the jet are thought to be the reason for the counter-rotating pair of jet vortices in the plumes. This general behavior has been seen in the earlier toe-in studies, listed in Appendix B. The high toe-in angles of the four-hole array are also thought to increase the mixing efficiency of the main plume and lift the plume off the wall. Though increasing the mixing efficiency with toe-in should not be taken for granted just yet. It was found in earlier CFD studies (Cox-Stouffer and Gruber[48]), with a nine-hole aero-ramp array with a smaller cross stream spacing, that toe-in of the outer jets caused the array to mix slower than an array with no toe-in at all. This seems to be contradictory to the experimental data taken in the toe-in study of Appendix B, however, the mixing analogy as defined by equation 5.1 did not exist at the time of this study and an earlier form was used which did not take into account the distortion of the concentration plume due to vorticity. Thus, more experiments should be performed to quantify the mixing field created by toe-in in an array injector. In addition, these experiments should not only attempt to quantify the mixing field with the new mixing analogy, but should also try to directly measure the concentration of the injectant by sampling. This would help to validate the existing mixing analogy model, or help to create a better one based on experimental results. There are several ways to quantify the mixing flow field. Note that the mixing analogy can also be derived in the same fashion for a flowfield with two different gases. One could inject nitrogen, or air with a trace of helium as in Tomioka et al.[44], a trace of NO_x or a hydrocarbon, or even straight ethylene fuel, if one did not have to deal with safely regulations.

There are several ways to measure the concentrations. For example, Raman scattering laser techniques can detect the concentration of ethylene or nitrogen, a helium concentration sampling probe can be used to deduce the local concentration of helium in air, and there are also direct sampling systems that can detect trace amounts of hydrocarbon fuels or NO_x down to a few parts per million.

The last phase of the research done in this project involved testing the final device design in a cold-flow environment at Mach 2.4 with hydrocarbon fuels and various torch feedstocks. Test conditions consisted of freestream static pressure and temperatures of 0.26 atm and 131 K, and injector and plasma-torch jet to freestream ratios of 1.4 – 3.3, and 1.2, respectively. Shadowgraph images were taken, and PSP was used to help understand the flowfield. Total temperature probing and spectroscopy were also performed at downstream locations with the torch in operation behind the ethylene fueled aero-ramp injector to help quantify differences in plasma torch effectiveness as a potential igniter. The main feedstocks studied were methane and nitrogen with minor additional work being performed with air and a nitrogen/hydrogen mixture. Three downstream plasma torch locations were tried in relation to the aero-ramp injector array, and regions where flame ignition and propagation would be likely were identified for the various torch feedstocks tested.

Of the main torch feedstocks studied, nitrogen was the most promising, as it produced the brightest visible flame with the highest penetration. Nitrogen also produced a hotter downstream plume as seen in the downstream total temperature profiles at each plasma torch location studied. In addition, nitrogen produced more excited species as observed with a spectrometer. This was shown by the spectral data of the C_2^* line, which gives an indicator of the flame plume location. This follows the assumption that an increase in excited species will help create a larger flame in a hot-flow environment. Though C_2^* is not an indicator associated directly with enhanced combustion, it is a good indicator of the overall excited region of the plume. This makes the C_2^*

line data useful in that the proper placement of the plasma torch excited species plume in relation to the main injector fuel plume should help drive the ignition process throughout the flowfield in a hot-flow combustor. Thus, the torch location with the highest level of excited species created from the fuel/air/plasma interface has the best chance of ignition if used in a hot-flow environment.

Of all the feedstocks studied, air produced the largest visible plume. Unfortunately, that plume came with a high electrode erosion cost, making air a poor choice for long-duration operation with the plasma torch in its current form.

A small amount of excited hydroxyl (OH^*) was measured with the spectrometer in the flame plumes using nitrogen as the torch feedstock. OH^* is an important chain branching intermediate reaction in the overall reaction of hydrogen-based fuels with air, such as ethylene. This is important because it means, that as the temperature is raised, as in a high temperature environment such as a scramjet combustor, there is a good chance for the flammability limits to be reached in a larger region near the plasma torch fuel-jet interface and increased flame propagation to occur. With increasing temperature, the flammability limits of the fuel air mixture will also increase; this will lead to a larger portion of the plume with the potential for ignition and flame propagation. With a concentration of OH^* inside this region, the overall reaction will have a better chance at propagation without being quenched due to an insufficient temperature level. This is because chain branching is a crucial and necessary step in the overall reaction and it helps to increase the overall reaction rate, which will need to be as fast as possible to allow the reaction to produce enough heat inside the flammability zone to self propagate. Thus, it is good to see a little OH^* in these cold, low-pressure conditions, because it implies that there is a potential for ignition and sustained combustion at higher temperatures.

In order to assess any possible advantages a radical producing plasma torch igniter may have over a more conventional sparkplug or pilot flame, additional experiments should be also be performed. These tests should include judging the igniter performance, power requirements, and durability. One should also take into account in the figures of merit the additional complexity of a pilot flame, in that it must also use an oxidizer. Therefore, it must store or generate what it requires, as must a plasma torch, if it does not use the fuel of the engine as its feedstock. The present results with the integrated configuration with methane as the torch feedstock suggest that experiments should be performed with the plasma torch in front of the aero-ramp array. Since the methane feedstock, as well as ethylene (not reported in this study), produced substantially higher temperature cores and excited species when exposed directly to the freestream.

The phase-three cold flow reactive mixture tests lead to the design and creation of a fuel injector block for near future testing in the scramjet combustor at the AFRL. This injector configuration was designed primarily for use with plasma torches in operation with nitrogen as the feedstock. Nitrogen was selected because of its observed higher performance levels over methane and the operational advantages over the air feedstock. The fuel injector block consists of four aero-ramp injector/igniter modules spaced evenly across the combustor test section. An additional injector block was also created consisting of four aero-ramp injectors alone. This configuration was designed for use with the cavity of the AFRL baseline injector configuration for more direct comparison to the integrated configurations combustion performance.

With the completion of this design, the first integrated fuel injection and ignition system for use with hydrocarbon fuels in supersonic flow has been created. It is hoped that this new type of design, which does not include any intrusive flame holding devices, may help to pave the way for the next generation of scramjet combustor fuel injection/ignition systems. These systems will need to mix faster and propagate the flame throughout the combustor more evenly, with fewer losses incurred by the system. This is an exciting time in the development of the scramjet engine. With the launch of the first operational scramjet engine, the Hyper-X, just weeks away at the time of this document, the world is looking to see if it will be a success. Regardless of the outcome, there is an increasing need for the development of hypersonic propulsion systems, as there is a growing need for cost reduction of the price to access space.

References

---

[1] Heiser, W.H., Pratt, D.T., Daley, D.H., and Mehta, U.B., "Hypersonic Airbreathing Propulsion," AIAA education series, Przemieniecki, J.S. (Edit.) AIAA, Washington, D.C., 1994.

[2] Scherrer, D., Dessornes, O., Montmayeur, N., and Ferrandon, O., "Injection Studies in the French Hypersonic Technology Program," AIAA Paper 95-6096, April 3-7, 1995.

[3] Bouchez, M., Montmayeur, N., Leboucher, C., and Souchet, M., "Scramjet Combustor design in France," AIAA Paper 95-6094, April 3-7, 1995.

[4] Kanda, T., Sunami, T., Tomioka, S., Tani, K., and Mitani, T., "Mach 8 Testing of a Scramjet Model," *Journal of Propulsion and Power*, Vol. 17, No. 1, January-February 2001.

[5] Tomioka, S., Murakami, A., Kudo, K., and Mitani, T., "Combustion Tests of a Staged Supersonic Combustor with a Strut," *Journal of Propulsion and Power*, Vol. 17, No. 2, pp. 293-300, March-April 2001.

[6] Mitani, T., Chinzei, N., and Kanda T., "Reaction and Mixing Controlled Combustion in Scramjet Engines," *Journal of Propulsion and Power*, Vol. 17, No. 2, pp. 308-314, March-April 2001.

[7] Wendt, M., Stalker, R., and Jacobs, P., "Effect of Fuel Temperature on Supersonic Combustion," AIAA Paper 95-6029, April 3-7, 1995.

[8] Situ, M., Sun, Y., Zhang, S., and Wang, C., "Investigation of Supersonic Combustion of Hydrocarbon Fuel-Riched Hot Gas in Scramjet Combustor," AIAA Paper 99-2245, June 20-24, 1999.

[9] Li, J., Yu, G., Zhang, X., and Huang, Q., "Combustion of Kerosene in a Supersonic Stream," AIAA-Paper 2000-0615, January 10-13, 2000.

[10] Yu, G., Li., J., Zhang, X., and Chen, L., "Investigation on Combustion Characteristics of Kerosene-Hydrogen Dual Fuel in a Supersonic Combustor," AIAA Paper 2000-3620, July 17-19, 2000.

[11] Lee, S., Kim, Y., and Mitani, T., "Mixing Augmentation of Transverse Injection in Scramjet Injection in Scramjet Combustor," AIAA Paper 2000-0090, January 10-13, 2000.

[12] Moon, G., Jeung, I., and Choi, J., "Numerical Study of Thermal Choking Processes in a Model SCRamjet Engine," AIAA Paper 2000-3706, July 17-19, 2000.

---

[13] Baev, V., Shumski, V., and Yaroslavtsev, M., "Pressure Distribution and Heat Exchange in a Gas Dynamic Model with Combustion over which a High Enthalpy Air Stream Flows," Novosiborsk, Translated from *Zhurnal Prikladnoi Mekhanki i Tekhnicheskoi Fiziki*, No. 5, pp56-65, September-October, 1985.

[14] Zvegintsev, V.I., "Experimental Studies of Aerodynamic Performances of Hypersonic Scramjet in Impulse Hot-Shot Tunnel," AIAA Paper 93-2446, June 28-30, 1993.

[15] Roudakov, A., Semenov, V., and Hicks, J., "Recent Flight Test Results of the Joint CIAM-NASA Mach 6.5 Scramjet Flight Program," AIAA Paper 98-1643, April 27-30, 1998.

[16] Thomas, S., Perkins, H., and Trefny, C., "Evaluation of an Ejector Ramjet Based Propulsion System for Air-Breathing Hypersonic Flight," NASA TM-107422, April 14-17, 1997.

[17] Georgiadis, N., Walker, J., and Trefny, C., "Parametric Studies of the Ejector Process within a Turbine-Based Combined Cycle Propulsion System," AIAA Paper 98-0936, January 12-15, 1998.

[18] Trefny, C., "An Air-Breathing Launch Vehicle Concept for Single-Stage-to-Orbit," AIAA Paper 99-2730, June 20-23, 1999.

[19] Taguchi, H., Maita, M., Yatsuyangi, N., and Yamanaka, T., "Airbreather / Rocket Combined Propulsion System Research for Japanese SSTO Spaceplane," AIAA Paper 99-4811, 1999.

[20] Hunt, J.L., and Eiswirth E.A., "NASA's Dual-Fuel Airbreathing Hypersonic Vehicle Study," AIAA Paper 96-4591, November 18-22, 1996.

[21] Siebenhaar, A., Campbell, B., and Nguyen, T., "Strutjet Engine Performance," AIAA Paper 99-4809, 1999.

[22] Faulkner, R., and Weber, J., "Hydrocarbon Scramjet Propulsion System Development, Demonstration, and Application," AIAA Paper 99-4922, November 1-5, 1999.

[23] McClinton, C.R., Hunt, J.L., Ricketts, R.H., Reukauf, P., and Peddie, C.L., "Airbreathing Hypersonic Technology Vision Vehicles and Development Dreams," AIAA Paper 99-4978, November 1-5, 1999.

[24] Tishkoff, J.M., Drummond, J.P., and Edwards, T., "Future Direction of Combustion Research: Air Force/NASA Workshop on Supersonic Combustion," Reno, Nevada: AIAA Paper 97-1017, January 6-9, 1997

[25] Hartfield, R.J., Hollo, S.D., and McDaniel, J.C., "Experimental Investigations of a Supersonic Swept Ramp Injector using Laser Induced Iodine Fluorescence," *Journal of Propulsion and Power*, Vol. 10 No. 1, 1994, pp. 129-135, January-February.

[26] Riggins, D.W. and Vitt, P.H., "Vortex Generation and Mixing in Three-Dimensional Supersonic Combustors," *Journal of Propulsion and Power*, Vol. 11, No. 3, 1995, pp. 419-426, May-June.

[27] Schetz, J.A., "Interaction Shock Shape for Transverse Injection," *Journal of Spacecraft and Rockets*, Vol. 7, No. 2, pp.143-149, February 1970.

[28] Rogers, R.C., "A Study of the Mixing of Hydrogen Injected Normal to a Supersonic Airstream," NASA TN L-7386, Langley Research Center, March 1971.

[29] Schetz, J.A., Thomas, R.H., and Billig, F.S., "Mixing of Transverse Jets and Wall Jets in Supersonic Flow," IUTAM Symposium on Separated Flows and Jets, Novosibirsk, July 1990.

[30] Mays, R.B. Thomas, R.H., and Schetz, J.A., "Low Angle Injection into a Supersonic Flow," AIAA Paper 89-2461, July 1989.

[31] McClinton, C.R., "The effect of Injection Angle on the Interaction Between Sonic Secondary Jets and a Supersonic Freestream," NASA TND-6669, February 1972.

[32] Fuller, E.J., Mays, R.B., Thomas, R.H., and Schetz, J.A., "Mixing Studies of Helium in Air at Mach 6," AIAA Paper 91-2268, June 1991.

[33] Fuller, E.J., Thomas, R.H., and Schetz, J.A., "Effects of Yaw on Low Angle Injection into a Supersonic Flow," AIAA Paper 91-0014, January 1991.

[34] Lewis, D.P. and Schetz, J.A., "Tangential Injection from Overlaid Slots into a Supersonic Stream," *Journal of Propulsion and Power*, Vol. 13, No. 1, , pp. 59-63, January-February 1997.

[35] Schetz, J.A., Billig, F.S., Favin, S., and Gilreath, H.E., "Effects of Pressure Mismatch on Slot Injection in a Supersonic Flow," *International Journal of Turbo and jet Engines*, Vol. 9, No. 2, 1992, pp. 135-146.

[36] Spaid, F.W. and Cassel, L.A., "Aerodynamic Interference induced by Reaction Controls," AGARD-AG-173, Dec. 1973.

[37] Jacobsen, L. J., Schetz, J. A., Gallimore, S. D., and O'Brien, W. F., "Mixing enhancement by Jet Swirl in a Multiport Injector Array in Supersonic Flow," FEDSM99-7248, July 1999.

[38] Kraus, D. K., and Cutler, A. D., "Mixing of Swirling Jets in a Supersonic Duct Flow," *Journal of Propulsion and Power*, Vol. 12, No. 1, 1996, pp. 170-177, January-February.

---

[39] Cutler, A. D., and Johnson C. H., "The Use of Swirling Jet Pairs to Provide Rapid Fuel Penetration in Scramjet Combustors," AIAA Paper 95-0099.

[40] Schetz, J.A., "Injection and Mixing in a Turbulent Flow," AIAA, New York, New York, 1980.

[41] Povinelli, L.A. and Ehlers, R.C., "Swirling Base Injection for Supersonic Combustion Ramjets," *AIAA Journal*, Vol. 10 No. 9, pp. 1243-1244, September 1972.

[42] Schetz, J.A. and Swanson R.C., "Turbulent jet Mixing at High Supersonic Speeds," *Zeitschrift Für Flugwissenschaften*, Vol.21, pp.166-173, 1973.

[43] Barber, M.J., Roe, L.A., and Schetz, J.A., "Simulated Fuel Injection Through a Wedge Shaped Orifice in a Supersonic Flow, " AIAA Paper 95-2559, July 1995.

[44] Tomioka, S., Jacobsen, L.S., and Schetz, J.A., "Interaction between a Supersonic Airstream and a Sonic Jet Injected through a Diamond-shaped Orifice," AIAA Paper 2000-0088, January 10-13, 2000.

[45] Tomioka, S., Jacobsen, L.S., and Schetz, J.A., "Angled Injection through Diamond-shaped Orifices into a supersonic Stream" AIAA Paper 2001-1762, April 24-27, 2001.

[46] Cox, S.K., Fuller, R.P., and Schetz, J.A., "Vortical Interactions Generated By a Injector Array to Enhance Mixing in a Supersonic Flow," AIAA Paper 94-0708, January 1994.

[47] Cox-Stouffer, S.K. and Gruber, M.R., "Effects of Spanwise Injector Spacing on Mixing Characteristics of Aerodynamic Ramp Injectors," AIAA Paper 98-3272, July 1998.

[48] Cox-Stouffer, S.K. and Gruber, M.R., "Effects of Injector Yaw on Mixing Characteristics of Aerodynamic Ramp Injectors," AIAA Paper 99-0086, January 1999.

[49] Cox-Stouffer, S.K. and Gruber, M.R., "Further Investigations of the Effects of Aerodynamic Ramp Design Upon Mixing Characteristics," AIAA Paper 99-2238, July 1999.

[50] Fuller R.P., Nejad, A.S., and Schetz, J.A., "Fuel-Vortex interactions For Enhanced mixing in Supersonic Flow," AIAA Paper 96-2661, July 1996.

[51] Schetz, J.A., Cox-Stouffer, S.K., and Fuller, R.P., "Integrated CFD and Experimental Studies of Complex Injectors In Supersonic Flows (Invited)," AIAA Paper 98-2780, June 1998.

[52] Jacobsen, L.J., Schetz, J.A., and Ng, W.F., "The Flowfield Near a Multiport Injector Array in a Supersonic Flow," *Journal of Propulsion and Power*, Vol. 16, No. 2, pp. 216-226, March-April, 2000.

[53] Eklund, D. R., and Gruber, M. R., "Study of a Supersonic Combustor Employing an Aerodynamic Ramp Pilot Injector," AIAA Paper 99-2249, June 1999.

---

[54] Gruber, M., Donbar, J., Jackson, T., Mathur, T., Eklund, D., and Billig, F., "Performance of an Aerodynamic Ramp Fuel Injector in a Scramjet Combustor," AIAA Paper 2000-3708, July 2000.

[55] Baurle, R.A., and Gruber, M.R., "A Study of Recessed Cavity Flows for Supersonic Combustion Applications," AIAA Paper 98-0938, January 1998.

[56] Ben-Yakar, A., and Hanson, R., "Cavity Flameholders for Ignition and Flame Stabilization in Scramjets: Review and Experimental Study," AIAA Paper 98-3122, July 1998.

[57] Mathur, T., Streby, G., Gruber, M., Jackson, K., Donbar, J., Donaldson, W., Jackson, T., Smith, C., and Billig, F., "Supersonic Combustion Experimetns with a Cavity Based Fuel Injector," AIAA Paper 99-2102.

[58] Gruber, M., Jackson, K., Mathur, T., Billig, F., "Experiments with a Cavity-Based Fuel Injector for Scramjet Applications," ISABE Paper 99-7154, 1999.

[59] Wagner, T., O'Brien, W., Northam, G., and Eggers, J., "Deign and Evaluation of a New Injector Configuration for Supersonic Combustion," *Proceedings of the 8th International Symposium on Air Breathing Engines*, pp. 390-397, 1987.

[60] Sato, Y., Sayama, M., Masuya, G., Komuro, T., Kudou, K., Murakami, A., Tani, K., and Chinzei, N., "Experimental Study on Autoignition in Scramjet Combustor," *Journal of Propulsion*, Vol. 7, No. 5, Setember-October, 1991.

[61] Tomioka, S., Hiraiwa, T., Mitani, T., Zamma, Y., Shiba, H., and Masuya, G., cAuto Ignition in a Supersonic Combustor with Perpendicular injection Behind Backward-Facing Step," AIAA Paper 97-2889, July 6-9, 1997.

[62] Rogers, R., Capriotti, D., and Guy, R., "Experimental Supersonic Combustion Research at NASA Langley," AIAA Paper 98-2506, June 15-18, 1998.

[63] Abdel-Salam, T., Tiwari, S., Chaturvedi, S., and Mohieldin, T., "Mixing and Combustion in Scramjet Combustor with Raised and Relieved Ramp," AIAA Paper 2000-3709, July 16-19, 2000.

[64] Weinberg, F., "Electrical Discharge-Augmented Flames and Plasma Jets in Combustion," Advanced Combustion Methods, 1986.

[65] Barbi, E., "Uncooled Choked Plasma Torch for Ignition and Flameholding in Supersonic Combustion," Masters Thesis, Virginia Polytechnic Institute and State University, Blacksburg, 1986.

---

[66] Stouffer, S., O'Brien, W., and Roby, R., "Improved Plasma Torch For Ignition and Flame Holding in Supersonic Combustion," AIAA Paper 89-2945, July 1989.

[67] Kim, J., Clemens, N., and Varghese, P., "Experimental Study of an Underexpanded Pulsed Plasma-Jet," AIAA Paper 99-0452, 1999.

[68] Kimura, I., Aoki, H., and Kato, M., "The Use of a Plasma Jet for Flame Stabilization and Promotion of Combustion in Supersonic Air Flows*," Combustion and Flame*, Vol. 42, pp. 297-305, 1981.

[69] Takita, K., Takatori, F., Ju, Y., and Masuya, G., "Effects of Addition of Radicals Supplied by Plasma Torch on Burning Velocity," AIAA Paper 99-2247, June 1999.

[70] Takita, K., Takatori, F., and Masuya, G., "Effect of Plasma Torch Feedstock on Ignition Charecteristics in Supersonic Flow," AIAA Paper 2000-3586, July 2000.

[71] Takita, K., Uemoto, T., Sato, T., Ju, Y., Masuya, G., and Ohwaki, K., "Ignition Carectoristics of Plasma Torch for Hydrogen Jet in an Airstream," *Journal of Propusion and Power*, Vol. 36, No. 4, July-August, 1999.

[72] Masuya, G., Takita, K., Sato, T., Ohwaki, K., Takahashi, K., Uemoto, T., Ju, Y., and Matsumoto, M., "Ignition of Parallel and Low Angle Hydrogen Jet by Plasma Torch," 14th ISABE Conference, September 1999.

[73] Wagner, T., O'Brien, W., Northam, G., and Eggers, J., "Plasma Torch Igniter For Scramjets," *Journal of Propulsion and Power*, Vol. 5, No. 5, September-October, 1989.

[74] Northam, G., McClinton, C., Wagner, T., and O'Brien, W., "Development and Evaluation of a Plasma Jet Flameholder for Scramjets," AIAA Paper 84-1408, June 1984.

[75] Sato, Y., Sayama, M., Ohwaki, K., Masuya, G., Komuro, T., Kudou, K., Murakami, A., Tani, K, Wakamatsu, Y., Kanda, T, Chinzei, N., Kimura, I. , "Effectiveness of Plasma Torches for Ignition and Flameholding in Scramjet," AIAA Paper 89-2564, July 1989.

[76] Warris, A., and Weinberg, F., "Ignition and Flame Stabilization by Plasma Jets in Fast Gas Streams," *Twentieth Symposium (International) on Combustion*, The Combustion Institute, pp. 1825-1831, 1984.

[77] Shuzenji, K., Kato, R., and Tachibana, T., "Ignition Characteristics of Arc Discharges Exposed to Supersonic Airflows," AIAA Paper 2000-0617, January 2000.

[78] Fuji, S., Shuzenji, K., Kato, R., and Tachibana, T, "Augmentation of Ignition Arcs for Air Breathing Combustion by Teflon Sublimates," AIAA Paper 1998-3215, July 1998.

---

[79] Kanda, T., Hiraiwa, T., Mitani, T., Tomioka, S., and Chinzei, N., "Mach 6 Texting of a Scramjet Engine Model," *Journal of Propulsion and Power*, Vol.13, No. 4, July-August, 1997.

[80] Gallimore, S., "A Study of Plasma Ignition Enhancement for Aeroramp Injectors in Supersonic Combustion Applications," Dissertation, Virginia Polytechnic Institute and State University, Blacksburg, 2001.

[81] Miller, R.W., "Flow Measurement Engineering Handbook, 2nd Edition," R.R. Donnelly & Sons Company, 1989.

[82] Holder, D.W., and North, R.J., "Optical Methods for Examining the flow in High-Speed Wind Tunnels. Part One Schlieren Methods," North Atlantic Treaty Organization Advisory Group for Aeronautical Research and development, November 1956.

[83] Crites, R. C., "Pressure Sensitive Paint Technique, " *von Karman Institute for Fluid Dynamics*, Lecture Series 1993-05, Measurement Techniques, April 19-23, 1993.

[84] Fuller, R.P., "Fuel Vortex Interactions for Enhanced Mixing in Supersonic Flow," Dissertation, Virginia Polytechnic Institute and State University, Blacksburg, 1996.

[85] Billig, F.S., "Overview of Propulsion Performance, "Pyrodyne Incorporated, Presented as a paper accompanying a lecture, 2000.

[86] Mao, M., Riggins, D.W., and McClinton, C.R., "Numerical Simulation of Transverse Fuel Injection," NASP CR 1089, May 1990.

[87] Pearse, R.W.B., and Gaydon, A.G., "The Identification of Molecular Sectra" John Wiley and Sons, Inc., New York, 1976.

Appendix A

A1 Pressure-Sensitive Paint

Pressure-Sensitive Paint, PSP, consists of an oxygen quenched photoluminescent compound, mixed with an oxygen permeable binder (Crites[1]). The paint molecules are excited with a light source, typically in the blue to ultraviolet range. In an environment with oxygen molecules, at this point one of two things may occur. After a short period, the excited paint molecules will emit photons, typically somewhere in the yellow to red wavelength range. Alternatively, if an oxygen molecule collides with an excited paint molecule, the excess energy is transferred to the oxygen molecule and no photon is emitted. The latter is known as the *oxygen quenching* effect. This effect gives us a pressure field on the painted surface or model that inversely proportional to the intensity of the light emitted by the paint. This relationship is expressed by the Stern-Volmer relation:

$$\frac{I_r}{I} = A + B\frac{P}{P_r} \tag{A.1}$$

Where,

$$A + B \equiv 1 \tag{A.2}$$

Note that the Coefficients A and B are functions of temperature, and I_r and P_r are reference intensity and pressure quantities used in the data reduction process. The amount of light emitted from pressure-sensitive paints is also sensitive to the paints temperature. In order to use PSP, a sample of the paint must be calibrated over the pressure and temperature ranges experienced in the desired experiment to obtain the coefficients A and B. To do this, a computer controlled calibration rig was used in collaboration with Innovative Scientific Solutions, Inc., the producers of the paint used in the experiments, to control the thermodynamic conditions.

The data reduction process consists of background images of the model with the lights off, wind-off images of the pressure field on the surface of the painted model, and wind-on measurements. The background images are used to subtract the light from the room, not involved in oxygen quenching of the paint. Then the reference conditions I_r and P_r are obtained from the wind-off conditions at the known atmospheric pressure and temperature. Finally, Having the reference intensity and pressure conditions along with the coefficients A and B from the calibration data, the Pressure field on the surface of the painted model during the wind-on images can be obtained using the Stern-Volmer relation, shown as equation A.1. The main source of error with this procedure is estimating the temperature over the surface of the injector. Due to difference of temperature of the freestream and the injectant, and above all, the change in temperature of the test section walls during the tunnels 15-second blowdown runs, the temperature field over the model varied highly from the beginning to the end of the run. Over each run, four wind-on images were obtained, and the last of the four pictures was used. This was done to assure some consistency in the data, since the temperature variation was smaller near the end as the tunnel came closer to equilibrium. In order to properly reduce the pressure field, the temperature field must also be known. However, since this was impossible with the current paint used in these experiments, an *in-situ* data reduction method was used. This method used data from one of the pressure taps located around the injector model to estimate the global calibration coefficients of the model. That is, knowing the pressure at the tap and the intensity field around it, the effective temperature for the model can be estimated. Using this method, the pressure field around the injector models was generated.

A2 Aerothermodynamic Data Reduction

There are three possible zones in the plume region and boundary layer, which require different data reduction methods. The Standard Supersonic Region reduction applies to the region of the flow where the local Mach number is supersonic, the shock is attached to the cone, and the polynomial curve fit solution of the Talyor-McColl differential equation is valid. The Lower Supersonic Region reduction applies to the rest of the supersonic flow region with a local Mach number below the region of validity of the polynomial curve fit equation, down to 1.0. In addition, for a supersonic flow of air, the shockwave becomes detached from the cone-static probe around Mach 1.12 making all solutions to the attached-flow cone problem invalid. The Subsonic Flow Region is the small region near the wall and possibly in the core area of a jet plume where the flow becomes subsonic. Depending on the resolution of the traverse points, thickness of the probes, freestream Mach number, and the boundary layer thickness, data may not contain many points in the lower supersonic region or any in the subsonic region.

The following data reduction method applies to the supersonic flow of calorically perfect air with a specific heat ratio, γ, of 1.4. This was all that was necessary to reduce the aerothermodynamic experiments performed in this work. The total pressure profile presented in

Chapter 4 involving the aero-ramp plume superimposed with the helium plume was reduced assuming the helium concentration was low enough to neglect in the calculation process. A reduction scheme for mixtures of air and helium is presented in R. Fuller[2].

A2.1 Standard Supersonic Region

Follow these steps to reduce data from the Outer Supersonic Region.

1. Begin with data at the largest value of y.
2. Calculate local Mach number.

The local Mach number can be calculated using the following polynomial curve fit solution to the Taylor-McColl equation for supersonic flow over a cone in conjunction with the Rayleigh-Pitot formula. For an axis-symmetric cone, with cone half angle f=10-degthe local Mach number can be expressed by the following equation:

$$M = C_0 + C_1\sigma + C_2\sigma^2 + C_2\sigma^3 + \ldots + C_2\sigma^9 + C_2\sigma^{10};\ \ (1.2 < M < 3.0) \qquad \textbf{(A.3)}$$

where,

$$\sigma = 1.0 - 1.8716\frac{P_c}{P_{t,2}}$$

and,

$C_0 = 1.10040$ $C_1 = 0.80168$ $C_2 = 0.36776$
$C_3 = 4.11422$ $C_4 = -10.88201$ $C_5 = 7.91840$
$C_6 = 11.29032$ $C_7 = -2.38249$ $C_8 = -0.873955$
$C_9 = -45.17647$ $C_{10} = 45.71429$

3. Calculate P_t from the Rayleigh-Pitot equation:

$$P_t = P_{t,2}\left[\left[\frac{(\gamma+1)M^2}{(\gamma-1)M^2+2}\right]^{\frac{\gamma}{\gamma-1}}\left[\frac{\gamma+1}{2\gamma M^2-(\gamma-1)}\right]^{\frac{1}{\gamma-1}}\right]^{-1} \qquad \textbf{(A.4)}$$

4. Calculate the local static pressure:

$$P = P_t\left[1+\frac{(\gamma-1)}{2}M^2\right]^{\frac{-\gamma}{\gamma-1}} \qquad \textbf{(A.5)}$$

5. Calculate the recovery factor, this should be done once by averaging a few data points in the freestream. This is the recovery factor of the total temperature probe and is assumed constant throughout the plume and boundary layer:

$$r = \left[1 + \frac{\gamma - 1}{2} M^2\right] \frac{\left[\dfrac{T_t}{T_{t,\infty}} - 1\right]}{\left[\dfrac{\gamma - 1}{2} M^2\right]} \tag{A.6}$$

6. Next, calculate the corrected total temperature at the sampling probe location:

$$T_{t,corr} = T_t \left[\frac{1 + \dfrac{\gamma - 1}{2} M^2}{r\left(1 + \dfrac{\gamma - 1}{2} M^2\right) - r + 1}\right] \tag{A.7}$$

7. Calculate the local static temperature:

$$T = T_{t,corr}\left[1 + \frac{\gamma - 1}{2} M^2\right]^{-1} \tag{A.8}$$

8. Calculate the local mean velocity:

$$u = M\sqrt{\gamma R T} \tag{A.9}$$

9. Calculate the static density from the ideal gas law:

$$\rho = \frac{P}{RT} \tag{A.10}$$

A2.2 Lower Supersonic Region

For this region, defined as having a local Mach number less than 1.2 and greater than 1.0, we make the common boundary layer assumption that the static pressure is constant and equal to the last point calculated in the standard supersonic region. Having the local static pressure and the Pitot pressure it is possible to solve for the local Total Pressure, P_t, and Mach number, M using the Rayleigh-Pitot formula (Equation A.4) and Equation A.5. Once the local Mach number has been calculated, all other quantities can be determined including the static temperature as done in the standard supersonic region reduction procedure.

A2.3 Subsonic Region

The subsonic region is where the local Mach number is below 1.0. Use the static pressure lower supersonic region reduction process and remember that in subsonic flow the Pitot pressure is the total pressure. This allows direct solution of the local Mach number using Equation A.5 of the outer supersonic region reduction process. Having the local Mach number, once again, all other quantities can be calculated.

A3 Mixing Analogy Theory

The original mixing analogy was based from an analysis performed by Schetz[3] pertaining to flows with mass transfer. For the special case, where the Prandtl number and the Lewis number are equal to unity, a direct relation between the temperature and concentration fields can be found using the energy and species equation. Two 2-D flows of particular interest to 3-D flush wall injection in compressible flow are shown in Figure A.1. These flows can be used as simplified examples of the injector jet region near the surface of a wall and the core region as shown in the mock concentration profile of a flush wall injector plume in a supersonic crossflow in Figure A.2.

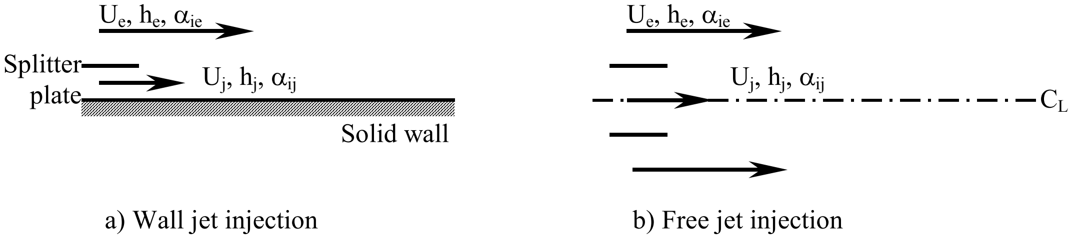

a) Wall jet injection

b) Free jet injection

Figure A.1 Schematics of Some Flows with a Foreign Fluid (Schetz[3]).

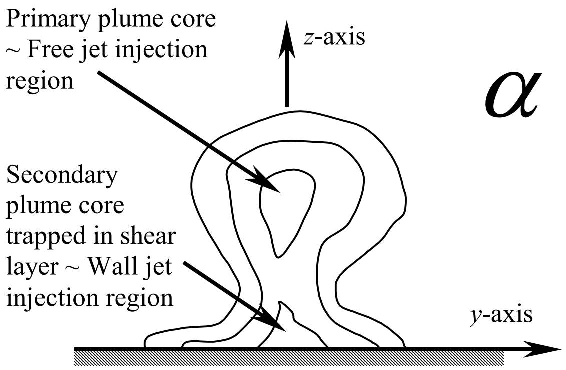

Figure A.2 Mock Concentration Profile. Example of Regions in a 3-D Jet in a Cross-Flow as Seen in the Cross-Stream Plane, Downstream of the Injection Location.

Using the various generalized Crocco integrals and the assumptions mentioned above, Schetz came up with the following relationship between species concentration and enthalpy:

$$\frac{\alpha_i - \alpha_{ie}}{\alpha_{ij} - \alpha_{ie}} = \frac{H - H_e}{H_j - H_e} \tag{A.11}$$

where α is concentration, and H denotes the total enthalpy of the flow. If one were to calculate the concentration α_i of a mixture of two gasses in terms of jet concentration, then α_e would equal zero and α_{ij} would be equal to unity. Furthermore, for jet and freestreams consisting of the same type of gas, or just similar constant pressure specific heats, c_p, this would simplify Equation A.11 into the form used in the first mixing analogy:

$$\alpha_i = \frac{T - T_e}{T_j - T_e} \tag{A.12}$$

This first form of the mixing analogy was used to evaluate the concentration profiles for the jet mixing studies shown in Appendices B and C. This method was shown to be successful in regions where the jet-vorticity levels were low, but in the regions of high vorticity, the mixing analogy inferred negative concentrations. Figure A.3 shows an example of the negative concentrations, as generated by a three-hole injector array, further details of which can be seen in Appendix B.

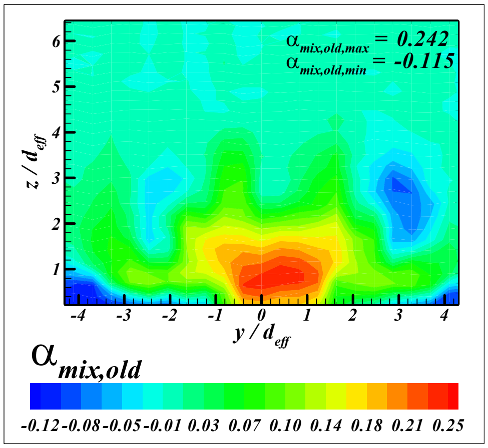

Figure A.3 Old Mixing Analogy Profile from Toe-In Study.

Equation A.11, with most of the assumptions of Equation A.12 can also be rearranged to look like the point wise enthalpy equation for a bimolecular mixture:

$$h_t = h_{t,j}\alpha + h_{t,\infty}(1-\alpha) \tag{A.13}$$

The new mixing analogy takes to form:

$$h_t = \left(h_{t,j}\alpha + h_{t,\infty}(1-\alpha)\right)(1-\beta) \tag{A.14}$$

where β is defined as the enthalpy deficit factor, which accounts for any changes in the enthalpy field due to vorticity. Now, in order to solve this equation, given only temperatures, one must now have information about the enthalpy field *a priori*. To remedy this problem, there must be two equations to solve the two unknowns. To do this, it was then assumed that two separate temperature-sampling profiles should be taken of the flowfield of interest with equal injector and freestream pressure values, but with different temperature ranges. To do this, profiles with heated and ambient injection were proposed, with the main assumption that the plume concentration field remains equivalent for both profiles. Doing so, it is then possible to solve for the new mixing anlalogy, α_{mix}, defined as:

$$\alpha_{mix} = \frac{\left.\frac{T_t}{T_{t,\infty}}\right|_H - \left.\frac{T_t}{T_{t,\infty}}\right|_C}{\left(\left.\frac{T_t}{T_{t,\infty}}\right|_H - \left.\frac{T_t}{T_{t,\infty}}\right|_C\right) - \left(\left.\frac{T_t}{T_{t,\infty}}\right|_H \left.\frac{T_{t,j}}{T_{t,\infty}}\right|_C - \left.\frac{T_t}{T_{t,\infty}}\right|_C \left.\frac{T_{t,j}}{T_{t,\infty}}\right|_H\right)} \quad \textbf{(A.15)}$$

where the H and C subscripts represent the heated (hot) and ambient (cold) profiles. Having α_{mix}, it is then possible to solve for the enthalpy deficit factor:

$$\beta = \frac{\alpha\left(\frac{T_{t,j}}{T_{t,\infty}} - 1\right) - \left(\frac{T_t}{T_{t,\infty}} - 1\right)}{\alpha\left(\frac{T_{t,j}}{T_{t,\infty}} - 1\right) + 1} \quad \textbf{(A.16)}$$

which can be solved using either the heated or ambient profile.

To give an estimate to how good the assumption that the concentration field for both profiles is the same, aerothermodynamic measurements of the local Mach number field were made for both the heated and unheated profiles. These profiles are presented in Figure A.4. As can be seen in the profiles, the two Mach number fields are very similar, with a little bit of misalignment in the heated case, which could be due to probe angularity at the time of the measurements. An example of the total temperature profiles of the heated and unheated injection cases are presented as Figure A.5. In this figure, the temperature separation effects can be seen, especially in the unheated total temperature profile. The old and new mixing analogy profiles, generated from the temperature sampling data are presented in Figure A. 6. The old mixing analogy comes from the heated profile alone and has a slight temperature variation towards the outsides of the cores of the vortex pair. The new mixing analogy, which accounts for the deficit in the enthalpy field due to vorticity, shows two more developed cores. Due to error in the sampling process and run-to-run variations of the momentum flux ratio in the profiles, along with the additional complexity from the utilization of two profiles, the new mixing analogy has in general a higher amount of uncertainty in it measurement (±0.05 – New, ±0.005 – Old). However, this is still a reasonable level of uncertainty and a very small price to pay for the mitigation of the temperature change due to vorticity.

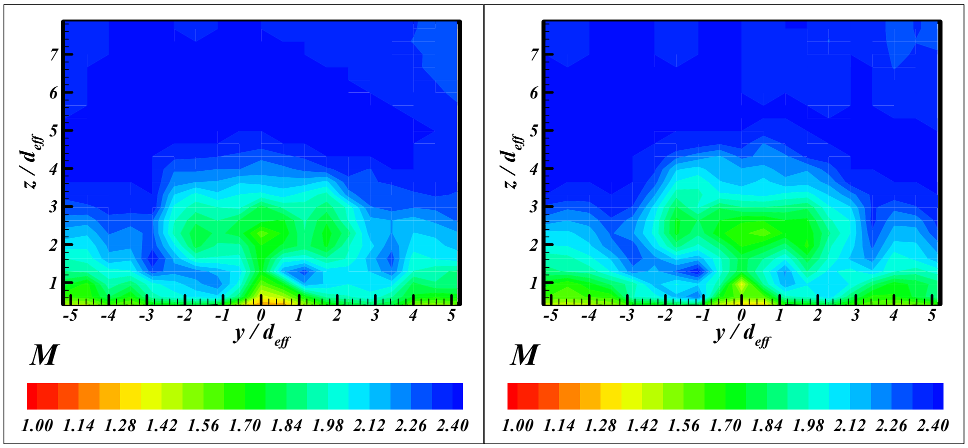

Figure A.4 Unheated (Left) and Heated (Right) Mach Number Profiles of Small Aero-Ramp Injector.

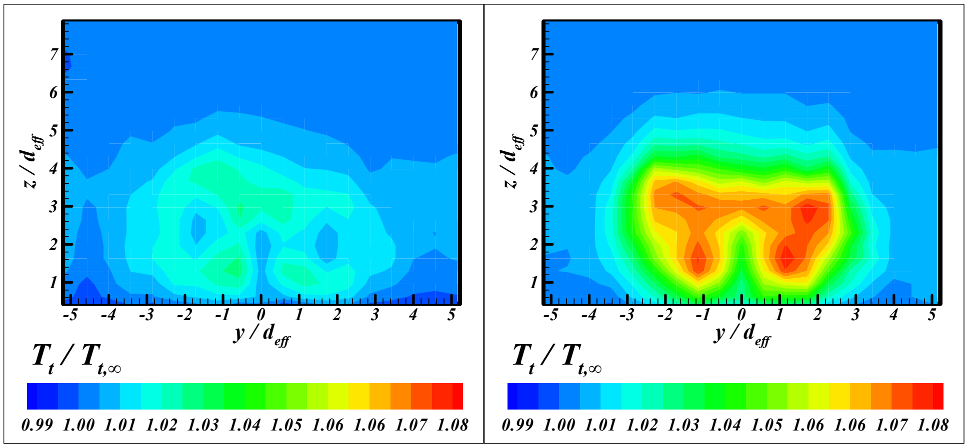

Figure A.5 Unheated (Left) and Heated (Right) Total Temperature Profiles of Small Aero-Ramp Injector.

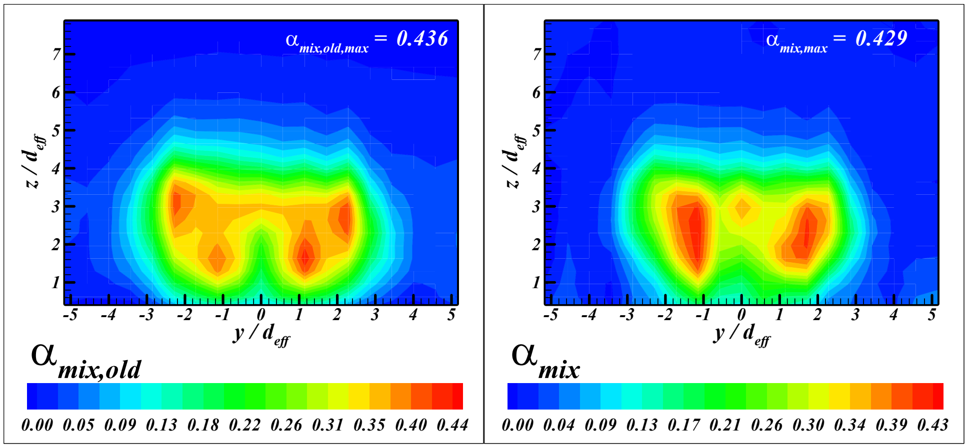

Figure A. 6 Old (Left) and New (Right) Mixing Analogy Profiles.

A4 Uncertainty Analysis

Measurements have uncertainty and we must have a means to quantify them or else we cannot know how accurate our results are. It is important to account for both systematic and imprecision-based errors. One can mitigate the influence of systematic error by calibration. An estimate of the imprecision of a given measurement is made possible through statistical methods.

The estimates of the systematic uncertainty in the measured quantities are based on error bounds of 95% (20:1 odds) and the Euclidean norm as a measure of the error.

The error in the freestream, various injector, and torch plenum chamber total pressure measurements, $P_{t,\infty}$, $P_{t,j}$, and $P_{t,T}$ were respectively, ±0.07, ±0.02, and ±0.02 atm. The higher value in the wind tunnel plenum chamber, $P_{t,\infty}$, was due to a high amount of electrical noise in the signal due to old wiring.

The error in the freestream, various injector, and torch plenums, $T_{t,\infty}$, $T_{t,j}$, and $T_{t,T}$ were each equal to ±2 K. This accounts for the sum of the squares of the standard deviation of the signal noise at a 95% confidence level (±0.4 K) and the temperature error range specified by the temperature measurement system (±2 K), which dominated the estimate.

The estimate of uncertainty of the helium concentration probe measurements was taken from R. Fuller[2]. The helium molar fraction was estimated at 5% corresponding to a 25% error in the helium mass fraction.

The uncertainty of the measurements made by the Pitot and cone-static probes was estimated at ±0.03 and ±0.0006 atm. The error measured by the total temperature probe, accounting for the measurement system and a 2-K lower difference in temperature to the true total temperature due to kinetic losses from deceleration process in the boundary layer. To mitigate the losses, the recovery factor of the probe was used to correct the total temperature for viscous effects using equations A.6 and A.7. This reduced the error in the total temperature back to ±2 K.

The reduced quantities and their uncertainties are presented in Table 1. These quantities are based on calculations using the Euclidean norm as a measure of the error. The derivatives of the equations corresponding to the quantities were either calculated or discretized, when necessary.

Table 1 Estimated Uncertainties of Reduced Quantities.

Quantity	Uncertainty
Total Pressure, P_t	±0.04 atm
Static Pressure, P	±0.001 atm
Static Temperature, T	±4 K
Density, ρ	±0.004 kg/m^3
Velocity, u	±0.7 m/s
Mach Number, M	±0.03
Mixing Analogy, α_{mix}	±0.05
Mixing Efficiency, η_m	±0.01
Total Pressure Loss Parameter, Π	±0.05

The error in the position of the sampling probe was calculated to be 2.5 mm in the x-direction for flexure of the probe, 0.1 mm in the y-direction due to manual positioning, and ±0.08 mm measured from the LVDT in the z-direction.

Errors higher than the stated uncertainty values were most likely due to misalignment and placement of the probes, along with the variation in momentum flux ratio from run to run. This effect is hard to get around in a blowdown facility, which had a variation in total pressure of ±0.4 atm on a run-to-run basis. To mitigate the differences in momentum flux ratio, additional repeated runs were necessary to reduce the overall variation in momentum flux ratio below ±5% of the stated values.

References

---

[1] Crites, R. C., "Pressure Sensitive Paint Technique, " *von Karman Institute for Fluid Dynamics*, Lecture Series 1993-05, Measurement Techniques, April 19-23, 1993.

[2] Fuller, R.P., "Fuel Vortex Interactions for Enhanced Mixing in Supersonic Flow," Dissertation, Virginia Polytechnic Institute and State University, Blacksburg, 1996.

[3] Schetz, J.A., “Boundary Layer Analysis” Prentice-Hall, 1993.

Appendix B

The Flowfield Near a Mulitiport Injector Array in a Supersonic Flow

(Abstract)

Experiments were performed to study the effects of toe-in angle on the exterior ports of a three-hole, low-downstream-angle injector array in a supersonic flow. The three jets were arranged flush with the test section floor so that the interference between the three plumes and the main flow would instill vortical motions. Three different configurations were tested involving three, 30° downstream angled, round injection holes in a row exposed to a Mach 3.0 cross stream. The two exterior holes of the row injector were set at toe-in angles of 0, 15, and 30 degrees. Test conditions involved sonic air and helium injection into a Mach 3.0 air cross stream with an average Reynolds number of 4.9×10^7 per meter at jet to freestream momentum flux ratios of 1 to 3.5. The injectors each had an equivalent jet diameter of 4.124 mm. and a cross stream spacing of 2.1 equivalent jet diameters between the jets. The primary qualitative observations were nano-shadowgraphs and surface oil flow visualization. A novel vertical plate flow visualization concept was also tested to help further understand the flow from the injector. The focus of the analysis of these pictures was based on understanding how toe-in angle of the outer injectors and the momentum flux ratio of the flow affect mixing and the shock wave structures in the jet area. Aerothermodynamic probe measurements were also performed at a downstream location with heated air injection to assess the total pressure losses and mixing potential of the flow. Results from the experiments showed improved mixing and core penetration with an increase of jet to freestream momentum and toe-in angle of the injector array. The observed oblique shock angle also increased with jet to freestream momentum ratio and toe-in angle of the exterior holes of the injector, but the integrated total pressure losses associated with the injector shock structure were found to be minimized with the 15 degree toe-in array injector.

Nomenclature

A = Cross-sectional area

α_s = C_2H_4-air stoichiometric mass fraction, 0.0680.

α_{mix} = Mass fraction mixing analogy

$\alpha_{mix,max}$ = Maximum mixing analogy mass fraction

β = Toe-in angle of the outer injector holes

C_d = Discharge coefficient

d_j = Jet diameter

d_{eq} = Equivalent jet diameter $=\sqrt{3}\ d_j$ for a 3-hole array

d_{eff} = Effective diameter of row injector

h = Visually measurable plume penetration height

h_{mix} = Maximum concentration penetration height

h_s = Stoichiometric plume penetration height

l = Injector hole length measured from the center

λ = Jet to freestream mass flux ratio $(\rho u)_j / (\rho u)_\infty$

γ = Specific heat ratio

η_m = Mixing efficiency

p = Static pressure

p_t = Total Pressure

$\bar{q}$ = Jet to freestream momentum flux ratio

ρ = Density

T = Static temperature

T_t = Total temperature

u = Flow speed

x = Streamwise coordinate

y = Spanwise coordinate

z = Vertical coordinate

Subscripts

∞ = Freestream

j = Injector

Introduction

Optimization of supersonic fuel injection systems is a critical step in the development of a viable hypersonic air-breathing propulsion system among other hypersonic application. In order to produce positive thrust the mixing of fuel in the combustor of a supersonic combustion ramjet engine (scramjet) must take place in as short a distance as possible. With superior mixing enhancement, the length of the mixing chamber in a supersonic combustor can be minimized in order to cut down on the total drag produced by skin friction on the walls of the engine. If the burning efficiency of the combustor is increased by enhancing the mixing characteristics of the injection system, then the total thrust produced by the scramjet will also increase. Thus, the maximization of mixing potential in such a flow would open up new avenues to hypersonic air-breathing flight and make operation of such a system feasible. At the same time, total pressure losses that result from the injection process must be minimized.

Application of a scramjet engine as the main power plant of a reusable launch vehicle or a tactical missile makes the concept valuable. Single-stage-to-orbit concepts such as the X-30 national aerospace plane, NASP, have entertained the use of theoretical scramjet propulsion systems. The current NASA Hyper-X program and airforce missile programs are based on such concepts. Related work is ongoing in France, Japan, and Russia. Another aspect of supersonic combustion is in the use of a rocket-based-combined-cycle engine, RBCC. In this ejector/ ramjet/ scramjet engine concept, the use of subsonic and supersonic fuel injection is employed to increase the total integrated average specific impulse over the flight trajectory into orbit. This gain in specific impulse would reduce the mass fraction of fuel required, thus allowing more room for payload.

The injection of fuel into the combustion chamber of a scramjet engine is usually accomplished through some type of orifice in either an in-stream strut or the walls of the combustor. Various injection schemes involve either ramps, transverse or stream-wise injection, and some type of flame holder/cavity (Tishkoff et al.[1]). Scramjet injectors may also use additional parameters such as non-circular orifices, tabs, and ramps to enhance the mixing characteristics of the fuel into the freestream flow.

For lower Mach number hypersonic flight the use of swept ramp injectors is prominent in both computational and experimental studies for scramjet combustors. Fuel injection ramps have been proven to be an effective means for mixing fuel into a scramjet engine. These ramps utilize vortex enhanced mixing, often referred to as "hypermixing", which involves the use of streamwise vortices to mix injected fuel into the combustor freestream flow (Hartfield Jr. et al.[2]) (Riggins and Vitt[3]). For true hypersonic applications, the protrusion of struts, ramps or other devices into the combustor flow should be avoided in order to minimize severe problems with thermal protection, drag, structural integrity, and total pressure losses (Tishkoff et al.[1]).

Further examination of specific injection devices is necessary to fully appreciate supersonic injection technology, especially the subject of transverse injection from round holes flush to a wall. The works up until 1990 were reviewed by Schetz et al.[4]. Low angled transverse injection studies in the range of 15° to 30° from the horizontal performed by Mays et al.[5] at Mach 3.0 analyzed the rate of mixing as affected by the ratio of exit jet pressure to effective back pressure. These studies found that the angle of injection primarily influences the initial disturbance but does not change the downstream mixing rate. This is important, because 90° injection implies larger total pressure losses in comparison to the lower angle transverse injection. Similar results were also presented by McClinton[6] for 30°, 45°, 60°, and 90° injection angles measured from the combustor wall. A comprehensive study of yaw angle was performed by E. Fuller et al.[7,8]. From these studies it was found that increasing the yaw angle of the injector increased the overall plume cross sectional area but decreased core penetration into the freestream.

The positive aspects of low angled injection and toe-in angle were incorporated into a nine-hole injector array called an "aerodynamic" ramp by J.A. Schetz, and some early results were reported in R. Fuller et al.[9]. Their studies compared the aerodynamic ramp to a physical ramp at jet to freestream momentum flux ratios of 1 and 2. These studies showed comparable performance of the aerodynamic ramp to the physical ramp injector at the higher momentum flux ratio. The aerodynamic ramp, as a transverse injector, also provided improved pressure recovery over the obtrusive physical ramp injector. This array incorporates the complex interaction between the nine holes, and the effects of baroclinic torque and shock induced vorticity between its three rows of injectors to produce vortical flow and enhance mixing efficiency. The multiple yaw angles of the injector holes also induce vortical effects, which further enhance mixing. The studies performed by R. Fuller et al.[9] suggest that further testing is needed to better understand the phenomena associated with the nine-hole injector. Analysis of a single row of three holes was suggested. Studying the effects of transverse injection at higher jet to freestream momentum flux ratios was also suggested to understand the trends of injector flow penetration into the freestream. Computational studies have also been employed by Cox et al.[10] and Schetz et al.[11] on the aero-ramp injector. Results from these studies have proved the injector to have a very complex 3-dimensional viscous flowfield.

Experiments performed at Virginia Tech were undertaken to further understand the complex interactions of a single row injector array. Three different configurations were tested involving three, 30° angled, round injection holes in a row exposed to a Mach 3.0 cross stream. The two exterior holes of the row injector were set at toe-in angles of 0, 15, and 30 degrees. Shadowgraph and surface flow visualization pictures were taken at various momentum flux ratios to help qualitatively understand the nature of the flows. Aerothermodynamic probing was also performed at a downstream location with heated air injection to help quantify the pressure losses and mixing capability incurred by the injector arrays.

Test Facilities

Experiments were performed in the Virginia Tech 23 X 23 cm blowdown supersonic wind tunnel. The tunnel was configured with a half nozzle test section resulting in a freestream Mach number of 3.0. The test section dimensions were 23 cm wide by 11.5 cm high and 30 cm long in the streamwise direction. The injector plenum chamber was located in the bottom test section wall in the upstream end of the test section similar to that in E. Fuller et al.[7]. Data acquisition was performed with a PC and a 16-channel 12-bit A/D converter.

Injector Models

The three transverse injector models used in this study each have three - 2.38-mm-diameter holes (determined by the orifice cross section) horizontally placed 8.47 mm apart in a row. The injectors each had an equivalent single jet diameter of 4.124 mm and a cross stream spacing of 2.1 equivalent jet diameters between the injector holes . The dimensions and diameters of the holes allow the flow to exit the injector sonically under all back pressure conditions associated with operable mainstream flow. The injection holes each had a length of 3.0 l/d_{eq} (measured from the center of the holes). With the 30 degree transverse injection angle the exit profiles of the injector holes are unknown and quite likely complex. The main difference between the three injectors is the toe-in angle of the two exterior injector holes. The three injector models have Toe-in angles of 0, 15, and 30 degrees. Another important feature of the injectors is the 30 degree downstream angle of the jets to the surface, which has been shown by

McClinton[6] and Mays et al.[5] to increase the penetration distance downstream while decreasing the total pressure loss associated with higher angled transverse injection. Figure 1 is a picture of the 30° toe-in angle transverse injector model.

Test Matrix

All wind tunnel tests were performed at a freestream Mach number of 3.0. Experiments were performed while injecting helium or air in order to simulate hydrogen and hydrocarbon fuels without the safety hazard associated with combustion. The tunnel average freestream conditions were 6.1 ATM, 285 K. The helium experiments were performed on average at a lower total pressure to obtain more control over the tunnel freestream conditions on a run-to-run basis. These conditions resulted in a corresponding freestream velocity of 607 meters per second and a Reynolds number of 4.9×10^7 per meter. Tests were performed with jet to freestream momentum flux ratios of 1 to 3.5. The jet to freestream momentum flux ratio was originally defined as follows:

$$\bar{q} = \frac{\left(\rho u^2\right)_j}{\left(\rho u^2\right)_\infty} = \frac{\left(\gamma p M^2\right)_j}{\left(\gamma p M^2\right)_\infty} \tag{1}$$

Since air from the plenum chamber was also used as the injectant through the injector block, the momentum flux ratios were limited to a maximum value of 2. A throttling valve in the line allowed reduction to a nominal value of 1. Due to a separate supply of helium the momentum flux ratios attainable were not as limited and shadowgraphs were taken at ratios of 1, 2, 3, and 3.5. The injector freestream flow coordinate system consists of right-hand Cartesian coordinates with the origin placed at the leading edge of the middle injection hole. The positive X-axis is in the downstream direction, the Y-axis in the horizontal direction, and the positive Z-axis in the vertical direction. Axial distance was normalized by what is known as the "effective" diameter, defined as:

$$d_{eff} = d_{eq}\sqrt{C_d} \tag{2}$$

where C_d is the discharge coefficient and d_{eq} is the injector equivalent jet diameter. The equivalent jet diameter is defined as the diameter of an equivalent single jet that has the same total area of the three jets of the injector. The equivalent jet diameter for all three of the array injectors was 4.124 mm.

Test Procedures

Nanoshadowgraphs

Spark shadowgraphs were taken using a nanopulser spark with an exposure time of $2\text{x}10^{-8}$ sec. With a 20-nanosecond pulse of light, it is possible to see the turbulent eddy structures in the flow significantly larger than 0.012mm.

Top-View Surface Flow Visualization

Visualization of the surface flow patterns near the injectors was accomplished via the use of 500 cS silicone oil mixed with two colors of fluorescent dye. A thin layer of fluorescent green oil was placed all around the injector, and a thin strip of fluorescent red oil was placed in front of the injector holes. This was done to help show the direction of the surface flow as it passed the injector holes. The patterns were illuminated with a 100 watt ultraviolet lamp and pictures were taken with a 35 mm camera after each run. The surface oil flow patterns were also recorded on videotape during tunnel operation.

Vertical Plate Flow Visualization

Visualization of the flow patterns in the plume and in the mainstream in a longitudinal vertical plane through the center of the middle injector was made possible with the use of a thin vertical plate. The plate was 1.59 mm. thick by 4.19 cm. high by 7.85 cm. long. In order to minimize the disturbance created by the plate on the freestream, a wedge of approximately 10 degrees was placed at the front edge of the plate and the plate was cut at an approximate angle of 45 degrees near the front. Lastly, the plate was sharpened to a knife-edge from the backside over the middle injector hole. A 500-cS silicone oil and dye was applied to the plate, and pictures were taken with a 35 mm camera while the oil was illuminated with a 100 watt ultraviolet lamp.

Aerothermodynamic Probing

Aerothermodynamic measurements of the flowfield were taken with heated air injection 27.3 d_{eq} downstream from the leading edge of the injector arrays. The sampling was accomplished with a Pitot, a cone-static, and a total temperature probe. The Pitot probe had a 1.59 mm outer diameter and 1.04 mm inner diameter, which gave a capture area of 0.85 mm^2. The cone-static probe consisted of 1.59-mm-outer-diameter pipe with a 10-degree cone half-angle. There were four small sampling ports arranged around the cone to help reduce effects of misalignment of the probe to the flow. The total temperature probe also consisted of 1.59-mm-outer-diameter tubing with an inner diameter of 1.04 mm giving the probe a 0.85 mm^2 capture area. The total temperature probe had 3 small holes drilled around the pipe to improve the recovery factor of the probe. The total temperature probes capture to recovery area ratio was 5 to 1. An exposed junction type-K thermocouple with a 0.25 mm diameter bead was placed inside the total temperature probe.

Species Composition Mixing Analogy

The air in the injector plenum chamber was heated by approximately 60 degrees Celsius during the aerothermodynamic sampling tests to obtain a temperature profile analogous to the mass fraction of a simulated hydrocarbon gas with a molecular weight similar to air, such as ethylene. The mass fraction mixing analogy, α_{mix}, is defined as:

$$\alpha_{mix} = \frac{T_t - T_{t,\infty}}{T_{t,j} - T_{t,\infty}} \tag{3}$$

where T_t is the total temperature, $T_{t,j}$ is the total temperature of the injected air, and $T_{t,\infty}$ is the total temperature of the freestream flow. The air in the injector plenum chamber was heated using two 1000W cartridge heaters. The inside walls of the injector plenum chamber were insulated to minimize the heat transfer through the outside walls.

Data Reduction

The aerothermodynamic measurements with heated air injection made with the three probes were reduced in a standard fashion (R. Fuller et al.[9]). The reduction was performed using an iterative scheme involving the perfect gas relations, the Rayleigh-Pitot formula, and the Taylor-McColl cone flow solutions.

Uncertainty Analysis

The measurement of the shock wave angles and visual plume heights from the shadowgraphs were made with a protractor and calipers. The uncertainty of the shock wave angle was estimated at 0.5 degrees. The uncertainty of the visual plume height was estimated at 0.3 mm.

The estimates of the uncertainty in the electrically measured quantities are based on error bounds of 95% (20:1 odds) and the Euclidean norm as a measure of the error. The calculated error in $P_{t,\infty}$, $P_{t,j}$, and $P_{t,1}$ were respectively, ±0.07 atm, ±0.004 atm, and ±0.04 atm. The error in $T_{t,\infty}$, $T_{t,j}$, and T_t were each equal to ±0.4 °K. The error in Mach number was ±0.03. The error in local velocity and density were ±0.7 m/s and ±0.004 kg/m^3. The error in the position of the sampling probe was calculated to be 2.5 mm in the x direction for flexure of the probe, 0.1 mm in the y-direction due to manual positioning , and ±0.08 mm measured from the LVDT in the z-direction. The calculated error in mixing analogy, α_{mix}, was ±0.005, mixing efficiency, η_m, was ±0.01, and total pressure loss parameter, Π, was ±0.05.

Results and Analysis

Nanoshadowgraphs

Figure 2 shows the shadowgraphs taken while injecting sonic jets of air into a Mach 3.0 air stream for various values of momentum flux ratio, $\bar{q}$, and toe-in angle, β. Figure 3 shows the shadowgraphs taken while injecting helium. The shadowgraph pictures are shown with the freestream flow going from left to right and the injection up from the bottom to the right. The injector holes are located just to the right of the shock wave. The second weaker shock wave, further downstream of the holes, shows a disturbance where the injector plate mates with the test section floor. The turbulent boundary layer on the wall can also be clearly seen. These shadowgraph pictures give an integrated two-dimensional image across a three-dimensional flow. From these images, one can observe penetration trends of the sonically injected helium into the air freestream as well as the oblique shock waves caused by both helium and air injection. The plumes of the helium jets are much more visible due to the larger density and index of refraction differences. The shadowgraph images have a lot of interesting features such as the structure of the bow shocks, the plume, kinks in the bow shocks, orthogonal shock waves propagating from those kinks, and penetration trends from the helium injection. One can measure maximum oblique shock wave angles as the angles nearest to the injection holes after the unification of the separation zone shocks and the bow shocks near the wall. As the distance increases downstream from the injector holes, the angles of the shock can be seen to approach that of a Mach wave, which is approximately 19.5 degrees in a Mach 3 flow. The thick boundary layer interferes with the interpretation of the shock wave structure in the region inside it and also obscures the front part of the jet plume.

Figure 4 shows the maximum oblique shock wave angles with helium injection after the unification of the shocks from the boundary layer. These angles were measured and plotted as a function of the momentum flux ratio. This graph shows the trend of increasing oblique shock wave angle with increasing momentum flux ratio and outer jet toe-in angle. The graph also shows that air injection produced higher oblique shock wave angles than helium at the same momentum flux ratios. Note that this study should be interpreted cautiously, since it does not give any information about the width of the interaction shock structure and other three-dimensional aspects of the flow. In a simple two-dimensional flow, increasing the angle of the oblique shock wave would directly imply an increase in total pressure loss across the shock wave. Due to the three dimensional effects associated with this flow, an overall increase in total pressure loss may not occur if the width of the shock wave is reduced with the increased toe-in angle of the injector.

An interesting comparison to help further understand the interaction shock wave structures comes from work done by Spaid and Cassel[12] on the subject of normal (90°) transverse injection. They describe the shock structures produced by a normal, sonic, transverse slot injector into a supersonic freestream flow. The importance of this study is that it shows many similarities between that case and the array injector shock wave structure here. Thus, the shock wave structure created by Spaid's injector can be used to help explain the bow shock wave trends seen with the increase in toe-in angle of the row injectors. For example, a double shock structure is clearly seen directly in front of the injector holes in the shadowgraph taken with the 30 degree toe-in injector in Fig. 3(f) at a momentum flux ratio of 2 while injecting helium. This structure is similar to that caused by the separation zone directly in front of the transverse slot injector. Furthermore, the increase in distinction and size of the separation shock can be seen with an increase in toe-in angle of the exterior injector holes. Therefore, as the increase in toe-in angle moves the jet momentum toward the center of the injector, it makes the injector behave more like a single slot injector by increasing the pressure in the center region of the injector. This increase in pressure created by the jets also increases the separation zone by restricting the freestream flow between the injectors. More evidence of this phenomenon will be seen by examination of the surface flow around the injector below.

Understanding the injector jet structures is important, because it helps define the jet trajectory. Due to the boundary layer thickness, the injector jet shock structures are barely visible. The injector jet shock structures come out clearer in the air shadowgraph pictures than in the pictures taken while injecting helium because of the higher density. In the air injection shadowgraphs, the barrel shocks and the Mach disk can be seen superimposed over each other, unfortunately making it harder to see each individual jet.

Kinks in the injector bow shocks and orthogonal shock waves propagating from these kinks can be seen in the helium injection shadowgraphs. In experiments done on a single transverse sonic jet by E. Fuller et al.[8], the kinks and orthogonal shock waves were shown to increase with the jet yaw angle. Also, it was shown that the eddies inside the helium plume grew with increasing yaw. These studies suggest that the turbulent eddies in the injection plume are directly related to the kinks in the bow shock and the orthogonal shock waves. Thus, the kinks in the bow shock and the orthogonal shock waves are formed from the local position of the eddies and expansion of the gas from the injector jets. This increasing trend was not as apparent in the array injectors. This may be because of the interference between the three jets from the injector, which may have just as much an effect on producing these unsteady phenomenon as yaw on a single injector. Another point of interest is that the kinks and orthogonal shock waves can not be seen in the present air injection shadowgraphs.

Using the data in Figure 3, the penetration and shock wave distances were measured at approximately 11 equivalent jet diameters downstream from the leading edge of the injector holes. Figures 5 – 7 show the visually measurable penetration, h, of the helium jet into the freestream, shock wave height, and the ratio of the helium visually measurable penetration, h, to shock wave distance, h_{shock}, respectively. These graphs show an increase in shock height and penetration distance with an increase in momentum flux ratio. The vertical injectant penetration distances in Fig. 7 of the 15-degree and 30-degree toe-in angle injectors are very comparable, and both are larger than the 0-degree toe-in injector. The penetration to shock wave height ratio of the 0-and 15-degree injectors are comparable, and both are larger than the 30-degree toe-in injector case. From these trends, the 15-degree toe-in angle injector is seen to have comparable short range penetration performance at a likely reduced total pressure loss when compared to the 30 degree injector. A toe-in angle greater than zero is desirable to induce a “spill over” of the mainstream flow passing over the plumes in order to induce large scale vortical patterns to enhance down stream mixing. These results also suggest that a $\bar{q}$ of 2-3 may be optimal.

Top-View Surface Flow Visualization

Surface oil flow visualization still pictures and video footage were taken of the three injection schemes for both air and helium injection. Figure 8 shows the air injection top-view surface oil flow pictures taken with jet to freestream momentum flux ratios of 1 and 2. Figure 9 shows the top-view surface oil flow pictures taken while injecting sonic helium jets at momentum flux ratios of 2 and 3.

In all the top-view surface flow pictures, the freestream flow is from left to right. The exit of the injectors can be seen as elliptical black holes near the left edge. The boundary where the downstream end of the injector block mates with test section floor, 10.7 equivalent jet diameters downstream from the leading edge of the middle injector hole, can be seen at the end of the pictures. Some paint buildup can be seen near the end of the injector plate. This is caused from the tunnel unstarting at the end of each run. This unstart can sometimes have a distorting effect by pushing the paint on the surface in all directions. Although the unstart causes some distortion in the images, the surface flow pictures still accurately represent the patterns created from the air and helium injection as determined by video and direct observations during the runs.

A close inspection of the individual images can tell much about the various features involved with the flow patterns created from the injectors. Some of these important features are the trajectory of the jet plumes along the wall, the width of the individual jets and overall plumes, the size of the separation zones in front of the injector hole, the separation regions behind the exterior holes trailing edges, and the rate at which the overall plume width recovers from the effects of toe-in angle on the exterior injector holes. The plume width is apparent in these pictures, because the plume impacts the wall at these low downstream angles and modest momentum flux ratios.

The width of the overall plume can be seen to increase with momentum flux ratio due to the under-expanded nature of the injector jets. The individual jets all show this same trend, but it is interesting to note that the exterior jet plumes along the surface appear to shrink in size with an increase in toe-in angle. This reduction in size is really the overlaying of the middle plume on the exterior ones which seems to dominate the flow near the surface of the injector. This overlapping of the plumes indicates increased mixing between the individual injector jets. Thus, as the jet momentum is angled in toward the center of the injector array, the penetration height of the injectant would be increased. For the 0-degree toe-in angle injector cases in Fig. 8 (a) and (b), the outer jets seem to trace a path along the wall that diverges outward from their initial direct downstream injector. The width of the overall shock is also seen to be reduced with the increase of toe-in. This can also be explained by the inward toe-in of the injector jet momentum. Thus as the jets are expanding inward, they have less an effect on the width overall shock and confine the blockage to a narrower cross stream space with a higher overall plume penetration.

The small separation zones created in front and behind the injector holes are clearly influenced by the increased injector toe-in angle and momentum flux ratio. The separation zones in front of the injector holes can be seen especially well in the 30-degree toe-in angle injector. In the lower angle cases with lower momentum flux ratios, the buildup of oil in this zone is seen to leak through between the injector holes. As the toe-in angle increases, the surface flow through this region is reduced and finally stopped in the 30-degree case. This separation zone can be seen in the higher toe-in angle injector shadowgraph pictures and also by examination of the surface flow video footage, which clearly shows the unsteady nature of this flow. Look at Fig. 8(f) for example, where the interaction shock does not penetrate close to the wall in front of the injectors as in the lower $\bar{q}$ and toe-in angle cases. The question about this flow separation zone is: how does it effect the performance of the injectors? The separation zone helps let the jet plume initially penetrate further by reducing the influence of the freestream momentum upon that of the jets. However, such separations can create unwanted "hot spots" on the wall of a real combustor. The second separation zone can be seen directly behind the exterior injector holes by the build up of oil in this region. This zone increases in size with toe-in angle and momentum flux ratio. Examination of the video footage shows the paint spinning around in this region during tunnel operation, clearly indicating that vortices are created by the injector.

Vertical Plate Flow Visualization

Vertical flow visualizations were performed on the line of symmetry of the injector using a vertical plate attached to the 15 degree toe-in angle injector. Figure 10 shows pictures of the vertical plate flow visualization at momentum flux ratios of 2 and 3. Figure 10(c) is a picture of a shadowgraph superimposed onto the vertical plate surface flow at a momentum flux ratio of 2. In these pictures, the shock structure near the injector holes and evidence of the separation zone in front of the injector can be seen with some clarity. Another interesting feature is the dark spot near the injector hole. These spots could represent the barrel shock of the injector plume. The vertical plate was cut to a sharp edge in the front to minimize, not eliminate its influence on the injector flowfield. From inspection of the comparison in Fig. 10(c), the angles of the shocks in the near field with respect to the injector holes on the vertical plate surface flow are quite close to that of the shadowgraphs. Only in the examination of the far field do the angles start to stray from that of the shadowgraph. This is due to interference caused by the vertical plate, which inevitably distorts the actual flow of the injector plume due to the boundary layer on the plate and the unstart of the tunnel after each run. Similar experimental techniques for plume visualization have been used successfully by Tomioka et al.[13].

Mixing Analogy Profiles

Figure 11 presents the results of the total temperature measurements for the heated air test cases in the form of the mixing analogy, α_{mix}. The three profiles were generated at the same sampling station at a nominal jet to freestream momentum flux of 2.0. The contour color scale and spacing are the same in all three plots. Note that the station location is constant, but due to the normalization of the data, the x/d_{eff} station sampling location varies from 28.1 to 29.4 as a result of small changes in the discharge coefficient. Two regions where the mixing analogy is reduced below 0.0 are the boundary layer, and the two locations to the sides of the jet plumes, which are due to induced vorticity in the flow. The vortically induced cold spots seem to become less apparent with the increase of injector toe-in angle and are hardly visible in the 30 degree toe-in injector case at all. The maximum values of the mixing analogy correspond to the local station maximums. Note that the two local maximums in the 0 degree toe-in injector represent the locations where the injected gas is converging between the injector jet plumes. Also, as the toe-in angle is increased, the analogous concentration maximums are shifted towards the center, penetrate further, and mix more efficiently. Other interesting features of the mixing analogy profiles are the horn-like protrusions on the top, and the bat-like arms on the sides of the main plumes. These features also tend to decrease and shift toward the center with the increase of injector toe-in angle.

Total Pressure Contours

Figure 12 presents the total pressure contours of the three injectors for the heated air test cases at the same station as the mixing analogy profiles. Once again, the experiments were performed at a jet to freestream momentum flux ratio of 2.0 and the contour color scale and spacing are consistent between the three plots. In Fig. 12(a), the three individual plumes of the 0 degree toe-in injector can be seen to already have an induced vorticular effect upon each other. This is due to the under-expanded nature of the jets and the close spacing between them. This vorticular motion is further increased in the 15 degree toe-in injector, and a singular pressure minimum is seen to emerge in the center in Fig. 12(b). As the toe-in angle increases to 30 degrees in Fig. 12(c), the vortices tend to wrap around even more. A reduction in the local boundary layer height is seen as an after effect of this vortical motion. Another interesting feature of the vortices is seen in comparisons to the mixing analogy pictures. Since the mixing analogy pictures are really profile of the total temperature, the local cold spots are at the same location as the leading ends of the total pressure loss plumes. The two profiles in conjunction with Crocco's vorticity theorem show good evidence of vorticular motion in the flow. Crocco's Theorem states for a steady, inviscid flow with negligible body forces:

$$T\nabla s = \nabla h_o - \nabla \times \omega \tag{4}$$

where s is the systems entropy, h_o is the enthalpy, and ω is the vorticity of the flow. Thus, it is possible for a vorticular structure and a change in entropy to effect the total temperature of the system, since total temperature can be directly expressed in terms of enthalpy.

Maximum Concentration Levels

The local maximum concentration levels of the three mixing analogy profiles, $\alpha_{mix,max}$, are presented in Fig. 13 and the vertical heights of the local maximums are shown in Fig. 14. The vertical penetration of the local maximums is represented by h_{mix}/d_{eff}. From the two graphs, it is evident that the maximum concentration level is reduced and the penetration distance is increased with an increase in toe-in angle.

Plume Penetration

The maximum penetration heights of the mixing analogy plumes were measured, and the results are presented in Figure 15. The plume penetration, h_s, is defined here as the vertical distance from the wall to the edge of the mixing region where the mass fraction mixing analogy is equal to the stoichiometric value of ethylene, 0.0680.

The results from the plume penetration show the 15 and 30 degree toe-in injectors to have increased plume penetration distances into the freestream, with the 15 degree case the highest. Note that these should be interpreted cautiously since the 15 degree toe-in injector has two horn-like structures on the top of the injector plume which increase the measured stoichiometric penetration level to that comparable of the thirty degree injector.

Plume Area

The overall plume area of the mass fraction mixing analogy is defined here as the total area of the plume which has an α_{mix} greater that the stoichiometric value of ethylene, 0.0680. Figure 16 shows the variation in over-stoichiometric plume area with Toe-in angle for the three injectors. The plume areas are non-dimensionalized by the area that the injector jet would expand to if the static pressure of the jet were equal to that of the freestream, and is denoted A_u.

This graph shows a decrease in the over-stoichiometric plume area as the toe-in angle is increased. Taking into account the decrease in the maximum concentration level with the decrease in plume area shows that the fuel mixing level is increased significantly with the increase of toe-in angle.

Mixing Efficiency

The mixing efficiency, as defined by Mao et al.[14], is represented as "that fraction of the least available reactant which would react if the fuel-air mixture were brought to a chemical equilibrium without additional local or global mixing". This means that the local fuel and air are considered mixed respectively in the rich and lean fuel areas. For the study of a single injector array in a relatively large duct the mixing efficiency can be defined as in R. Fuller et al[9]:

$$\eta_m \equiv \frac{\dot{m}_{f,mix}}{\dot{m}_{f,tot}} = \frac{\int \alpha_r \rho u dA}{\int \alpha \rho u dA} \tag{5}$$

where,

$$\alpha_r \equiv \begin{cases} \alpha & ,\alpha \le \alpha_s \\ \left(\dfrac{1-\alpha}{1-\alpha_s}\right)\alpha_s & ,\alpha > \alpha_s \end{cases} \tag{6}$$

and

α = fuel mass fraction

α_s = C_2H_4 - air stoichiometric mass fraction

A = plume Area

$\dot{m}_{f,mix}$ = mixed fuel mass flow rate

$\dot{m}_{f,tot}$ = total fuel mass flow rate

The integrated results of the mixing efficiency study performed with the mixing analogy profiles and the aerothermodynamic contours are presented in Fig. 17. The results show that the mixing efficiency increases with the injector toe-in angle. This study supports the conclusion that the overall mixing of the injector is improved with the increase of toe-in angle and is in agreement with the similar trends of increasing penetration, decreasing maximum concentration level and decreasing over-stoichiometric plume area.

Total Pressure Loss Parameter

The total pressure losses due to fuel injection in a supersonic flow have been quantified by examining the mass weighted field values of the total pressure normalized by the freestream conditions using the total pressure loss parameter defined by R. Fuller et al.[10]. This method simplifies the analysis by allowing an assessment of the losses within the sampling area. This total pressure loss parameter is defined as:

$$\Pi = \frac{\int \rho u \left(p_{t,\infty} - p_t\right) dA}{\rho_\infty u_\infty p_{t,\infty} A_s + \rho_j u_j p_{t,j} A_j} \tag{7}$$

where

$$A_s = \frac{\lambda}{\alpha_s} A_j \tag{8}$$

and A_s is the area required for a uniformly stoichiometric jet given the jet to freestream mass flux ratio, λ, and jet area, A_j. Thus for this parameter, a fuel injector incurring no losses would have $\Pi = 0$. Figure 18 presents the results of the total pressure loss parameter integrated over the sampling area. The results of this study show the 15-degree toe-in injector to have the lowest losses over the integrated area. The minimum result of the 15-degree injector could be due to having less blockage than the 0-degree injector and a lower initial shock height than the 30-degree injector.

Summary and Conclusions

Experiments were performed to study the effects of toe-in angle on the exterior ports of a sonic, three-hole array injector with a low downstream angle in a Mach 3.0 flow. The primary experiments performed were nano-shadowgraphs, surface oil flow visualization, and aero-thermodynamic probing. A novel vertical plate concept was also tested to help further understand the flow in the jet plume. The focus of the analysis was based on understanding how toe-in angle and the momentum flux ratio affect mixing, the shock wave structures in the jet area, and the total pressure losses of the injectors.

Mixing of the injectant into the freestream was first qualitatively studied by examining the penetration distance of the helium shadowgraphs approximately 11 jet diameters downstream from the leading edge of the middle injector hole and from examination of the surface plume width at various momentum flux ratios. The shock wave structures in the jet area were also studied via the analysis of the shadowgraph and surface oil flow visualization pictures. The shadowgraph pictures showed trends in the shock waves associated with increases in toe-in angle and momentum flux ratio. The effective size of the separation zones was studied in an attempt to understand how they affect the flow. Aerothermodynamic probing measurements with heated air injection were also performed at a downstream station to qualitatively assess the total pressure losses and mixing potential of the flow.

The main conclusions drawn from the experiments are as follows:

1. The vertical penetration distance of the 15-degree and 30-degree toe-in angle injectors are very comparable, and both are larger than the 0-degree toe-in injector.
2. The penetration to shock wave height ratio at nominally 11 jet diameters downstream of the 0 and 15 degree injectors are comparable, and both are larger than the 30-degree toe-in angle injector case.
3. Both penetration and shock height increase with momentum flux ratio.
4. The overall plume width increases with momentum flux ratio.
5. The initial oblique shock wave angle of the injector increases with momentum flux ratio and toe-in angle.
6. The size of the separation zones in front and behind the injector holes increases with toe-in angle and momentum flux ratio.
7. An increase in distinction and size of the separation shock can be seen with an increase in toe-in angle of the exterior injector holes.
8. The maximum concentration level of the mixing analogy plumes is reduced and the penetration distance is increased with an increase in toe-in angle.
9. There is a decrease in the over-stoichiometric plume area as the toe-in angle is increased. The decrease in the maximum concentration level combined with this decrease in plume area shows that the fuel mixing is increased significantly with an increase of toe-in angle.
10. The overall mixing and penetration of the injector is improved with an increase of toe-in angle.
11. The results of the total pressure loss parameter study show the 15-degree toe-in injector to have the lowest losses over the integrated area. The minimum result of the 15-degree injector could be due to having less blockage than the 0 degree injector and a lower initial shock height than the 30 degree injector.

12. The 30-degree toe-in angle injector showed the best mixing performance in terms of maximum analog to concentration, penetration, plume area, and mixing efficiency. On the other hand, a minimum in total pressure was found for the 15-degree toe-in angle injector. One cannot rigorously combine mixing performance and pressure loss into a single parameter to judge the an injector. However, based on the present results one might conclude that a good injector should have a toe-in angle in the range of 15-30 degrees at this spacing.

From the studies presented here it has been found that the thirty degree toe-in injector had the highest mixing potential of the three injector models. Further studies of interest might include the testing of higher toe-in angle injectors to see any further advantages associated with the induced vortical motion of the injector arrays. Another study of interest would be to vary the spacing between the jets to see how mixing and blockage are affected. Finally, non-circular injectors might prove beneficial in an array.

Acknowledgements

This work was sponsored by Taitech, Inc. through Wright Laboratories, Wright Patterson AFB, Ohio. The technical monitor was Dr. Raymond Fuller, and we thank him for his help and guidance throughout the research.

References

[1] Tishkoff, J.M., Drummond, J.P., and Edwards, T. “Future Direction of Combustion Research: Air Force/ NASA Workshop on Supersonic Combustion,” Reno, Nevada: AIAA-97-1017, January 6-9, 1997

[2] Hartfield Jr., R.J., Hollo, S.D., and McDaniel, J.C. “Experimental Investigation of a Swept Ramp Injector Using Laser Induced Iodine Fluorescence,” Journal of Propulsion and Power: Vol. 10 No 1., Jan.-Feb. 1994

[3] Riggins, D.W., and Vitt, P.H. “Vortex Generation and Mixing in Three-Dimensional Supersonic Combustors,” Journal of Propulsion and Power: Vol. 11 No 3., May-June 1995

[4] Schetz, J.A., Thomas, R.H., and Billig, F.S., “Mixing of Transverse Jets and Wall Jets in Supersonic Flow, in Separated Flows and Jets,” V.V. Kozlov and A.V. Dovgal (Edits.), Springer-Verlag, Berlin, Heidelberg 1991.

[5] Mays, R.B. Thomas, R.H., and Schetz, J.A., “Low Angle Injection into a Supersonic Flow,” AIAA Paper 89-2461, July 1989.

[6]McClinton, C.R., "The Effect of Injection Angle on the Interaction Between Sonic Secondary Jets and a Supersonic Freestream," NASA TND-6669, February 1972.

[7]Fuller, E.J., Thomas, R.H., and Schetz, J.A., "Effects of Yaw on Low Angle Injection into a Supersonic Flow," AIAA Paper 91-0014, January 1991.

[8]Fuller, E.J., Mays, R.B., Thomas, R.H., and Schetz, J.A., "Mixing Studies of Helium in Air at Mach 6," AIAA Paper 91-2268, June 1991.

[9]Fuller, R.P., Nejad, A.S., and Schetz, J.A., "Fuel-Vortex Interactions For Enhanced Mixing in Supersonic Flow," AIAA Paper 96-2661, July 1996.

[10]Cox, S.K., Fuller, R.P., Schetz, J.A., and Walters, R.W. "Vortical Interactions Generated by an Injector Array to Enhance Mixing in Supersonic Flow," AIAA Paper 94-0708, January 10-13, 1994

[11]Schetz, J.A., Cox-Stouffer, S., and Fuller, R.P., "Integrated CFD and Experimental Studies of Complex Injectors in Supersonic Flows (Invited)," AIAA Paper 98-2780, June 1998.

[12]Spaid, F.W. and Cassel, L.A., "Aerodynamic Interference Induced by Reaction Controls," AGARD-AG-173, December 1973.

[13]Sadatake T., Hiraiwa, T., Mitani, T., Zamma, Y., Shiba, H., and Masuya, G., "Auto Ignition in a Supersonic Combustor with Perpendicular Injection Behind Backward-Facing Step," AIAA Paper 97-2889, July 1997.

[14]Mao, M., Riggins, D.W., and McClinton, C.R., "Numerical Simulation of Transverse Fuel Injection," NASP CR 1089, May 1990.

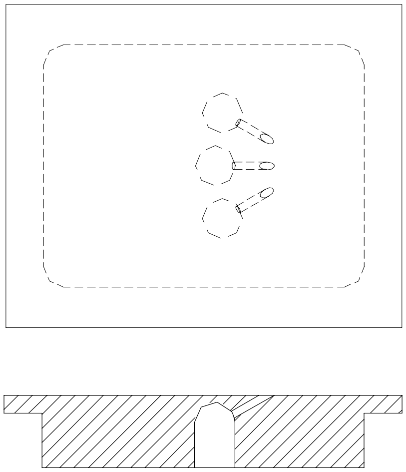

Figure 1. 30° toe-in angle transverse injector model.

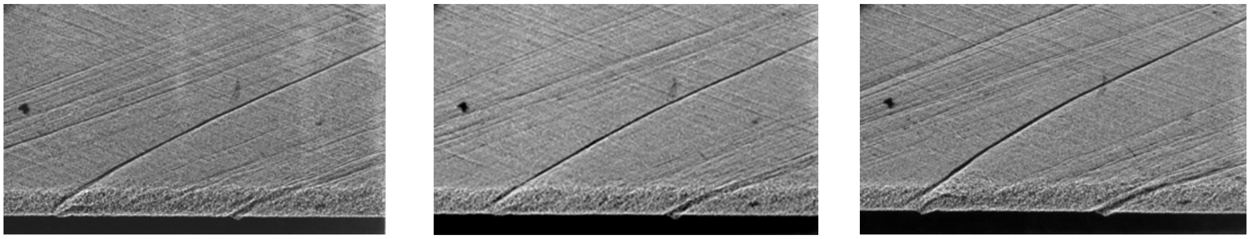

(a) $\bar{q}=1$, $\beta=0^\circ$ **(e)** $\bar{q}=1$, $\beta=30^\circ$ **(d)** $\bar{q}=2$, $\beta=15^\circ$

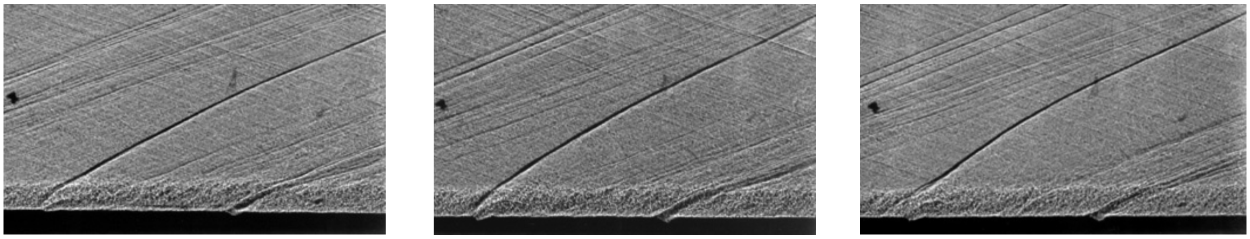

(c) $\bar{q}=1$, $\beta=15^\circ$ **(b)** $\bar{q}=2$, $\beta=0^\circ$ **(f)** $\bar{q}=2$, $\beta=30^\circ$

Figure 2. Nanoshadowgraphs with air injection.

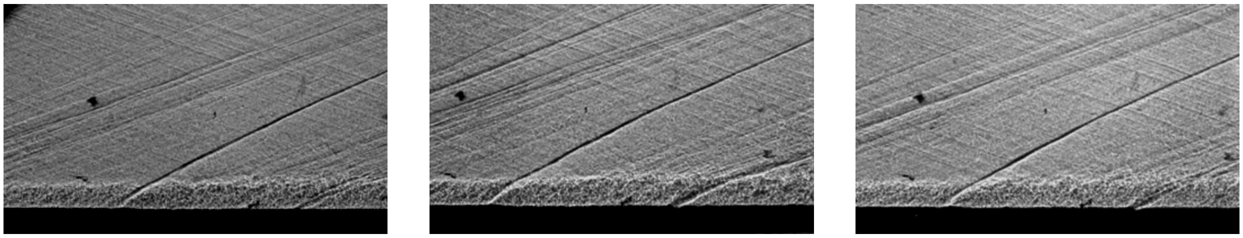

(a) $\bar{q}=1$, $\beta=0^{o}$ **(b)** $\bar{q}=1$, $\beta=15^{o}$ **(c)** $\bar{q}=1$, $\beta=30^{o}$

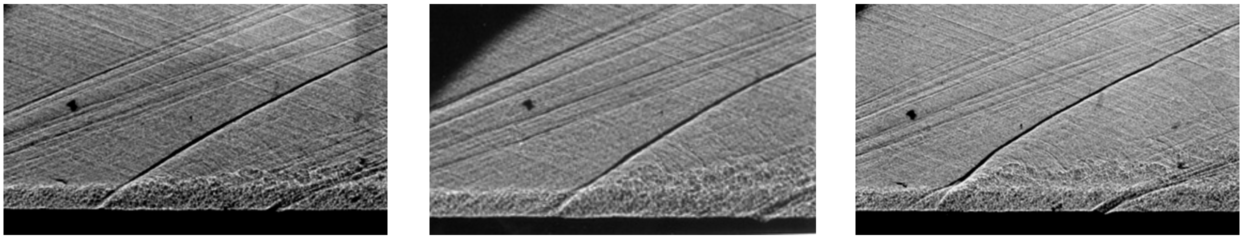

(d) $\bar{q}=2$, $\beta=0^{o}$ **(e)** $\bar{q}=2$, $\beta=15^{o}$ **(f)** $\bar{q}=2$, $\beta=30^{o}$

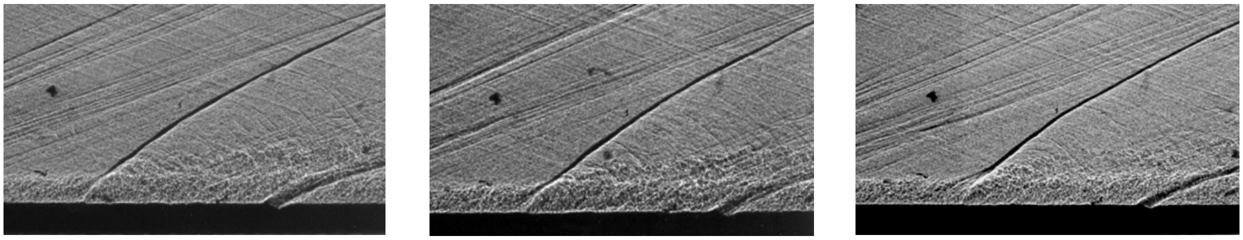

(g) $\bar{q}=3$, $\beta=0^{o}$ **(h)** $\bar{q}=3$, $\beta=15^{o}$ **(i)** $\bar{q}=3$, $\beta=30^{o}$

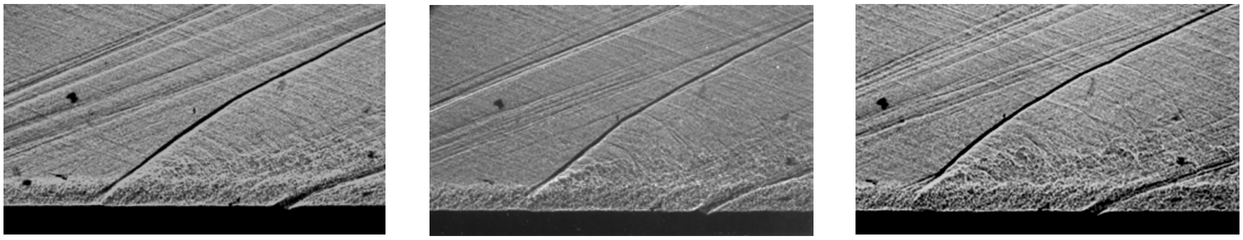

(j) $\bar{q}=3.5$, $\beta=0^{o}$ **(k)** $\bar{q}=3.5$, $\beta=15^{o}$ **(l)** $\bar{q}=3.5$, $\beta=30^{o}$

Figure 3. Nanoshadowgraphs with helium injection.

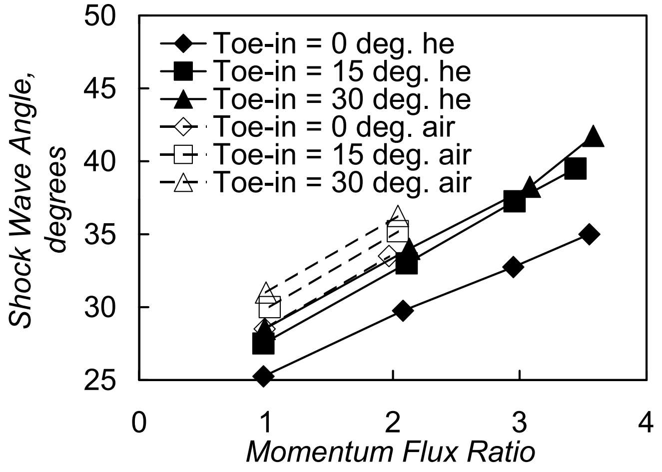

Figure 4. Initial oblique shock wave angles versus $\bar{q}$.

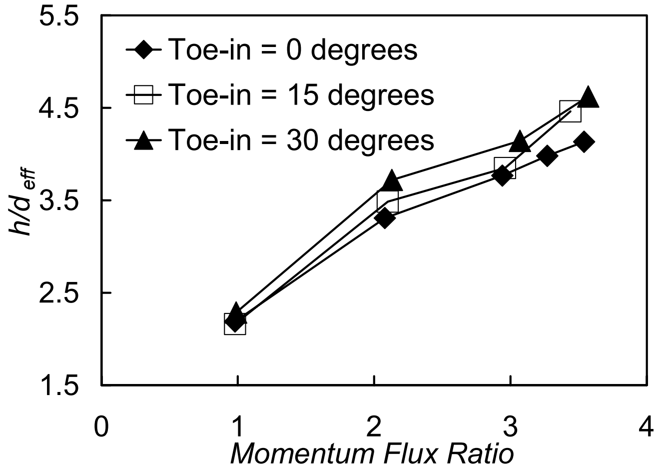

Figure 5. Penetration distance versus $\bar{q}$ with helium injection at an $x/d_{eq} = 11$.

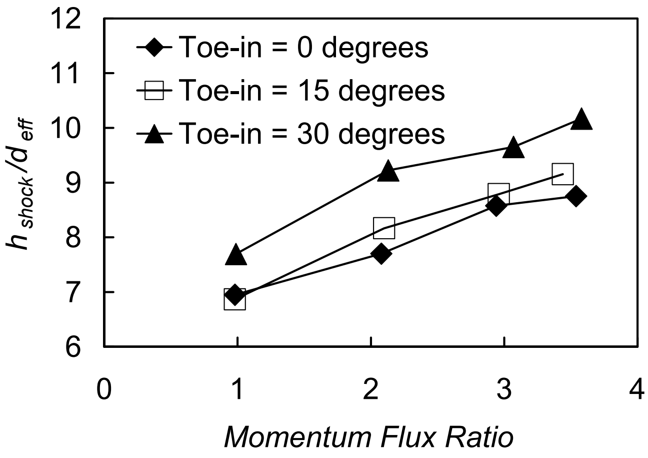

Figure 6. Oblique shock wave height versus $\bar{q}$ with helium injection at an $x/d_{eq} = 11$.

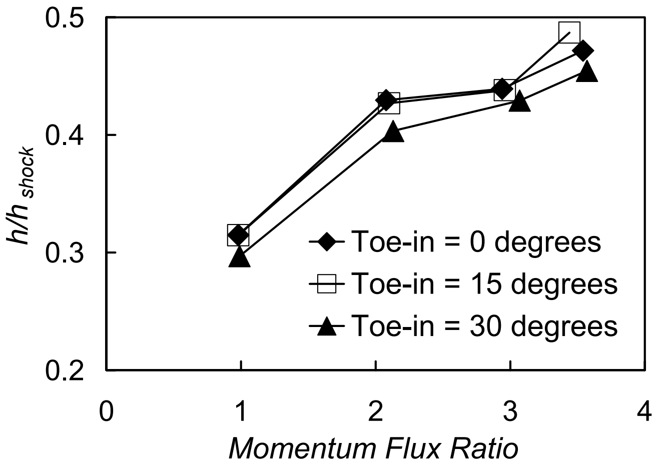

Figure 7. Penetration distance to shock wave height ratio versus $\bar{q}$ with helium injection at $x/d_{eq} = 11$.

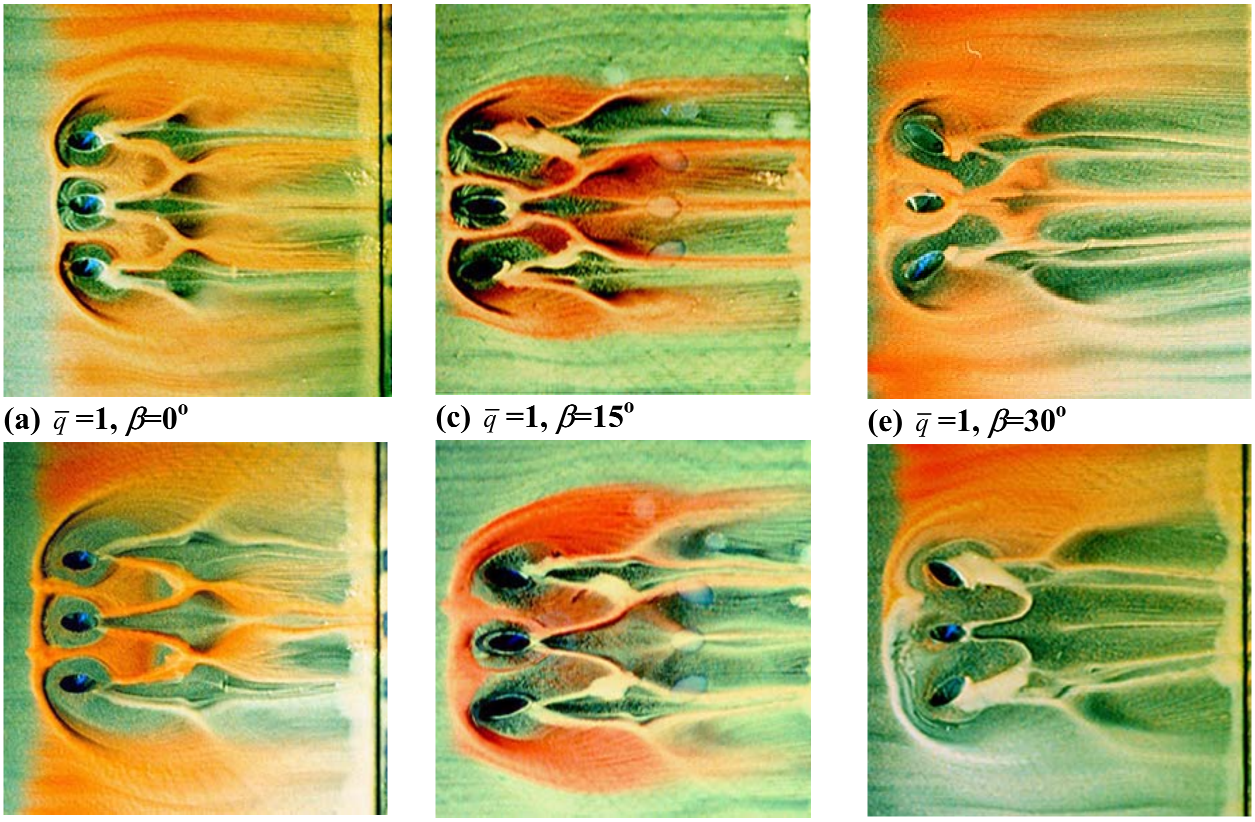

(a) $\bar{q}=1, \beta=0^{\circ}$ **(c)** $\bar{q}=1, \beta=15^{\circ}$ **(e)** $\bar{q}=1, \beta=30^{\circ}$

(b) $\bar{q}=2, \beta=0^{\circ}$ **(d)** $\bar{q}=2, \beta=15^{\circ}$ **(f)** $\bar{q}=2, \beta=30^{\circ}$

Figure 8. Surface Flow Pictures (Air).

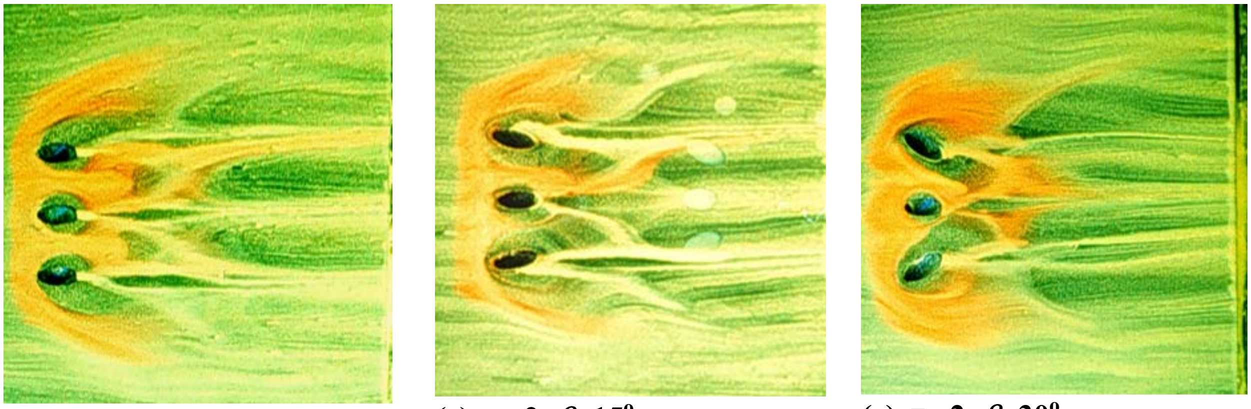

(a) $\bar{q}=2$, $\beta=0^{o}$ **(c) $\bar{q}=2$, $\beta=15^{o}$** **(e) $\bar{q}=2$, $\beta=30^{o}$**

(b) $\bar{q}=3$, $\beta=0^{o}$ **(d) $\bar{q}=3$, $\beta=15^{o}$** **(f) $\bar{q}=3$, $\beta=30^{o}$**

Figure 9. Surface Flow Pictures (Helium).

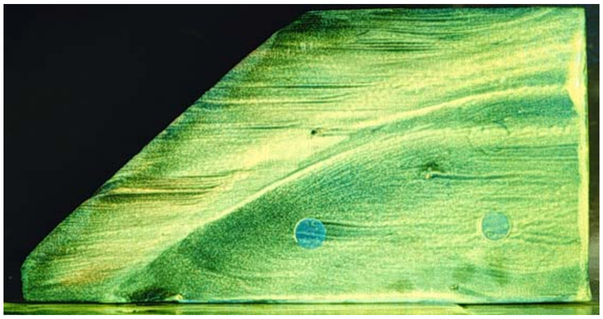

(a) $\bar{q}$ =2, β=15°

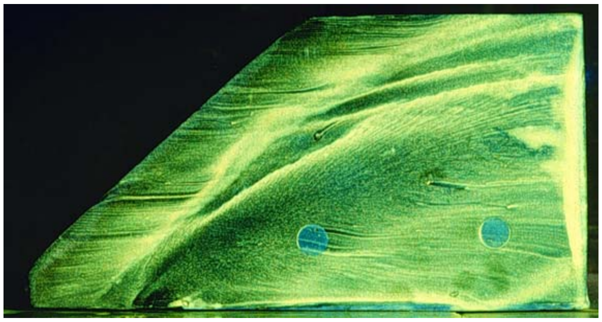

(b) $\bar{q}$ =3, β=15°

(c) Shadowgraph superimposed over the vertical plate, $\bar{q}$ =2, β=15°

Figure 10. Surface flow visualization on a longitudinal vertical plate through the center of the injector array with helium injection, β = 15°.

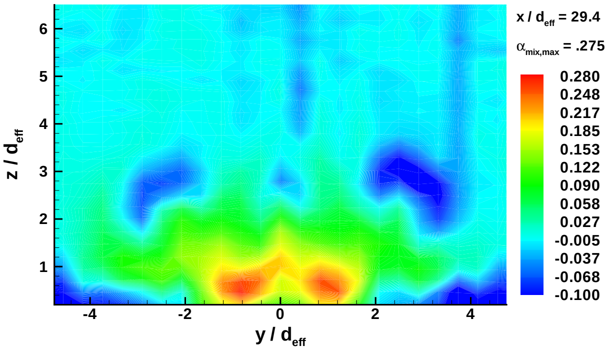

(a) $\bar{q} = 2, \beta = 0^{o}$

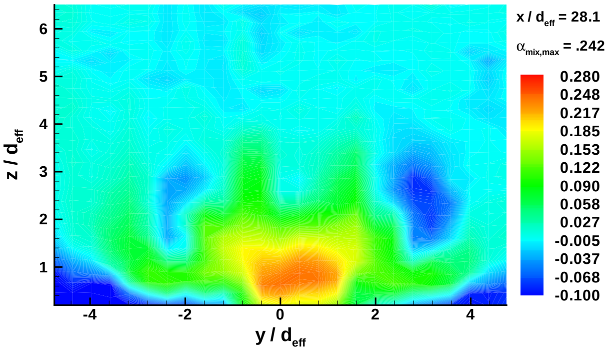

(b) $\bar{q} = 2, \beta = 15^{o}$

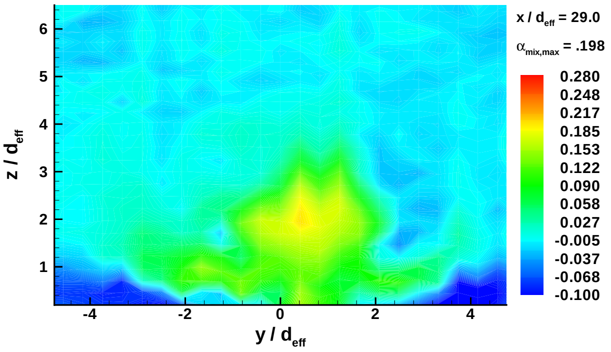

(c) $\bar{q} = 2, \beta = 30^{o}$

Figure 11. Mixing analogy profiles with heated air injection.

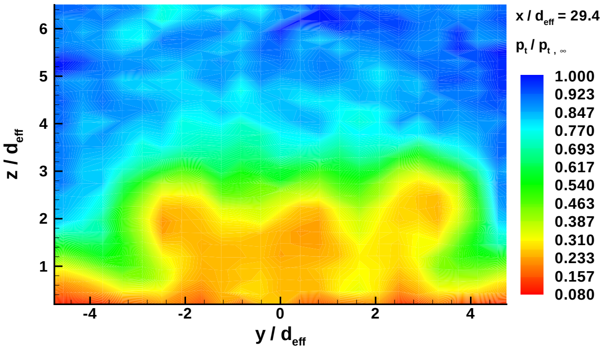

(a) $\bar{q} = 2, \beta = 0^o$

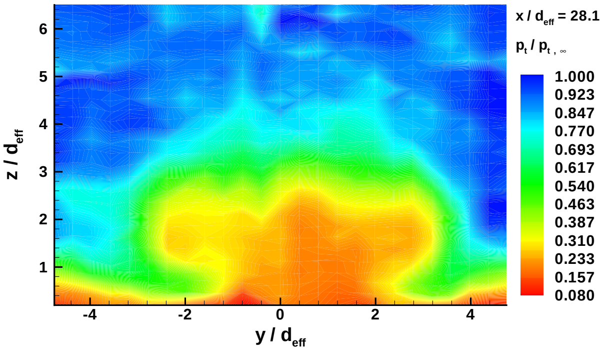

(b) $\bar{q} = 2, \beta = 15^o$

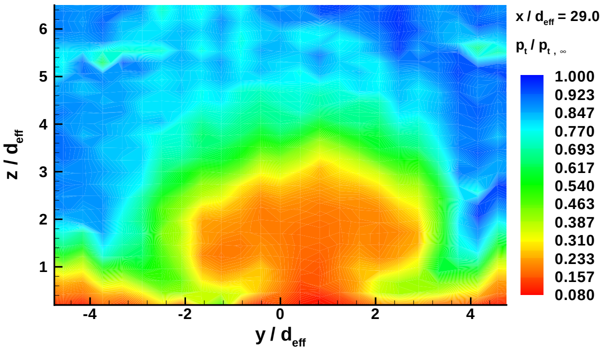

(c) $\bar{q} = 2, \beta = 30^o$

Figure 12. Total pressure contours with heated air injection.

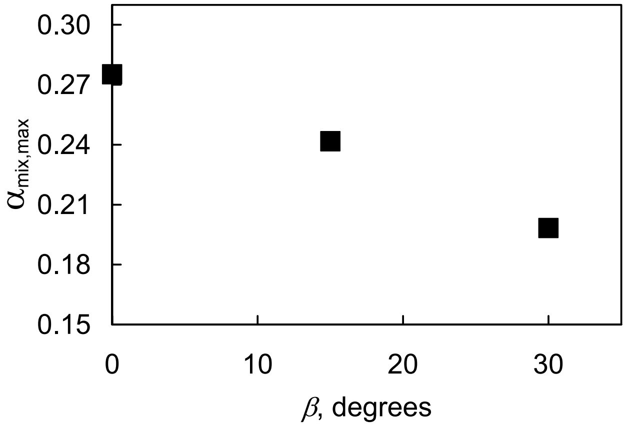

Figure 13. Maximum concentration levels vs. toe-in angle.

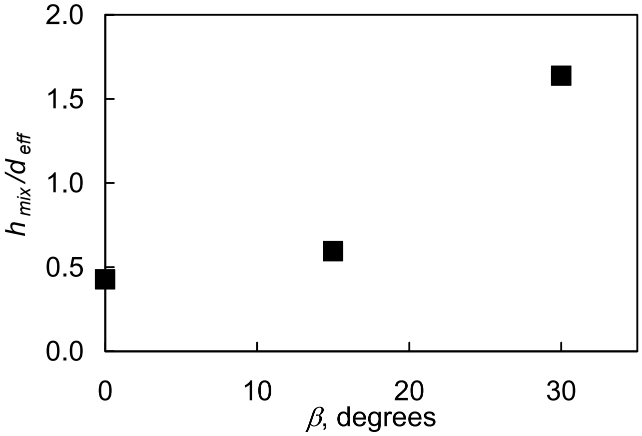

Figure 14. Maximum concentration vertical locations vs. toe-in angle.

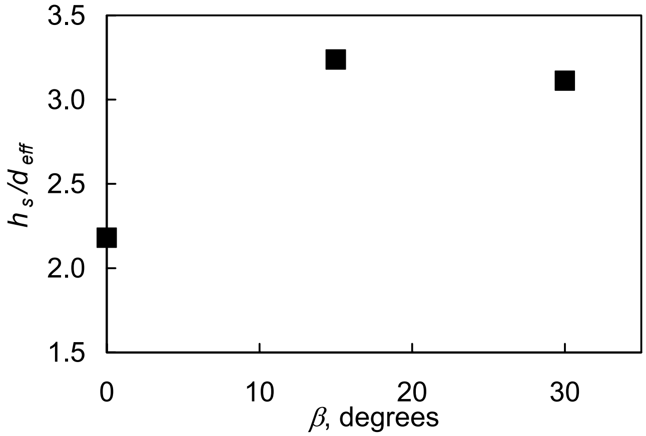

Figure 15. Plume penetration vertical distance vs. toe-in angle.

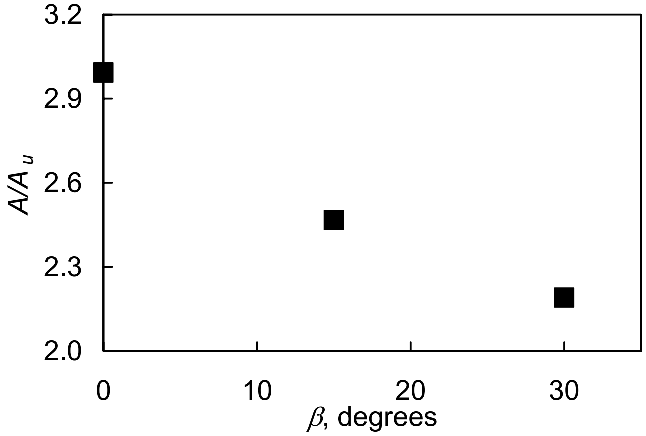

Figure 16. Over-stoichiometric plume areas vs. toe-in angle.

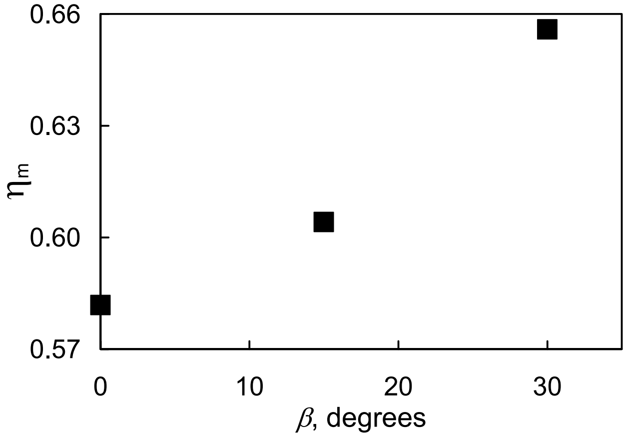

Figure 17. Injector mixing efficiency vs. toe-in angle.

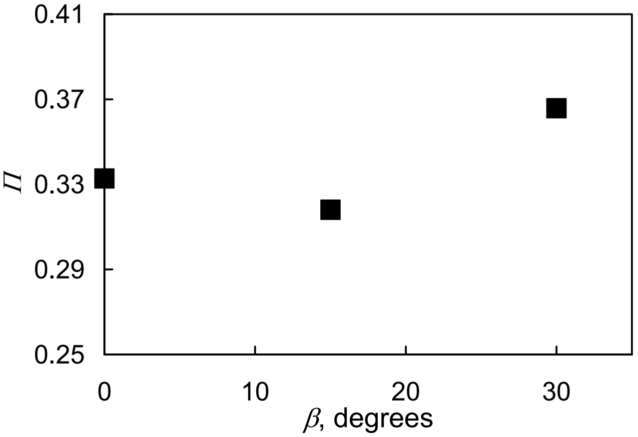

Figure 18. Total pressure loss parameter vs. toe-in angle.

Appendix C

Mixing Enhancement by Jet Swirl in a Multiport Injector Array in Supersonic Flow

(Abstract)

This paper presents the results of a study of the effects of swirl in the outer ports on the mixing of a three-hole injector array in a supersonic flow. The three jets were arranged flush with the test section floor and such that the interaction between the three plumes, the main flow and the jet swirl would instill strong vortical motions. Three different configurations were tested involving three round injection holes in a row. Swirlers were placed inside the two outer holes of the row injector to instill motion in the jets in two directions. Test conditions involved heated air injection into a Mach 3.0 air crosstream with an average Reynolds number of 4.9×10^7 per meter at jet to freestream momentum flux ratios of 1 and 2. The injectors each had an equivalent jet diameter of 4.12 mm. and a cross-stream spacing of 2.1 jet diameters between the jets. The primary qualitative observations were nano-shadowgraphs and surface oil flow visualization. The focus of the analysis of these pictures was based on understanding how the swirl of the outer injectors and the momentum flux ratio of the flow affect mixing and the shock wave structures in the jet area. Aerothermodynamic probe measurements were also performed at a downstream location with heated air injection to assess the total pressure losses and mixing potential of the flow. Results from the experiments showed improved mixing with an increase of jet to freestream momentum ratio and swirl of the injector array. Swirl also reduced the total pressure losses.

Nomenclature

A = Cross-sectional area

A_s = Area required for a uniformly stoichiometric jet.

α_s = C_2H_4-air stoichiometric mass fraction, 0.0680.

α_{mix} = Mass fraction mixing analogy

$\alpha_{mix,max}$ = Maximum mixing analogy mass fraction

C_d = Discharge coefficient

d_j = Jet diameter

d_{eq} = Equivalent jet diameter $=\sqrt{3}\, d_j$ for a 3-hole array

d_{eff} = Effective diameter of row injector

γ = Specific heat ratio

h_{mix} = Maximum concentration penetration height

h_o = Stagnation enthalpy

h_s = Stoichiometric plume penetration height

λ = Jet to freestream mass flux ratio $(\rho u)_j / (\rho u_{\infty}$

$\dot{m}_{f,mix}$ = Mixed fuel mass flow rate

$\dot{m}_{f,tot}$ = Total fuel mass flow rate

η_m = Mixing efficiency

p = Static pressure

p_t = Total Pressure

$\bar{q}$ = Jet to freestream momentum flux ratio

$\boldsymbol{S}$ = Swirl number

s = Entropy

ρ = Density

T = Static temperature

T_t = Total temperature

u = Streamwise velocity

u_s = Streamwise velocity with respect to the flow swirler

w_s = Spanwise velocity with respect to the flow swirler

x = Streamwise coordinate

y = Spanwise coordinate

z = Vertical coordinate

Subscripts

∞ = Freestream

j = Injector

Introduction

Studies of mixing enhancement in high speed flows have application in a number of fields such as fuel injection in ramjets and scramjets, thermal protection systems and vehicle control by jet thrusters. One of the many challenges involved in the pursuit of a viable hypersonic air-breathing propulsion system is mixing enhancement in supersonic fuel injectors. Enhanced mixing and rapid combustion imply a reduction of the combustor length in a supersonic ramjet engine, thus reducing the skin friction drag and increasing the potential for positive net thrust (Heiser et al., 1994).

A multitude of experiments have been performed in the field of injection in supersonic flows using numerous techniques, such as swept ramps (Hartfield et al., 1994) and (Riggins and Vitt, 1995), slots (Lewis and Schetz, 1997) and (Schetz et al., 1992), transverse injection (Schetz, 1970), (E. Fuller et al., 1991), (Barber et al., 1995), (McClinton, 1972), and (Rogers, 1971) and jet swirl (Schetz, 1980), (Povinelli and Ehlers, 1972), and (Schetz and Swanson, 1973). An extensive review of injector mixing characteristics is given in Schetz et al. (1990).

The general interference effects generated by multi-hole transverse injector arrays have been capitalized on, in the design of the "aero-ramp" injector by Cox et al. (1994,1998), R. Fuller et al. (1996), and Schetz et al. (1998). The effects of toe-in angle on a single row injector array have also been examined by Jacobsen et al. (1998). In that study it was found that increasing the toe-in angle of the exterior injector holes greatly increased the mixing efficiency and core penetration of the overall jet plume generated by the array.

Here, experiments were undertaken to further understand the complex interactions of a single row injector array. The effects of injector jet vorticity were explored using three round injection holes in a row exposed to a Mach 3.0 cross stream. Flow swirling guide vanes were place inside the two outer holes of the injector array. Shadowgraph and surface flow visualization pictures were taken at momentum flux ratios, $\bar{q}$, of 1 and 2 to help qualitatively understand the nature of the flows. Aerothermodynamic probing was also performed at a downstream location with heated air injection at $\bar{q}=2$ to help quantify the pressure losses and mixing capability of the injector array.

Test Facilities

Experiments were performed in the Virginia Tech 23 X 23 cm blowdown supersonic wind tunnel. The tunnel was configured with a half nozzle test section resulting in a freestream Mach number of 3.0. The test section dimensions were 23 cm wide by 11.5 cm high and 30 cm long in the streamwise direction. Data acquisition was performed with a PC and a 16 channel 16 bit A/D converter.

Injector Models

The injector model used in this study had three - 2.38 mm diameter holes horizontally placed 8.47 mm apart in a row as shown in Figure 1. The injector had an equivalent single jet diameter of 4.12 mm and a cross stream spacing of 2.1 equivalent jet diameters between the injector holes. The dimensions of the holes allow the flow to exit the middle injector sonically and the exterior holes supersonically under all back pressure conditions. The two outer holes were fitted with plugs with 0° or 45° angled guide vanes or "flow swirlers" just before their converging passages. The flow swirlers were inserted into the injector in order to either reinforce the vortices produced by the interference of the jets[19], produce no swirl or to go against the direction of the multiple jet interference induced vorticity. The middle hole was placed at a 30° transverse angle from the freestream to improve the jet penetration and help reduce the overall total pressure losses of the injector.

Test Matrix

All tests were performed at a freestream Mach number of 3.0. Experiments were performed while injecting air in order to simulate hydrocarbon fuels without the safety hazard associated with combustion. The tunnel average freestream conditions were 6.1 atm, 285 K. Corresponding to a freestream velocity of 607 m/s and a Reynolds number of $4.9\text{x}10^7$ per meter. Tests were performed with nominal jet to freestream momentum flux ratios of 1 and 2, where:

$$\bar{q}=\frac{\left(\rho u^2\right)_j}{\left(\rho u^2\right)_\infty}=\frac{\left(\gamma p M^2\right)_j}{\left(\gamma p M^2\right)_\infty} \tag{1}$$

The positive x-axis is in the downstream direction, the y-axis in the horizontal direction, and the positive z-axis in the vertical direction. Axial distance was normalized by the "effective" diameter:

$$d_{eff} = d_{eq}\sqrt{C_d} \tag{2}$$

where C_d is the discharge coefficient and d_{eq} is the injector equivalent jet diameter, defined as the diameter of an equivalent single jet that has the same area as the three jets.

The induced jet swirl of the injectors was quantified by the swirl number, ***S***, which is defined as:

$$S = w_s / u_s \tag{3}$$

where w_s and u_s are the spanwise and streamwise velocities through the guide vanes in the flow swirler. For the 45 degree swirl guide vanes, the swirl number was defined here as 1 for the reinforcing jet interference vortex swirl and -1 for the counter swirl.

Test Procedures

Nano-shadowgraphs

Spark shadowgraphs were taken using a Nanopulser spark with an exposure time of $2\text{x}10^{-8}$ sec. permitting a clear image of the turbulent eddies in the flow.

Surface Flow Visualization

Visualization of the surface flow patterns near the injectors was accomplished with 500 cS silicone oil mixed with two colors of fluorescent dye. A thin layer of fluorescent green oil was placed all around the injector, and a thin strip of fluorescent red oil was placed in front of the injector holes prior to a test. The patterns were illuminated with a 100-watt ultraviolet lamp, and pictures were taken with a 35 mm camera after each run and also recorded on videotape during tunnel operation.

Aerothermodynamic Probing

Aerothermodynamic measurements of the flowfield were taken with heated air injection 27.3 d_{eq} downstream from the leading edge of the injector arrays. The sampling was accomplished with a Pitot, a cone-static, and a total temperature probe. The Pitot probe had a 1.59 mm outer diameter and 1.04 mm inner diameter which gave a capture area of 0.85 mm^2. The cone-static probe consisted of a 1.59 mm outer diameter tube with a 10 degree cone half-angle. The total temperature probe also consisted of 1.59 mm outer diameter tubing with an inner diameter of 1.04 mm, and 3 small holes drilled around the tube to improve the recovery factor of the probe. The capture to recovery area ratio was 5 to 1. An exposed junction type-K thermocouple with a 0.25 mm diameter bead was placed inside the probe.

Species Composition Mixing Analogy

The air in the injector plenum chamber was heated by approximately 60 °C using two 2000W-cartridge heaters during the aerothermodynamic sampling tests to obtain a temperature profile analogous to the mass fraction of a simulated hydrocarbon gas with a molecular weight similar to air, such as ethylene. The mass fraction mixing analogy, α_{mix}, is defined as:

$$\alpha_{mix} = \frac{T_t - T_{t,\infty}}{T_{t,j} - T_{t,\infty}} \tag{4}$$

Data Reduction

The aerothermodynamic measurements with heated air injection made with the three probes were reduced in a standard fashion (R. Fuller et al[17]). The reduction was performed using an iterative scheme involving the perfect gas relations, the Rayleigh-Pitot formula, and the Taylor-McColl cone flow solutions.

Results and Analysis

Nano-shadowgraphs

Figure 2 shows the shadowgraphs taken with a $\bar{q}$ of 1 and 2. The pictures are shown with the freestream flow going from left to right and the injection up from the bottom. The injector holes are located just to the right of the main shock wave. The second weaker shock wave, shows a small disturbance where the injector plate mates with the test section floor. The turbulent boundary layer on the wall can be clearly seen. These shadowgraphs give an integrated 2-D image across a 3-D flow. One can observe penetration trends of the injected air into the air freestream as well as the oblique shock waves. The shadowgraph images have a lot of interesting features such as the structure of the bow shocks, the plume, kinks in the bow shocks, and penetration trends. As the distance increases downstream from the injector holes, the angles of the shock can be seen to approach that of a Mach wave, which is approximately 19.5 deg. in a Mach 3 flow. The thick boundary layer interferes with the interpretation of the shock wave structure of the region inside it and also obscures the front part of the jet plume.

One feature of interest is the change in the shock structure directly in front of the injector holes. In Figure 2(b) there is a clear difference in the position of the bow shock for the middle and outside injector holes. This effect is diminished with the advent of swirl in either direction. Swirl in the reinforcing direction seems to lessen the initial shock strength and to slightly reduce the shock wave height.

Surface Flow Visualization

Figure 3 shows the surface oil flow pictures taken while injecting heated air with jet to freestream momentum flux ratios of 1 and 2. The freestream flow is from left to right, and the exit of the injectors can be seen as black round or elliptical holes near the left edge. The boundary where the downstream end of the injector block mates with test section floor, 10.7 equivalent jet diameters downstream from the leading edge of the middle injector hole, can be seen at the end of the pictures.

A close inspection of the images can tell much about the various features involved with the flow patterns created by the injectors. Some of these important features are the trajectory of the jet plumes along the wall, the width of the individual jets and overall plumes, the size of the separation zones in front of the injector hole, the separation regions behind the exterior hole trailing edges, and the rate at which the overall plume width recovers from the effects of swirl in the exterior injector holes. The plume width is apparent in these pictures, because the plume impacts the wall at these modest momentum flux ratios. The width of the overall plume can be seen to increase with injector momentum flux ratio.

One interesting feature of the surface flow patterns is the size of the separation zone directly in front of the injector holes. The separation zone is greatly increased with the increase of momentum flux ratio for all three injectors configurations studied. The large increase in the separation zones size is partly due to the configuration of the three holes. Since the exterior holes extend further upstream than the middle hole, they create a pocket-like effect. Furthermore, with increased momentum flux ratio, the surface flow between the holes is cut off. Thus, the combination of these two effects increases the size of the separation zone. There is no real distinction between the effects of swirl in the surface flow near the injector holes. The plume structures seem to be very similar in all three configurations, though, as will be seen in the mixing analogy study, there is quite a difference in the plume height and structure in the three injector configurations.

Mixing Analogy Profiles

Figure 4 presents the results of the total temperature measurements for the heated air test cases in the form of the mixing analogy, α_{mix}. The three profiles were generated at the same sampling station at a nominal jet to freestream momentum flux of 2.0. The contour color scale and spacing are the same in all three plots. Note that the station location is constant, but due to the normalization of the data, the x/d_{eff} station sampling location varies from 30.8 to 31.4 as a result of small changes in the discharge coefficient. Two regions where the mixing analogy is reduced below zero are the boundary layer, and the three locations to the two sides and the top middle of the jet plumes which are due to induced vorticity in the flow. Any point where T_t falls below $T_{t,\infty}$ implies $\alpha_{mix}<0$ from equation (3). The vortically induced cold spots become more apparent with the reinforcing injector swirl and diminish substantially in the counter-swirl case. The maximum values of the mixing analogy correspond to the local station maximums. Note that the two local maximums in the mixing profiles represent the locations where the injected gas is converging between the injector jet plumes. One other interesting feature of the mixing analogy profiles is the horn-like protrusions on the top of the local maximum regions.

Total Pressure Contours

Figure 5 presents the total pressure contours of the three injectors, where the contour color scale and spacing are consistent between the three plots. Some interesting features in these profiles are the locations of the total pressure minimums in the flow, which correspond to the three injector plumes and the region of pressure loss above the middle plume. In the reinforcing swirl case in Figure 5(a), the left plume has a lower vertical position of the total pressure minimum, and this lower plume position reduces the overall pressure losses of the injector over the other two cases. Since the mixing analogy pictures are really profiles of the total temperature, the local cold spots are at the same location as the leading ends of the total pressure loss plumes. The profiles in conjunction with Crocco's vorticity theorem show good evidence of vorticular motion in the flow. Crocco's Theorem states for a steady, inviscid flow with negligible body forces:

$$T\nabla s = \nabla h_o - \nabla \times \omega \tag{5}$$

where s is the entropy, h_o is the enthalpy, and ω is the vorticity of the flow. Thus, it is possible for a vorticular structure and a change in entropy to reduce the total temperature of the system, since total temperature can be directly expressed in terms of enthalpy. Similar results were found in the examination of toe-in angle by Jacobsen et al. (1998).

Maximum Concentration Levels

The local maximum concentration levels of the three mixing analogy profiles, $\alpha_{mix,max}$, are presented in Figure 6, and the vertical heights of the local maximums, h_{mix}/d_{eff}, are shown in Figure 7. In both graphs, the right and left core concentration maximums are shown for each mixing analogy profile. From the graphs, it is evident that the maximum concentration levels are reduced and the penetration distance is increased with the introduction of swirl in either direction.

Plume Penetration

The maximum penetration heights of the mixing analogy plumes were measured, and the results are presented in Figure 8. The plume penetration, h_s, is defined here as the vertical distance from the wall to the edge of the mixing region where the mass fraction mixing analogy is equal to the stoichiometric value of ethylene, 0.0680. The results show no significant change in stoichiometric plume penetration height produced by introducing swirl to the flow.

Mixing Efficiency

The mixing efficiency, as defined by Mao et al. (1990), is represented as "that fraction of the least available reactant which would react if the fuel-air mixture were brought to a chemical equilibrium without additional local or global mixing". This means that the local fuel and air are considered mixed respectively in the rich and lean fuel areas. Here:

$$\eta_m \equiv \frac{\dot{m}_{f,mix}}{\dot{m}_{f,tot}} = \frac{\int \alpha_r \rho u dA}{\int \alpha_{mix} \rho u dA} \tag{6}$$

where,

$$\alpha_r \equiv \begin{cases} \alpha_{mix} & ,\alpha_{mix} \le \alpha_s \\ \left(\dfrac{1-\alpha_{mix}}{1-\alpha_s}\right)\alpha_s & ,\alpha_{mix} > \alpha_s \end{cases} \tag{7}$$

The results in Figure 9 show that the mixing efficiency of the reinforcing swirl configuration was increased by 7 percent over the no-swirl case. The mixing efficiency did not increase significantly in the counter-swirl test configuration. This supports the conclusion that the overall mixing of the injector is improved by reinforcing the already existing multiple jet interference vortex structures.

Total Pressure Loss Parameter

The total pressure losses have been quantified using the total pressure loss parameter defined by R. Fuller et al. (1996). This method simplifies the analysis by allowing an assessment of the losses within the sampling area. This total pressure loss parameter is defined as:

$$\Pi = \frac{\int \rho u \left(p_{t,\infty} - p_t\right) dA}{\rho_\infty u_\infty p_{t,\infty} A_s + \rho_j u_j p_{t,j} A_j} \tag{8}$$

where

$$A_s = \frac{\lambda}{\alpha_s} A_j \tag{9}$$

Thus for this parameter, a fuel injector incurring no losses would have $\Pi = 0$. Figure 10 presents the results, which show the reinforcing swirl test case to have the lowest losses. The minimum result for this injector configuration could be due to the lower initial shock angle over the other two cases, which can be seen in the shadowgraph images. Furthermore, the left plume of the reinforcing vortex swirl case as seen in the total pressure profiles in figure 5(a) is considerably lower than the other two plumes.

Plume Area

The overall plume area of the mass fraction mixing analogy is defined here as the total area of the plume which has an α_{mix} greater or equal to the stoichiometric value of ethylene, 0.0680. Results from this study showed that the stoichiometric plume area stayed relatively constant throughout the three test cases.

Summary and Conclusions

Experiments were performed to study the effects of swirl in the outer ports on the mixing of a three-hole injector array in a Mach 3.0 flow. The primary experiments performed were nano-shadowgraphs, surface oil flow visualization, and aero-thermodynamic probing. The focus of the analysis pictures was based on understanding how the swirl of the outer injectors and the momentum flux ratio of the flow affect mixing, the shock wave structures in the jet area, and the total pressure losses of the injectors.

The shock wave structures in the jet area were studied via the analysis of the shadowgraph and surface oil flow visualization pictures. The shadowgraph pictures showed trends in the shock waves associated with the introduction of swirl and momentum flux ratio. The effective size of the separation zones was studied in an attempt to understand how they affect the flow. Aerothermodynamic probing measurements with heated air injection were also performed at a downstream station to qualitatively assess the total pressure losses and mixing potential of the flow.

The main conclusions drawn from the experiments are as follows:

1. The vertical penetration distance of reinforcing and counter swirl injector configurations are very comparable, and both are larger than the no swirl baseline injector configuration.
2. Both penetration and shock height increase with momentum flux ratio.
3. The overall plume width increases with momentum flux ratio.
4. The initial oblique shock wave angle of the injector increases with momentum flux ratio and decreases with swirl.
5. The size of the separation zones in front and behind the injector holes increases with momentum flux ratio.
6. The maximum concentration level of the mixing analogy plumes are reduced and the penetration distances are increased with an increase in swirl.
7. There was relatively no change in the over-stoichiometric plume area with the introduction of swirl.
8. The overall mixing and penetration of the injector is improved with an increase of swirl.
9. The results of the total pressure loss parameter study show the reinforcing swirl injector configuration to have the lowest losses over the integrated area. The minimum result of the reinforcing swirl injector configuration could be due to a lower initial shock height than the other injector configurations.
10. The reinforcing swirl injector configuration showed the best mixing performance in terms of maximum analog to concentration, total pressure losses, and mixing efficiency. Based on the present results, one might conclude that a good injector should have flow swirl introduced in the outer injectors which would reinforce the naturally induced interference vortex structures, at this spacing.
11. Further studies of interest might include the integration of swirl and toe-in angle into the injector to see any further advantages associated with the induced vorticular motion of the injector arrays. Another study of interest would be to vary the spacing between the jets to see how mixing and blockage are affected.

Acknowledgements

This research was sponsored and funded by Phoenix Solutions Co., Minneapolis, MN, under a USAF SBIR Phase II award. The interest and support of Dr. Gary Hanus and Mr. Kevin Uznanski of Phoenix Solutions Co. and Mr. Charles Bauer, Technical Contract Manager, WL/POP, Wright Patterson AFB is greatly appreciated.

References

Barber, M.J., Roe, L.A., and Schetz, J.A., 1995, "Simulated Fuel Injection Through a Wedge Shaped Orifice in a Supersonic Flow," AIAA Paper 95-2559, July.

Cox, S.K., Fuller, R.P., and Schetz, J.A. 1994, "Vortical Interactions Generated By a Injector Array to Enhance Mixing in a Supersonic Flow," AIAA Paper 94-0708, January.

Cox-Stouffer, S.K. and Gruber, M.R., 1998, "Effects of Spanwise Injector Spacing on Mixing Characteristics of Aerodynamic Ramp Injectors," AIAA Paper 98-3272, July.

Fuller, E.J., Mays, R.B., Thomas, R.H., and Schetz, J.A., 1991, "Mixing Studies of Helium in Air at Mach 6," AIAA Paper 91-2268, June.

Fuller R.P., Nejad, A.S., and Schetz, J.A., 1996, "Fuel-Vortex interactions For Enhanced mixing in Supersonic Flow," AIAA Paper 96-2661, July.

Hartfield, R.J., Hollo, S.D., and McDaniel, J.C., 1994, "Experimental Investigations of a Supersonic Swept Ramp Injector using Laser Induced Iodine Fluorescence," *Journal of Propulsion and Power*, Vol. 10 No. 1, pp. 129-135, January-February.

Heiser, W.H., Pratt, D.T., Daley, D.H., and Mehta, U.B., 1994, "Hypersonic Airbreathing Propulsion," in AIAA education series, Przemieniecki, J.S. (Edit.) AIAA, Washington, D.C..

Jacobsen, L.J., Schetz, J.A., and Ng, W.F., 1998, "The Flowfield Near a Multiport Injector Array in a Supersonic Flow," AIAA Paper 98-3126, July.

Lewis, D.P. and Schetz, J.A., 1997, "Tangential Injection from Overlaid Slots into a Supersonic Stream," *Journal of Propulsion and Power*, Vol. 13, No. 1, pp. 59-63, January-February.

Mao, M. Riggins, D.W., and McClinton C.R., 1990, "Numerical Simulation of Transverse Fuel Injection," NASP CR 1089, May.

McClinton, C.R., 1972, "The effect of Injection Angle on the interaction Between Sonic Secondary Jets and a Supersonic Freestream," NASA TND-6669, February.

Povinelli, L.A. and Ehlers, R.C., 1972, "Swirling Base Injection for Supersonic Combustion Ramjets," *AIAA Journal*, Vol. 10 No. 9, pp. 1243-1244, September.

Riggins, D.W. and Vitt, P.H., 1995, "Vortex Generation and Mixing in Three-Dimensional Supersonic Combustors," *Journal of Propulsion and Power*, Vol. 11, No. 3, pp. 419-426, May-June.

Rogers, R.C., 1971, "A Study of the Mixing of Hydrogen Injected Normal to a Supersonic Airstream," NASA TN L-7386, Langley Research Center, March.

Schetz, J.A., 1970, "Interaction Shock Shape for Transverse Injection," *Journal of Spacecraft and Rockets*, Vol. 7, No. 2, pp.143-149, February.

Schetz, J.A. and Swanson R.C., 1973, "Turbulent jet Mixing at High Supersonic Speeds," *Zeitschrift Für Flugwissenschaften*, Vol.21, pp.166-173.

Schetz, J.A., 1980, "Injection and Mixing in a Turbulent Flow," AIAA, New York, New York.

Schetz, J.A., Thomas, R/H., and Billig, F.S., 1990, "Mixing of Transverse Jets and Wall Jets in Supersonic Flow," IUTAM Symposium on Separated Flows and Jets, Novosibirsk, July.

Schetz, J.A., Billig, F.S., Favin, S., and Gilreath, H.E., 1992, "Effects of Pressure Mismatch on Slot Injection in a Supersonic Flow," *International Journal of Turbo and jet Engines*, Vol. 9, No. 2, pp. 135-146.

Schetz, J.A., Cox-Stouffer, S.K., and Fuller, R.P., 1998, "Integrated CFD and Experimental Studies of Complex Injectors In Supersonic Flows (Invited)," AIAA Paper 98-2780, June.

Appendix (Uncertainty Analysis)

The estimates of the uncertainty in the measured quantities are based on error bounds of 95% (20:1 odds) and the Euclidean norm. The calculated error in $P_{t,\infty}$, $P_{t,j}$, and $P_{t,1}$ were respectively, ±0.07 atm, ±0.004 atm, and ±0.04 atm. The error in $T_{t,\infty}$, $T_{t,j}$, and T_t were each equal to ±0.4 °K. The error in local velocity, Mach number, and density were ±0.7 m/s, ±0.03, and ±0.004 kg/m^3. The error in position was ±0.08 mm. The error in α_{mix} was ±0.005, η_m was ±0.01, and in Π was ±0.05.

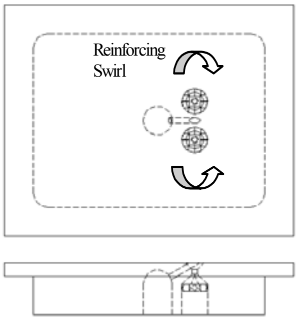

Figure 1 Transverse Injector Model

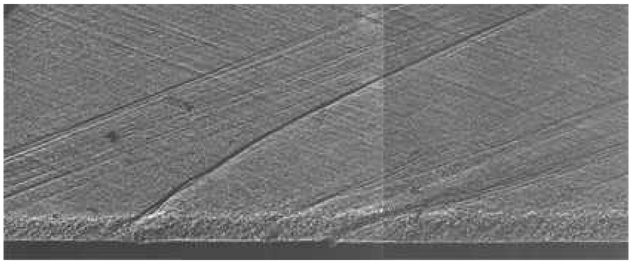

(a) $\bar{q} = 2$, Reinforcing Swirl

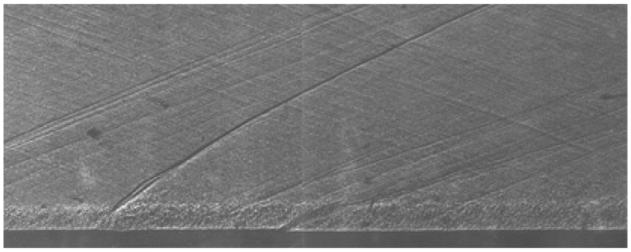

(b) $\bar{q} = 2$, No Swirl

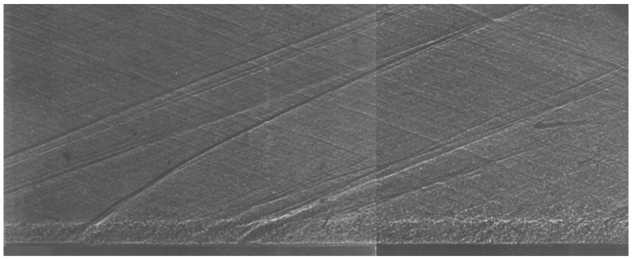

(c) $\bar{q} = 2$, Counter Swirl

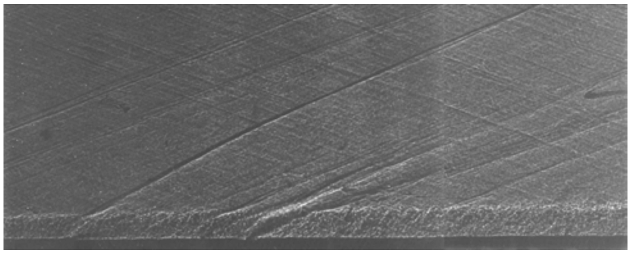

(d) $\bar{q} = 1$, Reinforcing Swirl

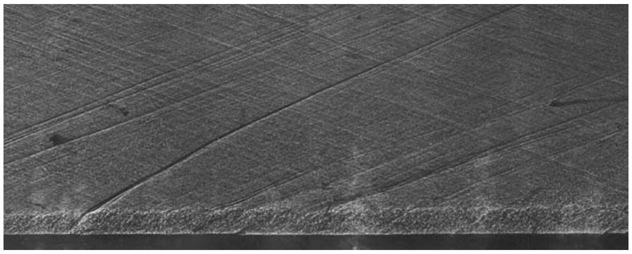

(e) $\bar{q} = 1$, No Swirl

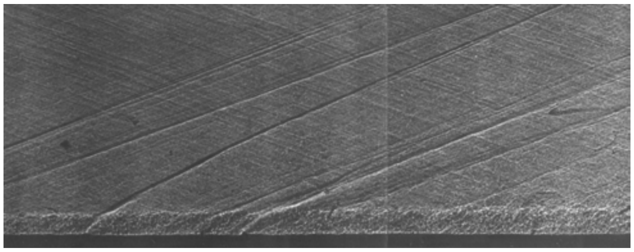

(f) $\bar{q} = 1$, Counter Swirl

Figure 2 Shadowgraphs

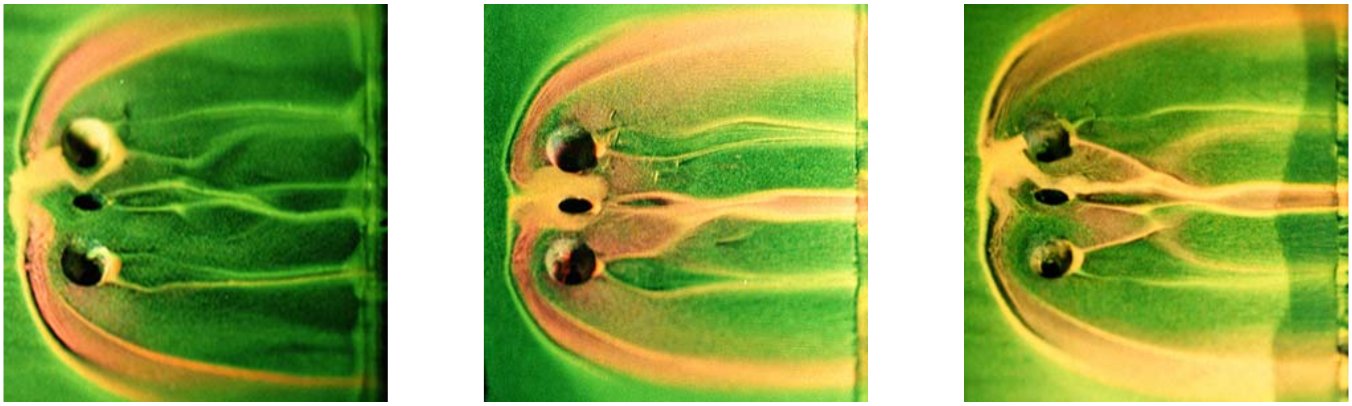

(a) $\bar{q}$ **= 2, Reinforcing Swirl** **(b)** $\bar{q}$ **= 2, No Swirl** **(c)** $\bar{q}$ **= 2, Counter Swirl**

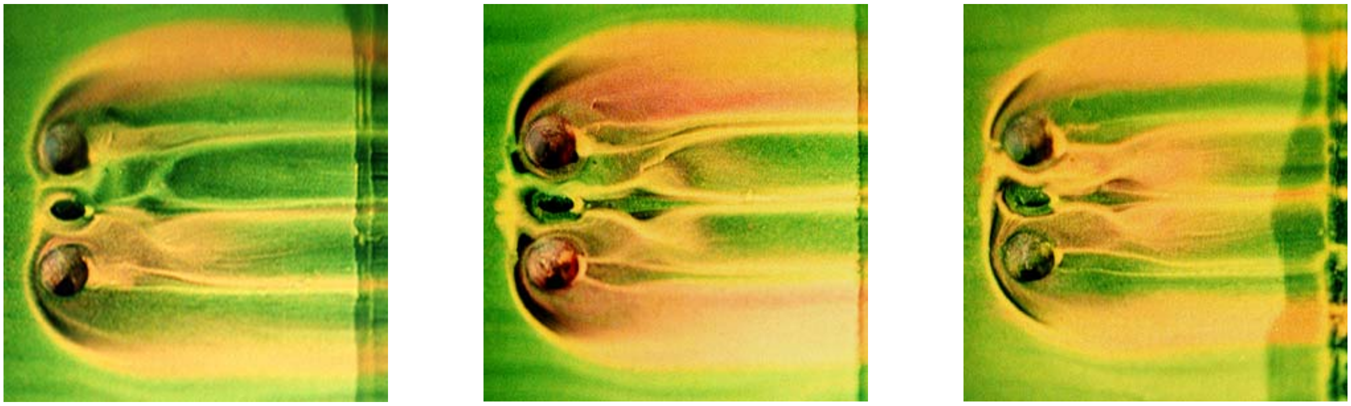

(d) $\bar{q}$ **= 1, Reinforcing Swirl** **(e)** $\bar{q}$ **= 1, No Swirl** **(f)** $\bar{q}$ **= 1, Counter Swirl**

Figure 3 Surface Oil Flow Visualization

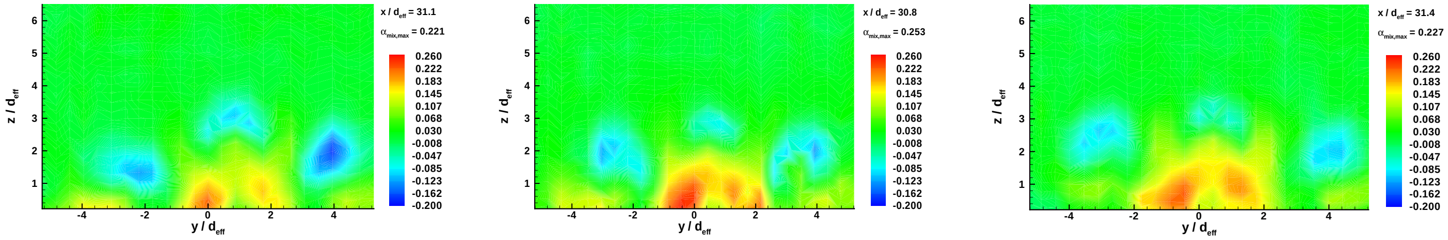

(a) $\bar{q} = 2$**, Reinforcing Swirl** **(b)** $\bar{q} = 2$**, No Swirl** **(c)** $\bar{q} = 2$**, Counter Swirl**

Figure 4 Mixing Analogy Profiles With Heated Air Injection

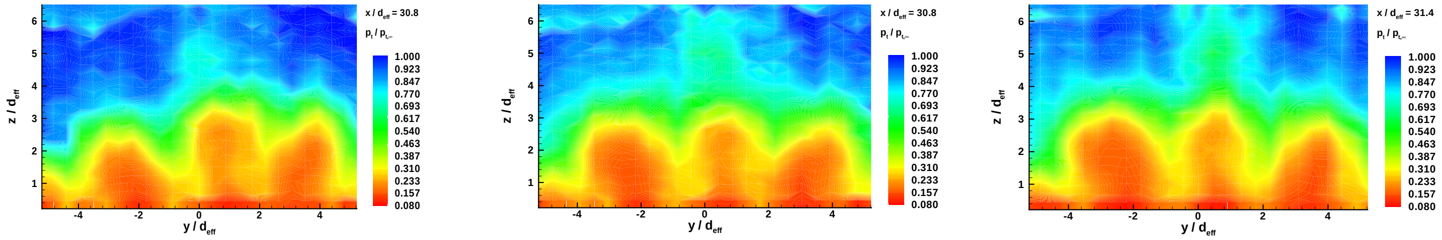

(a) $\bar{q} = 2$**, Reinforcing Swirl** **(b)** $\bar{q} = 2$**, No Swirl** **(c)** $\bar{q} = 2$**, Counter Swirl**

Figure 5 Total Pressure Contours With Heated Air Injection

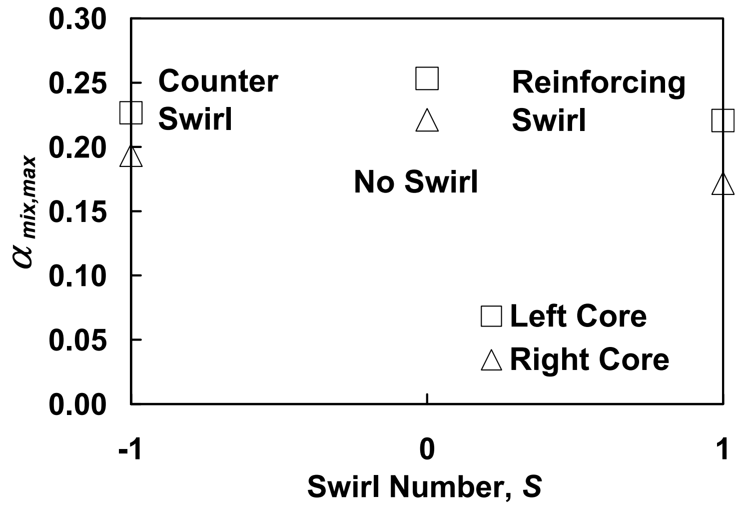

Figure 6 Maximum Concentration Levels vs. Guide Vane Angle

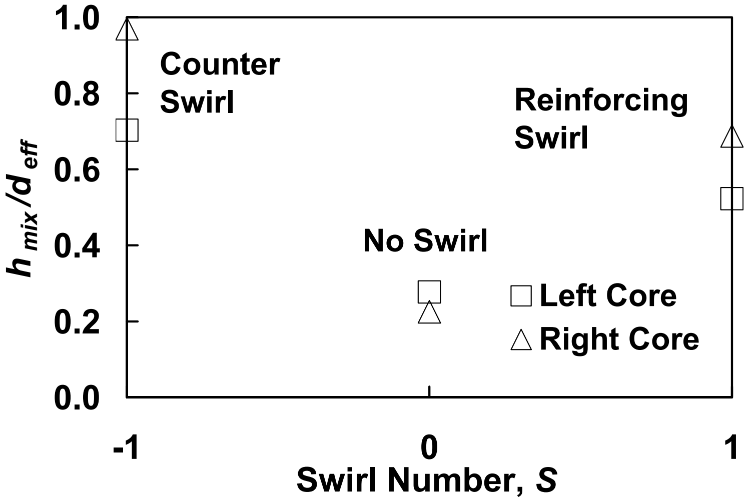

Figure 7 Maximum Concentration Vertical Locations vs. Guide Vane Angle

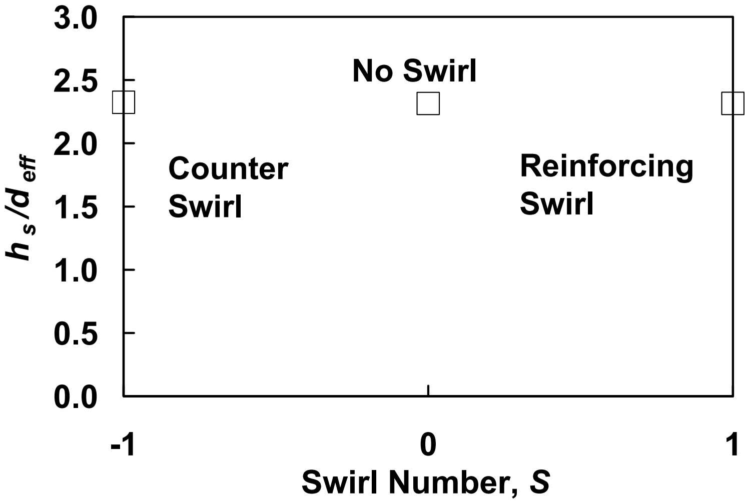

Figure 8 Plume Penetration Vertical Distance vs. Guide vane Angle

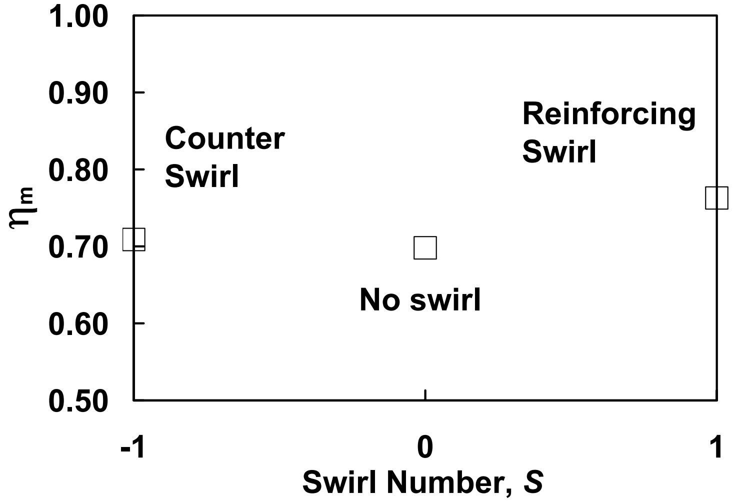

Figure 9 Injector Mixing Efficiency vs. Guide Vane Angle

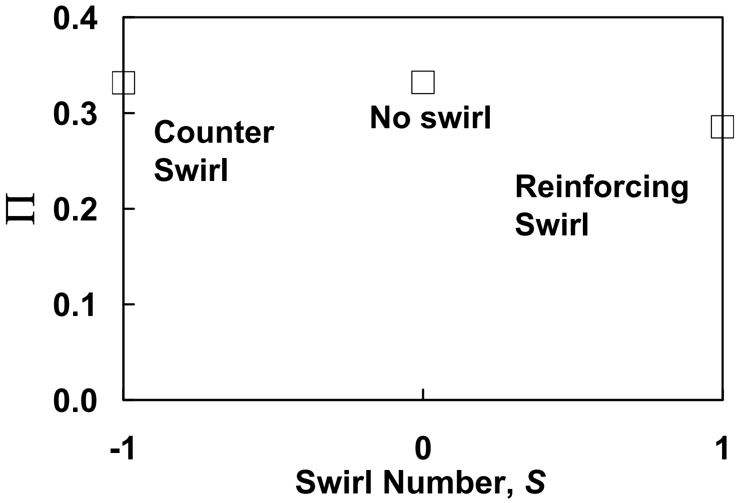

Figure 10 Total Pressure Loss Parameter vs. Guide Vane Angle

Vita

Lance S. Jacobsen

Lance Jacobsen received his bachelor's degree in aerospace engineering, graduating *magna cum laude* from Virginia Tech in 1998. He also received his Doctorate of philosophy in that same department in 2001. Currently, Lance is working at the Air Force Research Labs, in Dayton Ohio, funded by an award granted to him by the National Research Council's postdoctoral research associate program.

Lance began working for Professor Joseph A. Schetz in the junior year of his undergraduate education, helping conduct studies involving jet mixing in supersonic flows as applied to scramjet engines. As a graduate research assistant, his project involved the combination of fuel injection, mixing and combustion processes in supersonic flows for the purpose of developing an integrated fuel injector and flame holding system (using plasma torch igniters) for scramjet engines. Currently, Lance is applying his knowledge on the above-mentioned areas to scramjet-related projects for the Air Force Airbreathing Propulsion Directorate.

Born on May 19th, 1974, in Pretoria, South Africa, Lance and his family immigrated to America when he was four years old. He spent most of his adolescent life in San Diego, California, moving to Virginia in 1994. Since June of 2001, Lance has been living in Dayton, Ohio. He happily married Susanne B. Taylor on July 14th, 2001.

Lance intends to pursue a career in hypersonic propulsion and reusable launch vehicle technologies. He intends to use his knowledge of mixing and combustion to help further progression of air breathing engines for use as our next generation space access vehicles.